IMT School for Advanced Studies, Lucca
Lucca, Italy

Multi-field and multi-scale modeling of fracture for renewable energy applications

PhD Program in Systems Science

Track in Computer Science and Systems Engineering

XXXVI Cycle

By

Zeng Liu

2024

The dissertation of Zeng Liu is approved.

PhD Program Coordinator: Alberto Bemporad, IMT School for Advanced Studies Lucca

Advisor: Prof. Marco Paggi, IMT School for Advanced Studies Lucca

Co-Advisor: Prof. Jose Antonio Reinoso Cuevas, Universidad de Sevilla

The dissertation of Zeng Liu has been reviewed by:

Prof. Berkin Dortdivanlioglu, University of Texas at Austin

Prof. Guadalupe Vadillo, University Carlos III of Madrid

Prof. Alberto Sapora, Politecnico di Torino

IMT School for Advanced Studies Lucca
2024

I dedicate this thesis to my family for their unconditional love and support.

Contents

List of Figures

xv

List of Tables

Acknowledgements

Firstly, I am very grateful to my supervisors Prof. Marco Paggi and Prof. Jose Reinoso for their tremendous guidance and support in terms of both research and life during my PhD study. I enjoy a lot during this journey.

This thesis is based on the articles listed in the section of Publication. The work in Chapter 2 is taken from Publication 1 and 2, the work in Chapter 3 is taken from Publication 3 and 6 (In Preparation), and the work in Chpater 4 is taken from Publication 4 and 5.

Finally, I would like to extend my heartfelt appreciation to all my friends and family members.

Publications

1. Liu, Z., Reinoso, J. and Paggi, M., 2022. Hygro-thermo-mechanical modeling of thin-walled photovoltaic laminates with polymeric interfaces. Journal of the Mechanics and Physics of Solids, 169, p.105056.

2. Liu, Z., Lenarda, P., Reinoso, J. and Paggi, M., 2023. A multifield coupled thermo-chemo-mechanical theory for the reaction-diffusion modeling in photovoltaics. International Journal for Numerical Methods in Engineering, 124(12), pp.2876-2901.

3. Liu, Z., Reinoso, J. and Paggi, M., 2022. Phase field modeling of brittle fracture in large-deformation solid shells with the efficient quasi-Newton solution and global–local approach. Computer Methods in Applied Mechanics and Engineering, 399, p.115410.

4. Liu, Z., Marino, M., Reinoso, J. and Paggi, M., 2023. A continuum large-deformation theory for the coupled modeling of polymer–solvent system with application to PV recycling. International Journal of Engineering Science, 187, p.103842.

5. Liu, Z., Reinoso, J. and Paggi, M., 2022. A humidity dose-CZM formulation to simulate new end-of-life recycling methods for photovoltaic laminates. Engineering Fracture Mechanics, 259, p.108125.

6. Liu, Z., Lenarda, P., Reinoso, J. and Paggi, M, 2023. Phase field modeling of silicon crystalline cracking in 3D thin-walled photovoltaic laminates. (In Preparation)

Abstract

This thesis is mainly focused on the computational modeling of solar cell cracking, multiphyics phenomena, and recycling of photovoltaic (PV) modules through the finite element method. Specifically, it consists of three parts. In the first part, a comprehensive hygro-thermo-mechanical computational framework in the 3D setting is proposed to model the coupled degradation phenomena in the PV modules for the durability analysis, and it is applied to the simulation of three international standard tests of PV modules, namely the damp heat test, the humidity freeze test, and the thermal cycling test. The second part is focused on the crack modeling of very thin and brittle silicon solar cells in the PV modules, and a reliable computational framework integrating solid shell element formulation with phase field fracture modeling is developed using the efficient quasi-Newton solution scheme and global local approach. The excellent performance is showcased through the simulation of different boundary value problems, and then applied to predict the crack growth of silicon solar cells when the PV modules are subjected to different external loadings. The third part addresses the efficient recycling of PV modules through the numerical modeling method by the development of 3D interface finite element with humidity-dose enhanced cohesive zone model for the peeling simulation to separate different layers, and diffusion-swelling large deformation continuum theory for the nondestructive recovery of silicon cells in the PV recycling using the solvent method. With these tools at hand, it is possible to design suitable virtual testing procedures for PV durability and recyclability analysis.

Chapter 1

Introduction

1.1 Introduction to photovoltaic modules

Nowadays renewable energy plays a key role in the socio-economic development, and different types of solutions through various technologies rapidly emerge due to the increasing demand of reducing the energy deficit. Photovoltaic (PV) technology is the dominant choice in the renewable energy market, and it is not only widely used for the industry, but also for the individual needs.

A PV module is usually a laminate composed of tempered glass, solar cells, backsheet and encapsulant layers, see Fig. 1. Different components are adhesively bonded to each other [1]. This multilayer system can ensure the safety and performance of PV modules but forms a number of interfaces that are potential paths for contaminant ingress, causing delamination [2], which eventually promotes many other further ageing mechanisms such as polymer degradation, corrosion of metalic materials inside the system, loss of light transmission, and so on [3, 4]. The reliability of encapsulation is therefore crucial for the durability and the service life of PV modules [5, 6]. The most commonly used encapsulant material in the existing PV installations is Epoxy Vynil Acetate (EVA) that, interposed in the form of layers between the glass and the silicon solar cells, and between the solar cells and the backsheet, holds the components to-
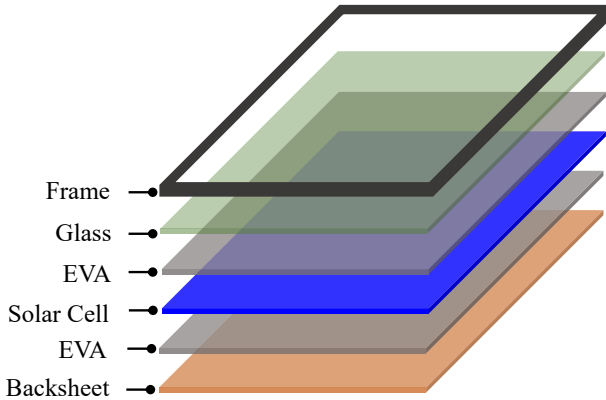
Figure 1: The general structure of a typical PV module [1].

gether and protects the module from outside harsh environments [7].

The conversion of solar energy into thermal energy for the various industrial processes not only reduces the dependency on fossil resources but only minimizes the harmful emissions [9]. Photovoltaic technologies are widely used in the industrial processes, such as steam demand processes, industrial space heating, buildings and so on [10]. The majority of solar energy applications lies in the solar water heating industry, which is regarded as the most effective alternative among all the available solar thermal technologies. Solar water heating system usually consists of solar collectors and storage space, which works on the basis of the density difference between hot and cold water. Another application of solar energy is the refrigeration and air-conditioning system, and generally there are two different solar air-conditioning systems including the closed and open systems. Closed air-conditioning solar systems are capable of being installed with high temperature collectors, while open air-conditioning solar systems can heat the ambient air to certain temperature and regenerate the sorbent. Fig. 2 shows the rooftop air-conditioning solar system [8]. Due to the increasing energy demand in agriculture, photovoltaic technologies have also been widely applied to
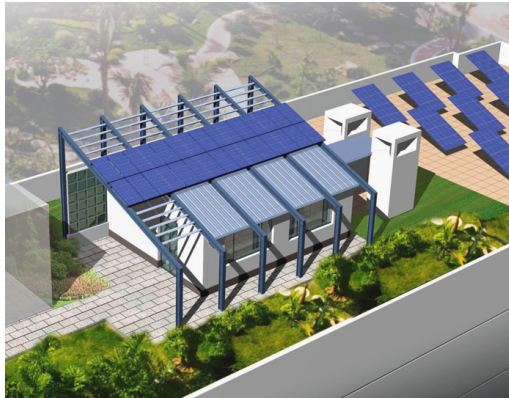
Figure 2: A typical solar air-conditioning system (adapted from [8]).

Figure 3: Photovoltaic greenhouses for agricultural purposes.

the agricultural greenhouses, which aims at creating an appropriate environment for crops growth. According to the previous studies [11, 12, 13], the amount of sunlight that enters the greenhouse can be significantly increased by the use of semi-transparent and transparent photovoltaic modules, and besides, light absorption with different wavelengths can be provided for the growth of different plants through the selective plastic films. As a result of the wide application of photovoltaic greenhouse, the anti-season planting becomes possible, leading to higher agricultural income [14]. Fig. 3 shows the photovoltaic greenhouse for agricultural purposes. Another interesting photovoltaic application is to improve the traditional breeding by providing sufficient green energy in harsh environment, such as fishery shown in Fig. 4. The combination of photovoltaic power generation and fishery can improve the efficiency of land usage and increase productivity per unit area with the establishment of photovoltaic panels over the water that breeds fishes and shrimps. On the other hand, the purification of waste water to alleviate the environmental pollution has received a lot of attention, and the photovoltaic technologies can also significantly contribute to this industrial process. Fig. 5 shows the integrated solar waste water purification system. The oxidation ditch driven by the solar system can work without the storage battery to remove the nitrogen and phosphate from the waste water [15]. Generally speaking, photovoltaic technologies have been explosively developed through its combination with new energy requirements and thus play a significant role in the modern industrialization.

1.2 Durability of photovoltaic modules: Accelerated hygro-thermo-mechanical ageing

Photovoltaic technology has been widely recognized as a promising solution for the energy security and the low-carbon economy in the near future owing to its high efficiency and low manufacturing cost [16]. Despite the advantages and strengths, the PV modules are sensitive to moisture diffusion as well as chemical reactions, especially in hygrothermal outdoor environments [17, 1, 18, 19, 20], and thus its reliability is not

Figure 4: Photovoltaic fishery.

Figure 5: Photovoltaic application in waste water purification.

still very competitive. A great deal of research has been focused on investigating the degradation mechanisms, see [21, 22], among many others, and most of them studied the diffusion phenomena at the constant temperature and humidity conditions. However, the realistic evaluation of PV durability is very challenging due to the coupling between the reaction-diffusion and thermo-mechanical problems, and thus requires a multiphysics framework to comprehensively study the different failure mechanisms under changing environments [23].

Reliability is defined as the probability that a product will perform normally under certain conditions for a certain period of time in the concept of engineering design [24]. In the field of PV industry, reliability and quality are strongly interrelated with each other. High-quality PV modules will lead to high reliability of the deployed products in the outdoor environment. It is worth noting that the power loss of the PV modules needs to be quantified for the assessment of the service lifetime. Accelerated testing of the PV modules to speed up the degradation process is frequently employed to identify different failure modes for research purposes. Compared with the uncontrolled outdoor ageing, the accelerated testing approaches show the monotonous degradation tendency. Accelerated ageing tests are requested by the International Electrotechnical Commission (IEC) standards for quality control and assessment of power loss after a certain number of humidity and temperature cycles inside the environmental chamber, including the thermal cycling tests, humidity freeze tests, and damp heat tests. The thermal cycling test requires the control of both humidity and temperature, and it is a stress test due to the difference of thermo-mechanical properties between different layers in the photovoltaic laminate. The humidity freeze test is similar to the thermal cycling test in terms of the maximum and minimum temperatures inside the chamber, but the time period range at the maximum temperature is much longer. In the damp heat test, the constant temperature and humidity are imposed on the photovoltaic modules to accelerate the ageing process during the entire period.

The EVA layer of PV modules is usually made of polymeric materials, and permeable to moisture, which diffuses from the edges, backsheet
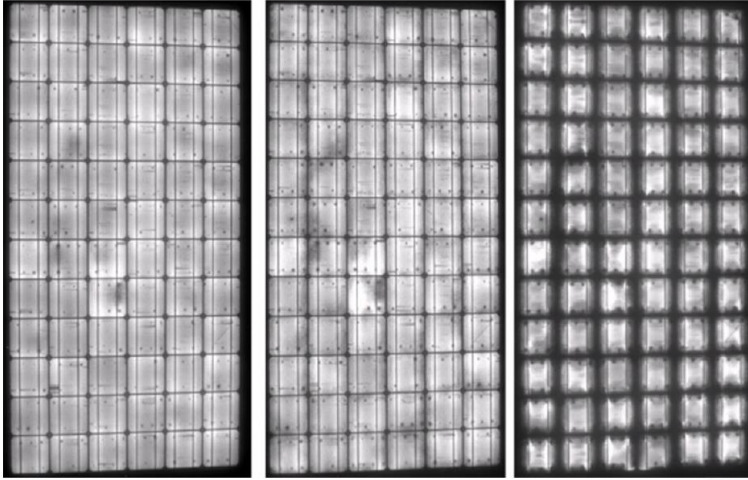
Figure 6: EL images of PV modules with moisture induced dimmer areas during the damp heat test (adapted from [25]).

and interspaces between different solar cells. This moisture diffusion can induce chemical oxidation of grid lines deposited on the surface of solar cells and subsequently lead to degradation and power loss, which has been reported in the damp heat test of PV modules exposed to the very aggressive environment with 85 °C temperature and 85% relative humidity [25, 26, 27]. As shown in Fig. 6, the dark bands can be observed at the edges of solar cells in the captured EL image after the test, which were not detected in the beginning but became thicker during aging. It is important to remark that in photovoltaics, the larger the dark – electrically inactive – area, the higher the electrical power loss of the module [28]. Particularly, the dark bands indicate the moisture ingress into the module from the edges of the solar cells over time. Since moisture can induce chemical reactions inside the modules and delamination failure between different laminae, it is crucial to establish a reliable and accurate modeling strategy of moisture diffusion along the EVA layer. The complexity regards the strong dependency of moisture diffusion coefficient of EVA on the temperature, which indicates the coupling between

the moisture and thermal fields, as shown in [29]. On the other hand, moisture diffusion also degrades the cohesive energy of EVA layer, giving rise to the delamination failure between the different laminae, such as the decohesion between solar cell and backsheet or tempered glass, which corresponds to the coupling between the mechanical and moisture fields [30, 31, 32].

Previous investigations on chemical reactions in EVA have been reported in the literature, including both experiments [33, 34] and computational modeling [29, 35]. Existing computational methods for predicting the environmental degradation of PV mainly study the diffusion under constant hygrothermal conditions and reliable models to predict the degradation phenomena under coupled thermo-mechanical loading cases are sorely lacking. Moreover, the diffusion processes are usually dependent on temperature, and spatial variation may also exist in the presence of cracks inside the PV modules. Therefore, it is essential to establish a comprehensive hygro-thermo-mechanical modeling framework to the coupled degradation phenomena over the 3D domain of the PV modules. This modeling method should enable the possibility to recall any realistic initial and boundary value problems and to simulate different accelerated aging tests with changing environmental loadings, such as the humidity freeze test, which could be very useful in estimating the maintenance costs and economic sustainability of PV systems.

1.3 Durability of photovoltaic modules: Silicon cell cracking

During the fabrication process of silicon solar cells, permanent deformations are induced from the thermomechanical loadings, which corresponds to the residual stress that leads to cracks. It was pointed out in [36] that 2 % of the silicon wafers are broken, causing the increase of production cost and material losses. Even though the fabrication process can be optimized, the imperfections inside the silicon cells during production are unavoidable, especially when the wafer thickness is reduced [37, 38]. Besides, crack formation of silicon cells can also take place during the

8

transportation and installation of PV modules in the field, as well as during the operation when subjected to the harsh environmental conditions such as wind, snow loading, hail impacts and so on [39, 40]. The cracks of silicon solar cells are usually invisible, but could produce electrically disconnected regions that significantly increase the electrical resistance, and hence reduce the power output of PV modules. Overall, the length, width and orientation of cracks in the silicon wafers directly influence the output of solar panels as pointed out in [41, 42, 43]. According to the survey of over 200 PV modules, more than 20 % of power loss has been detected due to the cell cracks in combination with EVA delamination and degradation [44]. Experimental studies in [45] reported that approximately 4 % power degradation are caused by cracks of solar cells in the mechanical load tests. When the disconnected cell area caused by crack formation and propagation is greater than 8 % of the total cell layer, the associated power loss was found to be roughly proportional to the electrically inactive area [27]. Regarding the crack direction in solar cells, several types of cracks can be observed from previous experimental studies, including parallel and perpendicular cracks, +45 and -45 cracks, and multiple direction cracks [46], as shown in Fig. 7. Different cracks lead to different power degradation of PV modules. Therefore, it is of utmost importance to develop reliable simulation tools for the fracture modeling of brittle thin-film solar cells in order to understand the impact of cracks on the performance of PV modules.

Microcracks of silicon solar cells can be formed at different stages, including the cutting of an ingot, the lamination of PV modules, the transportation and installation, and the environmental loadings during the service lifetime. The silicon substrates for the manufacturing of PV modules are typically produced by casting the silicon ingots and subsequent wafer sawing, and the wire sawing of silicon ingots can result into the cracking of wafers [48]. According to the previous study [47], the risks of crack formation increase as the thickness of the silicon solar cells has been drastically decreased. Besides, due to the difference of thermal expansion properties, thermo-mechanical residual stress can be generated during the soldering process, leading to the silicon solar cell crackings.

No crack	Several	+ 45
- 45	Parallel	Perpendicular
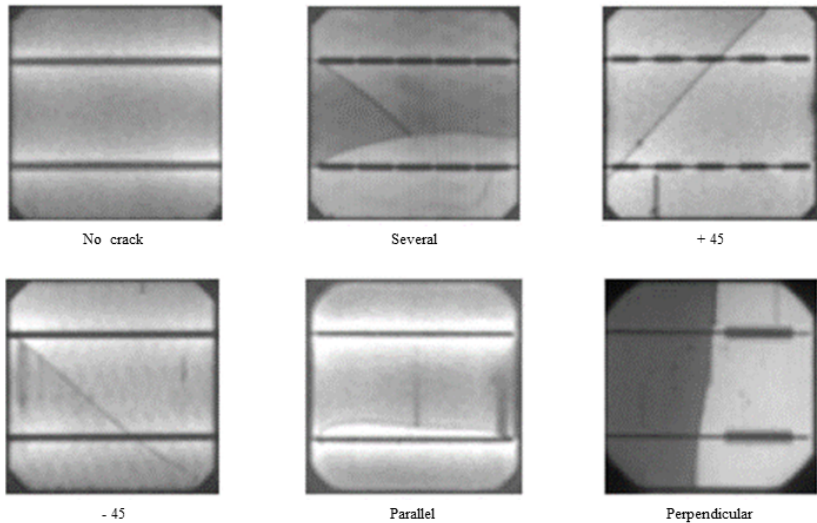
Figure 7: Different crack patterns in silicon solar cells [47].

On the other hand, the residual stress can also be generated during the lamination process of PV modules, which increases the propensity of crackings. Besides the factors during production, cracks of silicon solar cells can be produced due to improper transportation as reported in [49]. Currently there is no standardard on the way of PV transportation, and it is pointed out in [39] that transporting the PV products vertically can reduce the risks of breaking silicon solar cells compared to the way of transporting the modules horizontally. Finally, cracks of silicon solar cells and power degradation may be caused by the environmental loadings during the service lifetime, such as wind [50], snow loading [51], and hail impact [52]. Such environmental loadings increase the stress beyond the residual stress from the production processes, and lead to higher crack probability of silicon solar cells [36]. Although cracks of silicon solar cells are unavoidable as mentioned above, it is of significant importance to identify the crack characteristics so as to improve the durability of the photovoltaic modules.

1.4 Sustainability of photovoltaic modules: Recycling of the end-of-life PV modules

Massive PV modules have been deployed in the recent decades, and given the service lifetime of approximately 30 years, the pressure to handle the end-of-life modules starts to emerge. The PV modules that approach the end of the service lifetime can be reused or repaired so as to lower the environmental impacts without additional energy and material investment [38]. Although numerous economic and regulatory challenges must be addressed, the reusing strategies of PV modules are worth investigating from the circular-economy point of view. The key is that the burden from the repair or reuse of end-of-life PV modules should be lower than the environmental benefit from the subsequent reuse. Note that the reuse of PV modules requires the necessary repair for safety and performance. Due to the shorter service lifetime and lower power efficiency of reused PV modules, the system owners may not gain much economic values from the second-hand products [53]. However, to avoid the material loss of end-of-life modules, the landfills have been discouraged by the European policy since the beginning of this century. The values of end-of-life PV materials are estimated to be approximately 15 billion US dollars and 2 billion new PV products can be manufactured by the reuse of the reclaimed materials, which accounts for around 630 GW of new capacity [54]. Furthermore, there is a strong incentive to avoid environmental pollution for the recycling of end-of-life PV modules [55, 56]. In general, the environmental requirement and material recovery necessitate the development of reliable PV recycling techniques for the circular source of PV materials.

The improper disposal of PV panels by landfilling is intolerable nowadays as the hazardous metal components such as lead and cadmium, among others, would cause pollution to the environment [57]. Besides, it is of great importance to recover the precious silicon wafers and other metals for the manufacturing of new products to reduce the cost, supporting the sustainable development of energy production [58, 59, 60, 61]. Normally, the PV module is a laminate structure composing of dif-

ferent plies including tempered glass, silicon solar cells, and backsheet, which are bonded to each other by ethylene-co-vinyl acetate (EVA) layers [16]. Therefore, many approaches have been developed in the relatd literature in order to separate the different layers by the removal of EVA and then reclaim valuable materials in the end-of-life PV modules [1, 62, 63, 64]. The use of nitric acid to remove EVA layers was proposed in [65], but the resulting NO_x emissions are harmful to the environments. Thermal decomposition is another alternative method to remove EVA layers but leads to the release of harmful gas because of the existence of fluorinated compounds [66, 67, 68]. Also, some thermal or mechanical pretreatments are designed to dissemble the backsheet before the further recycling process [69, 70, 71]. In addition, recycling of PV modules using the organic solvent method has received a great deal of attention in the recent years [72, 73, 74, 75, 76]. In spite of these efforts, it is very challenging to reclaim unbroken silicon wafers, which is a key problem in the PV recyling as the thickness of silicon cell layers was reduced to approximately 0.1 mm after 2006 [77].

The major factor responsible for the degradation of PV modules is the aging of EVA layers, while the service lifetime of silicon wafers is much longer than that of PV modules [72]. In this regard, much cost can be saved with the reclaim of structurally intact silicon wafers for the manufacturing of new PV products, since the silicon ingot manufacturing process can be omitted. High environment pollution and energy consumption can be avoided with such an ideal reusing strategy that also reduces around 40% cost of PV production [78]. Unfortunately, very scarce research activities have been devoted to the nondestructive reclaim of intact silicon wafers in PV recycling, such as thermal decomposition at specific heating rates [79] and breakage of glass layer before thermal treatment [80]. Although it is possible to recover the intact silicon wafers using the these methods, the thermal decomposition is actually difficult to control and the cracking of glass during the treatment tends to break the the silicon wafers. In addition to this, results in [72] have indicated that the swelling of EVA during the recycling process using the solvent method can lead to the cracking of silicon cell layer. Therefore, there is

an urgent need to develop a suitable computational framework to help control the recycling process for the recovery of structurally intact silicon wafers.

In the recent decade, recycling of photovoltaic modules have received a lot attention, and different organizations are established to address this topic. PHOTORAMA is an EU funded innovation action striving to improve recycling of solar panels, and it is a consortium consisting of 13 organizations from 2021 to 2024. Another interesting project is the CABRISS, which is also an EU funded consortium with 11 companies and 5 research institutes for pioneering a circular economy on photovoltaics. A France-based start-up named ROSI has claimed to develop an innovative and viable process to recover silicon from the end-of-life photovoltaic modules. Besides, there is another European project ReProSolar led by Veolia Germany that designs a new delamination technology which is able to separate solar cells efficiently from the glass plate for the recovery of all materials without shredding the photovoltaic modules.

1.5   Outline of the thesis

This work is mainly focused on the computational modeling of thin-walled photovoltaic laminates with application to the durability and recycling analysis. In this section, each chapter in the following is outlined.

Chapter 2 presents the comprehensive computational framework at finite deformation for the multiphysics modeling of the degrdation phenomena in the photovoltaic modules. The developed framework is then applied to simulate the three standard international tests of PV modules, including the damp heat test, the humidity freeze test, and the thermal cycling test.

Chapter 3 addresses the crack modeling of brittle silicon solar cells in the photovoltaic modules using the global-local approach with solid shell element formulation. For the efficient modeling, the quasi-Newton monolithic solution scheme is proposed, and its excellent performance is demonstrated by the comparison with the standard staggered Newton solution scheme through the different boundary value problems. This

computational framework is then applied to the modeling of silicon solar cell crackings in the PV modules under different boundary conditions, which showcases its capacity to predict the crack growth in the thin-film silicon solar cells.

Chapter 4 outlines the numerical simulation of PV recycling problems. It consists of two parts. In the first part, a large deformation theory is proposed to model the swelling-diffusion problem in the PV recycling using the solvent method, which aims at predicting the EVA swelling induced cracking of silicon solar cells. In the second part, given the degradation of EVA in the end-of-life PV modules, a computational framework integrating large deformation interface element with the polynomial cohesive zone model incorporating the moisture and temperature effects is developed to simulate the peeling tests of PV panels.

Chapter 5 addresses the main conclusions and future developments of this thesis.

Chapter 2

Multiphysics modeling for the durability analysis of photovoltaic laminates

The main content of this chapter is taken from my own publication - Z. Liu, J. Reinoso, M. Paggi. "Hygro-thermo-mechanical modeling of thin-walled photovoltaic laminates with polymeric interfaces" [16].

The durability analysis of PV modules has received much attention in the past decades [81, 82, 16, 83], and modeling polymeric materials EVA is quite challenging as it requires a multiphysics framework to predict their overall performance and degradation accurately [84]. This chapter establishes a comprehensive computational framework for the coupled modeling of hygro-thermo-chemo-mechanical degradation phenomena of PV laminates for durability analysis.

Regarding the thermo-mechanical behavior, the EVA polymer shows a strong thermo-visco-elastic constitutive response, and its Young's modulus varies within a range by three orders of magnitude depending on temperature, as experimentally reported in [85, 86]. In order to approximate the power-law trend from experimental observation, the generalized Maxwell rheological models can be used to determine the relaxation modulus with exponential type equations. However, a great num-

ber of elements as well as model parameters have to be taken into account, which requires laborious calibration work. To simplify the procedure of parameter identification, the fraction calculus method has been proved to be very effective for the modeling of visco-elastic constitutive behaviour [87, 88, 89]. Thus this formulation has been adopted to describe the rheologically complex behaviour of polymeric EVA, whose microstructure changes with temperature, and according to [90], only two temperature dependent parameters are required for its complete description.

To model these coupled nonlinear hygro-thermo-mechanical problems in PV modules, a comprehensive computational framework in the three-dimensional space, where the coupled thermo-mechanical problem and the moisture diffusion are solved in a staggered manner, is required so that the dependency of diffusion properties of EVA on the thermo-mechanical fields can be accounted for properly. Analytical solution for the moisture diffusion along EVA layer proposed in [29] assumes constant diffusivity without any update based on the actual temperature, and the spatial variation due to temperature dependency is ignored. Although it might be feasible in the steady state temperature case, such as damp heat test, its validity in the cases of cyclic temperature boundary loading in the humidity freeze and thermal cycling tests is hard to guarantee. Besides, since moisture can also diffuse from the channel cracks and interspaces between the solar cells, it is almost impossible to obtain analytical solution in these complex cases. To overcome the limitations of analytical solution methods, the finite element modeling methodology in the three-dimensional setting is proposed to simulate the coupled problems in this work. The thermo-mechanical phenomena in the PV laminate, which is much faster than moisture diffusion, is firstly solved through a monolithic fully implicit solution scheme, see Fig. 8. The calculated temperature and displacement fields inside the EVA layer are then projected to the nodes of another finite element model specific for moisture diffusion, so that the diffusion properties at the corresponding time and space can be determined accordingly. With updated diffusion coefficient from thermo-mechanical solution at each time increment, the mois-
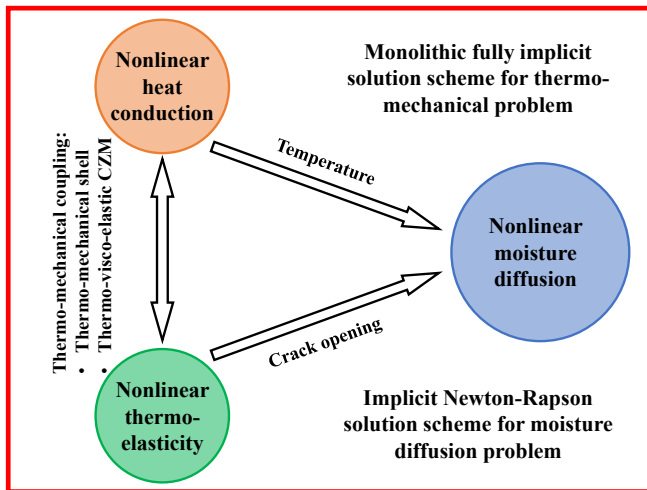
Figure 8: The proposed solution scheme for the 3D hygro-thermo-mechanical modeling framework.

ture diffusion can be solved by the Newton-Rapson scheme in a standard way.

To save the computational efficiency, the EVA layers are modelled using zero-thickness interfaces elements with thermo-visco-elastic cohesive zone model based on the fractional calculus method, and a thermo-mechanical solid shell formulation incorporating the EAS and ANS methods to remedy potential locking pathologies, which is kinematically compatible with the 3D interface element, is established here for the modeling of the different thin-walled laminae in PV modules such as glass layer, backsheet and silicon solar cell layer. Modeling thermo-mechanical responses in thin-walled structures necessitates the consistent derivation of formulations accounting for the stress and heat transfer across the internal interfaces. To use the 3D constitutive laws without further modifications, recent advances in shell element formulation aim at incorporating the three-dimensional effects into the corresponding implementation. To achieve this, it is pointed out in [91, 92] that a linear normal

strain distribution through the thickness direction has to be embodied in the shell element formulation. In this regard, two paths have been followed: (i) shell formulations that include the linear distribution using either quadratic displacement distribution or enhanced strain methods through the reference surface of body in the thickness direction [93, 94, 95, 96, 97, 98], and (ii) shell formulations relying on the solid shell concept through the parametrization of the top and bottom surfaces of the body [99, 100, 101, 102, 103]. The latter has been extensively developed in the past decades since the complex update procedure regarding the rotation tensor can be completely avoided. However, the extension of solid shell formulation to thermo-mechanical applications has received very limited attention, see [104, 105, 106, 107]. Besides, to alleviate the locking pathologies in shell formulations complying with the low-order kinematic interpolation, different numerical strategies have been proposed such as the EAS method [108, 109, 110, 111], the ANS method [112, 113], and combination of them [114, 115, 116].

This section is structured as follows. In Section 2.1, the primary aspects of coupled thermo-mechanical analysis along with the definition of kinematics and constitutive formulation, the thermo-visco-elastic cohesive zone model through the fractional calculus method, as well as temperature and gap dependent moisture diffusion is presented in detail. The weak forms of the governing equations for the hygro-thermo-mechanical problems and the corresponding finite element discretization are given in Section 2.1.4. In particular, the Hu-Washizu variational principle with thermo-mechanical solid shell formulation accounting for the EAS and ANS methods to alleviate locking effects is outlined, and this section also covers the 3D thermo-mechanical interface and moisture diffusion finite element implementation, respectively. Details of the numerical algorithm for the implementation of the hygro-thermo-mechanical framework with staggered solution scheme are provided in Section 2.1.5. Then this modeling methodology is applied to simulate the three international standard tests of PV laminates, namely the damp heat test, the humidity freeze test, and the thermal cycling test, and numerical predictions are compared with analytical solution for the damp heat case with

the constant temperature boundary condition, as well as experimental electroluminescence images obtained from the thermal cycling test with the cyclic temperature boundary condition, which is presented in Section 2.2.

2.1 Hygro-thermo-mechanical modeling framework for the PV laminate

In this section, the modeling framework for the thermo-mechanical coupling in thin-walled PV laminae separated by thermo-visco-elastic interfaces and moisture diffusion along the polymeric layers is presented. Moisture diffusion takes place in the polymeric encapsulant layers of laminate, which usually percolates from the free edges and towards the center of solar cell panels. The encapsulant layers are made of visco-elastic polymer materials and permeable to moisture, which is one of the dominant factors leading to the electrical degradation of PV modules during the service life. Besides, moisture diffusion can also degrade the adhesion strength of encapsulant layers, causing delamination failure between silicon solar cells and backsheet or the glass superstrate. In order to effectively model the cohesive mechanical behavior of encapsulant layers, a 3D cut-off traction-separation law is formulated.

2.1.1 Coupled thermo-mechanical kinematics formulation

For thermo-mechanical boundary value problems in solids, displacement and absolute temperature fields are usually chosen as the independent fields in the coupled governing equations. In the 3D setting, let $\mathcal{B}_0 \subset \mathbb{R}^3$ denotes the reference configuration, while $\mathcal{B}_t \subset \mathbb{R}^3$ denotes the current configuration. The position vectors of material points in the reference and current configurations are represented by $\mathbf{X}$ and $\mathbf{x}$, respectively. The displacement field is denoted as $\mathbf{u}(\mathbf{X}, t) : \mathcal{B}_0 \times [0, t] \to \mathbb{R}^3$, which is a vector valued function during the time interval $[0, t]$. The absolute temperature field $T(\mathbf{X}, t) : \mathcal{B}_0 \times [0, t] \to \mathbb{R}_+$ is a smooth scalar-value function. As shown in Fig. 9, the body motion denoted by $\boldsymbol{\varphi}(\mathbf{X}, t) : \mathcal{B}_0 \times [0, t] \to \mathbb{R}^3$

19
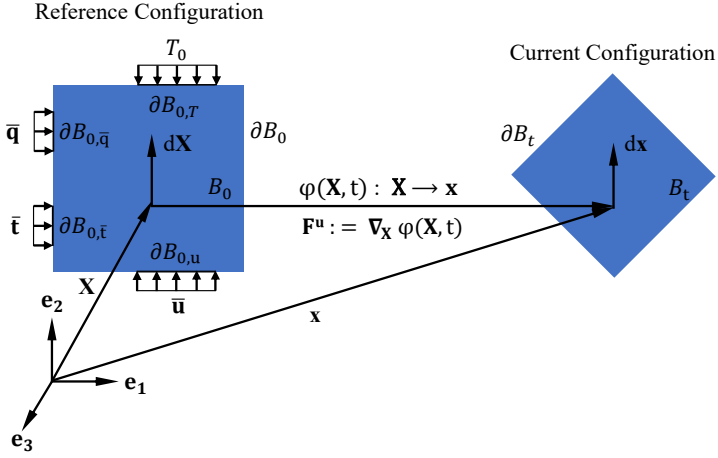
Figure 9: The finite thermo-mechanical deformation of a three-dimensional body from the reference configuration to the current configuration.

maps the material point $\mathbf{X}$ in the reference configuration onto its corresponding point $\mathbf{x}$ in the current configuration.

The mechanical boundary conditions are imposed on the boundary of deformable body in the reference configuration $\partial \mathcal{B}_0$, which is divided by disjoint sets $\partial \mathcal{B}_{0,u} \subset \partial \mathcal{B}_0$ and $\partial \mathcal{B}_{0,\bar{t}} \subset \partial \mathcal{B}_0$ with $\partial \mathcal{B}_{0,u} \cap \partial \mathcal{B}_{0,\bar{t}} = \emptyset$. The Dirichlet boundary condition $\mathbf{u} = \bar{\mathbf{u}}$ is applied on $\partial \mathcal{B}_{0,u}$, while Neumann boundary condition characterized by prescribed tractions $\boldsymbol{\sigma} \cdot \mathbf{n} = \bar{\mathbf{t}}(\mathbf{X}, t)$ is applied on $\partial \mathcal{B}_{0,\bar{t}}$. Similarly, the temperature boundary condition $T = T_0$ is prescribed over $\partial \mathcal{B}_{0,T} \subset \partial \mathcal{B}_0$, while the heat flux boundary condition $q = \bar{q}$ is prescribed over $\partial \mathcal{B}_{0,\bar{q}} \subset \partial \mathcal{B}_0$, such that $\partial \mathcal{B}_{0,T} \cap \partial \mathcal{B}_{0,\bar{q}} = \emptyset$. Besides, the deformable body can also be divided into parts $\mathcal{B}_0^i (i > 0)$ such that $\mathcal{B}_0 = \cup_i \mathcal{B}_0^i$, which could be assigned with different mechanical and thermal constitutive behaviors.

The deformation gradient, which is defined as the gradient of deformation map with regard to the reference configuration, can be expressed as

$$\mathbf{F}^u := \partial_{\mathbf{X}} \boldsymbol{\varphi}(\mathbf{X}, t) = \nabla_{\mathbf{X}} \boldsymbol{\varphi}(\mathbf{X}, t), \tag{2.1}$$

where $\nabla_{\mathbf{X}}[\bullet]$ denotes the Lagrangian gradient operator. This operator represents the map of line element $d\mathbf{X}$ in the reference configuration onto the corresponding line element $d\mathbf{x} = \mathbf{F}^u d\mathbf{X}$ in the current configuration. The Jacobian of the deformation is defined as the determinant of deformation gradient $J^u := \det[\mathbf{F}^u] > 0$, where $\det[\bullet]$ represents the determinant operator.

The covariant tangent vectors $\mathbf{G}_i(\boldsymbol{\xi})$ and $\mathbf{g}_i(\boldsymbol{\xi})$ are defined as the partial derivatives of position vectors with respect to the convective coordinates ξ^i in the reference and current configurations, respectively

$$\mathbf{G}_i(\boldsymbol{\xi}) := \frac{\partial \mathbf{X}(\boldsymbol{\xi})}{\partial \xi^i}, \quad \mathbf{g}_i(\boldsymbol{\xi}) := \frac{\partial \mathbf{x}(\boldsymbol{\xi})}{\partial \xi^i}, \quad i = 1, 2, 3. \tag{2.2}$$

The contravariant vectors are defined by $\mathbf{G}_i \cdot \mathbf{G}^j = \delta_i^j$ and $\mathbf{g}_i \cdot \mathbf{g}^j = \delta_i^j$, and the metric tensors are defined as $\mathbf{G} = G_{ij}\mathbf{G}^i \otimes \mathbf{G}^j = G^{ij}\mathbf{G}_i \otimes \mathbf{G}_j$, $\mathbf{g} = g_{ij}\mathbf{g}^i \otimes \mathbf{g}^j = g^{ij}\mathbf{g}_i \otimes \mathbf{g}_j$. The left and right Cauchy-Green deformation tensors, which are derived from displacement field vectors, are given by

$$\mathbf{C}^u := [\mathbf{F}^u]^{\mathrm{T}}\mathbf{g}[\mathbf{F}^u], \quad \mathbf{b}^u := [\mathbf{F}^u]\mathbf{G}^{-1}[\mathbf{F}^u]^{\mathrm{T}}. \tag{2.3}$$

The Green-Lagrange strain tensor $\mathbf{E}^u$ is defined as

$$\mathbf{E}^u := \frac{1}{2}\left[\mathbf{C}^u - \mathbf{G}\right]. \tag{2.4}$$

In order to alleviate the locking effects according to [106], an incompatible strain tensor $\tilde{\mathbf{E}}$ is incorporated into the displacement-derived quantities, and the total Green-Lagrange strain by additive decomposition takes the form of

$$\mathbf{E} := \mathbf{E}^u + \tilde{\mathbf{E}}. \tag{2.5}$$

This decomposition constitutes the fundamentals of assumed strain method, and thus the enhanced right Cauchy-Green tensor $\mathbf{C}$ is given by

$$\mathbf{C} := \mathbf{C}^u + \tilde{\mathbf{C}} = 2(\mathbf{E}^u + \tilde{\mathbf{E}}) + \mathbf{G}. \tag{2.6}$$

Then the enhanced deformation gradient $\mathbf{F}$ can be derived by the polar decomposition theorem. The displacement derived deformation gradient can be decomposed as $\mathbf{F}^u := \mathbf{R}\mathbf{U}^u$, where $\mathbf{R}$ and $\mathbf{U}^u$ represents the

rotation and right-stretch tensors, respectively. Based on Eq. (2.6), the modified right-stretch tensor $\mathbf{U}$ that accounts for the incompatible strain is calculated as

$$\mathbf{U} := \mathbf{C}^{1/2}. \tag{2.7}$$

Since the calculation of rotation tensor is straightforward, the modified deformation gradient $\mathbf{F}$ can be computed as

$$\mathbf{F} := \mathbf{R}\mathbf{U}. \tag{2.8}$$

The modified corresponding Jacobian is given by $J = \det[\mathbf{F}]$.

Consider $\mathcal{P}_0 \subset \mathcal{B}_0$ from the continuum body $\mathcal{B}_0$ in the reference configuration with the delimiting boundary $\partial\mathcal{P}_0$, and its spatial counterpart $\mathcal{P}_t \subset \mathcal{B}_t$, with the boundary $\partial\mathcal{P}_t$ in the current configuration. It is postulated in Cauchy stress theorem that there is a linear dependency between the normal vector $\mathbf{n}$ of $\partial\mathcal{P}_t$ and traction $\mathbf{t}$ through Cauchy stress tensor $\boldsymbol{\sigma}$, which is given by

$$\mathbf{t} = \boldsymbol{\sigma} \cdot \mathbf{n}. \tag{2.9}$$

In line with this theorem, the first Piola–Kirchhoff stress tensor $\mathbf{P}$, which is also known as nominal stress tensor, is defined as

$$\mathbf{P} = J\boldsymbol{\sigma} \cdot \mathbf{F}^{-1}. \tag{2.10}$$

The first Piola–Kirchhoff traction vector $\hat{\mathbf{T}}$ is defined as $\hat{\mathbf{T}} = \mathbf{P} \cdot \mathbf{N}$, which satisfies the force equality $\hat{\mathbf{T}}\mathrm{d}S = \mathbf{t}\mathrm{d}s$, and $\mathbf{N}$ denotes the normal direction in the reference configuration. Accordingly, the second Piola–Kirchhoff stress tensor $\mathbf{S}$, which is a symmetrical stress tensor, is given by

$$\mathbf{S} = \mathbf{F}^{-1} \cdot \mathbf{P} = J\mathbf{F}^{-1} \cdot \boldsymbol{\sigma} \cdot \mathbf{F}^{-1}. \tag{2.11}$$

Analogously, Stokes heat flux theorem in the current configuration reads,

$$q_n = \mathbf{q} \cdot \mathbf{n}, \tag{2.12}$$

where q_n and $\mathbf{q}$ represent the scalar and vector heat flux, respectively, and $\mathbf{n}$ denotes the normal direction in the current configuration. The material

heat flux $\mathbf{Q}$ can be determined from the equality condition $\mathbf{q} \cdot \mathbf{n}\mathrm{d}s = \mathbf{Q} \cdot \mathbf{N}\mathrm{d}S$, and thus its definition can be expressed as

$$\mathbf{Q} = J\mathbf{F}^{-1} \cdot \mathbf{q}. \tag{2.13}$$

Recalling the theoretical developments outlined in [117, 118], the Helmholtz free energy function for the thermo-elastic Kirchhoff-Saint-Venant constitutive material law is given by

$$\begin{aligned}
\Psi(\mathbf{E}, T) = &\frac{1}{2}\lambda \left(\mathrm{tr}[\mathbf{E}]\right)^2 + \mu\mathrm{tr}[\mathbf{E}^2] \\
&- 3\kappa\alpha\mathrm{tr}[\mathbf{E}] \left(T - T_0\right) + \rho_0 c_p \left[\left(T - T_0\right) - T\log\frac{T}{T_0}\right],
\end{aligned} \tag{2.14}$$

where κ is the bulk modulus, λ and μ are the Lame constants, ρ_0 is the mass density, α represents the thermal expansion coefficient and T_0 stands for the reference temperature.

The second Piola–Kirchhoff stress tensor can be obtained from the constitutive relationship, which reads

$$\mathbf{S} := \partial_{\mathbf{E}}\Psi = \lambda \left(\mathrm{tr}[\mathbf{E}]\right)\mathbf{1} + 2\mu\mathbf{E} - 3\kappa\alpha \left(T - T_0\right)\mathbf{1}, \tag{2.15}$$

where $\mathbf{1}$ is the second-order identity tensor. The constitutive operators in the curvelinear settting take the form

$$\mathbb{C} = \partial_{\mathbf{EE}}^2\Psi = \left[\lambda G^{ij}G^{kl} + \mu\left(G^{ik}G^{jl} + G^{il}G^{jk}\right)\right]\mathbf{G}_i \otimes \mathbf{G}_j \otimes \mathbf{G}_k \otimes \mathbf{G}_l, \tag{2.16a}$$

$$\mathbf{Z} = \partial_{T\mathbf{E}}^2\Psi = -3\kappa\alpha G^{ij}\mathbf{G}_i \otimes \mathbf{G}_j. \tag{2.16b}$$

where $\mathbb{C}$ is the fourth-order material stiffness tensor, and $\mathbf{Z}$ is the second-order tensor associated with the coupling term of the Helmholtz function.

Assuming isotropic conductivity $\mathbf{k} = kg^{ij}\mathbf{g}_i \otimes \mathbf{g}_i$ [119], the material heat flux vector in the curvilinear setting can be expressed as

$$\begin{aligned}
\mathbf{Q} &= -J\mathbf{F}^{-1}\mathbf{k}\mathbf{F}^{-T}\nabla_{\mathbf{X}}T \\
&= -Jk\left(\mathbf{G}_i \otimes \mathbf{g}^i\right)\left(g^{kl}\mathbf{g}_k \otimes \mathbf{g}_l\right)\left(\mathbf{g}^j \otimes \mathbf{G}_j\right)\nabla_{\mathbf{X}}T \\
&= -Jk\mathbf{C}^{-1}\nabla_{\mathbf{X}}T.
\end{aligned} \tag{2.17}$$

where $\mathbf{C}^{-1}$ stands for the inverse of right Cauchy-Green tensor. The formulation can be further simplified as $\mathbf{Q} = -k_0 \mathbf{G} \nabla_{\mathbf{X}} T$ under isotropic assumption, where k_0 represents the thermal conductivity in the reference configuration.

2.1.2 Thermo-visco-elastic cohesive interface model for polymeric layers

Assuming that the polymeric layers can be treated as zero-thickness imperfect interfaces, the displacement and temperature fields inside the encapsulant layers are allowed to be discontinuous through the thickness direction. The cohesive zone model assumes the existence of free energy density per unit undeformed area, and thermo-mechanical coupling can be achieved by making conductivity properties dependent on the cohesive damage and interface tractions dependent on the temperature field. Let define the displacement gaps along the interfaces in three-dimensional setting as: $\boldsymbol{\Delta} = (\Delta_n, \Delta_t, \Delta_s)$, where $\Delta_n, \Delta_s, \Delta_t$ stand for normal, tangential and shear displacement gaps, respectively, and temperature gap Δ_T along the interface, which play the role of internal variables for the description of the debonding process along polymeric interfaces.

Hence, the coupled thermo-mechanical model for deformable laminae body is enriched due to the presence of cohesive traction field and heat flux through the thickness direction of polymeric layer. Under the assumption of continuity along the interface, the out-of-plane tearing and in-plane sliding traction vectors are defined as

$$\tau_I = \begin{cases} K_I(t, \langle T \rangle) \Delta_I, & \text{if } \Delta_I \in J_I \\ 0, & \text{if } \Delta_I \notin J_I \end{cases} \tag{2.18}$$

where $J_I = (-\delta_I^c, +\delta_I^c)$, $\langle T \rangle$ is the average temperature along the interface and $I = t, s$, while the opening traction component σ is defined as

$$\sigma = \begin{cases} \epsilon \Delta_n, & \text{if } \Delta_n < 0 \\ K_n(t, \langle T \rangle) \Delta_n, & \text{if } \Delta_n \in J_n \\ 0, & \text{if } \Delta_n \notin J_n \text{ and } \Delta_n \geq 0 \end{cases} \tag{2.19}$$

24
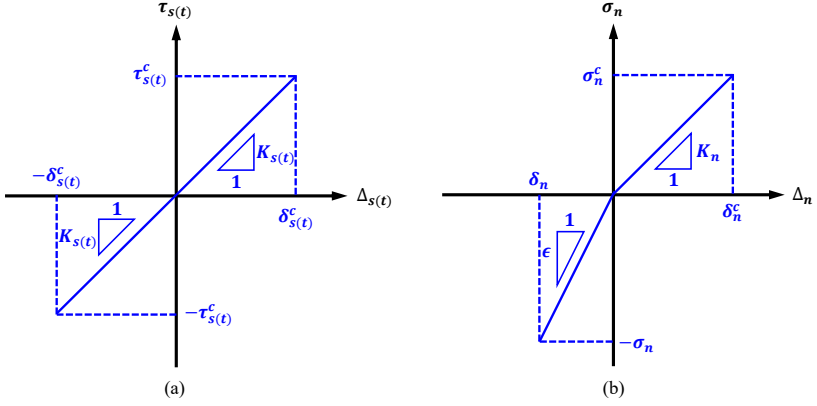
Figure 10: The traction versus separation curves of the polymeric interface: (a) sliding and shearing modes, and (b) the opening mode.

where $J_n = (0, \delta_n^c)$, and ϵ is the penalty parameter in compression [120]. This corresponds to a tension cut-off traction separation cohesive law, in which the interface cannot transfer tractions when the critical opening gap δ_n^c is reached. The similar brittle behavior is assumed for the tearing and sliding modes, see Fig. 10.

To obtain the structural response of encapsulant layers, the stiffness K_n is related to the actual stiffness of polymeric materials in the normal direction, which is calculated as the ration between the Young's modulus E_{poly} and its thickness h_{poly}, i.e., $K_n = E_{poly}/h_{poly}$. Analogously, the tearing and sliding stiffness can be expressed as: $K_s = K_t = E_{poly}/[2h_{poly}(1 + \nu_{poly})]$. Since polymeric materials have thermo-visco-elastic constitutive behaviors, the Young's modulus E_{poly} depends both on the average temperature $\langle T \rangle$ and time history t. To synthetically characterize these dependencies, a fractional calculus approach proposed in [88] is adopted here instead of the use of Prony series representation, which has been proved to be very effective for parameters identification

[90, 121]. Accordingly, the modulus E_{poly} is given by

$$E_{poly}(t, T) = \frac{a(T)h(t, T)^{-\alpha(T)}}{\Gamma(1 - \alpha(T))} \tag{2.20}$$

where a and α are two temperature dependent functions, such that $0 < a, \alpha < 1$, and $\Gamma(t)$ is the Euler gamma function

$$\Gamma(t) = \int_0^\infty e^{-x} x^{t-1} \, \mathrm{d}x \tag{2.21}$$

The function $h(t, T)$ is a time history and temperature dependent function, which is used to model the rheologically complex polymeric materials when the time-temperature superposition principle is not applicable. This can be ascribed to the change of polymer microstructure driven by temperature above a threshold. Hence, this history function $h(t, T)$ is equal to the difference between the current time t and t_0 corresponding to the microstructure modification.

With regard to the heat conduction, it is assumed that the heat flux across the interface is oriented in the direction orthogonal to the thin polymeric surface. Thus, $q_1 = q_2 = 0$ and $q = q_3$ is expressed as

$$q = \begin{cases} -h_0 \left(1 - \frac{\Delta_n}{\delta_n^c}\right) \langle T \rangle & \text{if } \Delta_n \in J_n \\ 0 & \text{if } \Delta_n \notin J_n \end{cases} \tag{2.22}$$

where h_0 is the thermal conductivity of interface without crack opening, i.e., $\Delta_n = 0$. Note that the heat conductivity is assumed to be a decreasing function of gap opening so that the partial heat transfer in case of damaged interface can be taken into account properly [122].

2.1.3 Moisture diffusion along polymeric interfaces

Durability tests of photovoltaic laminates, including damp heat test, humidity freeze test, and thermal cycling test, are characterized by time dependent temperature and moisture conditions in accordance with prescribed ramps inside a climate chamber. Moisture diffusion mainly takes place along the encapsulant polymeric layers between the solar cell and

tempered glass or backsheet. Generally, the aim of the numerical method is to predict the moisture content $c(x_1, x_2, x_3, t)$ inside the polymeric layer for each material point and time.

The boundary value problem for moisture diffusion, in which an imposed moisture content c^* is applied to the boundary, can be described as follows

$$
\begin{cases}
\frac{\partial c}{\partial t}(x_1, x_2, x_3, t) - D\nabla^2 c(x_1, x_2, x_3, t) = 0 & \text{in } \mathcal{B}_{poly} \times [0, t_f] \\
c(x_1, x_2, x_3, 0) = 0 & \text{in } \mathcal{B}_{poly} \\
c(x_1, x_2, x_3, t) = c^* & \text{in } \partial\mathcal{B}_{poly} \times (0, t_f]
\end{cases}
\tag{2.23}
$$

where D is the moisture diffusion coefficient.

It should be pointed out that the moisture diffusion is characterized with a different time scale from that of thermo-mechanical problem. The characteristic velocity of moisture diffusion is related to the diffusion coefficient D, while that of temperature diffusion is governed by the ratio $k_0/\rho c_p$. Given the characteristic values for polymeric layers, the ratio between these two physical phenomena is

$$
[k_0/(\rho c_p)]/D \approx 10^6.
$$

Hence, the moisture diffusion is dependent on the coupled thermo mechanical problem and not viceversa since heat transfer is about six order faster than moisture diffusion. Based on the experimental evidence reported in [29], the moisture diffusion coefficient should be considered as temperature and gap dependent Arrhenyus type function

$$
D = \begin{cases}
A \exp\left(-\frac{E_a}{TR}\right), & \text{if } \Delta_n \le \delta_n^c \\
A \exp\left(-\frac{E_a}{TR}\right)\frac{\Delta_n}{\delta_n^c}, & \text{if } \Delta_n > \delta_n^c
\end{cases}
\tag{2.24}
$$

For the purpose of accounting for the debonding effect of the encapsulant layer on the moisture diffusion, D is assumed to be a linear increasing function of the interfacial gap Δ_n when it overcomes the critical value δ_n^c. Given the different time scales of moisture diffusion and heat transfer, a staggered scheme is adopted for the solution of this computational framework, where the diffusion coefficient D is determined by the average temperature and gap displacement at the previous time increment computed from the coupled thermo-mechanical problem.

27

2.1.4 Variational form and finite element approximation

In this section, the derivations for the variational form and finite element formulation of the coupled thermo-mechanical problem with cohesive interface and 3D moisture diffusion are outlined. Firstly, this part introduces the multi-field Hu-Washizu variational principle and discretization for the coupled thermo-mechanical problem, which is particularized for solid shell formulation incorporating the EAS and ANS method to alleviate the locking effects. Subsequently, the consistent linearization of the governing equations for the thermo-mechanical cohesive interface is presented. Finally, the finite element implementation of the 3D moisture diffusion along the encapsulant polymeric layers is detailed.

In the following, the variational basis and finite element interpolation of the initial boundary value problem with the coupled thermo-mechanical solid shell formulation are presented. The laminae in photovoltaic modules are usually made of thin-walled structures, including tempered glass, silicon solar cell, and backsheet, and to accurately simulate their mechanical behaviors, a solid shell formulation incorporating the EAS and ANS methods for the alleviation of locking effects is derived from the mixed Hu-Washizu variational principle.

The weak form of energy balance equation in absence of heat sources and dissipative mechanism in the reference configuration is given by

$$
\mathcal{R}^T(\mathbf{u}, \tilde{\mathbf{E}}, T, \delta T) = \int_{\mathcal{B}_0} \rho_0 c_p \dot{T} \delta T \, \mathrm{d}\Omega - \int_{\mathcal{B}_0} T\mathbf{Z} : \dot{\mathbf{E}} \delta T \, \mathrm{d}\Omega
$$
$$
+ \int_{\mathcal{B}_0} \nabla \cdot \mathbf{Q} \delta T \, \mathrm{d}\Omega = 0,
\tag{2.25}
$$

where δT is the virtual temperature field. Invoking the Gauss's theorem, the third term relevant to the divergence of heat flux can be reformulated as

$$
\int_{\mathcal{B}_0} \nabla \cdot \mathbf{Q} \delta T \, \mathrm{d}\Omega = \int_{\partial \mathcal{B}_{0,\bar{q}}} Q_N \delta T \, \mathrm{d}\partial\Omega - \int_{\mathcal{B}_0} \mathbf{Q} \nabla_{\mathbf{X}} \delta T \, \mathrm{d}\Omega,
\tag{2.26}
$$

where $Q_N = \mathbf{Q} \cdot \mathbf{N}$ denotes the Neumann boundary condition on $\partial \mathcal{B}_{0,\bar{q}}$.

Subsequently, Eq. (2.25) can be rewritten as

$$
\mathcal{R}^T(\mathbf{u}, \tilde{\mathbf{E}}, T, \delta T) = \int_{\mathcal{B}_0} \rho_0 c_p \dot{T} \delta T \, \mathrm{d}\Omega - \int_{\mathcal{B}_0} T\mathbf{Z} : \dot{\mathbf{E}} \delta T \, \mathrm{d}\Omega
$$
$$
+ \int_{\partial \mathcal{B}_{0,\bar{q}}} Q_N \delta T \, \mathrm{d}\partial\Omega - \int_{\mathcal{B}_0} \mathbf{Q} \nabla_{\mathbf{X}} \delta T \, \mathrm{d}\Omega = 0. \tag{2.27}
$$

By inserting the Duhamel's law, i.e., simplified Eq. (2.17) under isotropic assumption, the previous expression can be formulated as

$$
\mathcal{R}^T = \int_{\mathcal{B}_0} \rho_0 c_p \dot{T} \delta T \, \mathrm{d}\Omega - \int_{\mathcal{B}_0} T\mathbf{Z} : \dot{\mathbf{E}} \delta T \, \mathrm{d}\Omega
$$
$$
+ \int_{\partial \mathcal{B}_{0,\bar{q}}} Q_N \delta T \, \mathrm{d}\partial\Omega + \int_{\mathcal{B}_0} [\nabla_{\mathbf{X}} \delta T]^{\mathrm{T}} k_0 \mathbf{G} \nabla_{\mathbf{X}} T \, \mathrm{d}\Omega = 0, \tag{2.28}
$$

with the internal residual $\mathcal{R}^T_{\mathrm{int}}$ and external counterpart $\mathcal{R}^T_{\mathrm{ext}}$ being identified as

$$
\mathcal{R}^T_{\mathrm{int}} = \int_{\mathcal{B}_0} \rho_0 c_p \dot{T} \delta T \, \mathrm{d}\Omega - \int_{\mathcal{B}_0} T\mathbf{Z} : \dot{\mathbf{E}} \delta T \, \mathrm{d}\Omega
$$
$$
+ \int_{\mathcal{B}_0} [\nabla_{\mathbf{X}} \delta T]^{\mathrm{T}} k_0 \mathbf{G} \nabla_{\mathbf{X}} T \, \mathrm{d}\Omega = 0, \tag{2.29}
$$

$$
\mathcal{R}^T_{\mathrm{ext}} = \int_{\partial \mathcal{B}_{0,\bar{q}}} Q_N \delta T \, \mathrm{d}\partial\Omega. \tag{2.30}
$$

Analogously, the weak form of the linear momentum balance governing equation can be derived in this procedure. However, low-order shell elements usually suffer from various locking pathologies, such as volumetric locking, Poisson thickness locking, transverse shear locking and so on. To alleviate such deficiencies, the mixed formulation proposed in [115, 123, 124] is adopted here, which incorporates the ANS and EAS methods through the enhancement of the displacement derived strain field by several collocation points and a set of incompatible strains. In this three-field Hu-Washizu variational principle, the displacement $\mathbf{u}$, the incompatible strain $\tilde{\mathbf{E}}$, and stress $\mathbf{S}$ are the independent unknown variables for this numerical strategy.

Given the use of EAS method, the strain field can be decomposed into a displacement derived compatible part $\mathbf{E}^u$ and an enhanced incompatible part $\tilde{\mathbf{E}}$ [106, 107], i.e., $\mathbf{E} = \mathbf{E}^u + \tilde{\mathbf{E}}$. Accounting for the orthogonality

29

condition between the stress spaces and enhanced strain fields, the stress field can be removed from the subsequent derivations. Hence, the weak form of the linear momentum balance equation can be expressed as

$$\mathcal{R}^u(\mathbf{u}, \tilde{\mathbf{E}}, T, \delta\mathbf{u}) = \int_{\mathcal{B}_0} \mathbf{S} : \delta\mathbf{E}^u \, d\Omega - \int_{\mathcal{B}_0} \rho_0\bar{\gamma}\delta\mathbf{u} \, d\Omega - \int_{\partial\mathcal{B}_{0,\bar{t}}} \hat{\mathbf{t}}\delta\mathbf{u} \, d\partial\Omega = 0,$$
(2.31)

$$\mathcal{R}^{\tilde{E}}(\mathbf{u}, \tilde{\mathbf{E}}, T, \delta\tilde{\mathbf{E}}) = \int_{\mathcal{B}_0} \mathbf{S} : \delta\tilde{\mathbf{E}} \, d\Omega = \mathcal{R}^{\tilde{E}}_{\text{int}} = 0,$$
(2.32)

where $\mathcal{R}^{\tilde{E}}_{\text{int}}$ represents the internal contribution from the enhanced strain field to the functional. Here the internal residual $\mathcal{R}^u_{\text{int}}$ and external residual $\mathcal{R}^u_{\text{ext}}$ corresponding to the kinematic compatible part can be defined as

$$\mathcal{R}^u_{\text{int}} = \int_{\mathcal{B}_0} \mathbf{S} : \delta\mathbf{E}^u \, d\Omega,$$
(2.33)

$$\mathcal{R}^u_{\text{ext}} = \int_{\mathcal{B}_0} \rho_0\bar{\gamma} \cdot \delta\mathbf{u} \, d\Omega - \int_{\partial\mathcal{B}_{0,\bar{t}}} \hat{\mathbf{t}} \cdot \delta\mathbf{u} \, d\partial\Omega.$$
(2.34)

The initial configuration $\mathcal{B}_0$ is discretized into n_e non-overlapping finite elements, i.e., $\mathcal{B}_0 \approx \bigcup_{e=1}^{n_e} \mathcal{B}_0^{(e)}$. For the thermo-mechanical modeling framework stated above, it is particularized for the so-called solid shell parametrization, which assumes the approximation of vector at any material point in terms of the counterparts on the corresponding top and bottom surfaces of the shell element.

In line with this parametrization, the position vectors and temperature of any material point in the reference and current configurations can be computed as

$$\mathbf{X}(\boldsymbol{\xi}) = \frac{1}{2}\left(1 + \xi^3\right)\mathbf{X}_t(\xi^1, \xi^2) + \frac{1}{2}\left(1 - \xi^3\right)\mathbf{X}_b(\xi^1, \xi^2),$$
(2.35a)

$$\mathbf{x}(\boldsymbol{\xi}) = \frac{1}{2}\left(1 + \xi^3\right)\mathbf{x}_t(\xi^1, \xi^2) + \frac{1}{2}\left(1 - \xi^3\right)\mathbf{x}_b(\xi^1, \xi^2),$$
(2.35b)

where the subscripts t and b stand for the top and bottom surfaces, respectively. The parametric space is given by: $\mathcal{A} := \{\boldsymbol{\xi} = (\xi^1, \xi^2, \xi^3) \in \mathbb{R}^3 | -1 \leq \xi^i \leq +1; i = 1, 2, 3\}$, where (ξ^1, ξ^2) represent the in-plane directions and ξ^3 identifies the thickness direction.

Based on the isoparametric concept, the approximation of position vectors $\mathbf{X}$ and $\mathbf{x}$ are interpolated through standard trilinear shape functions $\mathbf{N}_I$ as follows

$$\mathbf{X} \approx \sum_{I=1}^{n_n} \mathbf{N}_I(\boldsymbol{\xi})\mathbf{X}_I = \mathbf{N}\widetilde{\mathbf{X}}, \quad \mathbf{x} \approx \sum_{I=1}^{n_n} \mathbf{N}_I(\boldsymbol{\xi})\mathbf{x}_I = \mathbf{N}\widetilde{\mathbf{x}}, \qquad (2.36)$$

where $\mathbf{X}_I$ and $\mathbf{x}_I$ are the nodal position vectors in the reference and current configurations, respectively, with number of nodes $n_n = 8$, and $\widetilde{\mathbf{X}}$ and $\widetilde{\mathbf{x}}$ are the respective nodal position vectors in the element level. The shape functions $\mathbf{N}_I$ is defined as

$$\mathbf{N}_I = \mathbf{diag}\left[N_I, N_I, N_I\right] \qquad (2.37)$$

where $N_I = \frac{1}{8}\left(1 + \xi_I^1\xi^1\right)\left(1 + \xi_I^2\xi^2\right)\left(1 + \xi_I^3\xi^3\right)$, $I = 1, 2, ..., 8$. The interpolation of displacement and temperature fields $(\mathbf{u}, T)$, the variations $(\delta\mathbf{u}, \delta T)$, and the increments $(\Delta\mathbf{u}, \Delta T)$ are given by

$$\mathbf{u} \approx \sum_{I=1}^{n_n} \mathbf{N}_I(\boldsymbol{\xi})\mathbf{d}_I = \mathbf{N}\mathbf{d},$$

$$\delta\mathbf{u} \approx \sum_{I=1}^{n_n} \mathbf{N}_I(\boldsymbol{\xi})\delta\mathbf{d}_I = \mathbf{N}\delta\mathbf{d}, \qquad (2.38)$$

$$\Delta\mathbf{u} \approx \sum_{I=1}^{n_n} \mathbf{N}_I(\boldsymbol{\xi})\Delta\mathbf{d}_I = \mathbf{N}\Delta\mathbf{d},$$

$$T \approx \sum_{I=1}^{n_n} N_I(\boldsymbol{\xi})T_I = \hat{\mathbf{N}}\hat{\boldsymbol{T}},$$

$$\delta T \approx \sum_{I=1}^{n_n} N_I(\boldsymbol{\xi})\delta T_I = \hat{\mathbf{N}}\delta\hat{\boldsymbol{T}}, \qquad (2.39)$$

$$\Delta T \approx \sum_{I=1}^{n_n} N_I(\boldsymbol{\xi})\Delta T_I = \hat{\mathbf{N}}\Delta\hat{\boldsymbol{T}},$$

where $\mathbf{d}_I$ and T_I represent the nodal displacement and temperature, respectively, and $\mathbf{d}$ and $\hat{\boldsymbol{T}}$ are the corresponding vectors at the element level. The interpolation of the spatial temperature gradient in the reference configuration $\nabla_{\mathbf{X}}T$, its variation $\nabla_{\mathbf{X}}\delta T$ and its increment $\nabla_{\mathbf{X}}\Delta T$
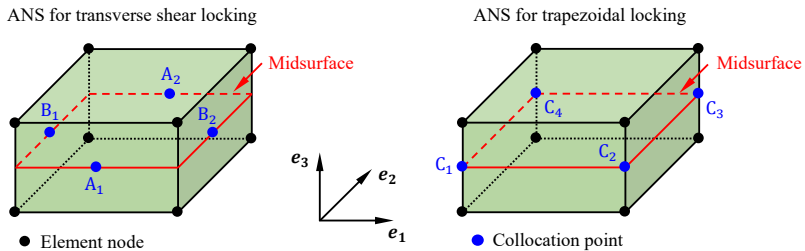
Figure 11: The position of collocation points in the parametric space for the ANS method.

reads

$$\nabla_{\mathbf{X}} T \approx \mathbf{G}^{-\mathrm{T}} \nabla_{\boldsymbol{\xi}} \hat{\mathbf{N}} \hat{\boldsymbol{T}},$$
$$\nabla_{\mathbf{X}} \delta T \approx \mathbf{G}^{-\mathrm{T}} \nabla_{\boldsymbol{\xi}} \hat{\mathbf{N}} \delta \hat{\boldsymbol{T}}, \qquad (2.40)$$
$$\nabla_{\mathbf{X}} \Delta T \approx \mathbf{G}^{-\mathrm{T}} \nabla_{\boldsymbol{\xi}} \hat{\mathbf{N}} \Delta \hat{\boldsymbol{T}},$$

where $\nabla_{\boldsymbol{\xi}}$ represents the gradient with respect to the natural coordinates in the curvilinear setting.

The Green-Lagrange strain vector is expressed as $\mathbf{E}^u = [E_{11}, 2E_{12}, 2E_{13}, E_{22}, 2E_{23}, E_{33}]^{\mathrm{T}}$. To overcome the curvature thickness locking, the ANS method proposed in [112] is adopted to modify the strain component E_{33}, which requires four collocation points defined in convective coordinates $\boldsymbol{\xi}_{\mathrm{C}_i}$ as $\boldsymbol{\xi}_{\mathrm{C}_1} = (-1, -1, 0)$, $\boldsymbol{\xi}_{\mathrm{C}_2} = (1, -1, 0)$, $\boldsymbol{\xi}_{\mathrm{C}_3} = (1, 1, 0)$, and $\boldsymbol{\xi}_{\mathrm{C}_4} = (-1, 1, 0)$, see Fig. 11. Besides, to prevent transverse shear locking, the ANS method proposed in [113] is also adopted in this work. The corresponding collocation points are $\boldsymbol{\xi}_{\mathrm{A}_1} = (0, -1, 0)$, $\boldsymbol{\xi}_{\mathrm{A}_2} = (0, 1, 0)$, $\boldsymbol{\xi}_{\mathrm{B}_1} = (-1, 0, 0)$, and $\boldsymbol{\xi}_{\mathrm{B}_2} = (1, 0, 0)$, see Fig. 11. Accounting for the ANS interpolations, the strain vector is given by

$$\mathbf{E}^u = \begin{bmatrix} \frac{1}{2}(g_{11} - G_{11}) \\ (g_{12} - G_{12}) \\ (1 - \xi^2)\left(g_{13}^{\mathrm{A}_1} - G_{13}^{\mathrm{A}_1}\right) + (1 + \xi^2)\left(g_{13}^{\mathrm{A}_2} - G_{13}^{\mathrm{A}_2}\right) \\ \frac{1}{2}(g_{22} - G_{22}) \\ (1 - \xi^1)\left(g_{23}^{\mathrm{B}_1} - G_{23}^{\mathrm{B}_1}\right) + (1 + \xi^1)\left(g_{23}^{\mathrm{B}_2} - G_{23}^{\mathrm{B}_2}\right) \\ \sum_{i=1}^{4} \frac{1}{4}\left(1 + \xi_i^1 \xi^1\right)\left(1 + \xi_i^2 \xi^2\right)\frac{1}{2}\left(g_{33}^{\mathrm{C}_i} - G_{33}^{\mathrm{C}_i}\right) \end{bmatrix} \qquad (2.41)$$

The approximation of strain variation and increment is interpolated by

$$\delta \mathbf{E}^u \approx \sum_{I=1}^{n_n} \mathbf{B}_I(\boldsymbol{\xi})\delta \mathbf{d}_I = \mathbf{B}\delta \mathbf{d}, \ \ \Delta \mathbf{E}^u \approx \sum_{I=1}^{n_n} \mathbf{B}_I(\boldsymbol{\xi})\Delta \mathbf{d}_I = \mathbf{B}\Delta \mathbf{d} \quad (2.42)$$

where $\mathbf{B}_I$ is defined as

$$\mathbf{B}_I = \begin{bmatrix} N_{I,1}\left(\mathbf{g}_1^{\mathrm{T}}\right) \\ N_{I,1}\left(\mathbf{g}_2^{\mathrm{T}}\right) + N_{I,2}\left(\mathbf{g}_1^{\mathrm{T}}\right) \\ \left(1-\xi^2\right)\left(N_{I,1}^{\mathrm{A1}}\left(\mathbf{g}_3^{\mathrm{A1}}\right)^{\mathrm{T}} + N_{I,3}^{\mathrm{A1}}\left(\mathbf{g}_1^{\mathrm{A1}}\right)^{\mathrm{T}}\right) + \left(1+\xi^2\right)\left(N_{I,1}^{\mathrm{A2}}\left(\mathbf{g}_3^{\mathrm{A2}}\right)^{\mathrm{T}} + N_{I,3}^{\mathrm{A2}}\left(\mathbf{g}_1^{\mathrm{A2}}\right)^{\mathrm{T}}\right) \\ N_{I,2}\left(\mathbf{g}_2^{\mathrm{T}}\right) \\ \left(1-\xi^1\right)\left(N_{I,2}^{\mathrm{B1}}\left(\mathbf{g}_3^{\mathrm{B1}}\right)^{\mathrm{T}} + N_{I,3}^{\mathrm{B1}}\left(\mathbf{g}_2^{\mathrm{B1}}\right)^{\mathrm{T}}\right) + \left(1+\xi^1\right)\left(N_{I,2}^{\mathrm{B2}}\left(\mathbf{g}_3^{\mathrm{B2}}\right)^{\mathrm{T}} + N_{I,3}^{\mathrm{B2}}\left(\mathbf{g}_2^{\mathrm{B2}}\right)^{\mathrm{T}}\right) \\ \sum_{i=1}^{4}\frac{1}{4}\left(1+\xi_i^1\xi^1\right)\left(1+\xi_i^2\xi^2\right)N_{I,3}\left(\mathbf{g}_3^i\right)^{\mathrm{T}} \end{bmatrix}$$
$$(2.43)$$

Similarly, the interpolation of enhanced incompatible strain field $\tilde{\mathbf{E}}$, its variation $\delta\tilde{\mathbf{E}}$ and its increment $\Delta\tilde{\mathbf{E}}$ take the form of

$$\tilde{\mathbf{E}} \approx \mathbf{M}(\boldsymbol{\xi})\boldsymbol{\varsigma}, \ \ \delta\tilde{\mathbf{E}} \approx \mathbf{M}(\boldsymbol{\xi})\delta\boldsymbol{\varsigma}, \ \ \Delta\tilde{\mathbf{E}} \approx \mathbf{M}(\boldsymbol{\xi})\Delta\boldsymbol{\varsigma}, \quad (2.44)$$

where $\boldsymbol{\varsigma}$ is the enhancing modes vector to prevent locking pathologies as pointed out in [123, 92], and $\mathbf{M}$ denotes the interpolation matrix of incompatible strain [98], which is given by

$$\mathbf{M}(\xi) = \left[\frac{\det \mathbf{J}_0}{\det \mathbf{J}}\right]\mathbf{T}_0^{-\mathrm{T}}\tilde{\mathbf{M}}(\xi) \quad (2.45)$$

where $\mathbf{J} = [\mathbf{G}_1, \mathbf{G}_2, \mathbf{G}_3]^{\mathrm{T}}$, $\mathbf{J}_0$ is its evaluation at the element center ($\xi^1 = 0, \xi^2 = 0, \xi^3 = 0$), and the transformation matrix $\mathbf{T}_0$ takes the form

$$\mathbf{T}_0 = \begin{bmatrix} J_{11_0}^2 & J_{21_0}^2 & J_{31_0}^2 & 2J_{11_0}J_{21_0} & 2J_{11_0}J_{31_0} & 2J_{21_0}J_{31_0} \\ J_{12_0}^2 & J_{22_0}^2 & J_{32_0}^2 & 2J_{12_0}J_{22_0} & 2J_{12_0}J_{32_0} & 2J_{22_0}J_{32_0} \\ J_{13_0}^2 & J_{23_0}^2 & J_{33_0}^2 & 2J_{13_0}J_{23_0} & 2J_{13_0}J_{33_0} & 2J_{23_0}J_{33_0} \\ J_{11_0}J_{12_0} & J_{21_0}J_{22_0} & J_{31_0}J_{32_0} & J_{11_0}J_{22_0}+J_{21_0}J_{12_0} & J_{11_0}J_{32_0}+J_{31_0}J_{12_0} & J_{21_0}J_{32_0}+J_{31_0}J_{22_0} \\ J_{11_0}J_{13_0} & J_{21_0}J_{23_0} & J_{31_0}J_{33_0} & J_{11_0}J_{23_0}+J_{21_0}J_{13_0} & J_{11_0}J_{33_0}+J_{31_0}J_{13_0} & J_{21_0}J_{33_0}+J_{31_0}J_{23_0} \\ J_{12_0}J_{13_0} & J_{22_0}J_{23_0} & J_{32_0}J_{33_0} & J_{12_0}J_{23_0}+J_{22}J_{13_0} & J_{12_0}J_{33_0}+J_{32_0}J_{13_0} & J_{22_0}J_{33_0}+J_{32_0}J_{23_0} \end{bmatrix}$$
$$(2.46)$$

where J_{IJ_0} in the transformation matrix $\mathbf{T}_0$ are the components of $\mathbf{J}_0$. To alleviate the membrane, volumetric and Poisson thickness locking effects, the interpolation matrix $\tilde{\mathbf{M}}(\xi)$ of the enhancing modes defined in

the parametric space $\boldsymbol{\xi} = \{\xi^1, \xi^2, \xi^3\}$ reads

$$\tilde{\mathbf{M}} = \begin{bmatrix} \xi^1 & 0 & 0 & 0 & \xi^1\xi^2 & 0 & 0 & 0 & 0 & 0 & 0 \\ 0 & 0 & \xi^1 & \xi^2 & 0 & 0 & \xi^1\xi^2 & 0 & 0 & 0 & 0 \\ 0 & 0 & 0 & 0 & 0 & 0 & 0 & 0 & 0 & 0 & 0 \\ 0 & \xi^2 & 0 & 0 & 0 & \xi^1\xi^2 & 0 & 0 & 0 & 0 & 0 \\ 0 & 0 & 0 & 0 & 0 & 0 & 0 & 0 & 0 & 0 & 0 \\ 0 & 0 & 0 & 0 & 0 & 0 & 0 & 1 & \xi^1 & \xi^2 & \xi^1\xi^2 \end{bmatrix}. \tag{2.47}$$

By inserting the interpolation formulae, the discrete forms of internal energy balance residual Eq. (2.29) is given by

$$\begin{aligned} \hat{\mathcal{R}}_{\text{int}}^T(\mathbf{d}, \boldsymbol{\varsigma}, \hat{\boldsymbol{T}}, \delta\hat{\boldsymbol{T}}) = \delta\hat{\boldsymbol{T}}^{\mathrm{T}} & \left[\int_{\mathcal{B}_0} \hat{\mathbf{N}}^{\mathrm{T}} \rho_0 c_p \dot{T} \, \mathrm{d}\Omega - \int_{\mathcal{B}_0} \hat{\mathbf{N}}^{\mathrm{T}} \left(\mathbf{Z}^{\mathrm{T}} \dot{\mathbf{E}} \right) T \, \mathrm{d}\Omega \right. \\ & \left. + \int_{\mathcal{B}_0} k_0 \mathbf{B}_T^{\mathrm{T}} \mathbf{G} \nabla_{\mathbf{X}} T \, \mathrm{d}\Omega \right], \end{aligned} \tag{2.48}$$

where $\mathbf{B}_T$ is the interpolation operator for the temperature gradient.

The discrete internal residual terms with regard to the kinematic compatible part, Eq. (2.33), and enhanced strain field, Eq. (2.32), can be expressed as

$$\hat{\mathcal{R}}_{\text{int}}^u(\mathbf{d}, \boldsymbol{\varsigma}, \hat{\boldsymbol{T}}, \delta\mathbf{d}) = \delta\mathbf{d}^{\mathrm{T}} \left[\int_{\mathcal{B}_0} \mathbf{B}^{\mathrm{T}} \mathbf{S} \, \mathrm{d}\Omega \right], \tag{2.49}$$

$$\hat{\mathcal{R}}_{\text{int}}^{\tilde{E}}(\mathbf{d}, \boldsymbol{\varsigma}, \hat{\boldsymbol{T}}, \delta\boldsymbol{\varsigma}) = \delta\boldsymbol{\varsigma}^{\mathrm{T}} \left[\int_{\mathcal{B}_0} \mathbf{M}^{\mathrm{T}} \mathbf{S} \, \mathrm{d}\Omega \right]. \tag{2.50}$$

For subsequent developments, the residual vectors associated with the displacement field, the incompatible strain field, and the temperature field, respectively, are defined as

$$\mathbf{R}_{\text{int}}^T = \int_{\mathcal{B}_0} \hat{\mathbf{N}}^{\mathrm{T}} \rho_0 c_p \dot{T} \mathrm{d}\Omega - \int_{\mathcal{B}_0} \hat{\mathbf{N}}^{\mathrm{T}} \left(\mathbf{Z}^{\mathrm{T}} \dot{\mathbf{E}} \right) T \mathrm{d}\Omega + \int_{\mathcal{B}_0} k_0 \mathbf{B}_T^{\mathrm{T}} \mathbf{G} \nabla_{\mathbf{X}} T \, \mathrm{d}\Omega, \tag{2.51a}$$

$$\mathbf{R}_{\text{int}}^d = \int_{\mathcal{B}_0} \mathbf{B}^{\mathrm{T}} \mathbf{S} \, \mathrm{d}\Omega, \tag{2.51b}$$

$$\mathbf{R}_{\text{int}}^\varsigma = \int_{\mathcal{B}_0} \mathbf{M}^{\mathrm{T}} \mathbf{S} \, \mathrm{d}\Omega. \tag{2.51c}$$

34

To solve the set of nonlinear residual equations, the iterative scheme is adopted for the multi-field coupled thermo-mechanical problem, and the consistent linearization of the system derived from the concept of Gateaux directional derivative in matrix form can be expressed as

$$
\begin{bmatrix}
\mathbf{k}_{dd} & \mathbf{k}_{d\varsigma} & \mathbf{k}_{dT} \\
\mathbf{k}_{\varsigma d} & \mathbf{k}_{\varsigma\varsigma} & \mathbf{k}_{\varsigma T} \\
\mathbf{k}_{Td} & \mathbf{k}_{T\varsigma} & \mathbf{k}_{TT}
\end{bmatrix}
\begin{bmatrix}
\Delta\mathbf{d} \\
\Delta\varsigma \\
\Delta\hat{\mathbf{T}}
\end{bmatrix}
=
\begin{bmatrix}
\mathbf{R}_{ext}^{d} \\
\mathbf{0} \\
\mathbf{R}_{ext}^{T}
\end{bmatrix}
-
\begin{bmatrix}
\mathbf{R}_{int}^{d} \\
\mathbf{R}_{int}^{\varsigma} \\
\mathbf{R}_{int}^{T}
\end{bmatrix}
\tag{2.52}
$$

where $\mathbf{k}_{ab}$ with $\{a, b\} = \{d, \varsigma, T\}$ are different element tangent operators.

Firstly the tangent operators derived from the linearized residual form of Eq. (2.51a) with respect to the energy balance reads

$$
\mathbf{k}_{TT} = \int_{\mathcal{B}_0} \hat{\mathbf{N}}^{\mathrm{T}} \frac{\rho_0 c_p}{\Delta t} \hat{\mathbf{N}} \, \mathrm{d}\Omega - \int_{\mathcal{B}_0} \hat{\mathbf{N}}^{\mathrm{T}} \left(\mathbf{Z}^{\mathrm{T}} \dot{\mathbf{E}} \right) \hat{\mathbf{N}} \, \mathrm{d}\Omega + \int_{\mathcal{B}_0} k_0 \mathbf{B}_T^{\mathrm{T}} \mathbf{G} \mathbf{B}_T \, \mathrm{d}\Omega,
\tag{2.53a}
$$

$$
\mathbf{k}_{T\varsigma} = -\int_{\mathcal{B}_0} \hat{\mathbf{N}}^{\mathrm{T}} \frac{T}{\Delta t} \mathbf{Z}^{\mathrm{T}} \mathbf{M} \, \mathrm{d}\Omega,
\tag{2.53b}
$$

$$
\mathbf{k}_{Td} = -\int_{\mathcal{B}_0} \hat{\mathbf{N}}^{\mathrm{T}} \frac{T}{\Delta t} \mathbf{Z}^{\mathrm{T}} \mathbf{B} \, \mathrm{d}\Omega,
\tag{2.53c}
$$

where Δt is the time increment.

Analogously, the tangent operators obtained from linearization of the residual equation Eq. (2.51b) with respect to the displacement field is given by

$$
\mathbf{k}_{dT} = \int_{\mathcal{B}_0} \mathbf{B}^{\mathrm{T}} \mathbf{Z} \hat{\mathbf{N}} \, \mathrm{d}\Omega
\tag{2.54a}
$$

$$
\mathbf{k}_{d\varsigma} = \int_{\mathcal{B}_0} \mathbf{B}^{\mathrm{T}} \mathbb{C} \mathbf{M} \, \mathrm{d}\Omega,
\tag{2.54b}
$$

$$
\mathbf{k}_{dd} = \int_{\mathcal{B}_0} \left(\mathbf{B}^{\mathrm{T}} \mathbb{C} \mathbf{B} + \mathbf{Q} \right) \, \mathrm{d}\Omega.
\tag{2.54c}
$$

where $\mathbf{Q}$ represents the geometrical nonlinearity, which is defined as

$$
\mathbf{Q} = \frac{\partial \mathbf{B}(\mathbf{d})^{\mathrm{T}}}{\partial \mathbf{d}} \mathbf{S} =
\begin{bmatrix}
\mathbf{Q}_{11} & \mathbf{Q}_{12} & \cdots & \mathbf{Q}_{18} \\
\mathbf{Q}_{21} & \mathbf{Q}_{22} & \cdots & \mathbf{Q}_{28} \\
\vdots & \vdots & \ddots & \vdots \\
\mathbf{Q}_{81} & \mathbf{Q}_{82} & \cdots & \mathbf{Q}_{88}
\end{bmatrix}
\tag{2.55}
$$

where $\mathbf{Q}_{IJ}$ is defined as $\mathbf{Q}_{IJ} = \mathrm{diag}\,[Q_{IJ}, Q_{IJ}, Q_{IJ}]$ for the combination of node I and J, and the scalar Q_{IJ} reads

$$
Q_{IJ} = \mathbf{S}^{\mathrm{T}}
\begin{bmatrix}
N_{I,1}\,N_{J,1} \\
N_{I,1}\,N_{J,2} + N_{I,2}\,N_{J,1} \\
\left(1-\xi^2\right)\left(N_{I,1}^{A_1} N_{J,3}^{A_1} + N_{I,3}^{A_1} N_{J,1}^{A_1}\right) + \left(1+\xi^2\right)\left(N_{I,1}^{A_2} N_{J,3}^{A_2} + N_{I,3}^{A_2} N_{J,1}^{A_2}\right) \\
N_{I,2}\,N_{J,2} \\
\left(1-\xi^1\right)\left(N_{I,2}^{B_1} N_{J,3}^{B_1} + N_{I,3}^{B_1} N_{J,2}^{B_1}\right) + \left(1+\xi^1\right)\left(N_{I,2}^{B_2} N_{J,3}^{B_2} + N_{I,3}^{B_2} N_{J,2}^{B_2}\right) \\
\Sigma_{i=1}^{4}\,\frac{1}{4}\left(1+\xi_i^1\xi^1\right)\left(1+\xi_i^2\xi^2\right) N_{I,3}\,N_{J,3}
\end{bmatrix}
\tag{2.56}
$$

where $\mathbf{S}$ is the approximate stress field in matrix form as $\mathbf{S} = [S^{11}, S^{12}, S^{13}, S^{22}, S^{23}, S^{33}]^{\mathrm{T}}$.

Similarly, the tangent operators derived from Eq. (2.51c) with respect to the incompatible strain field take the form

$$
\mathbf{k}_{\varsigma T} = \int_{\mathcal{B}_0} \mathbf{M}^{\mathrm{T}} \mathbf{Z} \hat{\mathbf{N}}\, \mathrm{d}\Omega,
\tag{2.57a}
$$

$$
\mathbf{k}_{\varsigma d} = \int_{\mathcal{B}_0} \mathbf{M}^{\mathrm{T}} \mathbb{C} \mathbf{B}\, \mathrm{d}\Omega,
\tag{2.57b}
$$

$$
\mathbf{k}_{\varsigma\varsigma} = \int_{\mathcal{B}_0} \mathbf{M}^{\mathrm{T}} \mathbb{C} \mathbf{M}\, \mathrm{d}\Omega,
\tag{2.57c}
$$

Since inter-element continuity is not required [100], the consistent linearization with respect to the incompatible strain field can be condensed out in the element level, and the condensed system of equations are given by

$$
\begin{bmatrix} \mathbf{k}_{dd}^{*} & \mathbf{k}_{dT}^{*} \\ \mathbf{k}_{Td}^{*} & \mathbf{k}_{TT}^{*} \end{bmatrix}
\begin{bmatrix} \Delta \mathbf{d} \\ \Delta T \end{bmatrix} =
\begin{bmatrix} \mathbf{R}_{\mathrm{ext}}^{d} \\ \mathbf{R}_{\mathrm{ext}}^{T} \end{bmatrix} -
\begin{bmatrix} \mathbf{R}_{\mathrm{int}}^{d*} \\ \mathbf{R}_{\mathrm{int}}^{T*} \end{bmatrix}
\tag{2.58}
$$

where the element stiffness contributions are

$$
\mathbf{k}_{dd}^{*} = \mathbf{k}_{dd} - \mathbf{k}_{d\varsigma}\mathbf{k}_{\varsigma\varsigma}^{-1}\mathbf{k}_{\varsigma d}, \quad \mathbf{k}_{dT}^{*} = \mathbf{k}_{dT} - \mathbf{k}_{d\varsigma}\mathbf{k}_{\varsigma\varsigma}^{-1}\mathbf{k}_{\varsigma T},
\tag{2.59a}
$$

$$
\mathbf{k}_{Td}^{*} = \mathbf{k}_{Td} - \mathbf{k}_{T\varsigma}\mathbf{k}_{\varsigma\varsigma}^{-1}\mathbf{k}_{\varsigma d}, \quad \mathbf{k}_{TT}^{*} = \mathbf{k}_{TT} - \mathbf{k}_{T\varsigma}\mathbf{k}_{\varsigma\varsigma}^{-1}\mathbf{k}_{\varsigma T},
\tag{2.59b}
$$

and the condensed element internal residual vectors render

$$
\mathbf{R}_{\mathrm{int}}^{d*} = \mathbf{R}_{\mathrm{int}}^{d} - \mathbf{k}_{d\varsigma}\mathbf{k}_{\varsigma\varsigma}^{-1}\mathbf{R}_{\mathrm{int}}^{\varsigma},
\tag{2.60a}
$$

$$
\mathbf{R}_{\mathrm{int}}^{T*} = \mathbf{R}_{\mathrm{int}}^{T} - \mathbf{k}_{T\varsigma}\mathbf{k}_{\varsigma\varsigma}^{-1}\mathbf{R}_{\mathrm{int}}^{\varsigma}.
\tag{2.60b}
$$
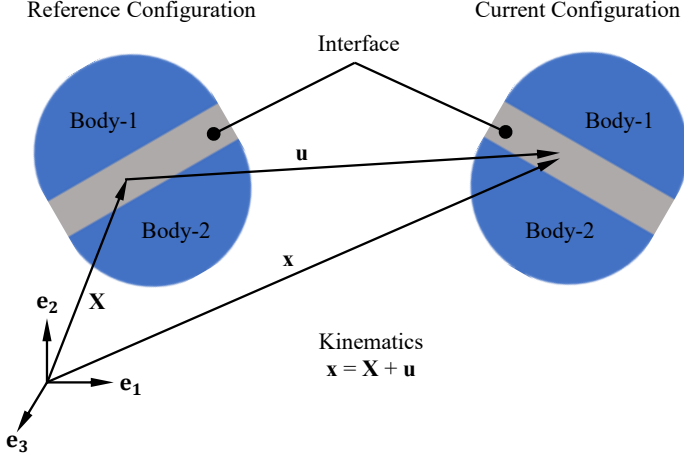
Figure 12: Sketch of the interface between the two bodies during the deformation process.

In the reference configuration for finite deformation setting, consider two deformable bodies $\mathcal{B}_0^{(1)} \subset \mathbb{R}^3$ and $\mathcal{B}_0^{(2)} \subset \mathbb{R}^3$ (identified as Body-1 and Body-2 in Fig. 12). The interface contribution of cohesive traction $\bar{\sigma} = (\sigma, \tau_t, \tau_s)$ and heat flux $\bar{q}$ to the Principle of Virtual Work of the whole mechanical system can be expressed as

$$\Pi_{\text{int}} = \int_{\Gamma_{\text{int}}} \mathbf{g}_{\text{loc}}^{\text{T}} \cdot \mathbf{T} \, \mathrm{d}\partial\Omega \tag{2.61}$$

where $\mathbf{g}_{\text{loc}} = (\Delta_n, \Delta_s, \Delta_t, \Delta_T)^{\text{T}}$ is the local gap vector including both mechanical and thermal gaps, and $\mathbf{T} = (\sigma, \tau_t, \tau_s, \bar{q})$ is the traction vector conjugate to the gap vector. Note that the traction vector vanishes when the interface is undergoing rigid body motions owning to the frame indifference of this formulation. The variational form of interface contribution is given by

$$\delta\Pi_{\text{int}}(\mathbf{g}_{\text{loc}}) = \int_{\Gamma_{\text{int}}} \left(\frac{\partial \mathbf{g}_{\text{loc}}}{\partial \hat{\mathbf{u}}} \delta\hat{\mathbf{u}} \right)^{\text{T}} \mathbf{T} \, \mathrm{d}\partial\Omega = \delta\hat{\mathbf{u}}^{\text{T}} \int_{\Gamma_{\text{int}}} \left(\frac{\partial \mathbf{g}_{\text{loc}}}{\partial \hat{\mathbf{u}}} \right)^{\text{T}} \mathbf{T} \, \mathrm{d}\partial\Omega \tag{2.62}$$

where $\hat{\mathbf{u}} = (\mathbf{u}, T)^{\text{T}}$ is the generalized vector.
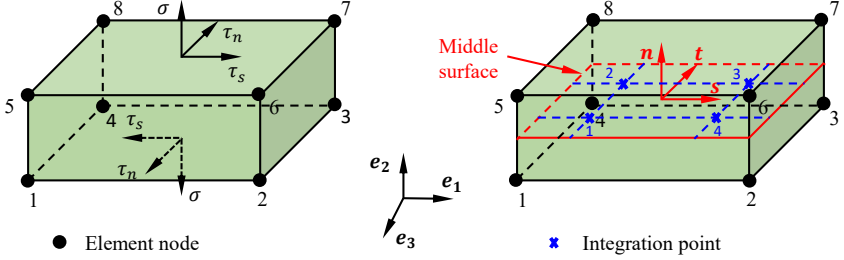
Figure 13: Sketch of the three-dimensional interface finite element.

To account for the rotations of configuration, a middle plane of the interface by averaging the position and displacement vector of the upper and lower faces is defined. Hence, the position vector on the middle surface $\bar{\mathbf{x}}$ and $\bar{\mathbf{X}}$ can be determined by multiplying the position vector with an averaging operator $\mathbf{M}^{cz}$,

$$\bar{\mathbf{x}} = \mathbf{M}^{cz}\mathbf{x}, \quad \bar{\mathbf{X}} = \mathbf{M}^{cz}\mathbf{X} \tag{2.63}$$

where the matrix $\mathbf{M}^{cz}$ is defined as $\mathbf{M}^{cz} = \frac{1}{2}(\mathcal{I}_{12}, \mathcal{I}_{12})$ with $\mathcal{I}_{12}$ identified as 12×12 identity matrix.

In line with derivations proposed in [125], the convective shear vector $\mathbf{s}$, tangential vector $\mathbf{t}$ and normal vector $\mathbf{n}$ to the middle surface, see Fig. 13, are defined via the differentiation of average position vector in the current configuration with respect to the natural coordinates ξ and η, and given by

$$\mathbf{s} = \frac{\partial\bar{\mathbf{x}}}{\partial\xi}, \quad \mathbf{t} = \frac{\partial\bar{\mathbf{x}}}{\partial\eta}, \quad \mathbf{n} = \mathbf{s} \times \mathbf{t}. \tag{2.64}$$

The gap vector $\mathbf{g}$ can be determined by multiplying the nodal displacement vector of the interface element with an appropriate operator $\mathbf{L}^{cz} = (-\mathcal{I}_{16}, \mathcal{I}_{16})$ with $\mathcal{I}_{16}$ identified as 16×16 identity matrix, which provides the difference between the bottom and upper surface displacements, and its expression is given by

$$\mathbf{g} = \mathbf{N}^{cz}\mathbf{L}^{cz}\hat{\mathbf{d}} \tag{2.65}$$

38

where $\hat{\mathbf{d}}$ is the vector collecting the degrees of freedom in the element level, and $\mathbf{N}^{cz}$ is the interpolation matrix of interface, which reads

$$\mathbf{N}^{cz} = [N_1^{cz}\mathcal{I}_4, N_2^{cz}\mathcal{I}_4, N_3^{cz}\mathcal{I}_4, N_4^{cz}\mathcal{I}_4], \tag{2.66}$$

where $N_1^{cz} = \dfrac{1}{4}(1-\xi)(1-\eta)$, $N_2^{cz} = \dfrac{1}{4}(1+\xi)(1-\eta)$, $N_3^{cz} = \dfrac{1}{4}(1+\xi)(1+\eta)$ and $N_4^{cz} = \dfrac{1}{4}(1-\xi)(1+\eta)$, and $\mathcal{I}_4$ is the 4×4 identity matrix.

To define the traction-separation law in the local frame, the local gap vector needs to be computed by multiplying the counterpart in the global frame with a rotation matrix operator

$$\mathbf{g}_{\text{loc}} = \mathbf{R}_{cz}\mathbf{g} = \mathbf{R}_{cz}\mathbf{N}^{cz}\mathbf{L}^{cz}\hat{\mathbf{d}}, \tag{2.67}$$

and the rotation matrix $\mathbf{R}_{cz}$ reads

$$\mathbf{R}_{cz} = \begin{bmatrix} s_x & s_y & s_z & 0 \\ t_x & t_y & t_z & 0 \\ n_x & n_y & n_z & 0 \\ 0 & 0 & 0 & 1 \end{bmatrix} \tag{2.68}$$

where its coefficients are all components of the convective vectors defined in Eq. (2.64).

Recalling the derivation of Eq. (4.75), the partial derivative of the local gap vector with respect to nodal displacements takes the form

$$\frac{\partial \mathbf{g}_{\text{loc}}}{\partial \hat{\mathbf{u}}} \approx \frac{\partial \mathbf{g}_{\text{loc}}}{\partial \hat{\mathbf{d}}} = \mathbf{R}_{cz}\mathbf{N}^{cz}\mathbf{L}^{cz} + \frac{\partial \mathbf{R}_{cz}}{\partial \hat{\mathbf{d}}}\mathbf{N}^{cz}\mathbf{L}^{cz}\hat{\mathbf{d}} = \mathbf{R}_{cz}\mathbf{B}_{cz} + \frac{\partial \mathbf{R}_{cz}}{\partial \hat{\mathbf{d}}}\mathbf{B}_{cz}\hat{\mathbf{d}}. \tag{2.69}$$

where $\mathbf{B}_{cz} = \mathbf{N}^{cz}\mathbf{L}^{cz}$ is introduced to simplify the equation. By inserting Eq. (2.69) into Eq. (2.61), where $\mathbf{u}$ is replaced by the nodal vector $\hat{\mathbf{d}}$, the general variational form of interface element formulation is given by

$$\delta\Pi_{\text{int}} = \delta\hat{\mathbf{d}}^{\text{T}} \int_{\text{int}} \left(\mathbf{R}_{cz}\mathbf{B}_{cz} + \frac{\partial \mathbf{R}_{cz}}{\partial \hat{\mathbf{d}}}\mathbf{B}_{cz}\hat{\mathbf{d}} \right)^{\text{T}} \mathbf{T} \, d\partial\Omega = \delta\hat{\mathbf{d}}^{\text{T}}\mathbf{f}_{\text{int}} \tag{2.70}$$

where the vector $\delta\hat{\mathbf{d}}$ represents the admissible virtual nodal vector, and $\mathbf{f}_{\text{int}}$ is the internal force vector of interface at the element level. The consistent linearization for the interface finite element formulation at the

$(k + 1)th$ iteration is given by

$$\mathbf{K}^{e,k}\Delta\hat{\mathbf{d}}^{k+1} = -\mathbf{f}_{\text{int}}^k \tag{2.71a}$$

$$\hat{\mathbf{d}}^{k+1} = \hat{\mathbf{d}}^k + \Delta\hat{\mathbf{d}}^{k+1} \tag{2.71b}$$

where $\mathbf{K}^{e,k} = \frac{\partial \mathbf{f}_{\text{int}}}{\partial \hat{\mathbf{d}}}$ is the element stiffness evaluated at the $(k)th$ iteration, which reads

$$\mathbf{K}^e = \int_{\Gamma_{\text{int}}} \left[2\mathbf{B}_{cz}^{\text{T}} \frac{\partial \mathbf{R}_{cz}^{\text{T}}}{\partial \hat{\mathbf{d}}} \mathbf{T} + \left(\mathbf{B}_{cz}^{\text{T}} \mathbf{R}_{cz}^{\text{T}} + \hat{\mathbf{d}}^{\text{T}} \mathbf{B}_{cz}^{\text{T}} \frac{\partial \mathbf{R}_{cz}^{\text{T}}}{\partial \hat{\mathbf{d}}} \right) \frac{\partial \mathbf{T}}{\partial \hat{\mathbf{d}}} \right] \ \mathrm{d}\partial\Omega. \tag{2.72}$$

It should be pointed out that the second derivative of the rotation matrix with respect to the nodal vector is omitted for convenience in the formulation [126]. The derivative of cohesive traction vector can be derived by chain rule as follows,

$$\frac{\partial \mathbf{T}}{\partial \hat{\mathbf{d}}} = \frac{\partial \mathbf{T}}{\partial \mathbf{g}_{\text{loc}}} \frac{\partial \mathbf{g}_{\text{loc}}}{\partial \hat{\mathbf{d}}} = \mathbf{C}_{cz} \mathbf{R}_{cz} \mathbf{B}_{cz} + \frac{\partial \mathbf{R}_{cz}}{\partial \hat{\mathbf{d}}} \mathbf{B}_{cz} \hat{\mathbf{d}} \tag{2.73}$$

where $\mathbf{C}_{cz}$ is the material tangent stiffness of the interface. In small displacement setting, the second term of Eq. (2.73) with respect to the partial derivative of rotation matrix can be neglected. After substituting Eq. (2.73) into Eq. (2.72), the final element stiffness matrix form of interface can be expressed as

$$\mathbf{K}^e = \int_{\Gamma_{\text{int}}} \mathbf{B}_{cz}^{\text{T}} \mathbf{R}_{cz}^{\text{T}} \mathbf{C}_{cz} \mathbf{R}_{cz} \mathbf{B}_{cz} \ \mathrm{d}\partial\Omega. \tag{2.74}$$

The weak form and finite element discretization of 3D moisture diffusion along the polymeric encapsulant layer will be presented in this section. Since a staggered scheme is adopted for the solution of hygro-thermo-visco-elastic problem, the spacing of mesh for moisture diffusion can be different from that of thermo-mechanical model. Hence, an appropriate interpolation scheme is required to project the nodal temperatures from the thermo-mechanical problem to the nodes of mesh for moisture diffusion to determine the diffusion coefficients as stated in Eq. (2.24). In the sequel, the finite element mesh for moisture diffusion coincident with the discretization for the thermo-mechanical interface of encapsulant layers is adopted for convenience.

By multiplying Eq. (2.23) with a test function $\delta c(\mathbf{X}, t)$, the weak form for moisture diffusion after integration by parts can be constructed as follows

$$\int_{\mathcal{B}_0} D\nabla_{\mathbf{X}}c \cdot \nabla_{\mathbf{X}}\delta c \, \mathrm{d}\Omega + \int_{\mathcal{B}_0} \delta c \frac{\partial c}{\partial t} \, \mathrm{d}\Omega = 0. \tag{2.75}$$

The interpolation of moisture concentration and its variation in a generic material point $\mathbf{X}$ and at the time point t is given by

$$c(\mathbf{X}, t) \approx \sum_{I=1}^{n_n} N_I(\boldsymbol{\xi})c_I = \mathbf{N}_c\tilde{\mathbf{c}}, \quad \delta c(\mathbf{X}, t) \approx \sum_{I=1}^{n_n} N_I(\boldsymbol{\xi})\delta c_I = \mathbf{N}_c\delta\tilde{\mathbf{c}}, \tag{2.76}$$

where $\mathbf{N}_c = [N_1, N_2, N_3, N_4, N_5, N_6, N_7, N_8]$ is the shape function matrix, and $\tilde{\mathbf{c}}$ is the moisture concentration nodal vector. Besides, the interpolation of the spatial concentration gradient $\nabla_{\mathbf{X}}c$ and its variation $\nabla_{\mathbf{X}}\delta c$ can be expressed as

$$\nabla_{\mathbf{X}}c \approx \mathbf{G}^{-\mathrm{T}}\nabla_{\boldsymbol{\xi}}\mathbf{N}_c\tilde{\mathbf{c}} = \mathbf{B}_c\tilde{\mathbf{c}}, \quad \nabla_{\mathbf{X}}\delta c \approx \mathbf{G}^{-\mathrm{T}}\nabla_{\boldsymbol{\xi}}\mathbf{N}_c\delta\tilde{\mathbf{c}} = \mathbf{B}_c\delta\tilde{\mathbf{c}}, \tag{2.77}$$

Introducing Eq. (2.76) and Eq. (2.77) into Eq. (2.75), the variational form of moisture diffusion is given by

$$\delta\tilde{\mathbf{c}}^{\mathrm{T}} \int_{\mathcal{B}_0} \left(D\mathbf{B}_c^{\mathrm{T}}\nabla_{\mathbf{X}}c + \mathbf{N}_c^{\mathrm{T}}\dot{c} \right) \mathrm{d}\Omega = \delta\tilde{\mathbf{c}}^{\mathrm{T}}\mathbf{f}_{\mathrm{int}}^c \tag{2.78}$$

where $\mathbf{f}_{\mathrm{int}}^c$ is the internal residual vector, which is defined as

$$\mathbf{f}_{\mathrm{int}}^c = \int_{\mathcal{B}_0} \left(D\mathbf{B}_c^{\mathrm{T}}\nabla_{\mathbf{X}}c + \mathbf{N}_c^{\mathrm{T}}\dot{c} \right) \mathrm{d}\Omega. \tag{2.79}$$

The linearization for moisture diffusion at the $(k + 1)th$ iteration in the Newton-Rapson iterative solution scheme reads

$$\mathbf{K}^{c,k}\Delta\tilde{\mathbf{c}}^{k+1} = -\mathbf{f}_{\mathrm{int}}^{c,k} \tag{2.80a}$$

$$\tilde{\mathbf{c}}^{k+1} = \tilde{\mathbf{c}}^k + \Delta\tilde{\mathbf{c}}^{k+1} \tag{2.80b}$$

where $\mathbf{K}^c$ is the element stiffness for moisture diffusion, which is given by

$$\mathbf{K}^c = \int_{\mathcal{B}_0} \left(D\mathbf{B}_c^{\mathrm{T}}\mathbf{B}_c + \frac{1}{\Delta t}\mathbf{N}_c^{\mathrm{T}}\mathbf{N}_c \right) \mathrm{d}\Omega \tag{2.81}$$

2.1.5 Staggered solution scheme for the multi-field framework

In this section, the staggered computational procedure for the solution of thermo-mechanical problem with solid shell element and interface element formulation and temperature dependent 3D moisture diffusion is outlined.

With regard to the thermo-mechanical governing equations incorporating the solid shell formulation, let consider the time increment $\left[t_n, t_{n+1}^{(k)}\right]$, where t_n and $t_{n+1}^{(k)}$ stand for the previous converged increment and prospective current increment at iteration k, respectively. Given the data $\{\mathbf{d}_n, \varsigma_n, \hat{\mathbf{T}}_n\}$ at the previous converged increment, the nonlinear incremental solution requires the Newton iterations at the intermediate state $\{\mathbf{d}_{n+1}^{(k)}, \varsigma_{n+1}^{(k)}, \hat{\mathbf{T}}_{n+1}^{(k)}\}$. Note that $\{\mathbf{d}_n, \varsigma_n, \hat{\mathbf{T}}_n\}$ and $\{\mathbf{d}_{n+1}^{(k)}, \varsigma_{n+1}^{(k)}, \hat{\mathbf{T}}_{n+1}^{(k)}\}$ denote the nodal displacement vector, the enhancing vector, and the nodal temperature vector at the previous converged increment and prospective current increment at $(k)th$ iteration, respectively. Based on the static condensation described in Section 2.1.4, the nodal displacement and temperature vectors are defined as unknowns in the element level, and the increment of enhancing vector in the $(k)th$ iteration of next time increment, $\Delta\varsigma_{n+1}^{(k)}$, should be determined. According to the procedure proposed in [100], it is calculated as $\Delta\boldsymbol{\varsigma}_{n+1}^{(k)}$ is given by

$$\Delta\varsigma_{n+1}^{(k)} = -\left[\mathbf{k}_{\varsigma\varsigma,n}\right]^{-1}\left[\mathbf{R}_{\text{int},n}^{\varsigma} + \mathbf{k}_{\varsigma d,n}\Delta\mathbf{d}_{n+1}^{(k)} + \mathbf{k}_{\varsigma T,n}\Delta\hat{\mathbf{T}}_{n+1}^{(k)}\right] \qquad (2.82)$$

It should be pointed out that the increments $\Delta\mathbf{d}_{n+1}^{(k)}$ and $\Delta\hat{\mathbf{T}}_{n+1}^{(k)}$ are provided by the solver, while the element matrices at the previous increment $[\mathbf{k}_{\varsigma\varsigma,n}]^{-1}$, $\mathbf{R}_{\text{int},n}^{\varsigma}$, $\mathbf{k}_{\varsigma d,n}$, $\mathbf{k}_{\varsigma T,n}$, and ς_n are all stored as internal variables. The numerical algorithm for the finite element implementation of thermo-mechanical problem with solid shell and interface element formulation is detailed in Algorithm 1. The Newton-Raphson iteration is performed until the machine precision is achieved, i.e., the tolerance of residual vector is up to 10^{-15}.

It is worth noting that the history variables h at the integration points need to be determined due to the time dependency of visco-elastic con-

Algorithm 1: Numerical implementation procedure of the coupled thermo-mechanical formulation

---

if *Solid shell element* **then**

    Data: $\mathbf{d}_n$, $\hat{\mathbf{T}}_n$, $\Delta\mathbf{d}_{n+1}^{(k)}$, $\Delta\hat{\mathbf{T}}_{n+1}^{(k)}$

    Result: $\mathbf{d}_{n+1}$, $\hat{\mathbf{T}}_{n+1}$

    Initialization of $\boldsymbol{\varsigma}_n$, $\mathbf{R}_{\mathrm{int},n}^{\varsigma}$, $\mathbf{k}_{\varsigma d,n}$, $[\mathbf{k}_{\varsigma\varsigma,n}]^{-1}$;

    while $||R_d^*|| > tolerance$ **do**

        Compute $\Delta\boldsymbol{\varsigma}_{n+1}^{(k)} = -[\mathbf{k}_{\varsigma\varsigma,n}]^{-1}\left[\mathbf{R}_{\mathrm{int},n}^{\varsigma} + \mathbf{k}_{\varsigma d,n}\Delta\mathbf{d}_{n+1}^{(k)} + \mathbf{k}_{\varsigma T,n}\Delta\hat{\mathbf{T}}_{n+1}^{(k)}\right]$;

        Update the enhancing vector $\boldsymbol{\varsigma}_{n+1}^{(k)} = \boldsymbol{\varsigma}_n + \Delta\boldsymbol{\varsigma}_{n+1}^{(k)}$;

        for *n ← 1* **to** *8 integration points* **do**

            Compute the curvilinear basis $\mathbf{G}_{n+1}^{(k)}$ *and* $\mathbf{g}_{n+1}^{(k)}$;

            Compute the B matrices $\mathbf{B}_{n+1}^{(k)}$ *and* $\mathbf{B}_{T,n+1}^{(k)}$;

            Modify the $\mathbf{B}_{n+1}^{(k)}$ *matrix according to the ANS method;*

            Compute $\mathbb{C}_{n+1}^{(k)}$, $\mathbf{S}_{n+1}^{(k)}$, *and* $\mathbf{Z}_{n+1}^{(k)}$;

            Compute the EAS operator $\mathbf{M}_{n+1}^{(k)}$;

        end

        Compute the element stiffness matrices $\mathbf{k}_{dd,n+1}^{(k)}$, $\mathbf{k}_{d\varsigma,n+1}^{(k)}$, $\mathbf{k}_{\varsigma d,n+1}^{(k)}$, $\mathbf{k}_{\varsigma\varsigma,n+1}^{(k)}$, *and* $\mathbf{k}_{TT,n+1}^{(k)}$;

        Compute the internal force vectors $\mathbf{R}_{\mathrm{int},n+1}^{d(k)}$, $\mathbf{R}_{\mathrm{int},n+1}^{\varsigma(k)}$, *and* $\mathbf{R}_{\mathrm{int},n+1}^{T(k)}$;

        Perform the static condensation and final assembly;

    end

end

else if *Cohesive interface element* **then**

    Data: $\mathbf{d}_n$, $\hat{\mathbf{T}}_n$, $\Delta\mathbf{d}_{n+1}^{(k)}$, $\Delta\hat{\mathbf{T}}_{n+1}^{(k)}$

    Result: $\mathbf{d}_{n+1}$, $\hat{\mathbf{T}}_{n+1}$

    while $||R_d^*|| > tolerance$ **do**

        Compute the operators $\mathbf{L}_{cz}$ *and* $\mathbf{M}_{cz}$;

        for *n ← 1* **to** *4 integration points* **do**

            Compute the shape function $\mathbf{N}_{cz,n+1}^{(k)}$;

            Compute the matrix $\mathbf{B}_{cz,n+1}^{(k)} = \mathbf{N}_{cz,n+1}^{(k)}\mathbf{L}_{cz}$;

            Compute the rotation matrix in the curvilinear system $\mathbf{R}_{cz,n+1}^{(k)}$;

            Compute the local gap $\mathbf{g}_{\mathrm{loc},n+1}^{(k)} = \mathbf{R}_{cz,n+1}^{(k)}\mathbf{B}_{cz,n+1}^{(k)}\hat{\mathbf{d}}_{n+1}^{(k)}$;

            Compute the temperature value at the integration point $T_{int,n+1}^{(k)}$;

            if $|T_{int,n+1}^{(k)} - T_{int,n}| > tolerance$ **then**

                Compute the history variable $h_{int,n+1}^{(k)} = h_{int,n}$;

            else

                Compute the history variable $h_{int,n+1}^{(k)} = h_{int,n} + \Delta t$;

            end

            Compute the stiffness matrix $\mathbf{C}_{cz,n+1}^{(k)}$ *and the traction vector* $\mathbf{T}_{n+1}^{(k)}$;

        end

        Compute the element stiffness matrix $\mathbf{K}_{\mathrm{int},n+1}^{e(k)}$;

        Compute the internal residual vector $\mathbf{f}_{\mathrm{int},n+1}^{(k)}$;

    end

end

---

stitutive equation, Eq. (2.20). To model relaxation, this history variable is set to zero in case of any temperature change, which is stored as a state variable in the interface element implementation, while updated by the current time increment if the temperature value remains constant compared with that of previous increment, see Algorithm 1. Hence, the drawback of temperature-time superposition principle for thermo-visco-elastic modeling of polymeric materials is overcome.

Once the temperature and displacement field in the coupled thermo-mechanical problem are solved in a given time increment, these nodal values are transferred to the moisture diffusion problem, which is solved by the Euler backward time integration scheme using the same temporal interval with that of the thermo-mechanical analysis. As stated in Section 2.1.3, given the time scale difference between the moisture diffusion and thermo-mechanical phenomena, the coefficient in the current increment of moisture diffusion analysis is determined from the nodal temperature and gap values at the previous time increment. The detailed computational procedure of moisture diffusion is outlined in Algorithm 2.

2.2 Numerical applications to photovoltaics

In this section, three international standard tests for photovoltaics, including damp heat test, humidity freeze test, and thermal cycling test, are simulated by the proposed computational framework. Note that the damp heat test requires constant temperature and humidity testing environments, which uncouples the moisture diffusion from the thermo-mechanical problem and thus allows the derivation of analytical solution useful for benchmark targets, while the latter require the fully coupled solution scheme due to the spatial variation of temperature. Besides, the role of cracks in silicon on moisture diffusion pattern is also investigated and compared to the experimental electroluminescence images.

Algorithm 2: Numerical implementation procedure of the moisture diffusion along the interface

---

Data: $\tilde{\mathbf{c}}_n$, $\Delta\tilde{\mathbf{c}}_{n+1}^{(k)}$
Result: $\tilde{\mathbf{c}}_{n+1}$
Initialization of $\mathbf{d}_n$ *and* $\hat{\mathbf{T}}_n$;
while $||\mathbf{f}_{int}^c|| >$ *tolerance* **do**
    for $n \leftarrow 1$ **to** *8 integration points* **do**
        Compute the shape function $\mathbf{N}_{c,n+1}^{(k)}$;
        Compute the B matrix $\mathbf{B}_{c,n+1}^{(k)}$;
        Compute the temperature value at the integration point $T_{int,n}$ *with* $\hat{\mathbf{T}}_n$;
        Compute the normal gap at the integration point $\Delta_{int,n}$ *with* $\mathbf{d}_n$;
        if $\Delta_{int,n} \leq \delta_n^c$ **then**
            Compute the coefficient $D_{int,n+1}^{(k)} = A\exp\left(-\frac{E_a}{T_{int,n}R}\right)$;
        else
            Compute the coefficient $D_{int,n+1}^{(k)} = A\exp\left(-\frac{E_a}{T_{int,n}R}\right)\frac{\Delta_{int,n}}{\delta_n^c}$;
        end
    end
    Compute the element stiffness matrices $\mathbf{K}_{c,n+1}^{(k)}$;
    Compute the internal force vectors $\mathbf{f}_{int,n+1}^{c(k)}$;
    Perform the final assembly;
end

2.2.1 Damp heat test

As prescribed by the international standard, the damp heat test is conducted in the environmental chamber with the constant temperature of 85 °C and relative humidity of 85% RH. Since temperature is kept constant in this test, the moisture diffusion problem can be solved independently from the coupled thermo-mechanical problem with the constant diffusivity. The specimen is a double-glass PV laminate of span $l = 40$ mm separated by EVA. The thickness of glass laminae is 3 mm, and the thickness of EVA is 0.5 mm. As glass is not permeable, the moisture will only diffuse from the free edges of EVA towards the central part in this test, see Fig. 14. The analytical solution was obtained in [127], which will be treated as a benchmark of the computational scheme proposed above. Assuming the initial laminate is dry, the spatial and temporal solution c can be obtained as

$$c = c^* + \frac{4c^*}{\pi}\sum_{m=0}^{\infty}\frac{1}{2m+1}\sin\left[\frac{(2m+1)\pi x}{l}\right]\mathrm{e}^{\left(-D(2m+1)^2\pi^2 t/l^2\right)} \quad (2.83)$$
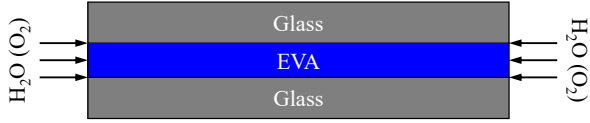
Figure 14: The sketch of double-glass structure in the damp heat test.

The mesh size of finite element model is 1 mm, and there are 1600 solid diffusion elements in total. The contour plot of moisture concentration inside the EVA is shown in Fig. 15, and as clearly seen, water concentration gradually diffuses from the edges into the middle area of EVA during simulation. At 100 h, the most area of EVA is still dry with almost zero concentration, see Fig. 15(a), while after 1000 h, the dry area becomes obviously smaller. To quantitatively validate the computational diffusion model, the predicted moisture concentration with respect to the distance from the edge after 1000 h (the black solid line in Fig. 16) is compared with that obtained from the analytical solution (the black dotted line Fig. 16), and they agree with each other very well. Besides, this model is also used to simulate the experimental results obtained from Miami as reported in [29], and numerical predictions also agree very well with the data from the impermeable double-glass laminate exposed to Miami environment for 1 year, 2 years, and 3 years, which further proves the reliability of the diffusion modeling method proposed in this work.

A series of damp heat tests were also examined with the double glass modules exposed to four different hot and humid conditions, namely 85 °C/85% RH, 65 °C/85% RH, 45 °C/85% RH, and 85 °C/40% RH, which correspond to the absolute humidity of 2.74 kg/cm^3, 1.25 kg/cm^3, 0.508 kg/cm^3, and 1.29 kg/cm^3, respectively [128].

The contour plots of moisture diffusion in the 85 °C/85% RH damp heat test obtained from simulation are shown in Fig. 17 and compared with the corresponding experimental EL images at different time points [128]. As can be seen from both predictions and EL images, moisture diffuses from the free edges of the EVA layer towards the central area during aging, and they agree with each other very well. The captured EL

0.0000 g/cm³   0.0056 g/cm³

(a) 100 h   (b) 300 h   (c) 400 h

(d) 500 h   (e) 600 h   (f) 700 h

(g) 800 h   (h) 900 h   (i) 1000 h
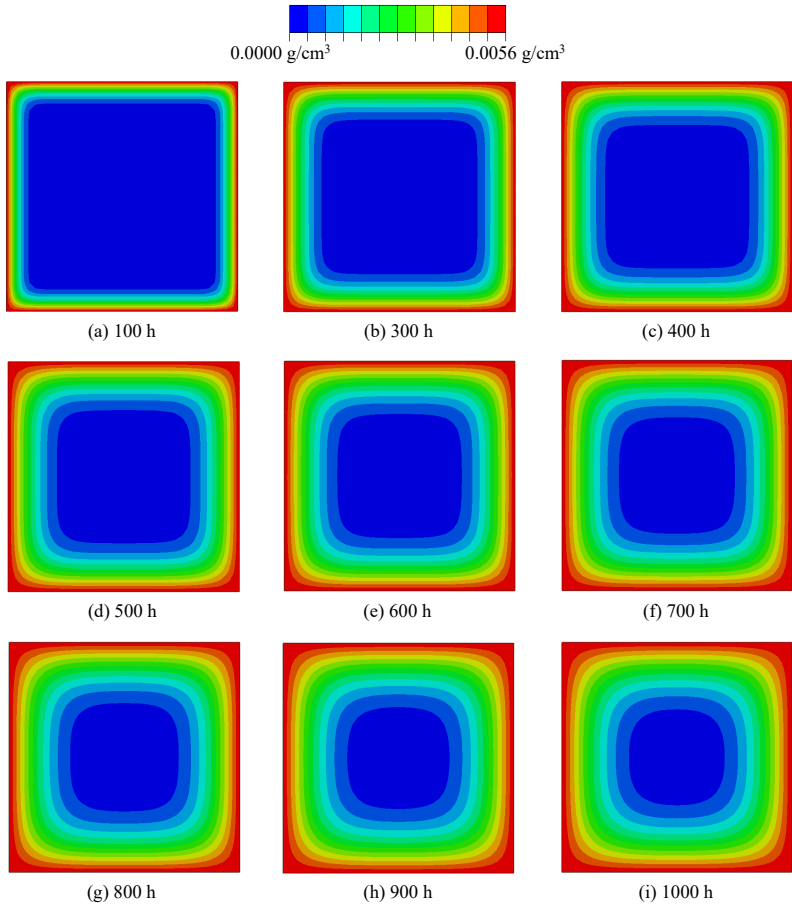
Figure 15: The contour plot of moisture diffusion along the EVA layer inside the double-glass laminate during the damp heat simulation.
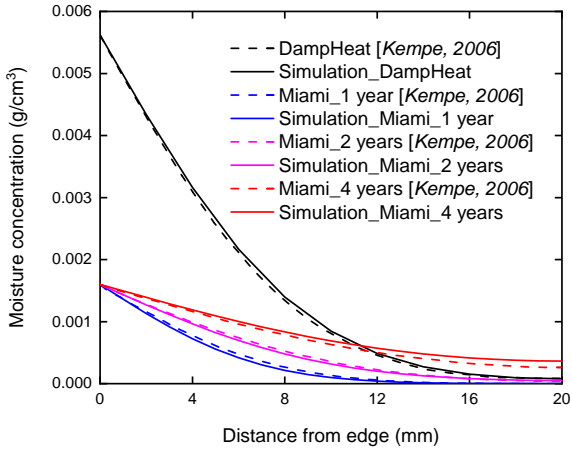
Figure 16: The comparison of moisture concentration vs. distance from the edge of laminate curves between diffusion simulation and damp heat test after 1000 h as well as experimental data in Miami.

images show the dark bands at the side area of EVA, which are not detected at the beginning (Fig. 17(a)), and get thicker after 43 h (Fig. 17(b)) and 81 h (Fig. 17(c)). This trend that indicates the moisture ingress into the module over time [128] is well reproduced by the modeling method proposed in this work. To see the temperature effect on the diffusion phenomena, the contour plots of moisture diffusion and experimental EL images in the 65 °C/85% RH and 45 °C/85% RH damp heat tests are also compared and shown in Fig. 18 and Fig. 19, respectively. Due to the temperature-dependent diffusion properties, the absolute humidity in these two cases differs from that in the 85 °C/85% RH case. The diffusion phenomena are much slower in low-temperature conditions since the diffusion coefficients are smaller. It is clearly observed that the process for dark bands in the 65 °C/85% RH case (see Fig. 18) or 45 °C/85% RH case (see Fig. 19) to become thick is slower than that in the 85 °C/85% RH damp heat case. Besides, it is worth noting that the absolute humidity in the 65 °C/85% RH (see Fig. 18) and 85 °C/40% RH (see Fig. 20) are

0.00 kg/cm³   2.74 kg/cm³

(a) 0 h   (b) 43 h   (c) 81 h
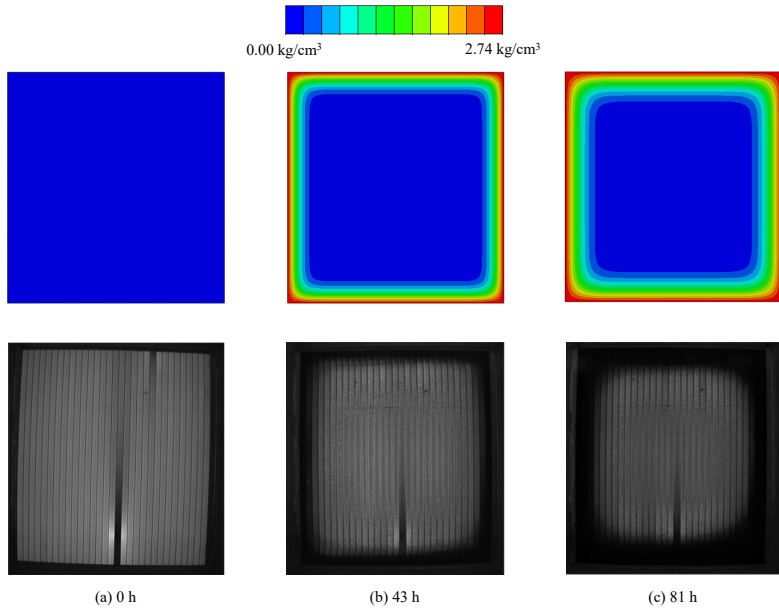
Figure 17: Comparison between the moisture diffusion contour plots obtained from simulation and the EL images taken from [128] in the 85 °C/85% RH damp heat test after 0 h, 43 h, and 81 h.

0.00 kg/cm³   1.25 kg/cm³

(a) 0 h   (b) 130 h   (c) 279 h
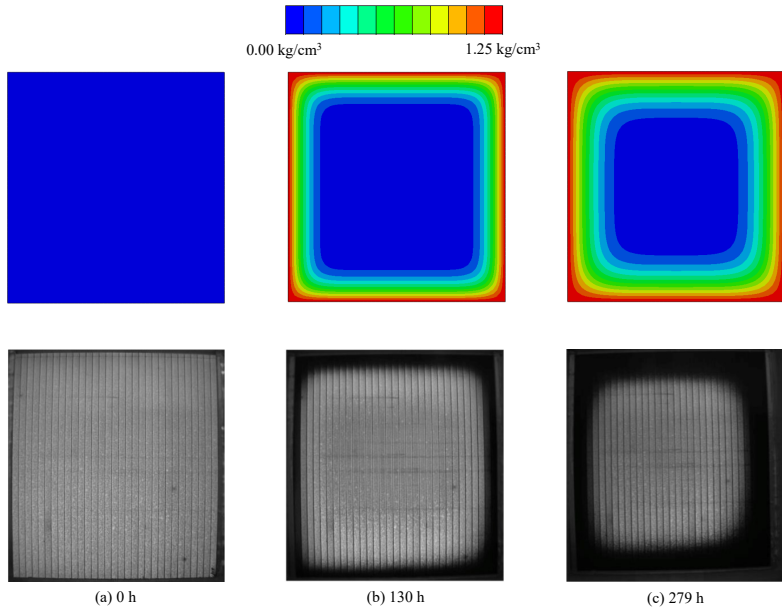
Figure 18: Comparison between the moisture diffusion contour plots obtained from simulation and the EL images taken from [128] in the 65 °C/85% RH damp heat test after 0 h, 130 h, and 279 h.

0.000 kg/cm³   0.508 kg/cm³

(a) 0 h   (b) 321 h   (c) 776 h
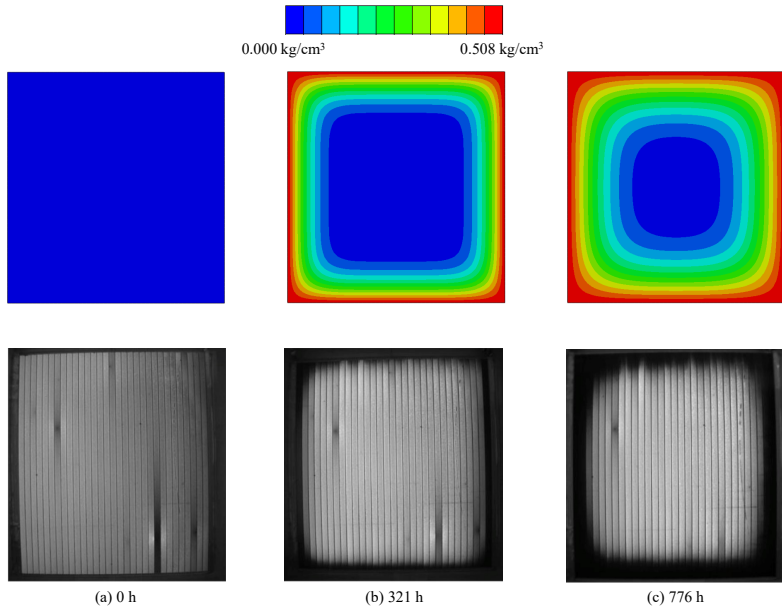
Figure 19: Comparison between the moisture diffusion contour plots obtained from simulation and the EL images taken from [128] in the 45 °C/85% RH damp heat test after 0 h, 321 h, and 776 h.

0.00 kg/cm³   1.29 kg/cm³

(a) 0 h   (b) 104 h   (c) 187 h
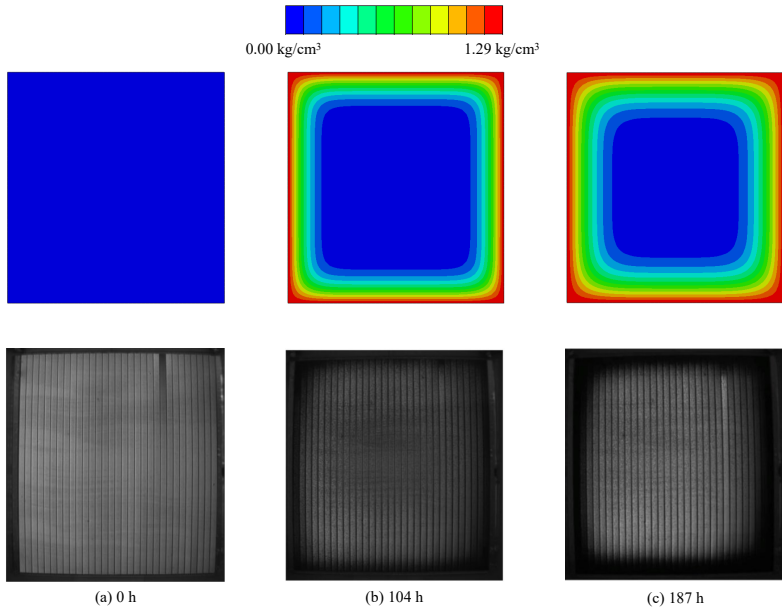
Figure 20: Comparison between the moisture diffusion contour plots obtained from simulation and the EL images taken from [128] in the 85 °C/40% RH damp heat test after 0 h, 104 h, and 187 h.

almost equal to each other (1.25 kg/cm^3 vs. 1.29 kg/cm^3). However, due to the temperature difference, the diffusion phenomena are still different in these two cases.

The predicted time history evolution of moisture concentration at the positions with different distances away from the edge in the four different cases is shown in Fig. 21. The moisture concentration at different positions increases over time as the diffusion phenomena proceed during the damp heat tests. Although the absolute humidity at the 65 °C/85% RH and 85 °C/40% RH cases are almost equal to each other, the diffusion time history demonstrates the significant difference, especially at the positions relatively far away from the free edge. As can be seen from Fig. 21(b) and Fig. 21(d), the trends of moisture concentration versus time curves at the position 10 mm far away from the edge in both cases are very similar, but as the distance increases from 20 mm to 70 mm away from the edge, the corresponding concentration versus time curve in the 85 °C/40% RH case is obviously higher than that in the 65 °C/85% RH case, indicating faster diffusion process in the former case that can be ascribed to its higher temperature.

The predicted spatial variation of moisture concentration in the four different damp heat cases after 200 h, 400 h, 600 h, and 800 h are shown in Fig. 22. Moisture diffusion takes place from the free edges towards the center of the EVA layer, and as a result, moisture concentration at the central area increases over time for all the different hygrothermal conditions. For the 85 °C/85% RH damp heat case, the concentration at the center of the module starts to increase after 400 h (see Fig. 22(b)), and reaches around 0.5 kg/cm^3 after 800 h (see Fig. 22(d)), while for the 45 °C/85% RH case, the moisture concentration at the center is still zero even after 800 h due to its low diffusivity. To further illustrate this point, it can also be observed that the spatial variation curves of moisture concentration in the 85 °C/40% RH damp heat case are always above the red curves corresponding to the 65 °C/85% RH damp heat case despite the approximate absolute humidity on the boundary.
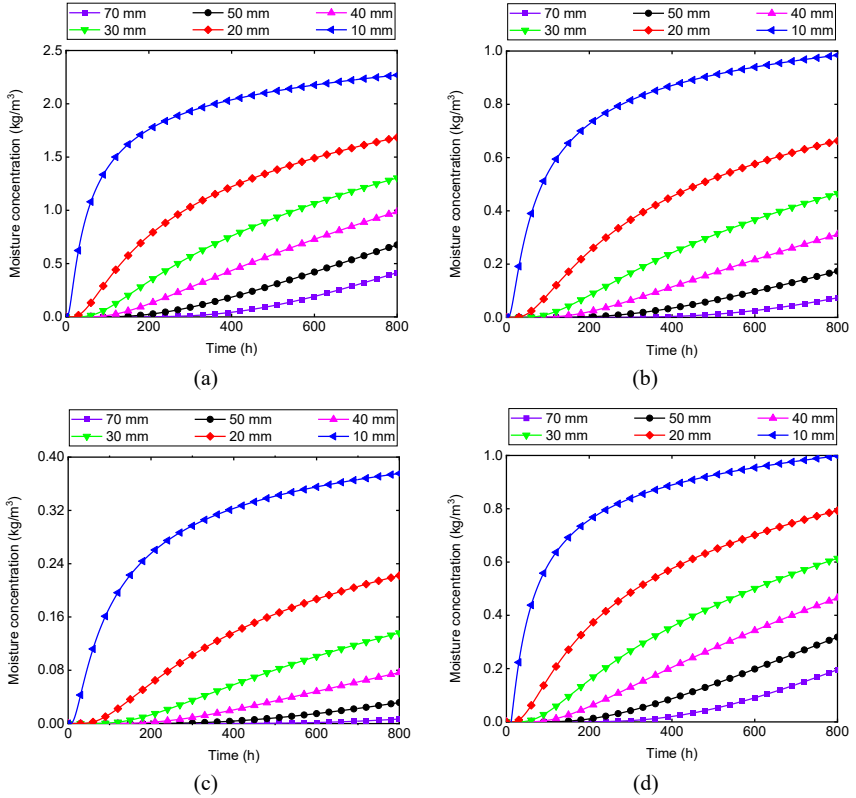
Figure 21: The plots of predicted moisture concentration vs. time at the positions (70 mm, 50 mm, 40 mm, 30 mm, 20 mm, and 10 mm away from the edge of EVA layer) in the (a) 85 °C/85% RH damp heat case, (b) 65 °C/85% RH damp heat case, (c) 45 °C/85% RH damp heat case, and (d) 85 °C/40% RH damp heat case.
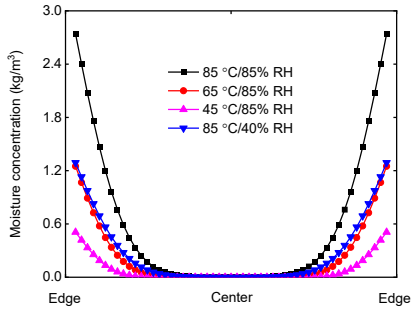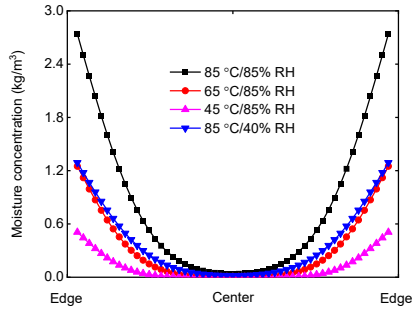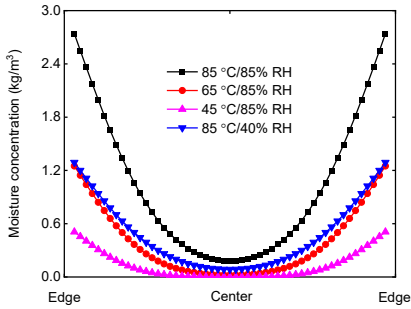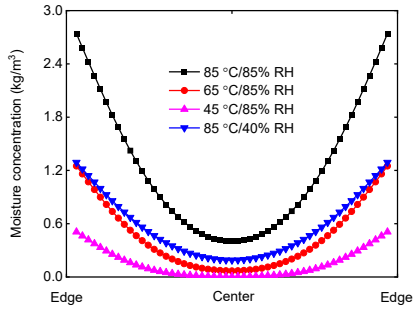
Figure 22: The spatial variation plots of predicted moisture concentration inside the EVA layer in the four different damp heat cases after (a) 200 h, (b) 400 h, (c) 600 h, and (d) 800 h.
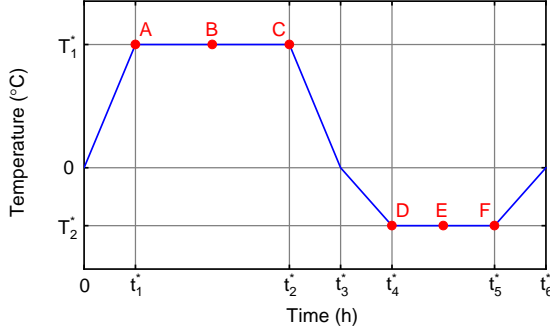
Figure 23: Temperature profile imposed inside the chamber during the humidity freeze test

2.2.2 Humidity freeze test

In the humidity freeze test of PV laminates, as requested by the international standard, the modules are subjected to the cycling temperature condition from -40 °C to 85 °C with the constant humidity condition of 85% RH. The temperature ramp can be expressed as

$$
T^*(t) = \begin{cases}
\frac{t}{t_1^*}T_1^* & 0 \leq t < t_1^* \\
T_1^* & t_1^* \leq t < t_2^* \\
\frac{t_3^*-t}{t_3^*-t_2^*}T_1^* & t_2^* \leq t < t_3^* \\
\frac{t-t_3^*}{t_4^*-t_3^*}T_2^* & t_3^* \leq t < t_4^* \\
T_2^* & t_4^* \leq t < t_5^* \\
\frac{t_6^*-t}{t_6^*-t_5^*}T_2^* & t_5^* \leq t < t_6^*
\end{cases}
\tag{2.84}
$$

where $T_1^* = 85$ °C, $T_2^* = -40$ °C, and $t_1^* = 1.0$ h, $t_2^* = 21.0$ h, $t_3^* = 22.0$ h, $t_4^* = 22.5$ h, $t_5^* = 23.5$ h, $t_6^* = 24.0$ h, as shown in Fig. 23.

Compared with the damp heat test, this case is much more complex and almost impossible to obtain the analytical solution due to the spatial and temporal temperature variation inside the EVA, to which a non-constant temperature boundary condition is applied. Particularly, the cohesive properties and diffusivity of EVA need to be updated during simulation, and to be specific, the viscoelastic parameters $\alpha(T)$ and $a(T)$ for

56

Table 1: Mechanical and thermal properties of the PV materials.

	E (GPa)	ρ (kg/m^3)	α	c_p (J/kg · K)	k_0 (W/m · K)
Backsheet	2.8	1200	5.04e-5	300	0.36
Glass	73	2300	8e-6	500	0.8
Silicon	130	2500	2.49e-6	715	148

the calibration of Young's modulus of EVA are temperature dependent as experimentally evaluated in [86] and interpreted through the fractional calculus method [122], see the plot of modulus E in Fig. 24. Regarding the properties of moisture diffusion, the coefficient D is determined according to the Arrhenius type equation Eq. (2.24) reported in [29]. The thermal and mechanical properties of different PV materials are taken from [85, 86], which are listed in Table 1. Besides, the critical opening of polymeric interface δ_n^c can be estimated from the experimental data of variation of Mode 1 fracture energy with respect to temperature in [31], since the area below the traction versus separation curve is the fracture energy.

The temperature variation inside the double glass laminate is strongly dependent on the heat conduction properties of different layers, as shown by the temperature contour of the cross section at time point A in Fig. 25. The contour plot of temperature distribution inside the EVA layer in the first cycle during simulation is shown in Fig. 26. At time point A, the boundary temperature reaches 85 °C, and is kept constant for 20 hours. As shown in Fig. 26(a)-(c), heat gradually diffuses from the edges into the middle area of EVA during this period. At time point D, the boundary temperature drops to -40 °C, but the temperature in the middle area of EVA layer is still higher than 65 °C due to the inertial effect of heat conduction, see Fig. 26(d)-(f). Remarkably, this spatial and temporal variation of temperature inside EVA leads to the difference of moisture diffusion properties from that of EVA subjected to constant condition in the damp heat test. To quantitatively describe the spatial variation of temperature inside EVA, the temperature versus distance from edge curves at the six different time points in the first cycle is plotted in Fig. 27. As
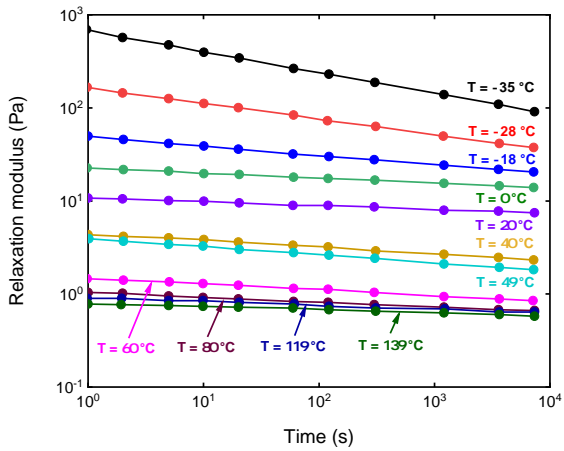
Figure 24: Relaxation modulus of EVA vs. time curves at different temperatures (adapted from [90]).
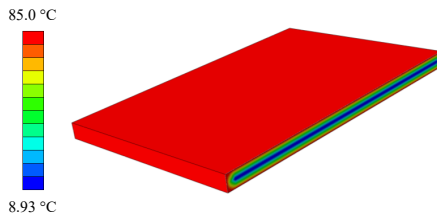
Figure 25: The temperature contour plot of the cross section of the double glass laminate at time point A in the first cycle during humidity freeze simulation.

can be seen, the platform, which denotes the central area temperature of EVA, gradually goes up from time point A to C with the evolution of thermal conduction. At time C, the temperature at almost all the area of EVA from the edge to the center reaches around 85 °C, which means the EVA layer is fully and evenly heated after 20 hours. Besides, the platform at the time period when boundary temperature changes to -40 °C, which can be ascribed to the hysteresis of heat conduction, gradually goes down from time point D to F. It is worth noting that the temperature at the central area is still higher than 30 °C at the end of one complete cycle due to the relatively short duration of constant low-temperature boundary loading.

The contour plot history of moisture diffusion during the humidity freeze simulation is shown in Fig. 28. The moisture gradually diffuses into the central area, which is very similar to the phenomena obtained from previous damp heat simulation. However, the amount of moisture concentration is totally different in two cases due to the spatial variation of temperature inside EVA in the humidity freeze simulation. As shown in Fig. 29, the difference of moisture concentration spatial variation after 700 hours and 1000 hours between the damp heat and humidity freeze simulation can be observed. Note that the amount of moisture concentration in all the area of EVA after 700 hours and 1000 hours in the damp heat case is higher than that in the humidity freeze case, since the moisture diffusion coefficient in the former case is much higher at the constant high-temperature condition (85 °C). Furthermore, It can be seen from Fig. 29 that the amount of moisture concentration at all the areas of EVA after 700 hours in the damp heat case is even higher than that in the humidity freeze case after 1000 hours, which further demonstrates the effect of temperature on the moisture diffusion. Besides the difference of spatial variation, the temporal variation between the damp heat and humidity freeze simulation is also shown and compared in this work, see Fig. 30. The time history of moisture concentration at three positions 3 mm, 5 mm, and 8 mm away from the edge is also plotted, and the curves obtained from the damp heat simulations (solid lines) are higher than all the counterparts obtained from the humidity freeze simulations (dotted

lines). Thus, conclusions can be drawn that temperature plays an import role on the moisture diffusion problem as the coefficient is determined from the Arrhenius equation, and this coupling can be described with the proposed modeling method, which can be demonstrated by the example of humidity freeze simulation.

2.2.3 Thermal cycling test

In this section, as shown in Fig. 31, a minimodule composed of 3×3 multicrystalline solar cells with a crack in the middle one, which was tested under the thermal cycling environmental condition with EL images taken regularly as reported in [129], was simulated using the proposed modeling framework. In this case, the temperature ramp is given by

$$T^*(t) = \begin{cases} \frac{t_1^*-t}{t_1^*}(T_1^* - T_2^*) + T_2^* & 0 \le t < t_1^* \\ T_2^* & t_1^* \le t < t_2^* \\ \frac{t-t_2^*}{t_3^*-t_2^*}(T_3^* - T_2^*) + T_2^* & t_2^* \le t < t_3^* \\ T_3^* & t_3^* \le t < t_4^* \\ \frac{t_5^*-t}{t_5^*-t_4^*}(T_3^* - T_1^*) + T_1^* & t_4^* \le t < t_5^* \end{cases} \tag{2.85}$$

where $T_1^* = 25\ °C$, $T_2^* = -40\ °C$, $T_3^* = 85\ °C$, and $t_1^* = 0.5$ h, $t_2^* = 1.5$ h, $t_3^* = 2.5$ h, $t_4^* = 3.5$ h, $t_5^* = 4.0$ h, as shown in Fig. 32. The sketch of the cross-section of the PV minimodule is shown in Fig. 33. The module consists of a tempered glass with the thickness of 4 mm, an encapsulanting EVA with the thickness of 0.5 mm, the silicon solar cell with the thickness of 0.166 mm, another layer of EVA, and finally a thin backsheet made of an ethylene tetrafluoroethylene core and silicon nitride coating with the thickness of 0.1 mm. The thermal and mechanical properties of all the component materials are listed in Table 1. The size of this PV module is 48 cm, and the adopted mesh size of the finite element model is 1 mm. Since backsheet is permeable to water and thus moisture can penetrate from it and percolates along the edges of each solar cell, it is possible in the numerical simulation to directly impose moisture boundary condition at the edges of each solar cell embedded in the module, see Fig. 33.

The temperature contour plots of the cross section of the minimod-
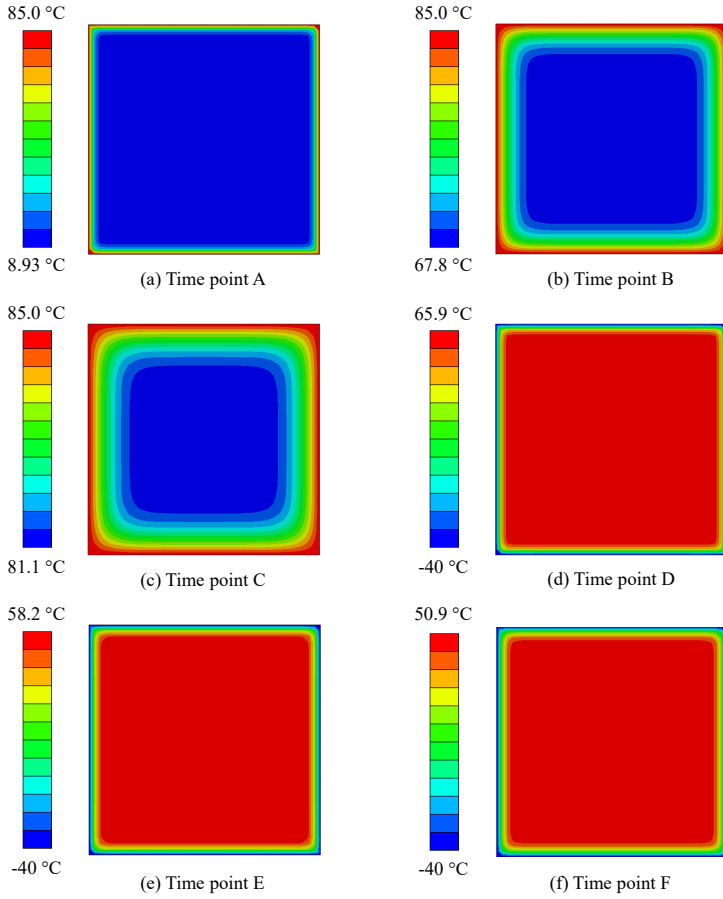
Figure 26: Temperature contour plot inside EVA at six different time points in the first cycle during humidity freeze simulation.
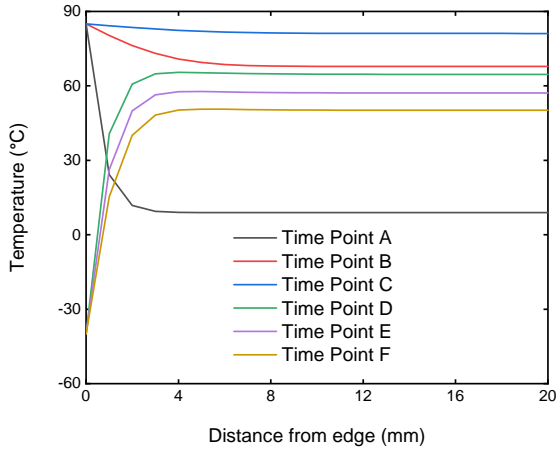
Figure 27: Temperature versus distance from edge curves at six different time points in the first cycle during humidity freeze simulation.

ule at time point B and time point E are shown in Fig. 34. Owning to the different heat conductivity properties of different layers (glass, backsheet, and silicon solar cells), the temperature inside the PV minimodule presents significant spatial variation at both the cooling and heating stages. The temperature distribution inside the EVA layer of the module at six time points of the first cycle during the thermal cycling simulation is shown in Fig. 35. At time point A, heat has diffused inside the panel. From time point A to C, the thermal boundary condition is kept constant with the temperature of 85 °C, and as can be clearly seen, the EVA layer is almost fully heated at the end of this heating period. When the temperature boundary condition drops to -40 °C at time point D, this layer starts to cool down from its edges, but the temperature in the most area is still very high after this period, and the lowest temperature is up to around 50 °C in the time point F, see Fig. 35(f). This trend is quantified in Fig. 36 by plotting the temperature versus the distance from edge at six time points during the first cycle. Compared with the previous curves obtained from
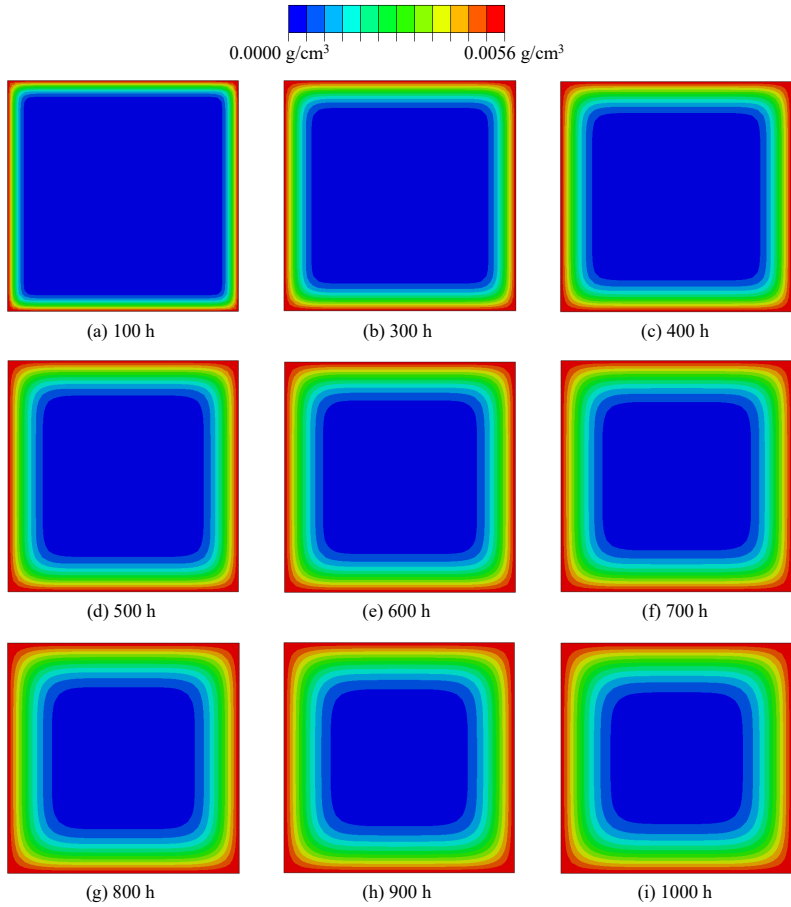
Figure 28: Contour plot of moisture diffusion along the EVA layer during the humidity freeze simulation
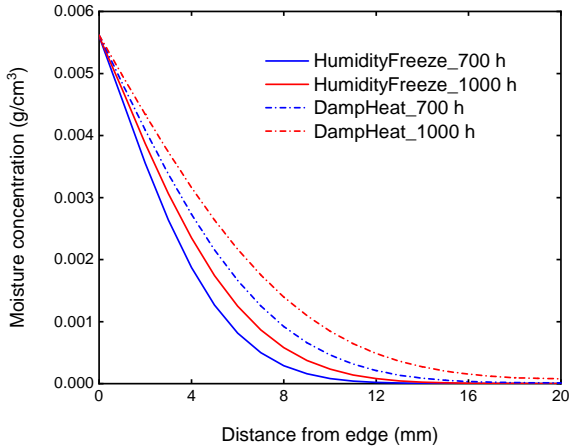
Figure 29: Comparison of moisture concentration versus distance from edge curves after 700 hours and 1000 hours between the damp heat and humidity freeze simulations.

humidity freeze simulation, the platforms are relatively lower at the temperature level of around 0 °C because of the much shorter heating period with the constant temperature boundary condition 85 °C.

The contour plots of moisture concentration inside the EVA layer above the silicon solar cell layer during the thermal cycling simulation are shown in Fig. 37. Notably, moisture diffusion can take place not only from the edges of module, but also along the interspaces between different solar cells as well as the crack indicated in Fig. 31. Thus the moisture boundary condition c^* is imposed on all these edges, and the numerical simulation is performed with this computational framework. As pointed out in [130], the moisture plays a significant role in the oxidation of silicon solar cell, which is demonstrated by the observed darkness in the EL images shown in Fig. 31. The silicon oxidation versus time history curves at the different moisture concentration are plotted in Fig. 38, and it can be seen that higher moisture concentration and longer exposure time lead to more silicon oxidation. The contour plots of normalized oxidation
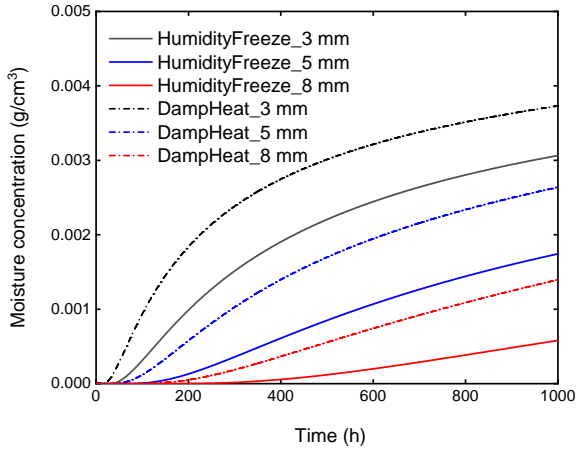
Figure 30: Comparison of time history of moisture concentration at the positions 3 mm, 5 mm, and 8 mm away from the edge between the damp heat and humidity freeze simulations.

of the minimodule during the thermal cycling simulation are shown in Fig. 39. The area close to the crack of the middle solar cell starts to become deeply oxidized resulting from moisture intrusion while all other cell areas show much lower degradation, which demonstrates the consistency between simulation and experiment. At the $460th$ cycle, as shown in Fig. 39, the upper right area of the middle solar cell area during simulation is almost fully oxidized due to the moisture intrusion from the crack channel, and the corresponding EL image (see Fig. 31) also shows much dimmer area at the same position compared with that at the previous cycle. At this stage, electric degradation is significantly enhanced by moisture diffusion from the crack channels and the corresponding oxidation. The contour plots of oxidation (see Fig. 39) correlates very well with the EL images in terms of the electrically inactivated area, which is impossible to be achieved by analytical methods.

120th cycle   160th cycle   200th cycle

240th cycle   280th cycle   320th cycle

360th cycle   400th cycle   460th cycle
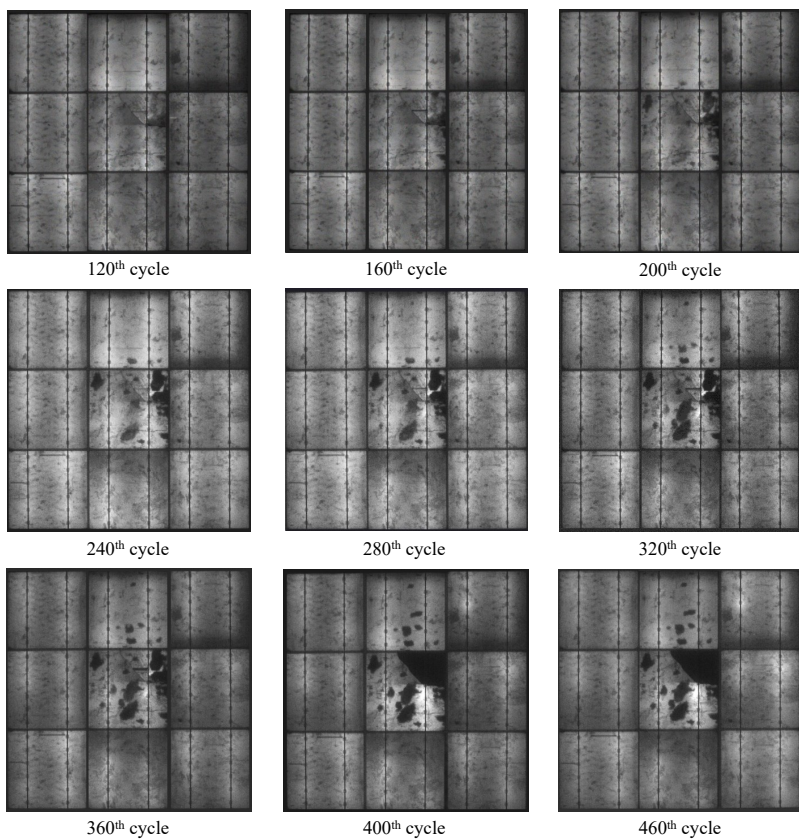
Figure 31: EL images of the minimodule taken at different cyles during the thermal cycling test (adapted from [129]).
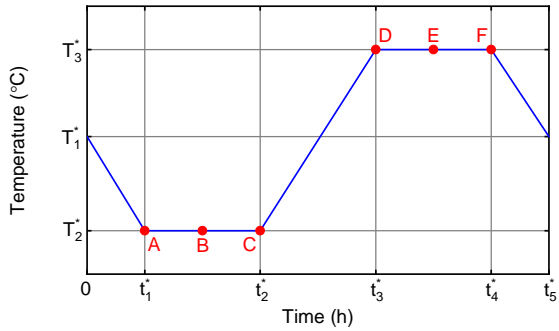
Figure 32: Temperature profile imposed inside the chamber during the thermal cycling test
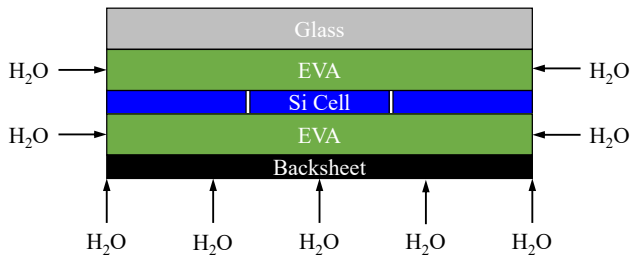
Figure 33: The sketch of the PV minimodule in the thermal cycling test.

(a) Time point B   (b) Time point E
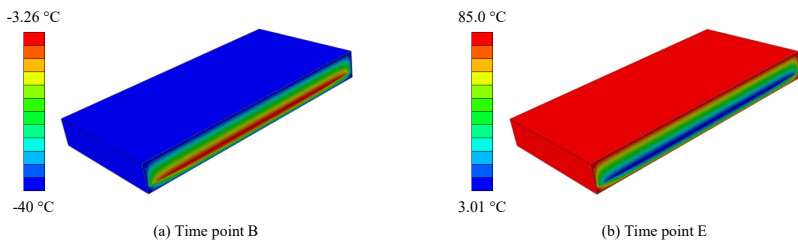
Figure 34: The temperature contour plot of the cross section of the minimodule at time points B and E in the first cycle during the thermal cycling test.

-1.67 °C

-40.0 °C
(a) Time point A

-3.26 °C

-40.0 °C
(b) Time point B

-4.79 °C

-40.0 °C
(c) Time point C

85.0 °C

-6.13 °C
(d) Time point D

85.0 °C

3.01 °C
(e) Time point E

85.0 °C

6.74°C
(f) Time point F
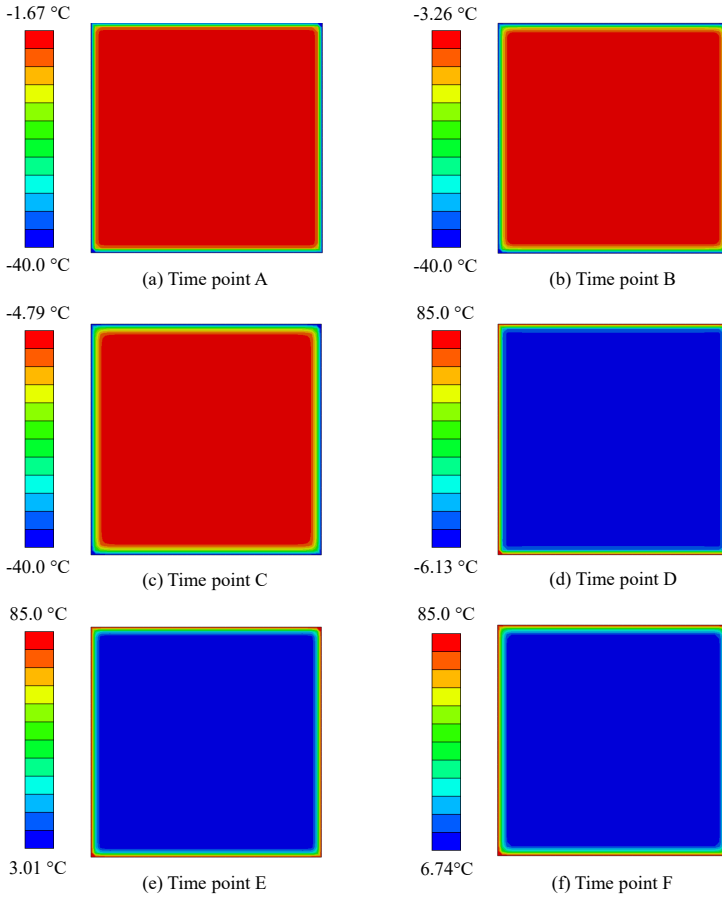
Figure 35: The temperature contour plot inside EVA at six different time points in the first cycle during thermal cycling simulation.
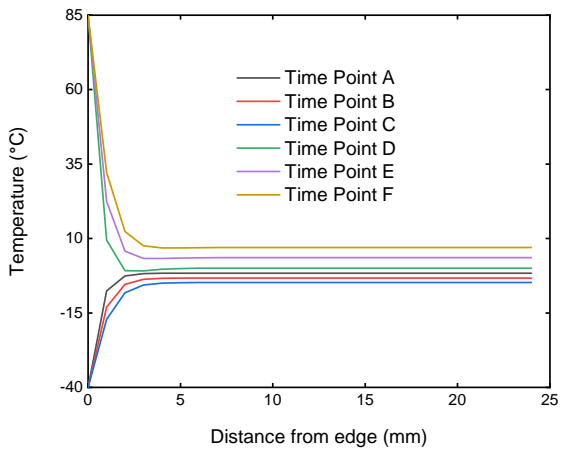
Figure 36: The temperature versus distance from edge curves at six different time points in the first cycle during thermal cycling simulation.
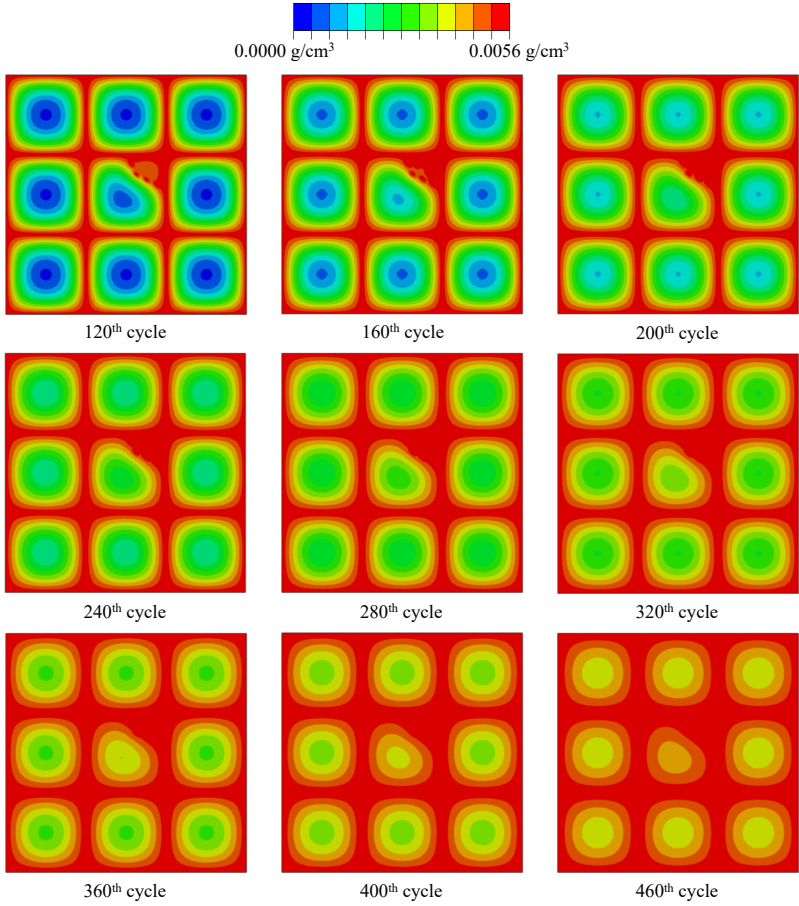
Figure 37: The contour plot of moisture diffusion along the EVA layer above the silicon solar cell layer during the thermal cycling simulation.
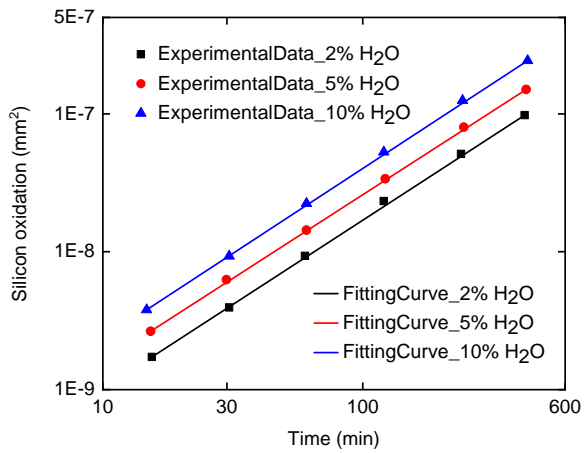
Figure 38: The silicon oxidation versus time history at the different moisture concentration (adapted from [130]).
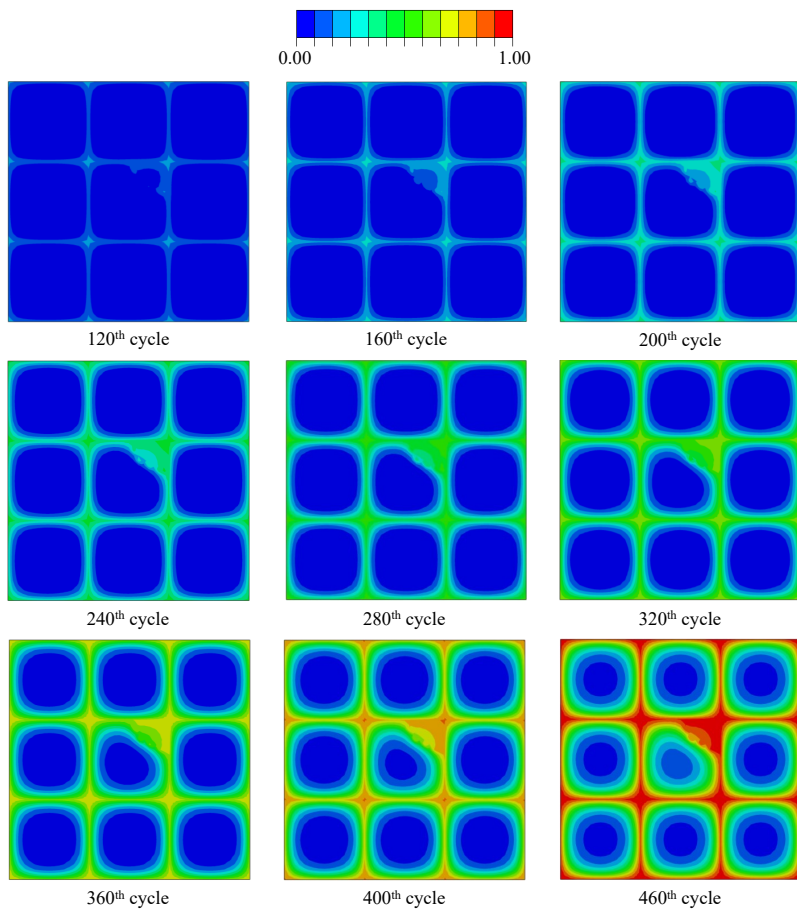
Figure 39: The contour plot of normalized silicon oxidation of the minimodule during the thermal cycling simulation.

Chapter 3

Global-local phase field modeling of silicon cell cracking in photovoltaic laminates

The main content of this chapter is taken from my own publication - Z. Liu, J. Reinoso, M. Paggi. "Phase field modeling of brittle fracture in large-deformation solid shells with the efficient quasi-Newton solution and global–local approach" [131].

Nowadays the crystalline silicon photovoltaic (PV) modules have been massively deployed all over the world since the last century, and according to [132], the installed capacity of PV approximately increases from 40 GW to 715 GW in the recent 10 years. Among the major components of PV products, including tempered glass, ethylene-co-vinyl acetate (EVA), silicon cells, and backsheet, the silicon wafer accounts for more than 40 % of the manufacturing cost of crystalline modules [47]. It was proposed in the 2010 International Technology Roadmap for Photovoltaics that the thickness of silicon cell should be signifcantly decreased so as to save cost of cystalline PV modules. However, the decrease of silicon cell thickness could reduce its robustness under mechanical loading and thus lead to

the formation of microcracking. Hence, the identification of crack initiation and propagation that may trigger performance degradation of PV modules has received a lot of attention in the recent decades.

To accurately predict the failure and crack propagation, several formulations on the basis of different numerical techniques have been developed in the past decades. Simplified phenomenological cohesive zone models specific for the crack modeling along internal boundaries have been proposed in [133, 134, 135, 136, 137], in which cracking events are triggered by the evaluation of traction-separation constitutive laws. This modeling technique has been widely employed to identify crack paths along the element edges by incorporating a characteristic length scale, see the discussions in [138, 84, 139, 140, 141], among many others. In contrast to the cohesive zone models, the extended finite element method has also been developed to model crack propagation, and it does not explicitly depend on the finite element discretization corresponding to the physical domain [142]. Other alternative computational techniques such as enhanced finite element method [143, 144] and generalized finite element method [145], can also be used to model crack events although possible operative difficulties to identify crack initiation and paths might arise. In order to overcome the disadvantages of the above-mentioned explicit modeling method for complex crack topologies, the phase field approach [146, 147] that is based on the Griffith's theory has been proposed to address the crack modeling of quasi-brittle materials such as silicon solar cells [148, 149]. In this approach, the sharp crack is generally diffused through the definition of so-called phase field variable and the crack propagation is characterized by the evolution of the corresponding governing equations. According to the Γ-convergence discussions in [150], the crack discontinuities are regularized by a characteristic phase field length scale. Note that the phase field formulation shares several common aspects with the gradient enhanced damage formulations, which is one of the most appealing advantages of this crack modeling method [151, 152, 153]. In view of this feature, the phase field approach accounting for thermodynamic consistency [146, 154] has been extended to the modeling of ductile fracture [155], anisotropic fracture [156], mul-

tiphysics fracture [157], and polycrystalline materials [158, 159], among many others. Given the promising aspects of phase field approach, this technique has been employed to model the crack propagation of brittle silicon solar cells in this work.

As mentioned above, to reduce the production cost of silicon solar panels, the average thickness of solar cells has decreased from 300 μm to 150 μm during the recent decades [160, 161, 162], which increases the breakage rates and crack events. Based on the computational framework developed in [131], the solid shell formulation combined with anisotropic phase field model at finite deformation is proposed to model the preferential crack propagation in thin-film solar cells. In the literature, phase field models have been coupled with shell kinematics for the fracture modeling of thin-walled structures through many different ways, see [163, 164] and references therein. Previous attempts in [165] have been made to model geometrically linear problems according to the Reissner-Midlin theory, but the developments are limited to standard finite elements. Alternative investigation adopting the Local Maximum-Entropy approximation is proposed in [166], making it difficult to be implemented into the standard finite element method. The tension-compression split method by integrating the energy contribution through the shell element thickness has been proposed in [167, 168], and later extended to the isogeometric modeling of multipatch structures [169, 170]. Recently, this approach has been adopted in [171, 172] for phase field fracture modeling of the Reissner–Mindlin shells and plates. Besides, other models have been developed in combination of phase field theory with solid shell and Kirchhoff–Love formulations to model brittle and ductile fracture [173, 174, 175, 176]. Hence, the attempt to employ the phase field solid shell formulation, extended to account for the anisotropic fracture orientation, is a proper choice for the crack modeling of solar cells in thin-walled PV laminates .

This chapter aims at presenting a global-local phase field approach with large-deformation solid shell element formulation so as to provide a very efficient modeling framework for the modeling of silicon solar cell crack propagation in the PV modules. The two main innovative as-

pects of this chapter are: (i) the coupling of phase field approach for fracture modeling with solid shell formulation considering the EAS and ANS methods for the alleviation of locking effects, and its efficient and robust quasi-Newton monolithic implementation into the commercial finite element code `ABAQUS`, which was comprehensively evaluated by comparison with the standard staggered Newton scheme through different benchmark examples, including single edge notched tension and shear, fracture of cylindrical structure under mixed bending and tension, and computationally demanding fatigue induced crack growth; (ii) a specific global-local approach in the 3D setting tailored for phase field modeling with solid shell elements is proposed here to save computational cost in fracture modeling of large-scale thin-walled structures, and its capability was demonstrated by simulating the local crack growth of cylindrical structure under both static and fatigue cyclic loading. Finally, to model the preferential crack patterns observed from the experimental electroluminescence images of solar cells, the fracture anisotropy is taken into account in the phase field modeling, and it is showcased through the simulation of crack growth of silicon solar cells when the PV modules are subjected to the different loading, as depicted in Section 3.4.7.

3.1 Phase field solid shell formulation

In this section, the phase field solid shell formulation is presented for the modeling of anisotropic crack propagataion in the thin-film brittle solar cells. Firstly, the basics of phase field approach are revisited in Section 3.1.1. For a more comprehensive description, the detailed derivation of this theory can be found in the significant work [146, 177, 178]. In Section 3.1.2, the solid shell kinetics at finite deformation are described in the convective curvilinear coordinate system.

3.1.1 Basics of phase field approach

In the 3D setting, let $\mathcal{B}_0 \subset \mathbb{R}^3$ and $\mathcal{B}_t \subset \mathbb{R}^3$ denote the reference configuration and current configuration of an arbitrary solid body with exist-
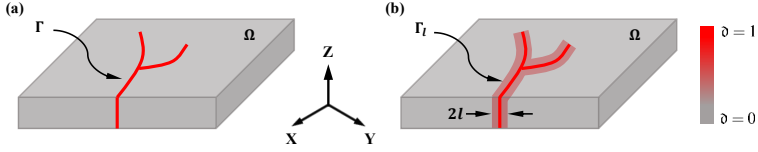
Figure 40: Schematic representation of solid body with (a) sharp crack topology, and (b) phase field approximation of diffusive crack

ing crack represented by Γ, and $\mathbf{X}$ and $\mathbf{x}$ stand for the position vectors in the corresponding configurations, respectively. Furthermore, let $\partial\mathcal{B}_0$ and $\partial\mathcal{B}_t$ be the exterior boundary of the solid body in the reference and current configuration, respectively. The motion of the material point $\mathbf{X}$ inside the body is denoted by $\varphi(\mathbf{X}, t) : \mathcal{B}_0 \times [0, t] \to \mathbb{R}^3$ that maps into the corresponding position $\mathbf{x}$ in the current configuration during the time interval $[0, t]$. The deformation gradient $\mathbf{F}^u$ is defined as $\mathbf{F}^u := \partial_{\mathbf{X}}\varphi(\mathbf{X}, t)$, where $\partial_{\mathbf{X}}$ represents the partial derivative with respect to the position $\mathbf{X}$ in the reference configuration, and its determinant $J^u = \det[\mathbf{F}^u]$ denotes the Jacobian. The phase field approach is conceived as the regularization of sharp crack topology within a diffusive crack zone characterized by the scalar-valued function $\mathfrak{d} : \mathcal{B}_0 \times [0, t] \to [0, 1]$ to model brittle fracture. The phase field variable $\mathfrak{d}$ smears out the sharp crack by a diffusive crack area of width l, as shown in Fig. 40. It is noted that the width of regularization area depends on the parameter l, which is called the phase field length scale that controls the transition between intact and damaged parts. In the modeling framework, $\mathfrak{d}$ is regarded as a smooth function of $(\mathbf{X}, t)$, and $\mathfrak{d} = 0$ and $\mathfrak{d} = 1$ denote intact and cracked states, respectively.

According to the variational theory of fracture [178], the total energy functional that governs the cracked body under external loadings takes the form of

$$\Pi(\mathbf{u}, \Gamma) = \Pi_{\text{int}}(\mathbf{u}, \mathfrak{d}, \Gamma) + \Pi_{\text{ext}}(\mathbf{u}) \tag{3.1}$$

where $\mathbf{u}$ denotes the displacement field, and Π_{int} and Π_{ext} represent the internal and external energy functionals, respectively. Note that the internal energy functional term Π_{int} is defined as the sum of elastic en-

77

ergy stored in the solid body Π_B and the energy dissipated through crack propagation Π_Γ. Based on the Griffith's theory, the internal energy functional Π_{int} is defined as

$$\Pi_{int}(\mathbf{u}, \mathfrak{d}, \Gamma) = \Pi_B(\mathbf{u}, \mathfrak{d}) + \Pi_\Gamma(\Gamma) = \int_{B \setminus \Gamma} \Psi(\mathbf{u}, \mathfrak{d}) \, d\Omega + \int_\Gamma \mathcal{G}_c \, d\Gamma \quad (3.2)$$

where Ψ denotes the specific elastic energy, and $\mathcal{G}_c$ is the critical energy release rate. The dissipated fracture energy during the crack propagation is evaluated through the Griffith theory. It should be pointed out that the competition between the elastic energy in the solid body and fracture energy is directly defined in the context of minimization problem. The evaluation of this competition is computationally challenging when the space discretization methods are used to track the crack propagation. To circumvent the use of tracking algorithms, the phase field approach that smears the crack over the whole domain of the body is employed in the same line with gradient damage formulations [150, 178, 179].

In the context of this approach, the dissipated surface energy can be approximated by a volume integral

$$\int_\Gamma \mathcal{G}_c \, d\Gamma \approx \int_{B_0} \mathcal{G}_c \gamma(\mathfrak{d}, \nabla_{\mathbf{X}} \mathfrak{d}) \, d\Omega \quad (3.3)$$

where $\gamma(\mathfrak{d}, \nabla_{\mathbf{X}} \mathfrak{d})$ is the crack surface density per unit volume, and $\nabla_{\mathbf{X}} \mathfrak{d}$ is the gradient of phase field variable. In this way, the sharp crack is regularized over the body inducing the diffusive representation, as shown in Fig. . The crack surface density $\gamma(\mathfrak{d}, \nabla_{\mathbf{X}} \mathfrak{d})$ is defined according to the modified Ambrosio-Tortorelli functional [180]

$$\gamma(\mathfrak{d}, \nabla_{\mathbf{X}} \mathfrak{d}, \boldsymbol{\omega}) = \frac{1}{2l} \mathfrak{d}^2 + \frac{l}{2} \boldsymbol{\omega} : (\nabla_{\mathbf{X}} \mathfrak{d} \otimes \nabla_{\mathbf{X}} \mathfrak{d}) \quad (3.4)$$

where $\boldsymbol{\omega}$ is the second order structural tensor characterising the material anisotropy. In order to make the energy release rate orientation-dependent [158, 181], the structural tensor can be defined as

$$\boldsymbol{\omega} = \mathbb{I}_2 + \alpha_p (\mathbb{I}_2 - \mathbf{N}_p \otimes \mathbf{N}_p) \quad (3.5)$$

where $\mathbb{I}_2$ is the second-order identity tensor, $\mathbf{N}_p$ represents the unit vector normal to the preferential cleavage plane, and α_p is the penalty parameter that is used to prevent damage to develop on planes not normal

to $\mathbf{N}_p$. According to the previous study [182], this parameter should be greater than 1.0, and in case of isotropic material, the value is equal to 0.0.

The specific elastic energy Ψ is influenced by the phase field variable $\mathfrak{d}$, which is motivated by the fact that this energy in the damage transition zone has to decrease so as to ensure the thermodynamic equilibrium. Furthermore, to avoid the asymmetric damage behaviour, the elastic energy density can be split into the active contribution Ψ_+ and the passive contribution Ψ_- [177]. During the reversal loading process, the crack closing precludes the damage evolution, and also provokes the stiffness discovery [183]. Based on the aforementioned viewpoints, the elastic energy Ψ can be defined as

$$\Psi = \mathfrak{g}(\mathfrak{d})\Psi_+ + \Psi_- \tag{3.6}$$

where $\mathfrak{g}(\mathfrak{d}) = (1-\mathfrak{d})^2 + \mathcal{K}$ denotes the monotonic degradation function, $\mathcal{K} \approx 0$ is a positive parameter to ensure numerical stability in case of fully material degradation.

3.1.2 Solid shell kinematics

In the concept of solid shell theory, the position vectors $\mathbf{X}$ and $\mathbf{x}$ in the reference and current configurations, and the phase field variable $\mathfrak{d}$ at any material point can be approximated by the corresponding vectors on the bottom and top surfaces of solid-like shell element, and can be defined as

$$\mathbf{X}\left(\xi^1, \xi^2, \xi^3\right) = \frac{1}{2}\left(1+\xi^3\right)\mathbf{X}_t\left(\xi^1, \xi^2\right) + \frac{1}{2}\left(1-\xi^3\right)\mathbf{X}_b\left(\xi^1, \xi^2\right) \tag{3.7a}$$

$$\mathbf{x}\left(\xi^1, \xi^2, \xi^3\right) = \frac{1}{2}\left(1+\xi^3\right)\mathbf{x}_t\left(\xi^1, \xi^2\right) + \frac{1}{2}\left(1-\xi^3\right)\mathbf{x}_b\left(\xi^1, \xi^2\right) \tag{3.7b}$$

$$\mathfrak{d}\left(\xi^1, \xi^2, \xi^3\right) = \frac{1}{2}\left(1+\xi^3\right)\mathfrak{d}_t\left(\xi^1, \xi^2\right) + \frac{1}{2}\left(1-\xi^3\right)\mathfrak{d}_b\left(\xi^1, \xi^2\right) \tag{3.7c}$$

where the parametric space is identified as: $\mathcal{A} := \{\xi = \left(\xi^1, \xi^2, \xi^3\right) \in \mathbb{R}^3 \mid -1 \leq \xi^i \leq +1; i = 1, 2, 3\}$, the subscript b and t represent bottom and
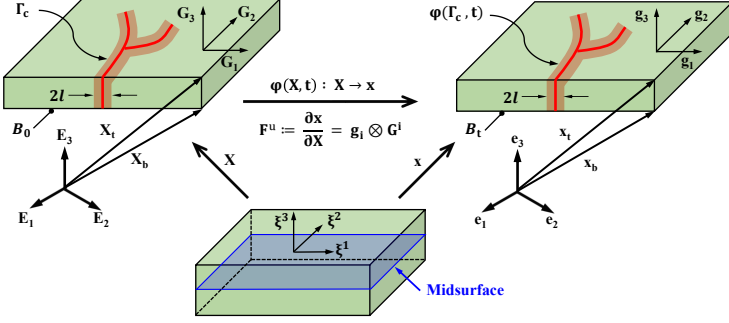
Figure 41: Definition of the cracking shell body in both the reference and current configurations with the solid shell concept and phase field approach for fracture modeling

top surfaces, respectively, and (ξ^1, ξ^2, ξ^3) represent the coordinates in the parametric space, see Fig. 41.

The kinematics of solid shell element can be described by the use of the convective curvilinear system so that the ANS interpolation for the transverse normal and shear strain components can be implemented. The covariant tangent vectors $\mathbf{G}_i(\boldsymbol{\xi})$ and $\mathbf{g}_i(\boldsymbol{\xi})$ in the reference and current configuration are defined as the partial derivatives of corresponding position vectors $\mathbf{X}$ and $\mathbf{x}$ with respect to the convective coordinates ξ^i

$$\mathbf{G}_i(\boldsymbol{\xi}) := \frac{\partial \mathbf{X}(\boldsymbol{\xi})}{\partial \xi^i}, \quad \mathbf{g}_i(\boldsymbol{\xi}) := \frac{\partial \mathbf{x}(\boldsymbol{\xi})}{\partial \xi^i}, \quad i = 1, 2, 3 \tag{3.8}$$

The contravariant basis vectors can be determined in a standard manner by $\mathbf{G}_i \cdot \mathbf{G}^j = \delta_i^j$ and $\mathbf{g}_i \cdot \mathbf{g}^j = \delta_i^j$, and metric tensors are defined as $\mathbf{G} = G_{ij}\mathbf{G}^i \otimes \mathbf{G}^j = G^{ij}\mathbf{G}_i \otimes \mathbf{G}_j$, $\mathbf{g} = g_{ij}\mathbf{g}^i \otimes \mathbf{g}^j = g^{ij}\mathbf{g}_i \otimes \mathbf{g}_j$.

In curvilinear setting, the deformation gradient $\mathbf{F}^u$ is given by

$$\mathbf{F}^u = \frac{\partial \mathbf{x}}{\partial \mathbf{X}} = \mathbf{g}_i \otimes \mathbf{G}^i \tag{3.9}$$

where the Einstein summation convention on repeated indices is adopted here. Through the definition of metric tensor components $G_{ij} = \mathbf{G}_i \cdot \mathbf{G}_j$ and $g_{ij} = \mathbf{g}_i \cdot \mathbf{g}_j$ in the reference and current configuration, the displace-

ment derived Green-Lagrange strain tensor is defined as

$$\mathbf{E}^u := \frac{1}{2}\left[(\mathbf{F}^u)^{\mathrm{T}}\mathbf{F}^u - \mathbb{I}_2\right] = \frac{1}{2}\left[g_{ij} - G_{ij}\right]\mathbf{G}^i \otimes \mathbf{G}^j \qquad (3.10)$$

The energetically conjugated second Piola-Kirchhoff stress tensor is defined as

$$\mathbf{S} = S^{ij}\mathbf{G}_i \otimes \mathbf{G}_j \qquad (3.11)$$

where S^{ij} represents the contravariant component.

3.2 Numerical implementation

In this section, the numerical strategy rooted in the use of finite element method for the spatial approximation is described briefly. Since this work is restricted to quasi-static analysis, no temporal integration scheme is required, which leads to an equilibrium problem at each pseudo-time step. Firstly, the variational formulation and finite element interpolations are derived in Section 3.2.1. Secondly, the solution schemes proposed for the phase field solid shell formulation are depicted in Section 3.2.2.

3.2.1 Finite element interpolation

The mixed Hu-Washizu variational principle is adopted for the derivation of phase field solid shell formulation incorporating the Enhanced Assumed Strain (EAS) and Assumed Natural Strain (ANS) methods to alleviate the locking pathologies. It should be pointed out that the EAS method is employed to remedy volumetric and Poisson thickness locking, while the membrane and in-plane locking effects are tackled by the ANS method [110, 113]. Given the enhancement based on the EAS method at finite deformation, the Green-Lagrange strain consists of two parts following the approach proposed in [106], including the displacement derived compatible strain $\mathbf{E}^u$ and incompatible strain $\tilde{\mathbf{E}}$, and its complete form reads: $\mathbf{E} = \mathbf{E}^u + \tilde{\mathbf{E}}$.

The multi-field variational functional of the solid body takes the form of

$$\Pi(\mathbf{S}, \tilde{\mathbf{E}}, \mathbf{u}, \mathfrak{d}) = \int_{\mathcal{B}_0} \frac{\mathcal{G}_c l}{2} \left[\frac{\mathfrak{d}^2}{l^2} + \boldsymbol{\omega} : (\nabla_{\mathbf{X}} \mathfrak{d} \otimes \nabla_{\mathbf{X}} \delta \mathfrak{d}) \right] d\Omega$$
$$+ \int_{\mathcal{B}_0} \Psi \left(\mathbf{E}^u, \tilde{\mathbf{E}}, \mathfrak{d} \right) d\Omega - \Pi_{\text{ext}}$$

(3.12)

where Π_{ext} identifies the external energy functional. Note that the displacement $\mathbf{u}$, the phase field variable $\mathfrak{d}$, and the imcompatible strain $\tilde{\mathbf{E}}$ are the independent variables. Given the orthogonality condition between the stress and strain fields, the stress field is ignored in line with the previous work [124]. The first variation of Eq. (3.12) with respect to the independent fields is given by

$$\mathcal{R}^u(\mathbf{u}, \delta\mathbf{u}, \tilde{\mathbf{E}}, \mathfrak{d}) = \int_{\mathcal{B}_0} \frac{\partial \Psi}{\partial \mathbf{E}} : \frac{\partial \mathbf{E}^u}{\partial \mathbf{u}} \delta\mathbf{u} \, d\Omega$$
$$- \delta\Pi_{\text{ext}}(\mathbf{u}) = 0, \ \ \forall \delta\mathbf{u} \in \mathfrak{V}^u$$

(3.13a)

$$\mathcal{R}^{\tilde{E}}(\mathbf{u}, \tilde{\mathbf{E}}, \delta\tilde{\mathbf{E}}, \mathfrak{d}) = \int_{\mathcal{B}_0} \frac{\partial \Psi}{\partial \mathbf{E}} : \delta\tilde{\mathbf{E}} \, d\Omega = 0, \ \ \forall \delta\tilde{\mathbf{E}} \in \mathfrak{V}^{\tilde{E}}$$

(3.13b)

$$\mathcal{R}^{\mathfrak{d}}(\mathbf{u}, \tilde{\mathbf{E}}, \mathfrak{d}, \delta\mathfrak{d}) = \int_{\mathcal{B}_0} \mathcal{G}_c l \left[\frac{1}{l^2} \mathfrak{d}\delta\mathfrak{d} + \boldsymbol{\omega} : (\nabla_{\mathbf{X}} \mathfrak{d} \otimes \nabla_{\mathbf{X}} \delta\mathfrak{d}) \right] d\Omega$$
$$+ \int_{\mathcal{B}_0} -2(1 - \mathfrak{d})\delta\mathfrak{d}\Psi_+ d\Omega = 0, \ \ \forall \delta\mathfrak{d} \in \mathfrak{V}^{\mathfrak{d}}$$

(3.13c)

where $\mathfrak{V}^u$, $\mathfrak{V}^{\tilde{E}}$ and $\mathfrak{V}^{\mathfrak{d}}$ are the admissible spaces of independent variables.

By means of isoparametric concept, the approximations of position vectors $\mathbf{X}$ and $\mathbf{x}$, displacement vector $\mathbf{u}$ and its variation $\delta\mathbf{u}$ on the solid shell element level are given by

$$\mathbf{X} = \mathbf{N}\tilde{\mathbf{X}}$$

(3.14a)

$$\mathbf{x} = \mathbf{N}\tilde{\mathbf{x}}$$

(3.14b)

$$\mathbf{u} = \mathbf{N}\mathbf{d}, \ \ \delta\mathbf{u} = \mathbf{N}\delta\mathbf{d}$$

(3.14c)

where $\tilde{\mathbf{X}}$ and $\tilde{\mathbf{x}}$ denote the nodal position vectors in the reference and current configurations, respectively, and $\mathbf{d}$ represents the nodal displacement vector. The shape function matrix $\mathbf{N}$ is defined as

$$\mathbf{N} = [\mathbf{N}_1, \ \mathbf{N}_2, \ \mathbf{N}_3, \ \mathbf{N}_4, \ \mathbf{N}_5, \ \mathbf{N}_6, \ \mathbf{N}_7, \ \mathbf{N}_8] \tag{3.15}$$

where $\mathbf{N}_I = \mathrm{diag}\,[\mathrm{N}_I, \mathrm{N}_I, \mathrm{N}_I]$ with $I = 1, 2, ..., 8$, and its component N_I is given by

$$\mathrm{N}_I = \frac{1}{8}\left(1 + \xi_I^1\xi^1\right)\left(1 + \xi_I^2\xi^2\right)\left(1 + \xi_I^3\xi^3\right) \tag{3.16}$$

with $\xi_I^1, \xi_I^2, \xi_I^3 = \pm 1$.

In a similar manner, the phase field variable $\mathfrak{d}$ and its variation $\delta\mathfrak{d}$ are interpolated as

$$\mathfrak{d} = \mathbf{N}^{\mathfrak{d}}\bar{\mathfrak{d}}, \ \ \delta\mathfrak{d} = \mathbf{N}^{\mathfrak{d}}\delta\bar{\mathfrak{d}} \tag{3.17}$$

where $\bar{\mathfrak{d}}$ represents the nodal phase field vector, and the shape function matrix $\mathbf{N}^{\mathfrak{d}}$ for interpolation of phase field is given by

$$\mathbf{N}^{\mathfrak{d}} = [\mathrm{N}_1, \ \mathrm{N}_2, \ \mathrm{N}_3, \ \mathrm{N}_4, \ \mathrm{N}_5, \ \mathrm{N}_6, \ \mathrm{N}_7, \ \mathrm{N}_8] \tag{3.18}$$

The material gradient of phase field $\nabla_{\mathbf{X}}\mathfrak{d}$ and its variation $\nabla_{\mathbf{X}}\delta\mathfrak{d}$ are interpolated as

$$\nabla_{\mathbf{X}}\mathfrak{d} = \mathbf{G}^{-\mathrm{T}}\nabla_{\xi}\bar{\mathfrak{d}} = \mathbf{B}^{\mathfrak{d}}(\boldsymbol{\xi})\bar{\mathfrak{d}}, \ \ \nabla_{\mathbf{X}}\delta\mathfrak{d} = \mathbf{G}^{-\mathrm{T}}\nabla_{\xi}\delta\bar{\mathfrak{d}} = \mathbf{B}^{\mathfrak{d}}(\boldsymbol{\xi})\delta\bar{\mathfrak{d}} \tag{3.19}$$

where ∇_{ξ} represents the gradient with respect to the natural coordinates in the curvilinear setting, and $\mathbf{B}^{\mathfrak{d}}$ is the gradient interpolation matrix of phase field variable.

The Green-Lagrange strain vector in this work is given by $\mathbf{E} = [\mathrm{E}_{11}, 2\mathrm{E}_{12}, 2\mathrm{E}_{13}, \mathrm{E}_{22}, 2\mathrm{E}_{23}, \mathrm{E}_{33}]^{\mathrm{T}}$. To overcome the deficiency of curvature thickness locking, the ANS interpolation proposed in [112] to modify transverse normal strain components E_{33} is adopted. This ANS method considers four collocation points defined in convective coordinates ξ_{C_i} as $\xi_{C_1} = (-1, -1, 0)$, $\xi_{C_2} = (1, -1, 0)$, $\xi_{C_3} = (1, 1, 0)$, and $\xi_{C_4} = (-1, 1, 0)$. Besides, to prevent transverse shear locking in case of distorted element geometry, the ANS interpolation method proposed in [113] is also employed in this work. The four collocation points for the treatment of

transverse shear strain components are $\xi_{A_1} = (0, -1, 0)$, $\xi_{A_2} = (0, 1, 0)$, $\xi_{B_1} = (-1, 0, 0)$, and $\xi_{B_2} = (1, 0, 0)$. With respect to the ANS interpolations, the approximation of strain vector is expressed as

$$
\mathbf{E}^u = \begin{bmatrix} \frac{1}{2} \left(g_{11} - G_{11} \right) \\ \left(g_{12} - G_{12} \right) \\ \left(1 - \xi^2 \right) \left(g_{13}^{A_1} - G_{13}^{A_1} \right) + \left(1 + \xi^2 \right) \left(g_{13}^{A_2} - G_{13}^{A_2} \right) \\ \frac{1}{2} \left(g_{22} - G_{22} \right) \\ \left(1 - \xi^1 \right) \left(g_{23}^{B_1} - G_{23}^{B_1} \right) + \left(1 + \xi^1 \right) \left(g_{23}^{B_2} - G_{23}^{B_2} \right) \\ \sum_{i=1}^{4} \frac{1}{4} \left(1 + \xi_i^1 \xi^1 \right) \left(1 + \xi_i^2 \xi^2 \right) \frac{1}{2} \left(g_{33}^{C_i} - G_{33}^{C_i} \right) \end{bmatrix} \tag{3.20}
$$

where the superscripts A_1, A_2, B_1, B_2, and C_i with $i = 1, 2, 3, 4$ denote the values at the corresponding collocation points.

The approximation of virtual strain is given by

$$
\delta \mathbf{E}^u = \mathbf{B} \delta \mathbf{d} \quad \text{with} \quad \mathbf{B} = [\mathbf{B}_1, \mathbf{B}_2, \mathbf{B}_3, \mathbf{B}_4, \mathbf{B}_5, \mathbf{B}_6, \mathbf{B}_7, \mathbf{B}_8] \tag{3.21}
$$

where $\mathbf{B}_I$ is the matrix for each node I considering ANS interpolation. According to the previous work [102, 92], the interpolations of incompatible strain vector $\tilde{\mathbf{E}}$ and its variation $\delta\tilde{\mathbf{E}}$ are given by

$$
\tilde{\mathbf{E}} \approx \mathbf{M}(\xi)\boldsymbol{\zeta}, \quad \delta\tilde{\mathbf{E}} \approx \mathbf{M}(\xi)\delta\boldsymbol{\zeta} \tag{3.22}
$$

where $\mathbf{M}(\xi)$ is the interpolation matrix of the enhancing modes $\boldsymbol{\zeta}$, and is defined as

$$
\mathbf{M}(\xi) = \left[\frac{\det \mathbf{J}_0}{\det \mathbf{J}} \right] \mathbf{T}_0^{-T} \tilde{\mathbf{M}}(\xi) \tag{3.23}
$$

where $\mathbf{J} = [\mathbf{G}_1, \mathbf{G}_2, \mathbf{G}_3]^T$, $\mathbf{J}_0$ is its evaluation at the element center, $\mathbf{T}_0$ is the tranformation matrix, and $\tilde{\mathbf{M}}(\xi)$ is the interpolation matrix in the parametric space [131].

Inserting the aforementioned interpolations into Eqs. (3.13), the discretes residual equations are given by

$$
\mathbf{R}^d(\mathbf{d}, \delta\mathbf{d}, \bar{\mathfrak{d}}, \boldsymbol{\zeta}) = \int_{\mathcal{B}_0} \mathfrak{g}(\mathfrak{d})\mathbf{B}(\mathbf{d})^T \mathbf{S} \, d\Omega - \mathbf{R}_{\text{ext}}^d \tag{3.24a}
$$

$$
\mathbf{R}^\zeta(\mathbf{d}, \bar{\mathfrak{d}}, \boldsymbol{\zeta}, \delta\boldsymbol{\zeta}) = \int_{\mathcal{B}_0} \mathfrak{g}(\mathfrak{d})\mathbf{M}(\xi)^T \mathbf{S} \, d\Omega \tag{3.24b}
$$

$$\mathbf{R}^{\eth}(\mathbf{d}, \bar{\eth}, \delta\bar{\eth}, \boldsymbol{\zeta}) = \int_{\mathcal{B}_0} -2(1-\eth)\mathbf{N}(\boldsymbol{\xi})^{\mathrm{T}}\Psi_+ \mathrm{d}\Omega$$
$$+ \int_{\mathcal{B}_0} \mathcal{G}_c l \left[(\mathbf{B}^{\eth})^{\mathrm{T}} \mathbf{W} \nabla_{\mathbf{X}}\eth + \frac{1}{l^2}\mathbf{N}(\boldsymbol{\xi})^{\mathrm{T}}\eth \right] \mathrm{d}\Omega \tag{3.24c}$$

To avoid the irreversible growth of the fracture process, a history variable H is introduced to modify the residual vector $\mathbf{R}^{\eth}$ [184], which is transformed into

$$\mathbf{R}^{\eth} = \int_{\mathcal{B}_0} -2(1-\eth)\mathbf{N}(\boldsymbol{\xi})^{\mathrm{T}}H\mathrm{d}\Omega$$
$$+ \int_{\mathcal{B}_0} \mathcal{G}_c l \left[(\mathbf{B}^{\eth})^{\mathrm{T}} \mathbf{W} \nabla_{\mathbf{X}}\eth + \frac{1}{l^2}\mathbf{N}(\boldsymbol{\xi})^{\mathrm{T}}\eth \right] \mathrm{d}\Omega \tag{3.25}$$

In view of the irrevisibility [177], the history variable H must obey the following Kuhn-Tucker conditions

$$\Psi_+ - H \leqslant 0, \quad \dot{H} \geqslant 0, \quad \dot{H}(\Psi_+ - H) = 0 \tag{3.26}$$

At the certain time point t, the history variable H can be expressed as

$$H = \max_{\tau \in [0,t]} \Psi_+(\tau) \tag{3.27}$$

To solve the multi-field problem, an iterative scheme is adopted, and the consistent linearization of Eqs. (3.24) obtained from the concept of Gateaux directional derivative can be derived as

$$\begin{bmatrix} \mathbf{k}_{dd} & \mathbf{k}_{d\zeta} & \mathbf{0} \\ \mathbf{k}_{\zeta d} & \mathbf{k}_{\zeta\zeta} & \mathbf{0} \\ \mathbf{0} & \mathbf{0} & \mathbf{k}_{\eth\eth} \end{bmatrix} \begin{bmatrix} \Delta\mathbf{d} \\ \Delta\boldsymbol{\zeta} \\ \Delta\bar{\eth} \end{bmatrix} = \begin{bmatrix} \mathbf{R}^d_{\mathrm{ext}} \\ \mathbf{0} \\ \mathbf{0} \end{bmatrix} - \begin{bmatrix} \mathbf{R}^d \\ \mathbf{R}^{\zeta} \\ \mathbf{R}^{\eth} \end{bmatrix} \tag{3.28}$$

The different components of the stiffness matrix are defined as

$$\mathbf{k}_{dd} = \int_{\mathcal{B}_0} \left[(1-\eth)^2 + \mathcal{K} \right] \left[\mathbf{Q} + \mathbf{B}(\mathbf{d})^{\mathrm{T}}\mathbb{C}\mathbf{B}(\mathbf{d}) \right] \mathrm{d}\Omega \tag{3.29a}$$

$$\mathbf{k}_{d\zeta} = \int_{\mathcal{B}_0} \left[(1-\eth)^2 + \mathcal{K} \right] \mathbf{B}(\mathbf{d})^{\mathrm{T}}\mathbb{C}\mathbf{M}(\boldsymbol{\xi})\mathrm{d}\Omega \tag{3.29b}$$

$$\mathbf{k}_{\zeta d} = \int_{\mathcal{B}_0} \left[(1-\eth)^2 + \mathcal{K} \right] \mathbf{M}(\boldsymbol{\xi})^{\mathrm{T}}\mathbb{C}\mathbf{B}(\mathbf{d})\mathrm{d}\Omega \tag{3.29c}$$

$$\mathbf{k}_{\zeta\zeta} = \int_{\mathcal{B}_0} \left[(1-\mathfrak{d})^2 + \mathcal{K}\right] \mathbf{M}(\boldsymbol{\xi})^{\mathrm{T}} \mathbb{C} \mathbf{M}(\boldsymbol{\xi}) \mathrm{d}\Omega \tag{3.29d}$$

$$\begin{aligned}
\mathbf{k}_{\mathfrak{d}\mathfrak{d}} &= \int_{\mathcal{B}_0} \left[\frac{\mathcal{G}_c}{l} + 2H\right] \mathbf{N}(\boldsymbol{\xi})^{\mathrm{T}} \mathbf{N}(\boldsymbol{\xi}) \mathrm{d}\Omega \\
&\quad + \int_{\mathcal{B}_0} \mathcal{G}_c l \left(\mathbf{B}^{\mathfrak{d}}(\boldsymbol{\xi})\right)^{\mathrm{T}} \mathbf{W} \mathbf{B}^{\mathfrak{d}}(\boldsymbol{\xi}) \mathrm{d}\Omega
\end{aligned} \tag{3.29e}$$

The derivative of $\mathbf{B}$ with respect to $\mathbf{d}$ in Eq. (3.29a) appears in order to compute $\Delta\delta\mathbf{E}^u : \mathbf{S}$, where $\Delta\delta\mathbf{E}^u$ is the linearized virtual strain tensor, and the matrix form is given by

$$\mathbf{Q} = \frac{\partial\mathbf{B}(\mathbf{d})^{\mathrm{T}}}{\partial\mathbf{d}}\mathbf{S} = \begin{bmatrix} \mathbf{Q}_{11} & \mathbf{Q}_{12} & \cdots & \mathbf{Q}_{18} \\ \mathbf{Q}_{21} & \mathbf{Q}_{22} & \cdots & \mathbf{Q}_{28} \\ \vdots & \vdots & \ddots & \vdots \\ \mathbf{Q}_{81} & \mathbf{Q}_{82} & \cdots & \mathbf{Q}_{88} \end{bmatrix} \tag{3.30}$$

where $\mathbf{Q}_{\mathrm{IJ}}$ is defined as $\mathbf{Q}_{\mathrm{IJ}} = \mathrm{diag}\left[Q_{\mathrm{IJ}}, Q_{\mathrm{IJ}}, Q_{\mathrm{IJ}}\right]$ for the combination of node I and J.

The isotropic Kirchhoff–Saint-Venant constitutive model is considered in this study, and the tangent material stiffness tensor $\mathbf{C}$ in the convective curvilinear setting can be expressed as

$$\mathbf{C} = \left[\lambda G^{ij} G^{kl} + \mu \left(G^{ik} G^{jl} + G^{il} G^{jk}\right)\right] \mathbf{G}_i \otimes \mathbf{G}_j \otimes \mathbf{G}_k \otimes \mathbf{G}_l \tag{3.31}$$

where λ and μ are the Lame parameters. The matrix form of stiffness $\mathbb{C}$ is given by

$$\mathbb{C} = \begin{bmatrix} C^{1111} & C^{1112} & C^{1113} & C^{1122} & C^{1123} & C^{1133} \\ & C^{1212} & C^{1213} & C^{1222} & C^{1223} & C^{1233} \\ & & C^{1313} & C^{1322} & C^{1323} & C^{1333} \\ & & & C^{2222} & C^{2223} & C^{2233} \\ & \text{sym.} & & & C^{2323} & C^{2333} \\ & & & & & C^{3333} \end{bmatrix} \tag{3.32}$$

Since inter-element continuity is not required, the enhanced strain term can be condensed out in the element level [106], and the system of equations that couples the kinematics with phase field is given by

$$\begin{bmatrix} \mathbf{k}_{dd}^* & \mathbf{0} \\ \mathbf{0} & \mathbf{k}_{\mathfrak{d}\mathfrak{d}} \end{bmatrix} \begin{bmatrix} \Delta\mathbf{d} \\ \Delta\mathfrak{d} \end{bmatrix} = \begin{bmatrix} \mathbf{R}_{\mathrm{ext}}^d \\ \mathbf{0} \end{bmatrix} - \begin{bmatrix} \mathbf{R}^{d*} \\ \mathbf{R}^{\mathfrak{d}} \end{bmatrix} \tag{3.33}$$

where components of modified stiffness matrix and residual vector are defined as

$$\mathbf{k}_{dd}^* = \mathbf{k}_{dd} - \mathbf{k}_{d\zeta}\mathbf{k}_{\zeta\zeta}^{-1}\mathbf{k}_{\zeta d} \qquad (3.34a)$$

$$\mathbf{R}^{d*} = \mathbf{R}^d - \mathbf{k}_{d\zeta}\mathbf{k}_{\zeta\zeta}^{-1}\mathbf{R}^\zeta \qquad (3.34b)$$

3.2.2 Solution schemes

Given the highly nonlinearity of residual equations with respect to the kinematic variables, two schemes are widely adopted to address the coupled phase field-displacement problem, including the monolithic scheme in which the displacement and phase field variables are solved simultaneously and the AM scheme in which the independent variables are solved separately as sequentially staggered field. Monolithic scheme retains unconditional stability and consequently large time increments are allowed, but the poor performance in achieving convergence has hindered its wide application. With regard to the staggered scheme, it is very robust and can overcome the convergence issues. However, sufficiently small increments must be employed to prevent the solution deviating from the equilibrium, and thus computational cost is very high. In the following, the quasi-Newton monolithic scheme with improved performance over conventional Newton schemes in terms of both convergence and computational efficiency is introduced into the numerical implementation of phase field solid shell formulation.

Within the time increment $\left[t_n, t_{n+1}^{(k)}\right]$, where t_n and $t_{n+1}^{(k)}$ represent the previous converged increment and prospective current increment at iteration k, respectively, given the data $\{\mathbf{d}_n, \boldsymbol{\zeta}_n, \bar{\mathbf{d}}_n\}$ at the previous converged increment, the final solution at the next increment requires Newton iterations around the intermediate state $\{\mathbf{d}_{n+1}^{(k)}, \boldsymbol{\zeta}_{n+1}^{(k)}, \bar{\mathbf{d}}_{n+1}^{(k)}\}$ due to nonlinearity. Note that $\{\mathbf{d}_n, \boldsymbol{\zeta}_n, \bar{\mathbf{d}}_n\}$ and $\{\mathbf{d}_{n+1}^{(k)}, \boldsymbol{\zeta}_{n+1}^{(k)}, \bar{\mathbf{d}}_{n+1}^{(k)}\}$ denote the nodal displacement vector, incompatible enhancing vector, and nodal phase field vector at the previous converged increment and prospective current increment at iteration k, respectively. According to the static condensation procedure in Section 4.2, the nodal phase field and displacement vectors are defined as unknowns in the element level, and the in-

crement of enhancing vector at the next time increment of iteration k, which is denoted as $\Delta\boldsymbol{\zeta}_{n+1}^{(k)}$, should be determined for the computational procedure. Based on the process described in [100], the increment $\Delta\boldsymbol{\zeta}_{n+1}^{(k)}$ is given by

$$\Delta\boldsymbol{\zeta}_{n+1}^{(k)} = -\left[\mathbf{k}_{\zeta\zeta,n}\right]^{-1}\left[\mathbf{R}_{\text{int},n}^{\zeta} + \mathbf{k}_{\zeta d,n}\Delta\mathbf{d}_{n+1}^{(k)}\right] \tag{3.35}$$

It should be pointed out that the increments $\Delta\mathbf{d}_{n+1}^{(k)}$ and $\Delta\bar{\boldsymbol{\mathfrak{d}}}_{n+1}^{(k)}$ are provided by the solver, while the element matrices at the previous increment $[\mathbf{k}_{\zeta\zeta,n}]^{-1}$, $\mathbf{R}_{\text{int},n}^{\zeta}$, $\mathbf{k}_{\zeta d,n}$, and $\boldsymbol{\zeta}_n$ are all stored as internal variables.

In contrast to standard Newton methods, the stiffness in the quasi-Newton method is not updated after each iteration, and instead, it is approximated after a certain number of iterations without achieving convergence [185]. Specifically, the approximated stiffness matrix must satisfy the following equation

$$\widetilde{\mathbf{K}}\delta\mathbf{z} = \delta\mathbf{R} \tag{3.36}$$

for the residual $\delta\mathbf{z} := \mathbf{z}_{t+\Delta t} - \mathbf{z}_t$, in which the kinematic variable vector is defined as $\mathbf{z} = [\mathbf{d}, \bar{\boldsymbol{\mathfrak{d}}}]^{\mathrm{T}}$, and the correction $\delta\mathbf{R} := \mathbf{R}_{t+\Delta t} - \mathbf{R}_t$, respectively. In the quasi-Newton method, the approximated stiffness matrix $\widetilde{\mathbf{K}}$ is given by

$$\widetilde{\mathbf{K}} = \widetilde{\mathbf{K}}_t - \frac{\left(\widetilde{\mathbf{K}}_t\delta\mathbf{z}\right)\left(\widetilde{\mathbf{K}}_t\delta\mathbf{z}\right)^{\mathrm{T}}}{\delta\mathbf{z}^{\mathrm{T}}\widetilde{\mathbf{K}}_t\delta\mathbf{z}} + \frac{\delta\mathbf{R}\delta\mathbf{R}^{\mathrm{T}}}{\delta\mathbf{z}^{\mathrm{T}}\delta\mathbf{R}} \tag{3.37}$$

In addition, as pointed out in [186], the updated stiffness matrix in case of symmetry can be written in its inverse form

$$\widetilde{\mathbf{K}}^{-1} = \left(\mathbf{I} - \frac{\delta\mathbf{z}\delta\mathbf{R}^{\mathrm{T}}}{\delta\mathbf{z}^{\mathrm{T}}\delta\mathbf{R}}\right)\widetilde{\mathbf{K}}_t^{-1}\left(\mathbf{I} - \frac{\delta\mathbf{z}\delta\mathbf{R}^{\mathrm{T}}}{\delta\mathbf{z}^{\mathrm{T}}\delta\mathbf{R}}\right)^{\mathrm{T}} + \frac{\delta\mathbf{z}\delta\mathbf{z}^{\mathrm{T}}}{\delta\mathbf{z}^{\mathrm{T}}\delta\mathbf{R}} \tag{3.38}$$

Accordingly, it can be easily implemented into the finite element code, and significant computational cost can be saved. The initial guess of the stiffness $\widetilde{\mathbf{K}}^{(0)}$ is defined as

$$\widetilde{\mathbf{K}}^{(0)} = \begin{bmatrix} \mathbf{K}_{dd}^* & \mathbf{0} \\ \mathbf{0} & \mathbf{K}_{\mathfrak{d}\mathfrak{d}} \end{bmatrix} \tag{3.39}$$

Note that, though it is not fully coupled, the subsequent approximation of the stiffness matrix couples the phase field and displacement, see Eq. (3.37). The quasi-Newton stiffness will be reformed whenever the number of iterations exceed 8 without obtaining the convergent solution in this work. The computational procedure for the quasi-Newton monolithic implementation of phase field solid shell formulation is outlined in Algorithm 3.

Algorithm 3: Numerical algorithm for the QN implementation of phase field solid shell formulation

Data: $\mathbf{d}_n$, $\bar{\mathfrak{d}}_n$, $\Delta\mathbf{d}_{n+1}^{(k)}$, $\Delta\bar{\mathfrak{d}}_{n+1}^{(k)}$
Result: $\mathbf{d}_{n+1}$, $\bar{\mathfrak{d}}_{n+1}$
Initialization of $\boldsymbol{\zeta}_n$, $\mathbf{R}_{\text{int},n}^{\zeta}$, $\mathbf{k}_{\zeta d,n}$, $[\mathbf{k}_{\zeta\zeta,n}]^{-1}$;
while $||R_d^*|| > tolerance$ **do**

    Compute $\Delta\boldsymbol{\zeta}_{n+1}^{(k)} = -[\mathbf{k}_{\zeta\zeta,n}]^{-1}\left[\mathbf{R}_{\text{int},n}^{\zeta} + \mathbf{k}_{\zeta d,n}\Delta\mathbf{d}_{n+1}^{(k)}\right]$;

    Update the enhancing vector $\boldsymbol{\zeta}_{n+1}^{(k)} = \boldsymbol{\zeta}_n + \Delta\boldsymbol{\zeta}_{n+1}^{(k)}$;

    for $n \leftarrow 1$ **to** *N integration points* **do**

        Compute the curvilinear basis $\mathbf{G}_{n+1}^{(k)}$ *and* $\mathbf{g}_{n+1}^{(k)}$;

        Compute the B matrices $\mathbf{B}_{n+1}^{(k)}$ *and* $\mathbf{B}_{n+1}^{\mathfrak{d}(k)}$;

        Modify the $\mathbf{B}_{n+1}^{(k)}$ *matrix according to the ANS method*;

        Compute $\mathbb{C}_{n+1}^{(k)}$, $\mathbf{S}_{n+1}^{(k)}$, $\Psi_{n+1}^{(k)}$, *and* $H_{n+1}^{(k)}$;

        Compute the EAS operator $\mathbf{M}_{n+1}^{(k)}$;

    end

    Compute the element stiffness matrices $\mathbf{k}_{dd,n+1}^{(k)}$, $\mathbf{k}_{d\zeta,n+1}^{(k)}$, $\mathbf{k}_{\zeta d,n+1}^{(k)}$, $\mathbf{k}_{\zeta\zeta,n+1}^{(k)}$, *and* $\mathbf{k}_{\mathfrak{d}\mathfrak{d},n+1}^{(k)}$;

    Compute the internal force vectors $\mathbf{R}_{\text{int},n+1}^{d(k)}$, $\mathbf{R}_{\text{int},n+1}^{\zeta(k)}$, *and* $\mathbf{R}_{\text{int},n+1}^{\mathfrak{d}(k)}$;

    Perform the static condensation in the element level;

    Do the final assembly;

end

3.3 The global-local fracture submodeling approach

The global-local modeling approach has been widely employed in a variety of technical applications, such as J-integral calculation in fracture problems [187], three-dimensional stress analysis [188, 125] and computation of stress intensity factors [189]. Generally, a global finite ele-
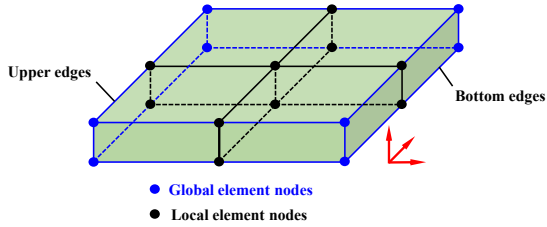
Figure 42: The sketch of solid shell elements from both global and local models

ment model with coarse mesh is used to calculate the displacement field and determine the size and location of the critical region with low computational cost. Subsequently, the displacement output obtained from the global-scale calculation will be employed to interpolate the boundary condition of the local model, which is a fine scale representation of the critical area with more detailed mechanical degradation to achieve a greater accuracy [28]. However, very limited work has been focused on the global local approach for phase field fracture modeling, see [190, 191, 192], among others.

To further reduce the computational cost in fracture modeling of large-scale thin-walled structures, a specific global-local submodeling approach in the 3D setting tailored for phase field modeling using solid shell formulation is proposed. The submodeling technique is a computational strategy frequently employed in fiber-reinforced composites for modeling with two different length scales, such as macro scale and meso scale of the laminate. The global and local model are solved sequentially in the submodeling approach, in which the global model is solved firstly, and subsequently its results are taken as boundary conditions to drive the local model. As a result, both global and local models are analysed separately, and local model has no influence on the global model. In this work, this approach is introduced for phase field fracture modeling of shell structures to improve computational efficiency when the crack in the local region has minor effect on the global stiffness. For instance, it is pointed out in [193, 28] that the stiffness of the global photovoltaic panel

is hardly degraded by the cracks in the local solar cells, and in this case, it is viable to apply the submodeling technique uncoupling the global linear elastic finite element analysis of photovoltaic module from the local fracture modeling of solar cell. To simulate the realistic loading condition driving the crack propagation of brittle silicon solar cell, it is essential to model the whole photovoltaic laminate, and on the other hand, for the prediction of cracking phenomena at the cell level, phase field approach can be employed with very refined mesh for the local model.

Algorithm 4: Numerical algorithm for displacement projection from global model to local model

---

for $t \leftarrow 1$ **to** T *time increments* **do**
   Impose boundary conditions on the global model;
   Solve the nodal displacements of global model using Newton-Rapson scheme;
   for $i \leftarrow 1$ **to** S *solid shells of the local model* **do**
      for $j \leftarrow 1$ **to** N *exterior facets of the local model* **do**
         for $k \leftarrow 1$ **to** M *edges (M=2, upper and bottom edges)* **do**
            Find the two closest nodes P_1 and P_2 belonging to the same edge and facet in
            the global model;
            Interpolate the nodal displacement $\boldsymbol{u}_k = N_1\boldsymbol{u}_1 + N_2\boldsymbol{u}_2$, where $\boldsymbol{u}_1$ and $\boldsymbol{u}_2$ are
            the nodal displacement vector of P_1 and P_2, N_1 and N_2 are linear shape
            functions.
         end
      end
   end
end

To efficiently model thin-walled global structures like photovoltaic panels, a solid-like continuum solid shell element is employed to simulate the structural response under complex loading conditions with relatively coarse mesh to save computational cost. Compared with Kirchhoff-Love shell elements and solid elements in thin-walled structure modeling [84], it is preferred since three dimensional constitutive laws are allowed and accuracy can be ensured with only one ply of element required through thickness of the global model. After obtaining the displacements of global coarse-scale model in the different directions by linear elastic finite element analysis, the boundary conditions applied to the nodes belonging to the edges of local fine-scale model can be determined by linear interpolation of global results. It is worth mentioning that the finite element discretization of the local model is not required to comply

with the one of the global finite element model, and a projection scheme can be used to map the displacement results from computation of global model onto the edge nodes of local model. In doing so, the mesh of local model can be more refined to perform the appropriate phase field fracture simulation. From the viewpoint of algorithm, since there is only one ply of solid shell element through the thickness direction, it is convenient to distinguish the nodes of exterior element facets belonging to the local model into upper and bottom edge nodes, see Fig. 42. For each node of local model on the exterior facets, the displacement boundary conditions are obtained by linear interpolation between the displacement values of two closest nodes of global model on the same upper or bottom edge. The projection scheme is illustrated in Algorithm 4.

3.4 Numerical examples

In this section, to investigate the performance of quasi-Newton monolithic solution scheme in phase field modeling using solid shell formulation, four different numerical tests, including single edge notched tension, single edge notched shear, cylindrical structure under mixed tension and bending, and fatigue induced crack propagation, are performed. The performance in attaining convergence and computational efficiency is assessed by comparison with that of the widely adopted staggered scheme through the different types of boundary value problems. Then the capability of the proposed global-local approach to further reduce the computational cost in phase field modeling is demonstrated by the numerical tests of cylindrical structure subjected to both constant and cyclic fatigue loading conditions. With regard to the application of the computational framework for crack modeling of silicon solar cells in the photovoltaic modules, the feasibility to model anisotropic fracture using the current approach is firstly shown through a demonstration problem, and then the solar cell cracking modeling in the photovoltaic module under two different loading cases are presented.
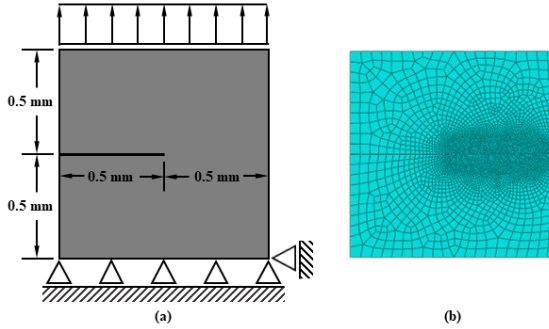
Figure 43: (a) Sketch of the single edge notched tension and (b) finite element mesh of the specimen

3.4.1 Single edge notched tension

The first numerical case is the mode I fracture of single edge notched specimen under monotonic loading, as indicated in Fig. 43(a). It is a very popular benchmark example for verification of phase field approach and challenging for the numerical algorithms used to solve the coupled governing equations [146]. Specimen dimensions and boundary conditions are shown in Fig. 43(a). The geometry is a square plate with unit lateral size of 1 mm and thickness of 0.001 mm. Note that there is an initial sharp crack with the length of 0.5 mm in the middle of the specimen. The degrees of freedom at the bottom edges of specimen are constrained, while the displacement boundary condition is imposed on the upper edges in the vertical direction, leading to a symmetric loading at the crack tip of specimen and subsequent mode I crack propagation. The Young's modulus and Poisson's ratio are equal to 210 GPa and 0.3, respectively, and regarding the fracture properties, the fracture toughness and phase field length scale are set to 2.7 N/mm and 0.024 mm, respectively. The model is discretised with solid shell elements, see Fig. 43(b), and notably, the characteristic elements along the potential crack path are refined to a size of 0.004 mm, being 6 times smaller than the length scale. The total number of elements is 7222. The contour plots of phase field values during the crack propagation are shown in Fig. 44.
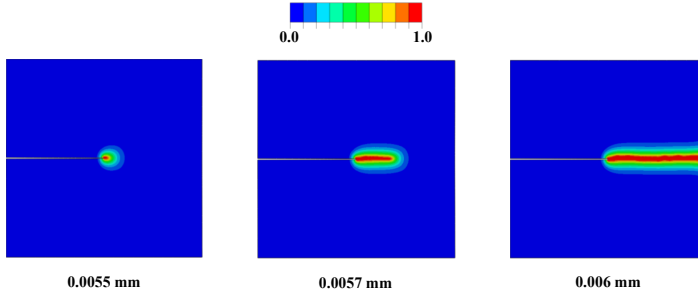
Figure 44: The contour plots of phase field values at the loading displacements equal to 0.0055 mm, 0.0057 mm, and 0.006 mm during the crack propagation in the single edge notched tension

The constrained force versus loading displacement curves are shown in Fig. 45. The numerical results obtained from the conventional staggered or AM scheme with different numbers of time increments are also presented here for comparison. It can be seen that the staggered scheme is very sensitive to the time increment size, and with the increase of the number of increments, the obtained force versus displacement curve will gradually coincide with that solved by the quasi-Newton monolithic scheme, which requires only 100 time increments. Both the quasi-Newton monolithic scheme and staggered scheme require a lot of iterations at the critical time increment when the crack starts to propagate. The total number of iterations versus loading displacement curves for the staggered schemes with different increment size and quasi-Newton monolithic scheme are shown in Fig. 46. Results indicate that reproducing the numerical result obtained by the quasi-Newton monolithic scheme through the staggered scheme requires at least around ten thousand iterations. It is also shown that the number of iterations by the staggered scheme with one thousand time increments is almost the same as that required by the quasi-Newton monolithic scheme, but its deviation from the convergent solution reaches around 20%. Note that the quasi-Newton monolithic scheme is roughly 15 times more efficient than the staggered scheme for the phase field modeling of this single edge

94

Figure 45: The force vs. displacement curves obtained from both the quasi-Newton monolithic and staggered schemes for the phase field modeling of single edge notched tension using solid shell formulation

notched tension using enhanced assumed strain shell formulation. The significant differences in computational cost are mainly due to the greatly reduced number of iterations in the quasi-Newton monolithic solution.

3.4.2 Single edge notched shear

In this section, the performance of the proposed quasi-Newton monolithic scheme in phase field modeling using solid shell element formulation is assessed in the context of mode II fracture of single edge notched specimen. The same material properties and specimen dimensions as the previous single edge notched tension are adopted but the shear loading is applied to the upper edges of specimen, see Fig. 47(a). The shear-dominated crack conditions lead to crack propagation towards the right bottom part of the specimen, which is discretized with uniform solid shell elements. The contour plots of phase field values during the crack propagation in the single edge notched shear test are shown in Fig. 48,

Figure 46: The total number of iterations vs. loading displacement curves obtained from both the quasi-Newton monolithic and staggered schemes for the phase field modeling of single edge notched tension using solid shell formulation
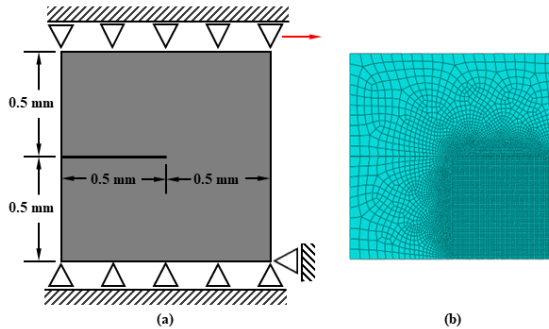
Figure 47: (a) Sketch of the single edge notched shear and (b) finite element mesh of the specimen
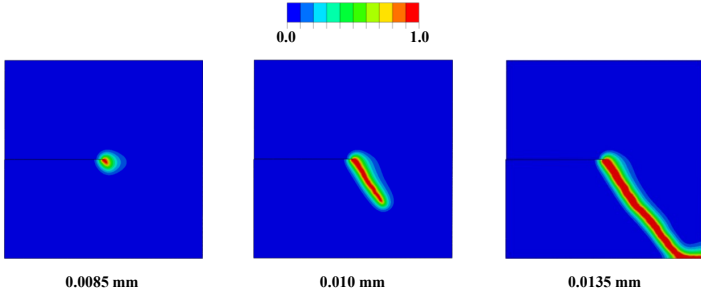
Figure 48: The contour plots of phase field values at the loading displacements 0.0085 mm, 0.010 mm, and 0.0135 mm during the crack propagation in the single edge notched shear

and it can be seen that the predicted crack trajectory agrees with results in the literature, see [146].

The constrained force versus displacement curves obtained from both the quasi-Newton and staggered schemes with different increment sizes are shown in Fig. 49. It can also be seen that reproducing the quasi-Newton monolithic result with staggered scheme requires the use of 10^4 number of increments. When using the less number of total increments, such as 10^3 or 2×10^3, the resultant curve deviates from the predicted quasi-Newton one, see Fig. 49. The total number of iterations versus displacement curves obtained from both the quasi-Newton monolithic and staggered schemes for the phase field modeling of single edge notched shear test using solid shell element formulation are shown in Fig. 50. Difference of total number of iterations between the two solution schemes is smaller compared with the previous single edge notched tension, but remains significant in this case. To obtain the same result as the quasi-Newton monolithic solution, the required total number of time increments for the staggered scheme is still one order larger than the former scheme. It can be concluded that the quasi-Newton monolithic scheme in the single edge notched shear is also much more efficient as its computational cost is around ten times smaller than that required in the staggered solution with 10^4 number of increments.
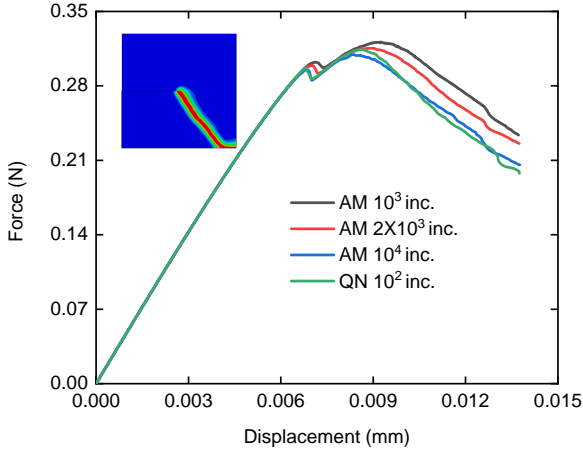
Figure 49: The force vs. displacement curves obtained from both the quasi-Newton monolithic and staggered schemes for the phase field modeling of single edge notched shear using solid shell formulation

3.4.3 Cylindrical structure under mixed tension and bending

The performance of the quasi-Newton monolithic scheme for phase field modeling using enhanced assumed strain shell formulation is further assessed in capturing fracture events of thin-walled structure with curved geometry under mixed tension and bending. In this section, we consider a quarter of cylindrical structure with an initial crack notch in the middle of the specimen, see Fig. 51(a). The dimensions of the specimen are as follows: the length is equal to 240 mm, the internal radius is 100 mm, the external radius is 100.1 mm, the width of the initial notch is 3 mm and its length is 6 mm. To comply with the symmetric boundary conditions, the translational degrees of freedom at the X=0 side of the specimen is constrained in the X direction, and the Y=0 side is constrained in the translational vertical direction Y. Besides, the translational degree of freedom in the Z direction at the back of the specimen is constrained,
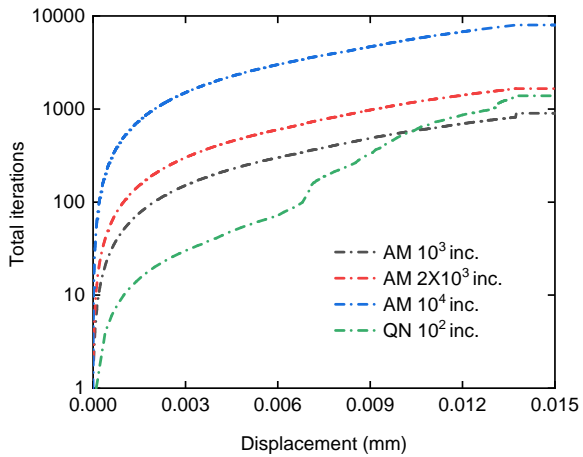
Figure 50: The total number of iterations vs. loading displacement curves obtained from both the quasi-Newton monolithic and staggered schemes for the phase field modeling of single edge notched shear using solid shell formulation
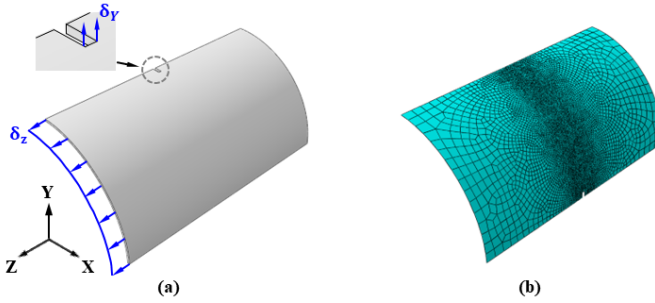
Figure 51: (a) Sketch of the cylindrical structure under mixed tension and bending and (b) finite element mesh of the specimen

while the displacement condition δ_Z is applied to the front edges and the displacement condition δ_Y is applied to the notch edges, as shown in Fig. 51(a). The same material properties as in the previous cases are used here. Regarding the fracture properties, the phase field length scale is set to 4 mm and fracture toughness is 2.7 N/mm. The specimen is discretized using 8474 solid shell elements with refinement in the potential crack propagation region, see Fig. 51(b). The contour plots of phase field and displacement during the crack propagation are shown in Fig. 52, which agrees well with the fracture pattern predicted by an alternate formulation proposed in [174].

The force versus displacement curves obtained from both the quasi-Newton monolithic and staggered schemes with different increment sizes are shown in Fig. 53. As with the previous single edge notched tension and shear cases, reproducing the exact numerical result from the quasi-Newton monolithic solution requires a large number of time increments for the staggered scheme. For the phase field fracture modeling of cylindrical structure under mixed tension and bending, the resultant curve obtained from the staggered scheme with 10^4 time increments agrees perfectly well with that solved by quasi-Newton monolithic scheme that requires only 100 time increments. The total number of iterations versus loading displacement curves obtained from both the quasi-Newton monolithic and staggered schemes are shown in Fig. 54.
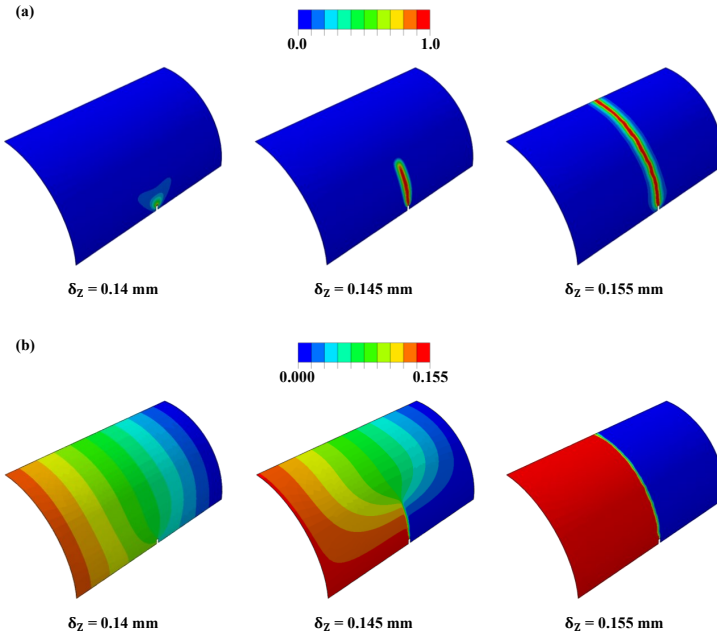
Figure 52: The contour plots of (a) phase field and (b) axial displacement at the loading displacements δ_Z equal to 0.14 mm, 0.145 mm, and 0.155 mm during the crack propagation in the fracture modeling of cylindrical structure under mixed tension and bending
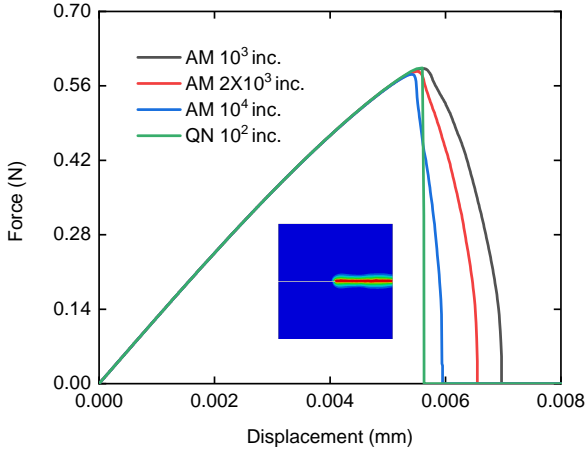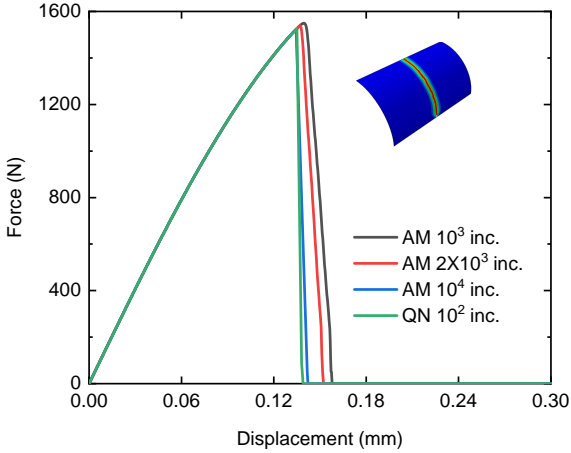
Figure 53: The force vs. displacement curves obtained from both the quasi-Newton monolithic and staggered schemes for the phase field modeling of cylindrical structure under mixed tension and bending using solid shell formulation

The same conclusion as the previous two cases can be drawn that the total number of iterations to obtain the same numerical result for the staggered scheme is 100 times larger than that required by the quasi-Newton monolithic scheme. It takes approximately 12 times longer using the staggered scheme with 10^4 time increments than that solved by the quasi-Newton monolithic scheme. It should be pointed out that the quasi-Newton scheme is very robust and efficient for the phase field modeling with solid shell formulation considering both EAS and ANS compared with the conventional Newton solution schemes.

3.4.4 Phase field fatigue modeling using solid shell formulation

In this section, the quasi-Newton monolithic scheme for phase field modeling with solid shell formulation is employed to address fatigue prob-
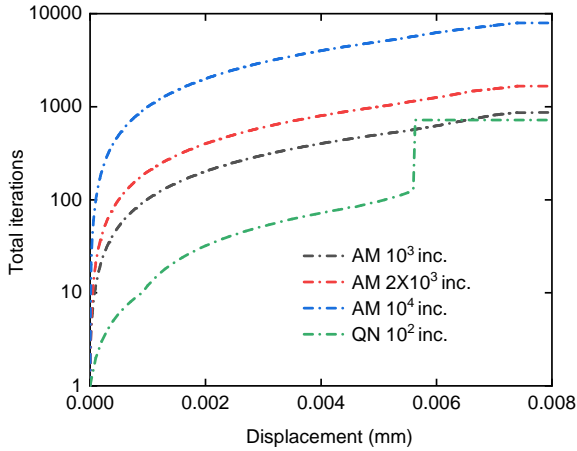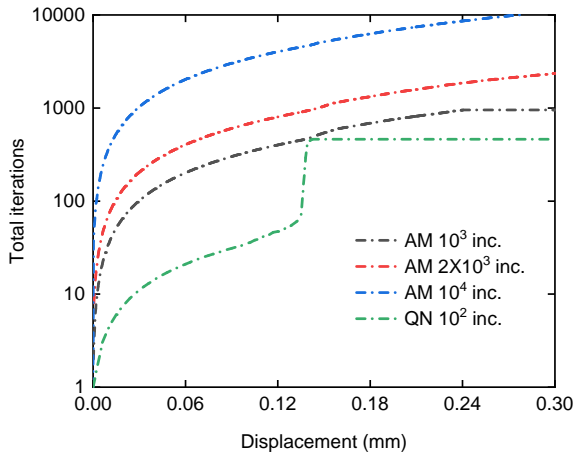
Figure 54: The total number of iterations vs. displacement curves obtained from both the quasi-Newton monolithic and staggered schemes for the phase field modeling of cylindrical structure under mixed tension and bending using solid shell formulation

lems. The framework presented in [194] has been adopted and implemented into the phase field solid shell formulation. Firstly, a history variable $\bar{\alpha}$ that governs the accumulation of fatigue is defined and the crack propagation is driven by a fatigue function $f(\bar{\alpha})$, which is employed to lower the fracture energy around the vicinity of crack. The governing equation for the phase field fracture driven by fatigue is given by

$$
\begin{aligned}
\mathbf{R}^{\mathfrak{d}} = &\int_{\mathcal{B}_0} -2(1-\mathfrak{d})\delta\mathfrak{d}\Psi\mathrm{d}\Omega \\
&+ \int_{\mathcal{B}_0} f(\bar{\alpha})\mathcal{G}_c l \left[\frac{1}{l^2}\mathfrak{d}\delta\mathfrak{d} + \nabla_{\mathbf{X}}\mathfrak{d}\cdot\nabla_{\mathbf{X}}(\delta\mathfrak{d}) \right] \mathrm{d}\Omega = 0
\end{aligned}
\tag{3.40}
$$

The history variable $\bar{\alpha}$ should be independent of the unloading process and takes the form

$$
\bar{\alpha}(t) = \int_0^t \theta(\alpha\dot{\alpha})|\dot{\alpha}|\mathrm{d}\tau
\tag{3.41}
$$

where $\theta(\alpha\dot{\alpha})$ is the Heaviside function and τ is the pseudo time. Note that the fatigue history variable $\bar{\alpha}$ is a scalar variable depending on the loading history of material, which is defined as $\alpha = \mathfrak{g}(\phi)\Psi$. The function $f(\bar{\alpha})$ characterizing the relationship between the degradation of fracture energy and the number of cycles in the fatigue loading is expressed as

$$
f(\bar{\alpha}(t)) = \begin{cases} 1 & \text{if } \bar{\alpha}(t) \leq \alpha_T \\ \frac{2\alpha_T}{\bar{\alpha}(t)+\alpha_T} & \text{if } \bar{\alpha}(t) \geq \alpha_T \end{cases}
\tag{3.42}
$$

where α_T is the threshold value of the fatigue variable, below which the fracture energy will not be influenced by fatigue loading, and its expression is given by

$$
\alpha_T = \frac{G_C}{12l}
\tag{3.43}
$$

The sketch of the single edge notched fatigue is shown in Fig. 55(a). The geometry and dimensions of specimen are all the same as those of the previous single edge notched tension and shear except the shape of initial notch. To avoid contact between the upper and lower faces during compression, a V-shaped notch is adopted here, see Fig. 55(a). The finite element mesh with refinement in the potential crack region is shown in
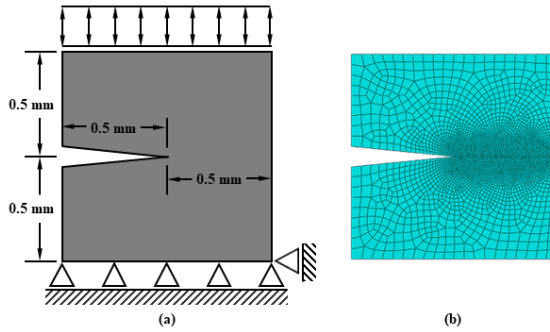
Figure 55: (a) Sketch of the single edge notched fatigue and (b) finite element mesh of specimen
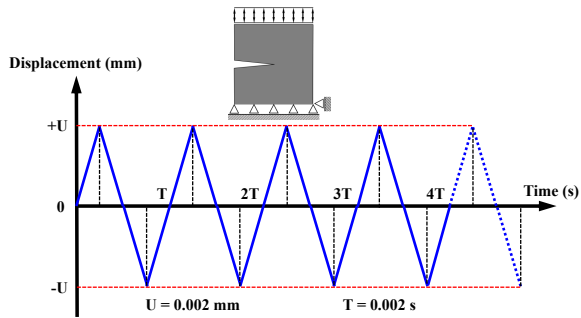
**Figure 56:** Cyclic fatigue loading with equal tension and compression for the single edge notched specimen

Fig. 55(b), and the total number of solid shell elements is 4878. The material and fracture properties are also the same as the previous study. The cyclic loading with equal tension and compression is applied to the upper surface of the specimen, and the amplitude and cycle are 0.002 mm and 0.002 s, respectively, see Fig. 56.

The curves of crack length driven by fatigue loading versus number of cycles for quasi-Newton monolithic and staggered schemes with different time increment sizes are shown in Fig. 57. It is clear that extremely small time increment size is required for the staggered scheme so as to obtain the same result as that of the quasi-Newton monolithic solution, and convergence rate of the staggered scheme is quite low. The curves of total iterations versus number of cycles for the two solution schemes in the phase field fatigue simulation are shown in Fig. 58. Results show that the quasi-Newton solution requires almost the same number of total iterations as the staggered solution with 80 time increments per cycle. However, even the staggered scheme with 200 time increments per cycle cannot reproduce the quasi-Newton monolithic solution, and obviously more increments per cycle are required, which is computationally too expensive. Notably, the staggered solution with 200 increments per cycle requires 6 times more computation times than that in the quasi-Newton monolithic analysis. It can be concluded that quasi-Newton monolithic scheme shows the tremendous advantage over the staggered scheme in computational efficiency for fatigue problems. The contour plots of phase field values in fatigue induced fracture modeling with solid shell formulation solved by the quasi-Newton monolithic scheme are shown in Fig. 59. As can be clearly seen, the crack propagation starts from the 15th cycle of fatigue loading, and it proceeds with the increase of fatigue cycles. The single edge notched specimen for fatigue modeling is fully cracked at the 50th cycle.
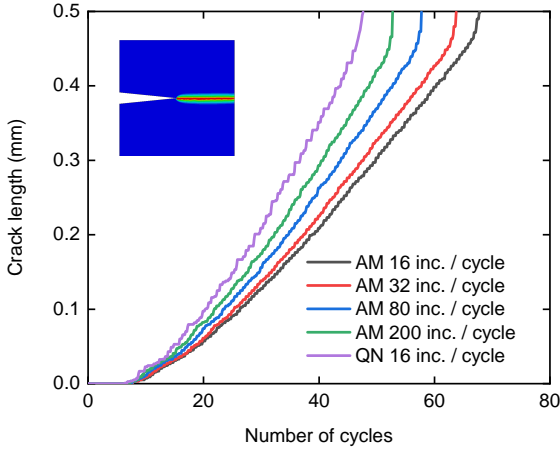
Figure 57: The curves of crack length vs. number of cycles obtained from both the quasi-Newton monolithic and staggered schemes for the phase field fracture modeling under fatigue loading

3.4.5 Global-local fracture modeling of thin-walled structure with curved geometry

In this section, the global-local phase field approach using solid shells is tested through the fracture modeling of cylindrical structure with an initial notch in the center as shown in Fig. 60(a). The dimensions of this specimen in the global level are the same as that in Section 3.4.3. As shown in Fig. 60(a), the global specimen is separated into 9 different blocks in total and the initial notch lies within the central block, which is chosen as the region of local model. To save computational cost, the global model is discretized with relatively coarse mesh using the uniform size of 3 mm, while to appropriately capture the crack propagation in the phase field modeling of local region, very refined mesh is used to discretize the potential crack area around the notch of local model. Specifically, the mesh size around the edge of local model is 3 mm, which is the same as that of global model, and characteristic mesh size along the
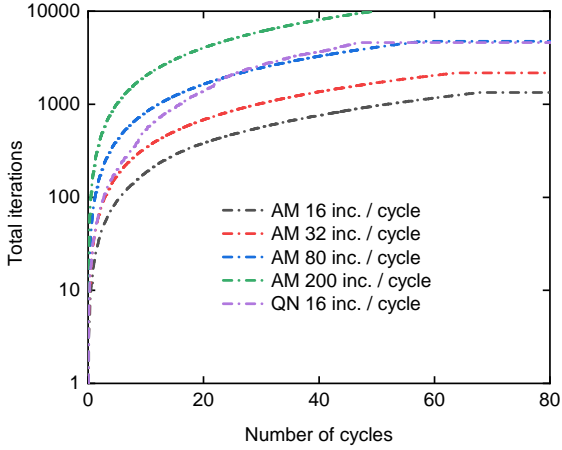
Figure 58: The curves of total iterations vs. number of cycles obtained from both the quasi-Newton monolithic and staggered schemes for the phase field fracture modeling under fatigue loading
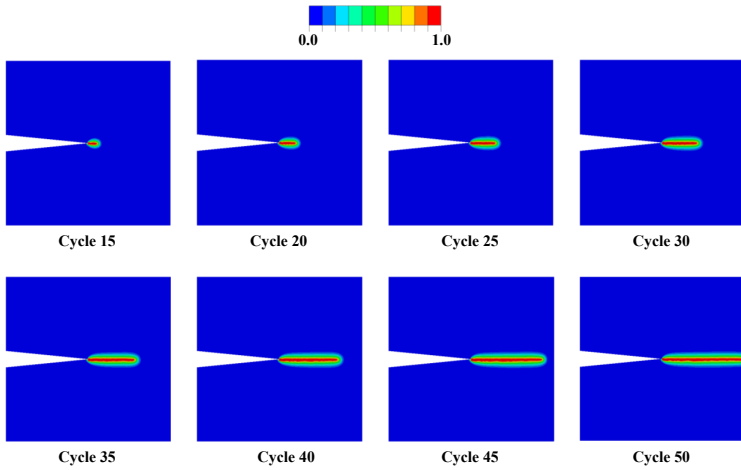
Figure 59: The contour plots of phase field values in fatigue modeling using solid shell element solved by the quasi-Newton monolithic scheme
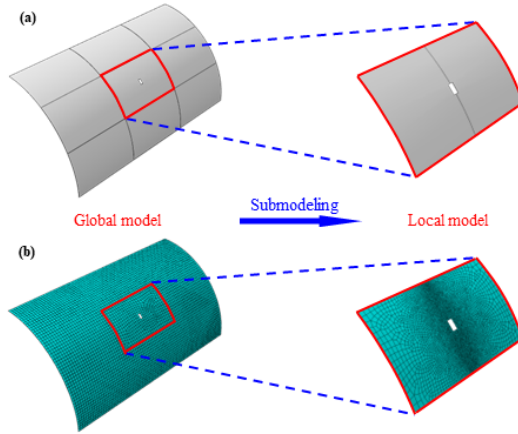
Figure 60: (a) Geometry and (b) finite element mesh of the global and local models in the phase field fracture submodeling of cylindrical structure

potential crack path is 0.8 mm, see Fig. 60(b). The continuum solid shell is chosen for the elastic finite element analysis of global model, and phase field modeling for solid shell using quasi-Newton monolithic scheme is subsequently employed for the analysis of refined local model. The same material properties are adopted for the global and local model with the Young's modulus equal to 210 GPa and the Poisson's ratio equal to 0.3, and both the phase field length scale and fracture toughness of local model are the same as the previous study in Section 3.4.3, which are equal to 4 mm and 2.7 N/mm, respectively.

The contour plots of phase field values of local model, displacement fields of both global and local models solved by quasi-Newton monolithic scheme at two different time points are shown in Fig. 61. The first time point is the time increment when the crack of local model starts to propagate under the drive of the boundary conditions interpolated from the displacement output of global model, while the second time point is the time increment when the local model with curved geometry is fully cracked. This global-local approach is very computationally efficient in fracture modeling of large thin-walled structures, since only the local re-

Time \ Type	Displacement of global model	Displacement of local model	Phase field of local model
Time 1	0.250 0.200 0.150 0.100 0.050 0.000	0.150 0.120 0.090 0.060 0.030 0.000	1.0 0.8 0.6 0.4 0.2 0.0
Time 2	0.250 0.200 0.150 0.100 0.050 0.000	0.150 0.120 0.090 0.060 0.030 0.000	1.0 0.8 0.6 0.4 0.2 0.0
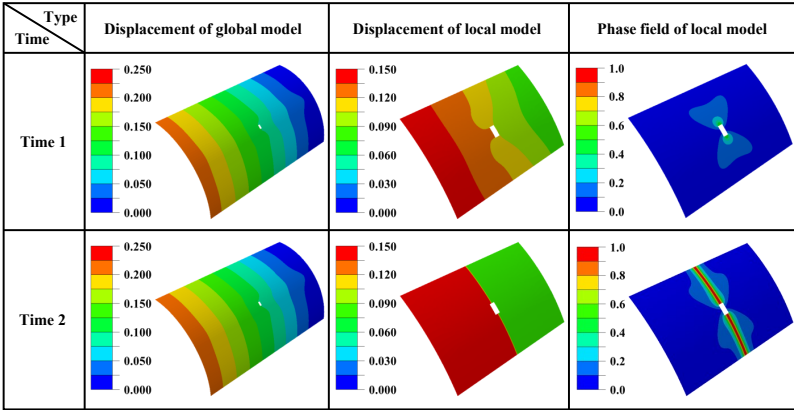
Figure 61: The contour plot of global and local displacement as well as phase field variable in the fracture submodeling of cylindrical structure with solid shell element formulation

gion of interest needs to be modeled by phase field approach. In the global model, the degree of freedom corresponding to phase field variable is ignored, and thus significant computational cost can be saved. Besides, mesh in the local fracture region of interest can be refined with more flexibility, which is very appealing for realistic application of phase field approach in fracture modeling of large-scale structures.

To further assess the global-local phase field approach using solid shells, the above case study is extended to the analysis of fatigue induced crack growth by applying the cyclic loading to the frontal end of global model. The cyclic loading is characterized by the amplitude of 0.05 mm and the cycle of 0.01 s, as shown in Fig. 62. The time duration is 1 s, and thus there are 100 cycles in total. The phase field plots of local model in the fatigue submodeling solved by quasi-Newton monolithic scheme are shown in Fig. 63. It should be pointed out that the boundary conditions of local model are obtained by the interpolation of the displacement output from the global finite element analysis, which is subjected to cyclic loading shown in Fig. 62. In this fatigue submodeling case, the crack of local model starts to propagate from the 40th cycle and after 28 cycles of
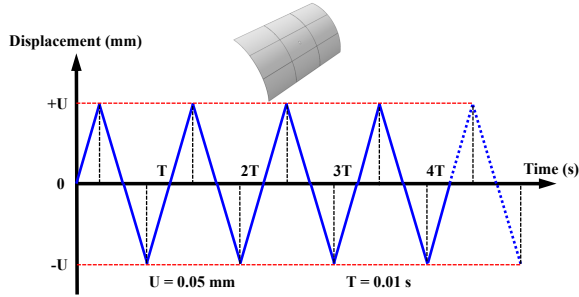
Figure 62: Cyclic fatigue loading with equal tension and compression for the global model of the cylindrical structure

fatigue loading, the local model is fully cracked along the expected crack path, which further demonstrates the capability of this global-local phase field approach for fracture modeling.

3.4.6 Benchmark example of anisotropic fracture

In this example, the model will be assessed through a benchmark problem consisting in a square specimen that contains two parts and an initial crack, as shown in Fig. 64. The size of the specimen is 1 mm, and meshed with uniform solid shell elements. The elastic modulus and critical fracture energy release rate are set to 160 GPa and 4.32 N/m, respectively, which are the typical material properties of silicon solar cells in photovoltaic modules [148]. The preferential crack plane of the Grain 2 with an initial crack is oriented with a fixed angle of 45 degree, while the preferential crack direction of the Grain 1 varies with respect to the horizontal axis of the whole domain. Regarding the boundary condition, the bottom facet is constrained in the vertical direction, and a tensile loading is applied to the upper facet of the specimen.

The predicted contour plots of phase field with different preferential crack orientations of Grain 1 are shown in Fig. 65. Different crack patterns can be observed with different preferential crack planes. The crack propagates from the initial crack following the fixed crack orientation
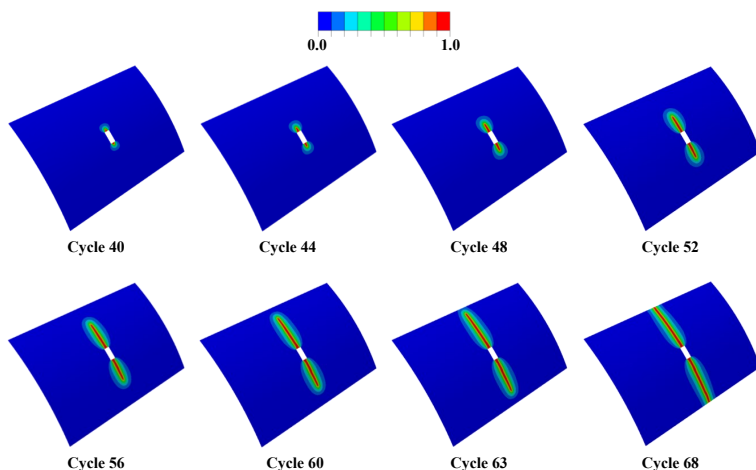
Figure 63: The contour plots of phase field values of local model in fatigue submodeling solved by quasi-Newton monolithic scheme
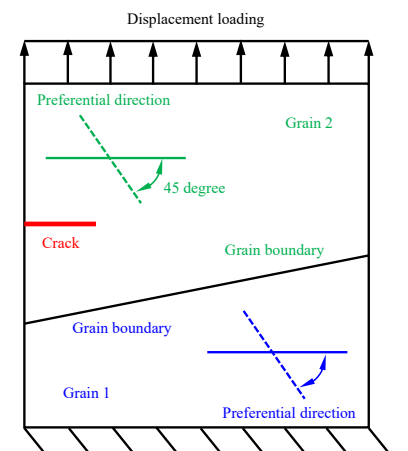
Figure 64: Schematic diagram of the benchmark problem for anisotropic fracture modeling.
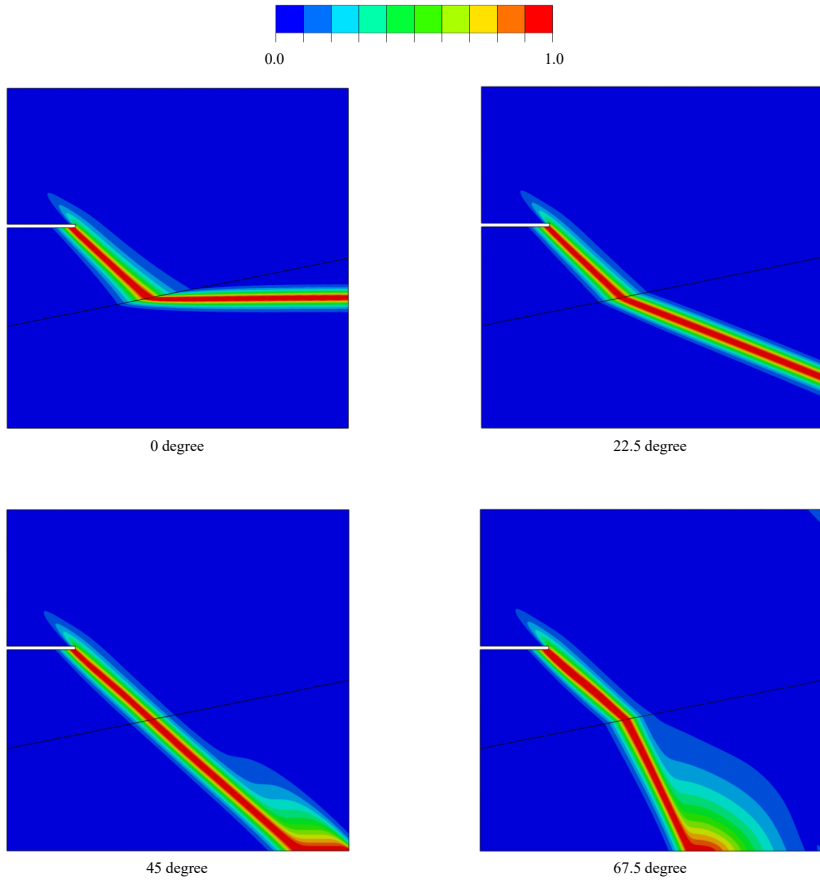
Figure 65: The phase field contour plots of fully cracked specimen with the preferential crack orientation of Grain 1 equal to 0 degree, 22.5 degree, 45 degree, and 67.5 degree.

through the domain of Grain 2, and when approaching the boundary between the two grains, crack deviation occurs due to the different nature of Grain 1. As shown in Fig. 65, the crack path through the Grain 1 when the specimen is fully cracked exactly follows the expected orientation. The force versus displacement curves for the different crack orientations of Grain 1 are plotted in Fig. 66. It can be seen that the crack preferential orientation of Grain 1 has negligible influence on the mechanical response. The approximate linear behaviour can be observed before the specimen is fully cracked when the loading displacement reaches around 0.0005 mm. After the peak values, all the curves drops down to zero immediately except the curve with crack orientation angle of Grain 1 equal to 67.5 degree, which can be ascribed to the fact that part of specimen is still constrained even when reaching the fully cracked state in this case. It should be pointed out that the different crack patterns can create different electrically inactive area in the silicon solar cell, leading to different power loss of the photovoltaic modules. Hence, the fracture anisotropy must be taken into account for the modeling of cracking events [28].

3.4.7 Silicon solar cell cracking in the photovoltaic module

The modeling framework is further assessed in this section with application to the more realistic simulation of silicon solar cell cracking when the photovoltaic modules are subjected to the different external loading. According to the experimental investigations [193, 28], the cracking events of silicon solar cells have negligible influence on the global stiffness of photovoltaic modules, and as a result, the global-local approach proposed in [131] can be employed to reduce the computational cost by decoupling the elastic modeling of photovoltaic module with the fracture modeling of silicon solar cells. In this approach, the photovoltaic module is assumed to be purely elastic corresponding to the global model, and its solution at each time step is used to drive the local fracture modeling of silicon solar cell with the phase field approach. Hence, the global and local models are solved in a staggered manner, which features the one-
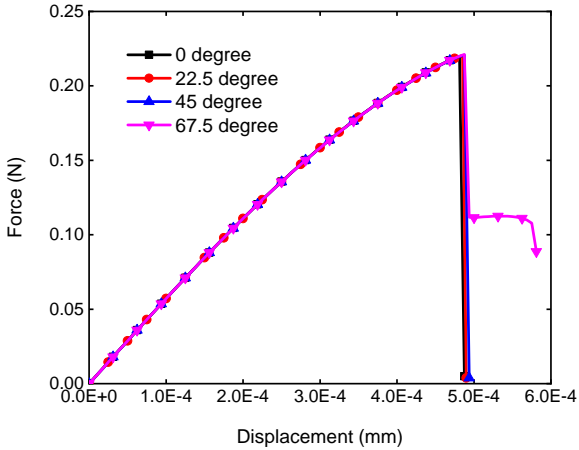
Figure 66: The obtained force vs. displacement curves with the preferential crack orientation of Grain 1 equal to 0 degree, 22.5 degree, 45 degree, and 67.5 degree.

way coupling in line with experimental evidence. The cracking events of one single silicon solar cell when the photovoltaic modules are subjected to two different loading cases are investigated to comprehensively showcase the capability of the modeling framework.

In the first case, the tensile loading is applied to the photovoltaic module, and there is an initial notch perpendicular to the loading direction in the middle of one single solar cell, as shown in Fig. 67. The photovoltaic module is basically a thin-walled laminate structure that consists of dif-

Table 2: Mechanical properties for Photovoltaic modules [86, 52].

	E (GPa)	Density (kg/m^3)
Backsheet	2.8	1200
EVA	0.01	1180
Glass	73	2500
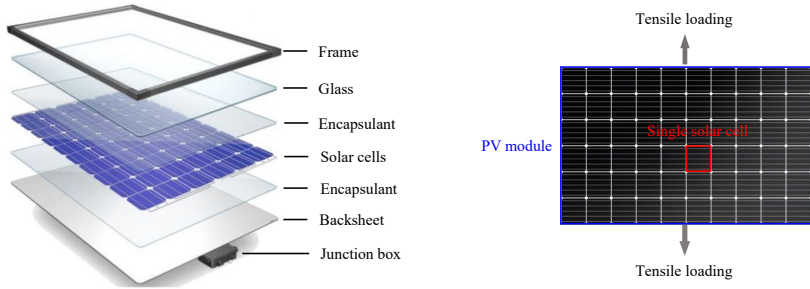
Figure 67: Schematic diagram of the local fracture modeling of one single solar cell when the photovoltaic module is subjected to tensile loading.

ferent layers, including glass, backsheet, solar cells, and so on [16]. The material properties of photovoltaic modules are listed in Table 2, which are taken from [86, 52]. The key component of the photovoltaic module is the silicon cell layer that converts the solar energy into electrical energy. It is very thin with the thickness of aproximately 0.1 mm [38], and can be broken easily due to the fragility. Each module contains 60 silicon solar cells, and the local crack propagation in the one single thin-film solar cell can be modeled by the phase field approach with solid shell formulation. The predicted contour plots of displacement in the module at the loading displacement 1.24 mm, 1.34 mm, 1.42 mm, and 1.48 mm are shown in Fig. 68. At each time step, the global solution is used to drive the crack propagation of local model with uniform fine mesh by interpolation [131]. Hence, the boundary condition of the local model is determined by the global solution at each time step. Due to fracture anisotropy, the local model can have different crack paths. In case of isotropic fracture, the phase field contour plots of the local model corresponding to the four loading stages are shown in Fig. 69. On the other hand, when the preferential crack orientation angle is set to 45 degree, the crack growth can be observed from Fig. 70.

In the second case, the photovoltaic module is subjected to the three point bending, as shown in Fig. 71. The predicted displacement contour plots of the module along the loading direction at four loading stages
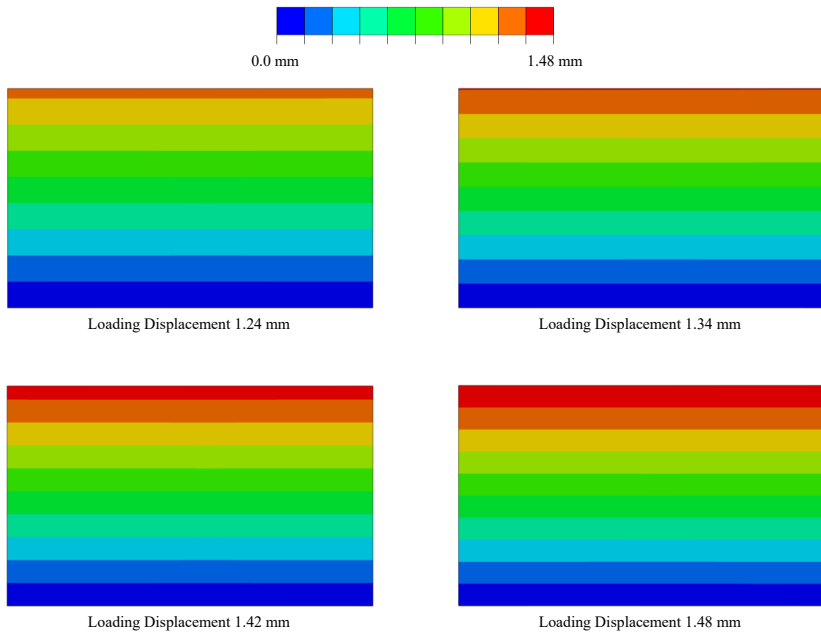
Figure 68: The predicted displacement contour plots of the whole photo-voltaic module when subjected to tensile loading at the loading displacement 1.24 mm, 1.34 mm, 1.42 mm, and 1.48 mm.
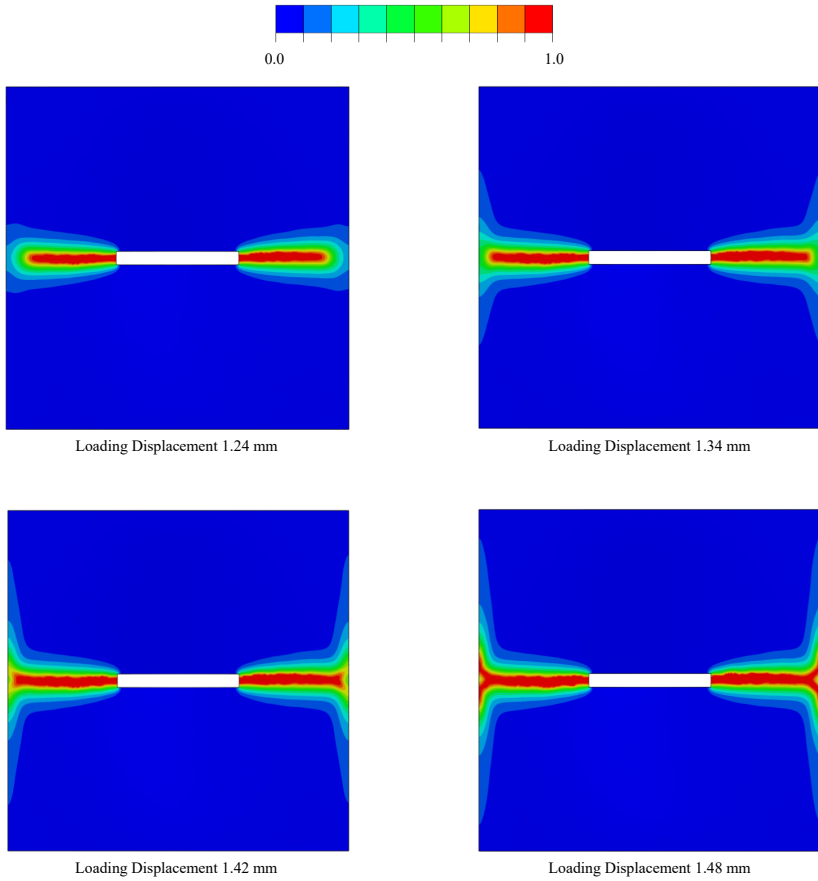
Figure 69: The predicted phase field contour plots of the local model with no fracture anisotropy at the loading displacement 1.24 mm, 1.34 mm, 1.42 mm, and 1.48 mm.
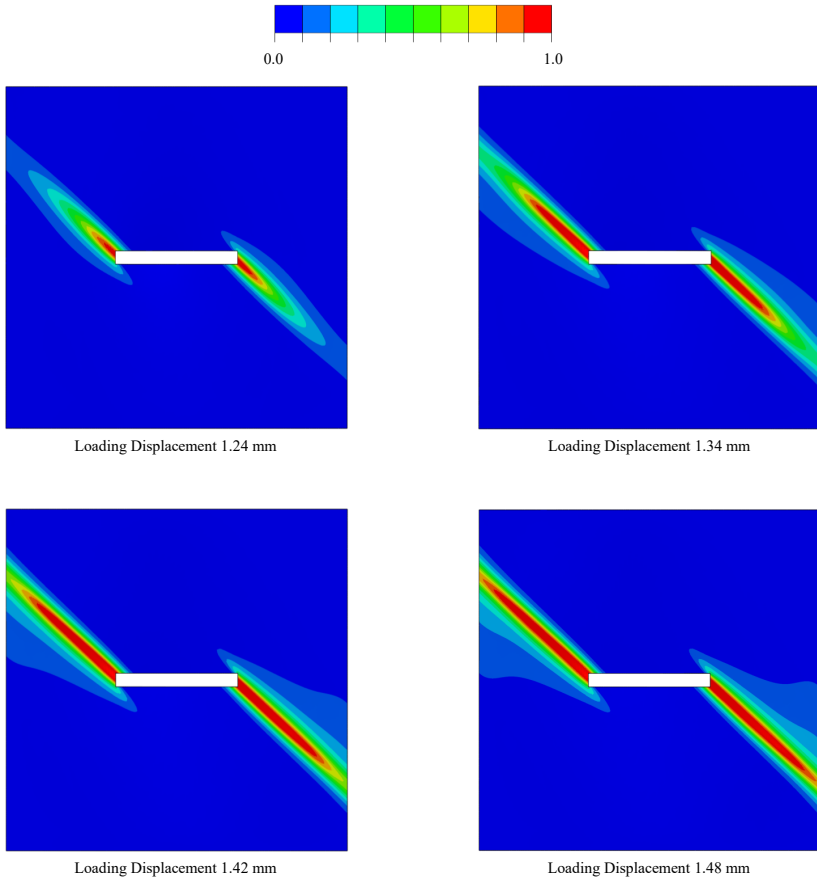
Figure 70: The predicted phase field contour plots of the local model with the preferential crack orientation angle equal to 45 degree at the loading displacement of 1.24 mm, 1.34 mm, 1.42 mm, and 1.48 mm.
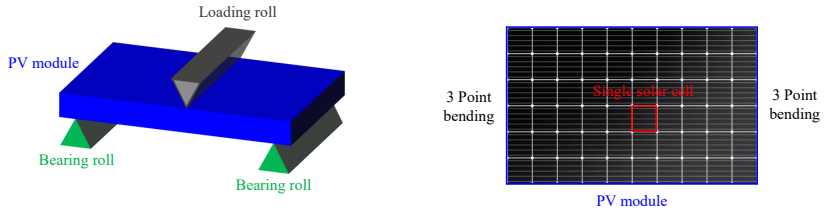
Figure 71: Schematic diagram of the local fracture modeling of one single solar cell when the photovoltaic module is subjected to three point bending.

are shown in Fig. 72. The local model driven by the global solution at each time step should have mixed boundary conditions in this case, including both pure bending and tension. Fig. 73 shows the phase field contour plots of the local model with no fractrue anisotropy at four different loading stages, while Fig. 74 indicates the phase field contour plots of the local model with the preferential crack orientation angle equal to 45 degree, which presents complete different crack patterns compared to the former.

-76.55 mm   72.04 mm

Loading Displacement 67.5 mm   Loading Displacement 70.5 mm

Loading Displacement 73.5 mm   Loading Displacement 76.5 mm
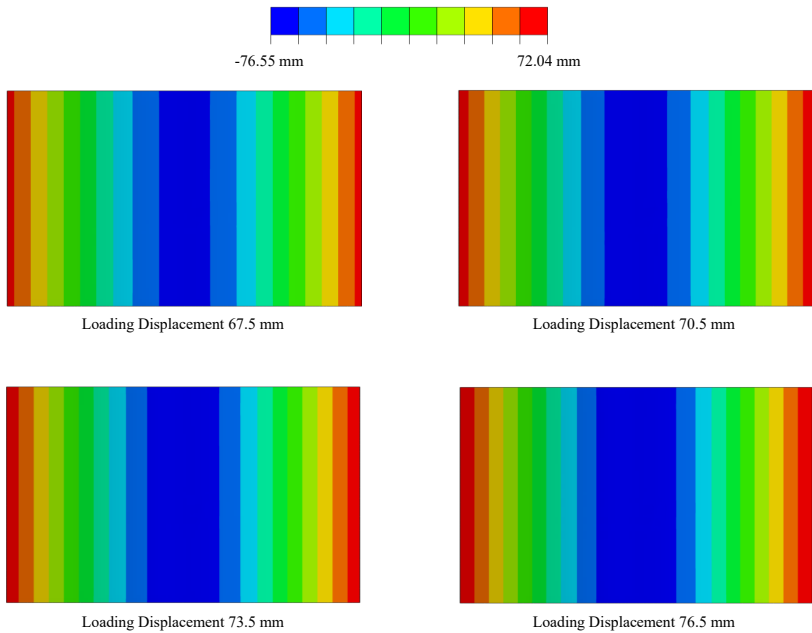
Figure 72: The predicted displacement contour plots of the whole photovoltaic module when subjected to three point bending at the loading displacement 67.5 mm, 70.5 mm, 73.5 mm, and 76.5 mm.

0.0　　　　　　　　1.0

Loading Displacement 67.5 mm

Loading Displacement 70.5 mm

Loading Displacement 73.5 mm

Loading Displacement 76.5 mm
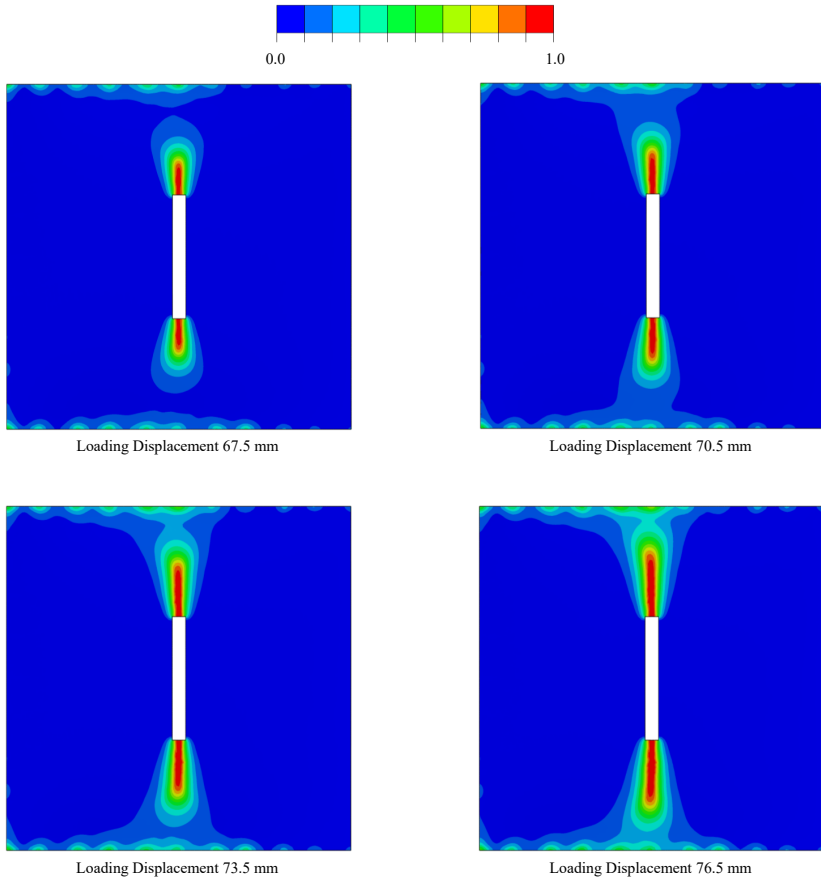
Figure 73: The predicted phase field contour plots of the local model with no fracture anisotropy at the loading displacement 67.5 mm, 70.5 mm, 73.5 mm, and 76.5 mm.

Loading Displacement 100.5 mm

Loading Displacement 103.5 mm

Loading Displacement 106.5 mm

Loading Displacement 109.5 mm
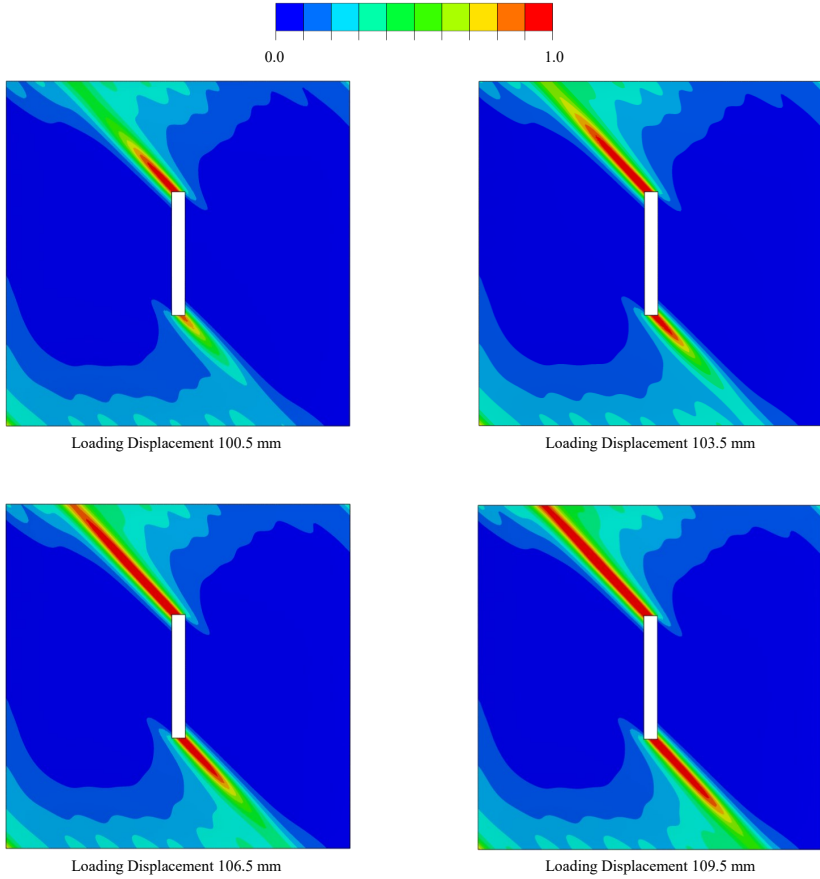
Figure 74: The predicted phase field contour plots of the local model with the preferential crack orientation angle equal to 45 degree at the loading displacement 100.5 mm, 103.5 mm, 106.5 mm, and 109.5 mm.

Chapter 4

Modeling and simulation of the recycling process for end-of-life photovoltaic laminates

The main content of this chapter is taken from my own publications - Z. Liu, J. Reinoso, M. Paggi. "A humidity dose-CZM formulation to simulate new end-of-life recycling methods for photovoltaic laminates" [1] and Z. Liu, M. Marino, J. Reinoso, M. Paggi, "A continuum large-deformation theory for the coupled modeling of polymer–solvent system with application to PV recycling" [38].

In the past decades, the development of environmentally friendly energy production techniques has resulted into the fast-growing increase of photovoltaic (PV) modules all over the world [26, 27, 195, 54, 196]. In view of the limited service lifetime (around 25 years) of PV modules [197, 84, 23, 28], a significant amount of these end-of-life products, which are defined as waste of electronic equipment [198], will continuously pose challenges to the sustainable energy production and environmental protection [199, 200, 201, 57, 1]. Hence, there is an urgent need to develop reliable techniques to dispose end-of-life PV modules [202, 203, 204, 205,

206, 207].

EVA is a kind of polymeric material consisting of 3D network of polymer molecules that are bonded to each other, and thus capable of recoverable large-deformation [208, 209, 210, 211]. During the recycling process using the solvent method, the solvent can penetrate into the EVA network when coming into contact, and the molecules can be absorbed by the skeletal polymeric network of EVA, forming a swollen aggregate. The solvent molecules can interact with each other as well as with the polymer structure, and also migrate in and out of the swollen aggregate. The theory of mass transport in the continuum solids dates back to [212], and have been further developed for the description of coupled deformation and diffusion with application to the response of hydrogels, including swelling and deswelling induced by mechanical deformation and forced fluid permeation [213, 214, 215]. The purpose of this work is to develop a thermodynamically consistent large-deformation theory on the continuum level for the description of EVA polymer-solvent system in the PV recycling, so as to provide guidance to the design of experimental procedures for the nondestructive recovery of ultrathin and brittle silicon wafers. Similarly to the theories developed by [213], the polymer-solvent system is treated as homogenized continuum in which the solvent flux is allowed. In the development of constitutive theory, the Flory-Huggins theory for the free energy change due to the mixing of solvents with different solubility parameters and EVA polymer network is adopted, and the statistical-mechanical model is accounted for to describe the entropic change of EVA polymer chains due to the mechanical stretching.

The adhesion strength of PV modules is greatly influenced by the operating environment, depending on different factors, including humidity, temperature, and irradiance [216, 217]. Moisture will weaken the ionic attraction of the bond and physical adsorption across the interface due to the high permittivity of water, which is highly relevant to the properties of high polarity adherend [218]. Both the ionic attraction force and van der Waals forces are inversely proportional to the relative permittivity, and a small amount of water will significantly reduce the adhesion strength [219]. Besides, the high surface tension resulting from the

high polarity of water will reduce the thermodynamic work of adhesion and thus damage interface durability [220]. Temperature mechanically affects the performance of PV modules through differential thermal expansion, as can be seen in real life because of daily and seasonal thermal cycles. However, it is assumed that the loss of adhesion strength is primarily reduced by moisture ingress, and temperature acts as the accelerator of the effects of humidity [221, 222]. This research aims at understanding the influence of moisture penetration accelerated by temperature on the adhesion durability of interfaces in the PV system. More specifically, the target is to develop a computational framework allowing for the accurate simulation of delamination in PV modules for different ageing conditions. In this regard, research is motivated by the fact that peeling techniques could be exploited to partially disassemble PV laminates at the end of their lifetime. This can be energetically and economically favourable over the actual recycling operations which consider a full crushing of the glass laminate and then separation of its recyclable components afterwerds.

During the past decades, cohesive zone models (CZM) have been widely incorporated into the nonlinear finite element method for engineering applications concerning the formation of free surfaces due to fracture. Compared with other methods such as the virtual crack closure technique (VCCT) [223], CZM can be easily implemented into research and commercial codes and is highly versatile to accommodate different physical phenomena. CZM is a nonlinear traction–relative displacement relationship between the interface tractions across the discontinuity and the sliding and opening displacements. Applications cover many fields, like quasi-static fracture in solids [224, 225], snap-back instabilities during crack propagation [226, 227], crack propagation in composites [125, 228], micromechanical and multiscale analyses [229, 135], and crack assessment in bio-inspired materials [136], among others. However, to the best knowledge of the authors, no previous research considers effect of environmental factors including both moisture and temperature on the interfacial strength in CZM for numerical prediction of fracture especially towards PV lifetime recycling.

Peeling of layers of the laminate from the layer of solar cells would require large deformation simulations [230], since the deformed configuration cannot be approximated by the undeformed one. As a result, the interfacial gap calculated according to the initial undeformed configuration can result in errors that cannot be ignored when assessing the total energy required for peeling, which is the quantity of primary interest for recycling. To accurately predict the large deformation framework, both the surface separation and relative rotation between two sides of the interface need to be taken into account. A first attempt has been proposed in [138], which adopted the middle surface of the cohesive element in the deformed configuration as the reference plane to calculate the normal and tangential directions of the interface. Nevertheless, this formulation stemming from differentiation of cohesive tractions with regard to normal unit vector led to non-symmetric geometric stiffness. Based on that research, a 3D interface finite element was used to simulate the standard fracture mechanics tests in thin aluminum panels, in which residual with rotation matrix is updated during the deformation process [231]. However, its linearization does not consider the dependence of differential operator with respect to the kinematic field. Another alternative formulation for large displacement interface element was proposed in [232] by introducing a co-rotational reference system coincident with one of the deformed surfaces of the interface element, but not easy to be implemented into the finite element method due to this co-rational description. In order to account for large deformation of the interface, the interface element formulation for both geometrical and material nonlinearity developed in [126] is herein adopted and extended to 3D application in this work.

The first part of this section proposes a computational framework at finite strains for the modeling of EVA polymer-solvent system in PV recycling using the solvent method, which takes into account the coupled solvent diffusion, swelling and shrinking of EVA polymers, as well as effects of mechanical constraints and initial crosslinking of EVA during PV lamination. In Section 4.1.1 and 4.1.2, the basic continuum kinematics in the large-deformation framework and balance laws for force and mass

balance are given according to the standard modern continuum mechanics. Section 4.1.3 presents the derivation of thermodynamics and constitutive theory, and the specific free energy definition is given in Section 4.1.4. The numerical implementation of this theory is derived in detail using the finite element method in Section 4.1.5, and then applied to the PV recycling through some examples in Section 4.1.6. In the second part of this section, the polynomial CZM [233] coupled with strength degradation by the humidity dose model [221] is proposed for the peeling simulation in PV recycling, as shown in Section 4.2.1. Then it is incorporated into the 3D large deformation interface element extended from the 2D version proposed in [126], see Section 4.2.2. The numerical results obtained from this coupling strategy correlate with experimental results [221] very well for adhesion strength between backsheet and encapsulant layer in PV. In section 4.2.3, the difference between the specific energy required in peeling and traditional crushing for recycling of PV panels is compared and discussed.

4.1 Coupled modeling of polymer-solvent system in PV recycling

4.1.1 Continuum kinematics

According to the standard concepts of continuum mechanics framework [234, 235], the EVA body in PV modules can be described as a macroscopically homogeneous continuum solid within the Euclidean space $\mathbb{E}^3$. It is assumed that kinematic fields in the continuum theory are applied at large length scales compared to that associated with the polymer molecule network and pore-structure of EVA [236, 237]. We identify the macroscopically homogeneous EVA with the space it occupies in the reference configuration $\mathcal{B}_0$, and describe the current configuration $\mathcal{B}$ by a smooth one-to-one transformation mapping $\varphi : \mathcal{B}_0 \rightarrow \mathbb{E}^3$. The position vector of an arbitrary material point in the reference configuration $\mathcal{B}_0$ is denoted by $\mathbf{X}$, and the corresponding vector in the current configuration $\mathcal{B}$ is represented by $\mathbf{x} = \varphi(\mathbf{X}, t)$.

The displacement field in the reference configuration is defined as $\mathbf{u}(\mathbf{X}, t) = \mathbf{x} - \mathbf{X} = \boldsymbol{\varphi}(\mathbf{X}, t) - \mathbf{X}$, and the transformation mapping is described by the deformation gradient $\mathbf{F}$, which reads

$$\mathbf{F} = \frac{\partial \boldsymbol{\varphi}(\mathbf{X}, t)}{\partial \mathbf{X}} = \nabla_{\mathbf{X}} \boldsymbol{\varphi}(\mathbf{X}, t) \tag{4.1}$$

where $\nabla_{\mathbf{X}}$ denotes the material gradient. The determinant of the deformation gradient is defined as $J = \det \mathbf{F} \neq 0$, representing the volume change from the reference configuration to the current configuration. The velocity $\mathbf{v}$ and its gradient with respect to the position vector $\mathbf{x}$ in the current configuration $\mathbf{L}$ are given by

$$\mathbf{v} = \dot{\boldsymbol{\varphi}}(\mathbf{X}, t) \quad \text{and} \quad \mathbf{L} = \nabla_{\mathbf{x}} \mathbf{v} = \dot{\mathbf{F}} \cdot \mathbf{F}^{-1} \tag{4.2}$$

where $\nabla_{\mathbf{x}}$ denotes the spatial gradient.

To describe the coupled mechanical behavior of polymer and solvent, the multiplicative decomposition of deformation gradient is given by

$$\mathbf{F} = \mathbf{F}^e \cdot \mathbf{F}^s \tag{4.3}$$

where $\mathbf{F}^e$ and $\mathbf{F}^s$ represent the elastic and swelling parts of deformation gradient $\mathbf{F}$, respectively. The swelling distortion $\mathbf{F}^s$ is defined as

$$\mathbf{F}^s = \lambda^s \mathbf{1}, \quad \text{with} \quad \lambda^s \geq 0 \tag{4.4}$$

where λ^s is the swelling stretch, which accounts for the swelling of the polymeric body due to absorbed solvents that are pinned to the network structure in the intermediate local space at the material point $\mathbf{X}$. For convenience, the determinant J can be written as

$$J = J^e J^s, \quad \text{with} \quad J^e = \det \mathbf{F}^e \quad \text{and} \quad J^s = \det \mathbf{F}^s = (\lambda^s)^3 \tag{4.5}$$

Remarkably, $(J^s - 1)$ represents the volume change per unit reference volume of EVA resulting from the swelling behaviour due to the change in the solvent content. Analogous to the theory developed for hydrogels, the swelling constraint is defined as

$$J^s = 1 + \upsilon C_{\mathrm{R}} \quad \text{and} \quad \phi = (1 + \upsilon C_{\mathrm{R}})^{-1} \tag{4.6}$$

where υ denotes the volume of a mole of solvent molecules, C_{R} represents the number of moles of absorbed solvent molecules by the polymeric body per unit reference volume, and ϕ is the polymer volume fraction.

Following the standard decomposition of deformation gradient, we have

$$\mathbf{F} = \mathbf{R} \cdot \mathbf{U} = \mathbf{V} \cdot \mathbf{R} \quad \text{and} \quad \mathbf{F}^e = \mathbf{R}^e \cdot \mathbf{U}^e = \mathbf{V}^e \cdot \mathbf{R}^e \qquad (4.7)$$

where $\mathbf{R}$ and $\mathbf{R}^e$ are rotation tensors, $\mathbf{U}$ and $\mathbf{U}^e$ are right stretching tensors, and $\mathbf{V}$ and $\mathbf{V}^e$ are left stretching tensors. Subsequently, the total right and left Cauchy-Green tensors $\mathbf{C}$ and $\mathbf{B}$, and the elastic corresponding tensors $\mathbf{C}^e$ and $\mathbf{B}^e$ are defined as

$$\mathbf{C} = \mathbf{U}^2 = \mathbf{F}^{\mathrm{T}} \cdot \mathbf{F} \quad \text{and} \quad \mathbf{B} = \mathbf{V}^2 = \mathbf{F} \cdot \mathbf{F}^{\mathrm{T}} \qquad (4.8a)$$

$$\mathbf{C}^e = \mathbf{U}^{e2} = \mathbf{F}^{e\mathrm{T}} \cdot \mathbf{F}^e \quad \text{and} \quad \mathbf{B}^e = \mathbf{V}^{e2} = \mathbf{F}^e \cdot \mathbf{F}^{e\mathrm{T}} \qquad (4.8b)$$

Next, by substituting Eq. (4.3) into Eq. (4.2)$_2$, the velocity tensor $\mathbf{L}$ can be expressed as

$$\mathbf{L} = \mathbf{L}^e + \mathbf{F}^e \cdot \mathbf{L}^s \cdot \mathbf{F}^{e-1} \qquad (4.9)$$

where the elastic and swelling velocity tensors $\mathbf{L}^e$ and $\mathbf{L}^s$ are given by

$$\mathbf{L}^e = \dot{\mathbf{F}}^e \cdot \mathbf{F}^{e-1} \quad \text{and} \quad \mathbf{L}^s = \dot{\mathbf{F}}^s \cdot \mathbf{F}^{s-1} \qquad (4.10)$$

4.1.2 Balance laws

In the current configuration, the local form of force balance in the absence of dynamic effects can be expressed as

$$\nabla_{\mathbf{x}} \cdot \boldsymbol{\sigma} + \mathbf{b} = \mathbf{0} \qquad (4.11)$$

where $\mathbf{b}$ is the body force per unit deformed body, and $\boldsymbol{\sigma}$ is the Cauchy stress tensor deriving from the balance of angular momentum. As is standard [238], the first Piola-Kirchhoff stress tensor $\mathbf{P}$ and Kirchhoff stress tensor $\boldsymbol{\tau}$ can be related to the symmetric Cauchy stress tensor $\boldsymbol{\sigma}$ by

$$\mathbf{P} = J\boldsymbol{\sigma} \cdot \mathbf{F}^{-\mathrm{T}} \qquad (4.12a)$$

$$\boldsymbol{\tau} = J\boldsymbol{\sigma} \tag{4.12b}$$

and thus

$$\boldsymbol{\sigma} = J^{-1}\mathbf{P} \cdot \mathbf{F}^{\mathrm{T}} \tag{4.13}$$

Let $\partial\mathcal{B}_{\mathbf{u}}$ and $\partial\mathcal{B}_{\mathbf{t}}$ be the complementary surfaces of the polymeric body $\mathcal{B}$ with $\partial\mathcal{B} = \partial\mathcal{B}_{\mathbf{u}} \cup \partial\mathcal{B}_{\mathbf{t}}$ and $\partial\mathcal{B}_{\mathbf{u}} \cap \partial\mathcal{B}_{\mathbf{t}} = \varnothing$. The boundary conditions imposed on the body in the current configuration can be given by

$$\mathbf{u} = \bar{\mathbf{u}} \quad \text{on} \quad \partial\mathcal{B}_{\mathbf{u}} \tag{4.14a}$$

$$\boldsymbol{\sigma} \cdot \mathbf{n} = \bar{\mathbf{t}} \quad \text{on} \quad \partial\mathcal{B}_{\mathbf{t}} \tag{4.14b}$$

where $\mathbf{n}$ is the outward unit normal on the external boundary $\partial\mathcal{B}$ of the body $\mathcal{B}$.

Let $\mathbf{j}$ denotes the fluid flux per unit deformed area per unit time, and thus $-\int_{\partial\mathcal{B}} \mathbf{j} \cdot \mathbf{n} \, \mathrm{d}\partial\Omega$ represents the total moles of solvent molecules entering the EVA body $\mathcal{B}$ across $\partial\mathcal{B}$ per unit time. In the current configuration, the mass balance equation reads

$$\dot{C}_{\mathrm{R}} = -J\nabla_{\mathbf{x}} \cdot \mathbf{j} \tag{4.15}$$

By the substitution of Eq. $(4.6)_2$, Eq. (4.15) can be rewritten as

$$\frac{\dot{\phi}}{Jv\phi^2} - \nabla_{\mathbf{x}} \cdot \mathbf{j} = 0 \tag{4.16}$$

in which the fluid flux $\mathbf{j}$ is defined as [213]

$$\mathbf{j} = -m(\phi) \cdot \nabla_{\mathbf{x}}\mu \quad \text{with} \quad m(\phi) = \frac{D}{RTv}\left[(1-\gamma)\phi + \gamma\right] \tag{4.17}$$

where m is the mobility coefficient that depends on the polymer volume fraction ϕ and diffusion coefficient D, R is the universal gas constant, T represents the absolute temperature, and γ is the correlation coefficient that determines the change of polymer network due to the increase of solvent content.

Let $\partial\mathcal{B}_{\mu}$ and $\partial\mathcal{B}_{\mathbf{j}}$ be the complementary surfaces of the polymeric body $\mathcal{B}$ with $\partial\mathcal{B} = \partial\mathcal{B}_{\mu} \cup \partial\mathcal{B}_{\mathbf{j}}$ and $\partial\mathcal{B}_{\mu} \cap \partial\mathcal{B}_{\mathbf{j}} = \varnothing$. The boundary conditions imposed on the EVA body in the current configuration are given by

$$\mu = \bar{\mu} \quad \text{on} \quad \partial \mathcal{B}_\mu \tag{4.18a}$$

$$-\mathbf{j} \cdot \mathbf{n} = \bar{j} \quad \text{on} \quad \partial \mathcal{B}_\mathbf{j} \tag{4.18b}$$

where μ is the chemical potential that will be derived in the following.

4.1.3 Thermodynamics and constitutive laws

Following the discussion of thermodynamics and ignoring inertial effects and kinetic energy [234], the balance law for energy under the isothermal condition using Lagrangian description is given by

$$
\begin{aligned}
\int_{\mathcal{B}_0} \dot{\psi}_\mathrm{R} \, \mathrm{d}\Omega_\mathrm{R} \leq & \int_{\partial \mathcal{B}_0} (\mathbf{P} \cdot \mathbf{N}_\mathrm{R}) \cdot \dot{\boldsymbol{\varphi}} \, \mathrm{d}\partial\Omega_\mathrm{R} \\
& + \int_{\mathcal{B}_0} \mathbf{B}_\mathrm{R} \cdot \dot{\boldsymbol{\varphi}} \, \mathrm{d}\Omega_\mathrm{R} - \int_{\partial \mathcal{B}_0} \mu \mathbf{J}_\mathrm{R} \cdot \mathbf{N}_\mathrm{R} \, \mathrm{d}\partial\Omega_\mathrm{R}
\end{aligned}
\tag{4.19}
$$

where the subscript R means the description of fields in the reference configuration, $\mathbf{J}_\mathrm{R}$ is the solvent fluid flux in the reference configuration that is pulled back from the current configuration (i.e., $\mathbf{J}_\mathrm{R} = J\mathbf{F}^{-1}\mathbf{j}$), $\mathbf{N}_\mathrm{R}$ stands for the unit normal in the reference configuration, $\mathbf{B}_\mathrm{R}$ represents the body force in the reference configuration, and ψ_R denotes the Helmholtz free energy density per unit reference volume. By using the divergence theorem, Eq. (4.19) can be rewritten as

$$
\int_{\mathcal{B}_0} \left[\dot{\psi}_\mathrm{R} - (\nabla_\mathbf{X} \cdot \mathbf{P} + \mathbf{B}_\mathrm{R}) \cdot \dot{\boldsymbol{\varphi}} - \mathbf{P} : \dot{\mathbf{F}} + \mu \nabla_\mathbf{X} \cdot \mathbf{J}_\mathrm{R} + \mathbf{J}_\mathrm{R} \cdot \nabla_\mathbf{X}\mu \right] \mathrm{d}\Omega_\mathrm{R} \leq 0
\tag{4.20}
$$

Given the material description of Eq. (4.11) and Eq. (4.15), and using the fact that Eq. (4.20) must hold for every part of the EVA body, the local form of energy imbalance in the reference configuration is given by

$$\dot{\psi}_\mathrm{R} - \mathbf{P} : \dot{\mathbf{F}} - \mu \dot{C}_\mathrm{R} + \mathbf{J}_\mathrm{R} \cdot \nabla_\mathbf{X}\mu \leq 0 \tag{4.21}$$

By using Eq. (4.3), Eq. (4.9), Eq. (4.10), and Eq. (4.12a), the stress-power term can be written as

$$
\begin{aligned}
\mathbf{P} : \dot{\mathbf{F}} = J\left(\boldsymbol{\sigma} \cdot \mathbf{F}^{-\mathrm{T}}\right) : \dot{\mathbf{F}} &= J\boldsymbol{\sigma} : \left(\mathbf{L}^e + \mathbf{F}^e \cdot \mathbf{L}^s \cdot \mathbf{F}^{e-1}\right) \\
&= J\boldsymbol{\sigma} : \left(\dot{\mathbf{F}}^e \cdot \mathbf{F}^{e-1}\right) + J\boldsymbol{\sigma} : \left(\mathbf{F}^e \cdot \mathbf{L}^s \cdot \mathbf{F}^{e-1}\right) \\
&= J\boldsymbol{\sigma} : \left(\dot{\mathbf{F}}^e \cdot \mathbf{F}^{e-1}\right) + J\left(\mathbf{F}^{e\mathrm{T}} \cdot \boldsymbol{\sigma} \cdot \mathbf{F}^{e-\mathrm{T}}\right) : \mathbf{L}^s \\
&= \frac{1}{2}J\left(\mathbf{F}^{e-1} \cdot \boldsymbol{\sigma} \cdot \mathbf{F}^{e-\mathrm{T}}\right) : \dot{\mathbf{C}}^e + J\left(\mathbf{F}^{e\mathrm{T}} \cdot \boldsymbol{\sigma} \cdot \mathbf{F}^{e-\mathrm{T}}\right) : \mathbf{L}^s
\end{aligned}
\tag{4.22}
$$

For convenience, two stress measures are defined as

$$
\mathbf{S}^e = J\mathbf{F}^{e-1} \cdot \boldsymbol{\sigma} \cdot \mathbf{F}^{e-\mathrm{T}} \quad \text{and} \quad \mathbf{M}^e = J\mathbf{F}^{e\mathrm{T}} \cdot \boldsymbol{\sigma} \cdot \mathbf{F}^{e-\mathrm{T}}
\tag{4.23}
$$

so that

$$
\mathbf{P} : \dot{\mathbf{F}} = \frac{1}{2}\,\mathbf{S}^e : \dot{\mathbf{C}}^e + \mathbf{M}^e : \mathbf{L}^s
\tag{4.24}
$$

where $\mathbf{S}^e$ and $\mathbf{M}^e$ are the second Piola stress tensor and Mandel stress tensor, respectively. Given Eq. (4.4), Eq. (4.5) and Eq. (4.10), the stress-power Eq. (4.24) can be written as

$$
\begin{aligned}
\mathbf{P} : \dot{\mathbf{F}} &= \frac{1}{2}\,\mathbf{S}^e : \dot{\mathbf{C}}^e + \mathbf{M}^e : \left(\dot{\mathbf{F}}^s \cdot \mathbf{F}^{s-1}\right) \\
&= \frac{1}{2}\,\mathbf{S}^e : \dot{\mathbf{C}}^e + \frac{1}{3}J^{s-1}\dot{J}^s\mathbf{M}^e : \mathbf{1} \\
&= \frac{1}{2}\,\mathbf{S}^e : \dot{\mathbf{C}}^e - \bar{p}\dot{J}^s
\end{aligned}
\tag{4.25}
$$

in which $\bar{p}$ is the mean normal pressure defined as $\bar{p} = -\frac{1}{3}J^{s-1}\mathbf{M}^e : \mathbf{1}$. Hence, by substituting Eq. (4.25) into Eq. (4.21), the local form of free energy imbalance in the reference configuration is given by

$$
\dot{\psi}_{\mathrm{R}} - \frac{1}{2}\,\mathbf{S}^e : \dot{\mathbf{C}}^e + \bar{p}\dot{J}^s - \mu\dot{C}_{\mathrm{R}} + \mathbf{J}_{\mathrm{R}} \cdot \nabla_{\mathbf{X}}\mu \leq 0
\tag{4.26}
$$

Recalling Eq. (4.6), it results into $\dot{J}^s = v\dot{C}_{\mathrm{R}}$ that yields

$$
\dot{\psi}_{\mathrm{R}} - \frac{1}{2}\,\mathbf{S}^e : \dot{\mathbf{C}}^e - (\mu - v\bar{p})\dot{C}_{\mathrm{R}} + \mathbf{J}_{\mathrm{R}} \cdot \nabla_{\mathbf{X}}\mu \leq 0
\tag{4.27}
$$

The Helmholtz free energy ψ_{R} is assumed to depend on the deformation $\mathbf{C}^e$, solvent concentration C_{R}, and thus its rate is given by

$$
\dot{\psi}_{\mathrm{R}}\left(\mathbf{C}^e, C_{\mathrm{R}}\right) = \frac{\partial\psi_{\mathrm{R}}}{\partial\mathbf{C}^e} : \dot{\mathbf{C}}^e + \frac{\partial\psi_{\mathrm{R}}}{\partial C_{\mathrm{R}}}\dot{C}_{\mathrm{R}}
\tag{4.28}
$$

Eq. (4.27) yields,

$$\left(\frac{\partial \psi_{\mathrm{R}}}{\partial \mathbf{C}^e} - \frac{1}{2}\mathbf{S}^e\right) : \dot{\mathbf{C}}^e - \left[\frac{\partial \psi_{\mathrm{R}}}{\partial C_{\mathrm{R}}} - (\mu - v\bar{p})\right]\dot{C}_{\mathrm{R}} + \mathbf{J}_{\mathrm{R}} \cdot \nabla_{\mathbf{X}}\mu \leq 0 \quad (4.29)$$

Given that this inequality should hold for any values of $\mathbf{C}^e$ and C_{R}, the following thermodynamics restrictions can be obtained

$$\mathbf{S}^e = 2\frac{\partial \psi_{\mathrm{R}}\left(\mathbf{C}^e, C_{\mathrm{R}}\right)}{\partial \mathbf{C}^e} \quad \text{and} \quad \mu = \frac{\partial \psi_{\mathrm{R}}\left(\mathbf{C}^e, C_{\mathrm{R}}\right)}{\partial C_{\mathrm{R}}} + v\bar{p} \qquad (4.30)$$

Next, recalling Eq. (4.12a) and Eq. (4.23), the Piola stress tensor and Cauchy stress tensor can be written as

$$\boldsymbol{\sigma} = 2J^{-1}\mathbf{F}^e \cdot \frac{\partial \psi_{\mathrm{R}}\left(\mathbf{C}^e, C_{\mathrm{R}}\right)}{\partial \mathbf{C}^e} \cdot \mathbf{F}^{e\mathrm{T}} \qquad (4.31a)$$

$$\mathbf{P} = 2\mathbf{F}^e \cdot \frac{\partial \psi_{\mathrm{R}}\left(\mathbf{C}^e, C_{\mathrm{R}}\right)}{\partial \mathbf{C}^e} \cdot \mathbf{F}^{s-\mathrm{T}} \qquad (4.31b)$$

Notably, in view of Eq. (4.17), the solvent-transport inequality is followed

$$\mathbf{J}_{\mathrm{R}} \cdot \nabla_{\mathbf{X}}\mu = -Jm||\nabla_{\mathbf{x}}\mu||^2 \leq 0 \qquad (4.32)$$

4.1.4 Free energy definition

Following the well-established methods [236], the Helmholtz free energy ψ_{R} can be specialized as

$$\psi_{\mathrm{R}}\left(\mathbf{C}^e, C_{\mathrm{R}}\right) = \bar{\mu}_{\mathrm{R}}C_{\mathrm{R}} + \psi_{\mathrm{R,mech}}\left(\mathbf{C}^e, C_{\mathrm{R}}\right) + \psi_{\mathrm{R,mix}}\left(\mathbf{C}^e, C_{\mathrm{R}}\right) \qquad (4.33)$$

where $\bar{\mu}_{\mathrm{R}}$ is the reference chemical potential of the solvent, $\psi_{\mathrm{R,mech}}\left(\mathbf{C}^e, C_{\mathrm{R}}\right)$ denotes the mechanical contribution to the free energy, and $\psi_{\mathrm{R,mix}}\left(\mathbf{C}^e, C_{\mathrm{R}}\right)$ represents the energy contribution due to the mixing of the solvent with the EVA body.

The mixing free energy per unit reference volume of the polymeric body is defined as

$$\psi_{\mathrm{R,mix}}\left(\mathbf{C}^e, C_{\mathrm{R}}\right) = RTC_{\mathrm{R}}\ln\left(\frac{vC_{\mathrm{R}}}{1 + vC_{\mathrm{R}}}\right) + RT\chi\left(\frac{C_{\mathrm{R}}}{1 + vC_{\mathrm{R}}}\right) \qquad (4.34)$$

where χ is the dimensionless parameter. Recalling the definition of polymer volume fraction in Eq. (4.6), the mixing free energy in Eq. (4.34) can be written as

$$\psi_{R,mix}\left(\mathbf{C}^e, C_R\right) = RT\frac{1-\phi}{\upsilon\phi}\ln\left(1-\phi\right) + RT\frac{\chi\left(1-\phi\right)}{\upsilon} \qquad (4.35)$$

It should be pointed out that the enthalphy term in Eq. (4.34) is introduced for the mixing of polymer-solvent system in line with the Flory Huggins theory. According to [239], the Flory-Huggins parameter χ can be determined as

$$\chi = \chi_S + \chi_H = \chi_S + \frac{\upsilon}{RT}\left(\delta_s - \delta_p\right)^2 \qquad (4.36)$$

where χ_S and χ_H are the entropic and enthalphic contributions of the parameter, respectively, δ_p is the solubility parameter of polymer, and δ_s is the solubility parameter of the specific solvent, which is given by

$$\delta_s = \left(\delta_{s,d}^2 + \delta_{s,p}^2 + \delta_{s,h}^2\right)^{1/2} \qquad (4.37)$$

where $\delta_{s,d}$ is the apolar part, $\delta_{s,p}$ is the polar part, and $\delta_{s,h}$ is the hydrogen bonding part.

By coupling an energetic contribution with a Gaussian statistics based entropic term [240], the mechanical free energy $\psi_{R,mech}$ can be expressed as

$$\psi_{R,mech} = \frac{1}{2}G(\alpha)\left(\phi^{-2/3}\mathbf{C}^e : \mathbf{1} - 2\ln J - 3\right) + \frac{1}{2}K(\alpha)\left(\ln J^e\right)^2 \qquad (4.38)$$

where α is the crosslinking degree during the lamination process, and $G(\alpha)$ and $K(\alpha)$ represent the shear modulus and bulk modulus of EVA polymer network, respectively. To account for the crosslinking effects on polymer structure [241, 242, 243], the shear modulus is assumed to depend on the gelation, and defined as

$$G(\alpha) = (1-\alpha)G^0 + \alpha G^1 \qquad (4.39)$$

in which G^0 is the shear modulus of polymer network with no crosslinking ($\alpha = 0$), and G^1 is the shear modulus of polymer network with full

crosslinking ($\alpha = 1$). As a result of Eq. (4.39), the bulk modulus can be determined as

$$K(\alpha) = \frac{2G(\alpha)(1+\nu)}{3(1-2\nu)} \tag{4.40}$$

where ν denotes the Poisson's ratio of the polymer network.

Thus, using Eq. (4.35) and Eq. (4.38) in Eq. (4.33), the free energy function accounting for the combination of mixing, swelling and elastic stretching effects takes the form of

$$\psi_{\mathrm{R}}\left(\mathbf{C}^e, C_{\mathrm{R}}\right) = \bar{\mu}_{\mathrm{R}} C_{\mathrm{R}} + RT \frac{1-\phi}{\upsilon\phi} \ln\left(1-\phi\right) + RT \frac{\chi\left(1-\phi\right)}{\upsilon}$$
$$+ \frac{1}{2}G(\alpha)\left(\phi^{-2/3}\mathbf{C}^e : \mathbf{1} - 2\ln J - 3\right) + \frac{1}{2}K(\alpha)\left(\ln J^e\right)^2 \tag{4.41}$$

Recalling Eq. (4.31a), the Cauchy stress tensor is given by

$$\boldsymbol{\sigma} = J^{-1}\left[G(\alpha)\phi^{-2/3}\mathbf{B}^e - G(\alpha)\mathbf{1} + K(\alpha)\left(\ln J^e\right)\mathbf{1}\right] \tag{4.42}$$

Next, by the use of

$$\mathbf{B} = \mathbf{F} \cdot \mathbf{F}^T = \phi^{-2/3}\mathbf{B}^e \tag{4.43}$$

Eq. (4.42) reduces to

$$\boldsymbol{\sigma} = J^{-1}\left[G(\alpha)\left(\mathbf{B}-\mathbf{1}\right) + K(\alpha)\left(\ln J^e\right)\mathbf{1}\right] \tag{4.44}$$

Hence, according to Eq. (4.31a), the first Piola-Kirchhoff stress tensor is given by

$$\mathbf{P} = G(\alpha)\left(\mathbf{F} - \mathbf{F}^{-\mathrm{T}}\right) + K(\alpha)\left(\ln J^e\right)\mathbf{F}^{-\mathrm{T}} \tag{4.45}$$

Also, using Eq. (4.30)$_2$ and Eq. (4.41) and taking into account $J = J^e/\phi = J^e(1+\upsilon C_{\mathrm{R}})$, the chemical potential μ is given by

$$\mu = \bar{\mu}_{\mathrm{R}} + RT\left[\ln(1-\phi) + \phi + \chi\phi^2\right] + \frac{1}{3}\upsilon G(\alpha)\phi^{1/3}\mathbf{C}^e : \mathbf{1} - \upsilon G(\alpha)\phi + \upsilon\bar{p} \tag{4.46}$$

Recalling that

$$\bar{p} = -\frac{1}{3}J^{s-1}\mathbf{M}^e : \mathbf{1} = -\frac{1}{3}J^e\left(\mathbf{F}^{e\mathrm{T}}\cdot\boldsymbol{\sigma}\cdot\mathbf{F}^{e-\mathrm{T}}\right) : \mathbf{1} = -\frac{1}{3}J^e\boldsymbol{\sigma} : \mathbf{1} \tag{4.47}$$

and Eq. (4.42), Eq. (4.46) can be reduced to

$$\mu = \bar{\mu}_{\mathrm{R}} + RT\left[\ln(1-\phi) + \phi + \chi\phi^2\right] - \upsilon K(\alpha)(\ln J^e)\phi \tag{4.48}$$

136

4.1.5 Numerical implementation

Recalling Eq. (4.11) and Eq. (4.14), together with Eq. (4.16) and Eq. (4.18) that represents the boundary value problems, and in the absence of body forces, the corresponding weak forms can be obtained by multiplying Eq. (4.11) and Eq. (4.16) with the weighting functions $\delta\mathbf{u}$ and $\delta\mu$, respectively. Integration over the region Ω of the body yields the scalar-valued functions

$$\int_{\mathcal{B}} (\nabla_{\mathbf{x}} \cdot \boldsymbol{\sigma}) \cdot \delta\mathbf{u} \, d\Omega = 0 \tag{4.49a}$$

$$\int_{\mathcal{B}} \left(\frac{\dot{\phi}}{Jv\phi^2} - \nabla_{\mathbf{x}} \cdot \mathbf{j} \right) \delta\mu \, d\Omega = 0 \tag{4.49b}$$

By the use of divergence theorem and accounting for the boundary conditions Eq. (4.14) and Eq. (4.18), the weak forms can be reformulated as

$$\int_{\mathcal{B}} \left(\boldsymbol{\sigma} : \frac{\partial \delta\mathbf{u}}{\partial \mathbf{x}} \right) d\Omega = \int_{\partial\mathcal{B}_{\mathbf{t}}} (\delta\mathbf{u} \cdot \bar{\mathbf{t}}) \, d\partial\Omega \tag{4.50a}$$

$$\int_{\mathcal{B}} \left(\delta\mu \frac{\dot{\phi}}{Jv\phi^2} \right) d\Omega = -\int_{\mathcal{B}} \left(\frac{\partial \delta\mu}{\partial \mathbf{x}} \cdot \mathbf{j} \right) d\Omega - \int_{\partial\mathcal{B}_{\mathbf{j}}} (\delta\mu\bar{\jmath}) \, d\partial\Omega \tag{4.50b}$$

Through the standard Galerkin approach [235], the displacement fields $\mathbf{u}$, the chemical potential μ, and their corresponding weighting functions $\delta\mathbf{u}$ and $\delta\mu$ can be interpolated by the shape functions N, and expressed as

$$\mathbf{u} = \sum \mathbf{u}^I N^I \quad \text{and} \quad \delta\mathbf{u} = \sum \delta\mathbf{u}^I N^I \tag{4.51a}$$

$$\mu = \sum \mu^I N^I \quad \text{and} \quad \delta\mu = \sum \delta\mu^I N^I \tag{4.51b}$$

with I and J denote the node number of the element. By substituting Eq. (4.51) into Eq. (4.50), the following system of equations in the element level read

$$\int_{\mathcal{B}^e} \left(\boldsymbol{\sigma} \cdot \frac{\partial N^I}{\partial \mathbf{x}} \right) d\Omega = \int_{\partial\mathcal{B}_{\mathbf{t}}^e} (N^I \bar{\mathbf{t}}) \, d\partial\Omega \tag{4.52a}$$

$$\int_{\mathcal{B}^e} \left(N^I \frac{\dot{\phi}}{Jv\phi^2} \right) d\Omega = -\int_{\mathcal{B}^e} \left(\frac{\partial N^I}{\partial \mathbf{x}} \cdot \mathbf{j} \right) d\Omega - \int_{\partial\mathcal{B}_{\mathbf{j}}^e} (N^I \bar{\jmath}) \, d\partial\Omega \tag{4.52b}$$

137

This set of coupled equations can be solved by the iterative Newton-Raphson solution scheme by defining the following residuals for the displacement $\mathbf{u}$ and the chemical potential μ in the element level

$$\mathbf{R}_{\mathbf{u}}^I = -\int_{\mathcal{B}^e} \left(\boldsymbol{\sigma} \cdot \frac{\partial N^I}{\partial \mathbf{x}} \right) \mathrm{d}\Omega + \int_{\partial \mathcal{B}_{\mathbf{t}}^e} \left(N^I \bar{\mathbf{t}} \right) \mathrm{d}\partial\Omega \qquad (4.53\text{a})$$

$$R_{\mu}^I = \int_{\mathcal{B}^e} \left(N^I \frac{\dot{\phi}}{J v \phi^2} \right) \mathrm{d}\Omega + \int_{\mathcal{B}^e} \left(\frac{\partial N^I}{\partial \mathbf{x}} \cdot \mathbf{j} \right) \mathrm{d}\Omega + \int_{\partial \mathcal{B}_{\mathbf{j}}^e} \left(N^I \bar{j} \right) \mathrm{d}\partial\Omega$$
$$(4.53\text{b})$$

and given the definition of solvent flux in Eq. (4.17), the residual equations in the index form can be written as

$$R_{u_i}^I = -\int_{\mathcal{B}^e} \left(\sigma_{ij} \frac{\partial N^I}{\partial x_j} \right) \mathrm{d}\Omega + \int_{\partial \mathcal{B}_{\mathbf{t}}^e} \left(N^I \bar{t}_i \right) \mathrm{d}\partial\Omega \qquad (4.54\text{a})$$

$$R_{\mu}^I = \int_{\mathcal{B}^e} \left(N^I \frac{\dot{\phi}}{J v \phi^2} \right) \mathrm{d}\Omega - \int_{\mathcal{B}^e} \left(m \frac{\partial N^I}{\partial x_i} \frac{\partial \mu}{\partial x_i} \right) \mathrm{d}\Omega + \int_{\partial \mathcal{B}_{\mathbf{j}}^e} \left(N^I \bar{j} \right) \mathrm{d}\partial\Omega$$
$$(4.54\text{b})$$

The consistent linearization of the coupled polymer-solvent system in the matrix form is given by

$$\begin{bmatrix} \mathbf{K}_{\mathbf{uu}} & \mathbf{K}_{\mathbf{u}\mu} \\ \mathbf{K}_{\mu\mathbf{u}} & \mathbf{K}_{\mu\mu} \end{bmatrix} \begin{bmatrix} \Delta\mathbf{u} \\ \Delta\boldsymbol{\mu} \end{bmatrix} = - \begin{bmatrix} \mathbf{R}_{\mathbf{u}} \\ \mathbf{R}_{\mu} \end{bmatrix} \qquad (4.55)$$

with the components of tangents corresponding to the node number I and J defined as

$$\mathbf{K}_{\mathbf{uu}}^{IJ} = -\frac{\partial \mathbf{R}_{\mathbf{u}}^I}{\partial \mathbf{u}^J} \quad \text{and} \quad \mathbf{K}_{\mathbf{u}\mu}^{IJ} = -\frac{\partial \mathbf{R}_{\mathbf{u}}^I}{\partial \mu^J}$$
$$\mathbf{K}_{\mu\mathbf{u}}^{IJ} = -\frac{\partial R_{\mu}^I}{\partial \mathbf{u}^J} \quad \text{and} \quad K_{\mu\mu}^{IJ} = -\frac{\partial R_{\mu}^I}{\partial \mu^J} \qquad (4.56)$$

For convenience, the tangent component $\mathbf{K}_{\mathbf{uu}}^{IJ}$ in index form is de-

rived as

$$K_{u_i u_k}^{IJ} = -\frac{\partial R_{u_i}^I}{\partial u_k^J} = \int_{\mathcal{B}_0^e} \frac{\partial}{\partial u_k^J}\left(J\sigma_{ij}\frac{\partial N^I}{\partial x_j}\right) \, \mathrm{d}\Omega_\mathrm{R} - \int_{\partial\mathcal{B}_\mathbf{t}^e} N^I N^J \frac{\partial \bar{t}_i}{\partial u_k} \, \mathrm{d}\partial\Omega$$

$$= \int_{\mathcal{B}_0^e} \frac{\partial}{\partial u_k^J}\left(\tau_{ij}\frac{\partial N^I}{\partial X_a} F_{aj}^{-1}\right) \, \mathrm{d}\Omega_\mathrm{R} - \int_{\partial\mathcal{B}_\mathbf{t}^e} N^I N^J \frac{\partial \bar{t}_i}{\partial u_k} \, \mathrm{d}\partial\Omega$$

$$= \int_{\mathcal{B}_0^e} \frac{\partial N^I}{\partial X_a}\left(\frac{\partial F_{aj}^{-1}}{\partial F_{mn}}\tau_{ij} + F_{aj}^{-1}\frac{\partial \tau_{ij}}{\partial F_{mn}}\right)\frac{\partial F_{mn}}{\partial u_k^J} \, \mathrm{d}\Omega_\mathrm{R}$$
$$- \int_{\partial\mathcal{B}_\mathbf{t}^e} N^I N^J \frac{\partial \bar{t}_i}{\partial u_k} \, \mathrm{d}\partial\Omega$$

$$= \int_{\mathcal{B}_0^e} \frac{\partial N^I}{\partial X_a}\left(-F_{nj}^{-1}F_{am}^{-1}\tau_{ij} + F_{aj}^{-1}\frac{\partial \tau_{ij}}{\partial F_{mn}}\right)\frac{\partial N^J}{\partial X_n}\delta_{mk} \, \mathrm{d}\Omega_\mathrm{R}$$
$$- \int_{\partial\mathcal{B}_\mathbf{t}^e} N^I N^J \frac{\partial \bar{t}_i}{\partial u_k} \, \mathrm{d}\partial\Omega$$

$$= \int_{\mathcal{B}_0^e} \frac{\partial N^I}{\partial X_a}\left(-F_{ak}^{-1}F_{nj}^{-1}\tau_{ij} + F_{aj}^{-1}\frac{\partial \tau_{ij}}{\partial F_{kn}}\right)\frac{\partial N^J}{\partial X_n} \, \mathrm{d}\Omega_\mathrm{R}$$
$$- \int_{\partial\mathcal{B}_\mathbf{t}^e} N^I N^J \frac{\partial \bar{t}_i}{\partial u_k} \, \mathrm{d}\partial\Omega$$

$$= \int_{\mathcal{B}_0^e} \frac{\partial N^I}{\partial x_r}F_{ra}\left(-F_{ak}^{-1}F_{nj}^{-1}\tau_{ij} + F_{aj}^{-1}\frac{\partial \tau_{ij}}{\partial F_{kn}}\right)F_{ln}\frac{\partial N^J}{\partial x_l} \, \mathrm{d}\Omega_\mathrm{R}$$
$$- \int_{\partial\mathcal{B}_\mathbf{t}^e} N^I N^J \frac{\partial \bar{t}_i}{\partial u_k} \, \mathrm{d}\partial\Omega$$

$$= \int_{\mathcal{B}_0^e} \frac{\partial N^I}{\partial x_r}\left(-\delta_{rk}\tau_{il} + F_{ln}\frac{\partial \tau_{ir}}{\partial F_{kn}}\right)\frac{\partial N^J}{\partial x_l} \, \mathrm{d}\Omega_\mathrm{R} - \int_{\partial\mathcal{B}_\mathbf{t}^e} N^I N^J \frac{\partial \bar{t}_i}{\partial u_k} \, \mathrm{d}\partial\Omega$$

$$= \int_{\mathcal{B}^e} \frac{\partial N^I}{\partial x_r}\left(-J^{-1}\delta_{rk}\tau_{il} + J^{-1}F_{ln}\frac{\partial \tau_{ir}}{\partial F_{kn}}\right)\frac{\partial N^J}{\partial x_l} \, \mathrm{d}\Omega$$
$$- \int_{\partial\mathcal{B}_\mathbf{t}^e} N^I N^J \frac{\partial \bar{t}_i}{\partial u_k} \, \mathrm{d}\partial\Omega$$

$$= \int_{\mathcal{B}^e} \frac{\partial N^I}{\partial x_r}\left(-J^{-1}\delta_{rk}\tau_{il} + J^{-1}F_{ln}F_{rm}\frac{\partial P_{im}}{\partial F_{kn}} + J^{-1}\delta_{rk}\tau_{il}\right)\frac{\partial N^J}{\partial x_l} \, \mathrm{d}\Omega$$
$$- \int_{\partial\mathcal{B}_\mathbf{t}^e} N^I N^J \frac{\partial \bar{t}_i}{\partial u_k} \, \mathrm{d}\partial\Omega$$

$$= \int_{\mathcal{B}^e} \frac{\partial N^I}{\partial x_r}\left(J^{-1}F_{ln}F_{rm}\frac{\partial P_{im}}{\partial F_{kn}}\right)\frac{\partial N^J}{\partial x_l} \, \mathrm{d}\Omega - \int_{\partial\mathcal{B}_\mathbf{t}^e} N^I N^J \frac{\partial \bar{t}_i}{\partial u_k} \, \mathrm{d}\partial\Omega$$

139

$$\text{(4.57)}$$

with

$$\frac{\partial P_{im}}{\partial F_{kn}} = \frac{\partial}{\partial F_{kn}} \left[G(\alpha) \left(F_{im} - F_{mi}^{-1} \right) + K(\alpha)(\ln J^e) F_{mi}^{-1} \right]$$

$$= G(\alpha)\delta_{ik}\delta_{mn} - G(\alpha)\frac{\partial F_{mi}^{-1}}{\partial F_{kn}}$$

$$+ K(\alpha)F_{mi}^{-1}\frac{\partial(\ln J^e)}{\partial F_{kn}} + K(\alpha)(\ln J^e)\frac{\partial F_{mi}^{-1}}{\partial F_{kn}}$$

$$= G(\alpha)\delta_{ik}\delta_{mn} + G(\alpha)F_{ni}^{-1}F_{mk}^{-1}$$

$$+ K(\alpha)F_{mi}^{-1}\frac{\partial(\ln J^e)}{\partial F_{kn}} - K(\alpha)(\ln J^e)F_{ni}^{-1}F_{mk}^{-1} \tag{4.58}$$

$$= G(\alpha)\delta_{ik}\delta_{mn} + G(\alpha)F_{ni}^{-1}F_{mk}^{-1}$$

$$+ K(\alpha)F_{mi}^{-1}\frac{\partial(\ln \phi J)}{\partial F_{kn}} - K(\alpha)(\ln J^e)F_{ni}^{-1}F_{mk}^{-1}$$

$$= G(\alpha)\left(\delta_{ik}\delta_{mn} + F_{ni}^{-1}F_{mk}^{-1}\right)$$

$$+ K(\alpha)\left[F_{mi}^{-1}F_{nk}^{-1} - (\ln J^e)F_{ni}^{-1}F_{mk}^{-1}\right]$$

Next, recalling Eq. (4.44) and Eq. (4.48), the tangent $\mathbf{K}_{u\mu}^{IJ}$ in index form is given by

$$K_{u_i\mu}^{IJ} = -\frac{\partial R_{u_i}^I}{\partial \mu^J} = \int_{\mathcal{B}^e} \frac{\partial N^I}{\partial x_j} \left(\frac{\sigma_{ij}}{\partial \phi} \frac{\partial \phi}{\partial \mu} \right) N^J \, d\Omega$$

$$= \int_{\mathcal{B}^e} \frac{\partial N^I}{\partial x_j} \frac{K(\alpha)}{J\phi} \delta_{ij} \left(\frac{\partial \mu}{\partial \phi} \right)^{-1} N^J \, d\Omega \tag{4.59}$$

Then the tangent $\mathbf{K}_{\mu\mathbf{u}}^{IJ}$ in index form can be derived as

$$
\begin{aligned}
K_{\mu u_k}^{IJ} &= -\frac{\partial R_{u_i}^I}{\partial u_k^J} = \frac{\partial}{\partial u_k^J}\left(\int_{\mathcal{B}^e} m\frac{\partial N^I}{\partial x_i}\frac{\partial \mu}{\partial x_i}\,\mathrm{d}\Omega\right) \\
&= \frac{\partial}{\partial u_k^J}\left(\int_{\mathcal{B}_0^e} mJ\frac{\partial N^I}{\partial X_a}F_{ai}^{-1}\frac{\partial \mu}{\partial X_b}F_{bi}^{-1}\,\mathrm{d}\Omega_{\mathrm{R}}\right) \\
&= \int_{\mathcal{B}_0^e} m\frac{\partial N^I}{\partial X_a}\frac{\partial \mu}{\partial X_b}\frac{\partial\left(JF_{ai}^{-1}F_{bi}^{-1}\right)}{\partial u_k^J}\,\mathrm{d}\Omega_{\mathrm{R}} \\
&= \int_{\mathcal{B}_0^e} m\frac{\partial N^I}{\partial X_a}\frac{\partial \mu}{\partial X_b}\frac{\partial\left(JF_{ai}^{-1}F_{bi}^{-1}\right)}{\partial F_{mn}}\frac{\partial F_{mn}}{\partial u_k^J}\,\mathrm{d}\Omega_{\mathrm{R}} \\
&= \int_{\mathcal{B}_0^e} m\frac{\partial N^I}{\partial X_a}\frac{\partial \mu}{\partial X_b}\left(JF_{nm}^{-1}F_{ai}^{-1}F_{bi}^{-1}\right)\frac{\partial F_{mn}}{\partial u_k^J}\,\mathrm{d}\Omega_{\mathrm{R}} \\
&\quad -\int_{\mathcal{B}_0^e} m\frac{\partial N^I}{\partial X_a}\frac{\partial \mu}{\partial X_b}\left(JF_{am}^{-1}F_{ni}^{-1}F_{bi}^{-1}+JF_{ai}^{-1}F_{bm}^{-1}F_{ni}^{-1}\right)\frac{\partial F_{mn}}{\partial u_k^J}\,\mathrm{d}\Omega_{\mathrm{R}} \\
&= \int_{\mathcal{B}^e} m\frac{\partial N^I}{\partial X_a}\frac{\partial \mu}{\partial X_b}\left(F_{nm}^{-1}F_{ai}^{-1}F_{bi}^{-1}\right)\frac{\partial N^J}{\partial X_n}\delta_{mk}\,\mathrm{d}\Omega \\
&\quad -\int_{\mathcal{B}^e} m\frac{\partial N^I}{\partial X_a}\frac{\partial \mu}{\partial X_b}\left(F_{am}^{-1}F_{ni}^{-1}F_{bi}^{-1}+F_{ai}^{-1}F_{bm}^{-1}F_{ni}^{-1}\right)\frac{\partial N^J}{\partial X_n}\delta_{mk}\,\mathrm{d}\Omega \\
&= \int_{\mathcal{B}^e} m\frac{\partial N^I}{\partial X_a}\frac{\partial \mu}{\partial X_b}\left(F_{nk}^{-1}F_{ai}^{-1}F_{bi}^{-1}\right)\frac{\partial N^J}{\partial X_n}\,\mathrm{d}\Omega \\
&\quad -\int_{\mathcal{B}^e} m\frac{\partial N^I}{\partial X_a}\frac{\partial \mu}{\partial X_b}\left(F_{ak}^{-1}F_{ni}^{-1}F_{bi}^{-1}+F_{ai}^{-1}F_{bk}^{-1}F_{ni}^{-1}\right)\frac{\partial N^J}{\partial X_n}\,\mathrm{d}\Omega \\
&= \int_{\mathcal{B}^e} m\left(\frac{\partial N^I}{\partial x_i}\frac{\partial \mu}{\partial x_i}\frac{\partial N^J}{\partial x_k}-\frac{\partial N^I}{\partial x_k}\frac{\partial \mu}{\partial x_i}\frac{\partial N^J}{\partial x_i}-\frac{\partial N^I}{\partial x_i}\frac{\partial \mu}{\partial x_k}\frac{\partial N^J}{\partial x_i}\right)\,\mathrm{d}\Omega \\
&= \int_{\mathcal{B}^e} m\frac{\partial N^I}{\partial x_i}\left(\delta_{jk}\frac{\partial \mu}{\partial x_i}-\delta_{ik}\frac{\partial \mu}{\partial x_j}-\delta_{ij}\frac{\partial \mu}{\partial x_k}\right)\frac{\partial N^J}{\partial x_j}\,\mathrm{d}\Omega
\end{aligned}
$$

(4.60)

Similarly, the last tangent $K_{\mu\mu}^{IJ}$ is given by

$$
\begin{aligned}
K_{\mu\mu}^{IJ} &= -\frac{\partial R_\mu^I}{\partial \mu^J}\\
&= \frac{\partial}{\partial \mu^J}\left[\int_{\mathcal{B}^e}\left(-N^I\frac{\dot{\phi}}{Jv\phi^2}+m\frac{\partial N^I}{\partial x_i}\frac{\partial \mu}{\partial x_i}\right)\,\mathrm{d}\Omega - \int_{\partial\mathcal{B}_j^e}\left(N^I\bar{j}\right)\,\mathrm{d}\partial\Omega\right]\\
&= \int_{\mathcal{B}^e}-\frac{N^I}{Jv}\frac{\partial}{\partial \mu^J}\left(\frac{\dot{\phi}}{\phi^2}\right)\,\mathrm{d}\Omega + \int_{\mathcal{B}^e}\frac{\partial N^I}{\partial x_i}\frac{\partial}{\partial \mu^J}\left(m\frac{\partial \mu}{\partial x_i}\right)\,\mathrm{d}\Omega\\
&\quad - \int_{\partial\mathcal{B}_j^e}N^I\frac{\partial\bar{j}}{\partial \mu^J}\,\mathrm{d}\partial\Omega\\
&= \int_{\mathcal{B}^e}-\frac{N^I}{Jv}\left(-2\frac{\dot{\phi}}{\phi^3}\frac{\partial \phi}{\partial \mu^J}+\frac{1}{\phi^2}\frac{\partial\dot{\phi}}{\partial \mu^J}\right)\,\mathrm{d}\Omega + \int_{\mathcal{B}^e}\frac{\partial N^I}{\partial x_i}\frac{\partial m}{\partial \mu^J}\frac{\partial \mu}{\partial x_i}\,\mathrm{d}\Omega\\
&\quad + \int_{\mathcal{B}^e}m\frac{\partial N^I}{\partial x_i}\frac{\partial N^J}{\partial x_i}\,\mathrm{d}\Omega - \int_{\partial\mathcal{B}_j^e}\left(N^I N^J\frac{\partial\bar{j}}{\partial \mu}\right)\,\mathrm{d}\partial\Omega\\
&= \int_{\mathcal{B}^e}-\frac{N^I N^J}{Jv\phi^2}\left(-2\frac{\dot{\phi}}{\phi}\frac{\partial \phi}{\partial \mu}+\frac{\partial\dot{\phi}}{\partial \mu}\right)\,\mathrm{d}\Omega + \int_{\mathcal{B}^e}\frac{\partial N^I}{\partial x_i}N^J\frac{\partial m}{\partial \mu}\frac{\partial \mu}{\partial x_i}\,\mathrm{d}\Omega\\
&\quad + \int_{\mathcal{B}^e}m\frac{\partial N^I}{\partial x_i}\frac{\partial N^J}{\partial x_i}\,\mathrm{d}\Omega - \int_{\partial\mathcal{B}_j^e}\left(N^I N^J\frac{\partial\bar{j}}{\partial \mu}\right)\,\mathrm{d}\partial\Omega\\
&= \int_{\mathcal{B}^e}-\frac{N^I N^J}{Jv\phi^2}\left[-2\frac{\dot{\phi}}{\phi}\left(\frac{\partial \mu}{\partial \phi}\right)^{-1}+\frac{\partial\dot{\phi}}{\partial \mu}\right]\,\mathrm{d}\Omega\\
&\quad + \int_{\mathcal{B}^e}\frac{\partial N^I}{\partial x_i}N^J\frac{\partial m}{\partial \phi}\left(\frac{\partial \mu}{\partial \phi}\right)^{-1}\frac{\partial \mu}{\partial x_i}\,\mathrm{d}\Omega\\
&\quad + \int_{\mathcal{B}^e}m\frac{\partial N^I}{\partial x_i}\frac{\partial N^J}{\partial x_i}\,\mathrm{d}\Omega - \int_{\partial\mathcal{B}_j^e}\left(N^I N^J\frac{\partial\bar{j}}{\partial \mu}\right)\,\mathrm{d}\partial\Omega
\end{aligned}
$$

$$(4.61)$$

Notably, by the use of Eq. (4.48) and $J^e = J\phi$, the polymer volume fraction ϕ in the numerical solution is determined explicitly from the following nonlinear equation

$$
\frac{\bar{\mu}_{\mathrm{R}}-\mu}{RT}+\ln(1-\phi)+\phi+\chi\phi^2-\frac{vK(\alpha)}{RT}(\ln J\phi)\phi = 0 \qquad (4.62)
$$

142

Besides, its rate $\dot{\phi}$ is calculated through the difference approximation

$$\dot{\phi} = \frac{\phi_{n+1} - \phi_n}{\Delta t} \tag{4.63}$$

where ϕ_{n+1} and ϕ_n denote the values of polymer volume fraction at the current and previous time increments, respectively. The computational framework is implemented into the finite element program Abaqus, and convergence is accepted if both the largest residual and correction to the solution are less than the prescribed tolerance values at each time increment.

4.1.6 Numerical examples

In this section, the coupled chemo-mechanical responses of EVA copolymer with application to the recycling of end-of-life photovoltaic modules using the organic solvent method are simulated to illustrate the capability of the computational framework. The first case is the numerical simulation of the free-swelling experiments of cylindrical EVA samples with different types of solvents (Toluene, Tetrahydrofuran, and Octane), and subsequent comparison with available testing data is addressed for validation purposes. It should be pointed out that these solvents have been chosen because they cannot dissolve the EVA copolymer at the particular temperatures but cause swelling when coming into contact [244]. Then the second case demonstrates the capability of this computational framework to model the effects of initial crosslinking and mechanical constraints on the time history evolution of complex coupled response. Finally, since the cracking of silicon solar cells due to EVA swelling is the critical problem in PV recyling using the solvent method [72], the complete PV laminate is modeled in the 3D setting to study the deformation and diffusion mechanisms, and the mechanical and swelling responses under different conditions are analyzed in detail. Based on the well-established experimental evidence in the literature, the basic model parameters associated with the properties of EVA copolymer are listed in Table 3. The initial chemical potential of dry EVA polymer is defined by Eq. (4.48) with the reference chemical potential of the solvent $\bar{\mu}_R$ equal to

Table 3: Model parameters of EVA copolymer for the coupled modeling.

Parameter	Value
G^0 (298 K)	5 MPa [245]
G^1 (298 K)	20 MPa
ν	0.495 [245]
χ_S	0.34 [239]
δ_p	17.5 MPa$^{1/2}$ [239]
γ	100
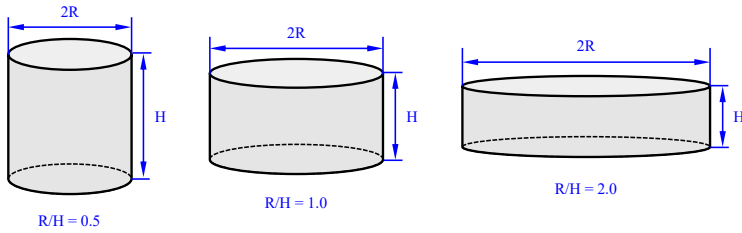
Figure 75: Cylindrical EVA samples with three different aspect ratios (0.5, 1.0, and 2.0) between radius and height.

0.0 J/mol, and the default initial crosslinking degree is set to 0.0 unless specified in the following. It should be pointed out that the value of polymer volume fraction ϕ at time 0.0 is set to 0.999 rather than 1.0 to avoid numerical difficulties. For convenience, the swelling degree is specified as the ratio between the solvent volume and total volume of both solvent and EVA polymer [244].

The first numerical example is the free swelling simulation of cylindrical EVA samples. In this example, the transient free swelling of cylindrical EVA samples with different types of solvents is simulated according to the experiments [244]. To study the swelling kinetics of EVA polymer in different solvents, the apparatus consisting of two round reservoirs connecting to each other with a graduated tube was designed to perform the experiments as reported in [244]. Before testing, the solvent level in the tube was recorded when the apparatus was vertical and

Table 4: Solvent properties for the swelling simulation [244, 246].

	Toluene	Tetrahydrofuran	Octane
υ (m^3/mol)	1.068×10^{-4}	7.79×10^{-5}	1.635×10^{-4}
D (m^2/s)	4.04×10^{-11}	4.0×10^{-11}	4.0×10^{-11}
$\delta_{s,d}$ (MPa$^{1/2}$)	18.0	16.8	15.6
$\delta_{s,p}$ (MPa$^{1/2}$)	1.4	5.7	0.0
$\delta_{s,h}$ (MPa$^{1/2}$)	2.0	8.0	0.0

there was no contact between solvent and the dry EVA polymer samples. On turning the apparatus to the horizontal state, the solvent penetrated into the specimen and the kinematic measurements started. After certain time periods, the apparatus was turned back to the vertical state and the solvent level in the graduated tube was recorded again. In this way, the volume decrease of solvent level is equal to the volume increase of the polymer specimen. The initial volume of the specimen is 0.15 cm^3, but the shape is not mentioned in [244]. To investigate this influence, cylindrical specimens with three different aspect ratios between radius and height (0.5, 1.0, and 2.0) are chosen in the following simulation, see Fig. 75. The isothermal condition with the constant temperature of 298 K is assumed in this work. Three different solvents including Toluene, Tetrahydrofuran, and Octane are considered, and their basic properties are reported in Table 4. Due to symmetry, only a half of axisymmetric cylindrical slice is modeled to save computational cost. Zero chemical potential boundary condition is prescribed on the outer surfaces of specimen.

The contour plots of polymer volume fraction ϕ for the three cylindrical models with different ratios between the radius and height obtained from simulation after 15 min, 30 min, and 45 min in the solvent of Tetrahydrofuran are shown in Fig. 76. Note that as the solvent penetrates into the EVA copolymer, the volumes of models change with time for all the three different shapes. The EVA models gradually increases their volumes because of the entry of solvent molecules and subsequent combination with the polymer molecules by physical forces. This swelling
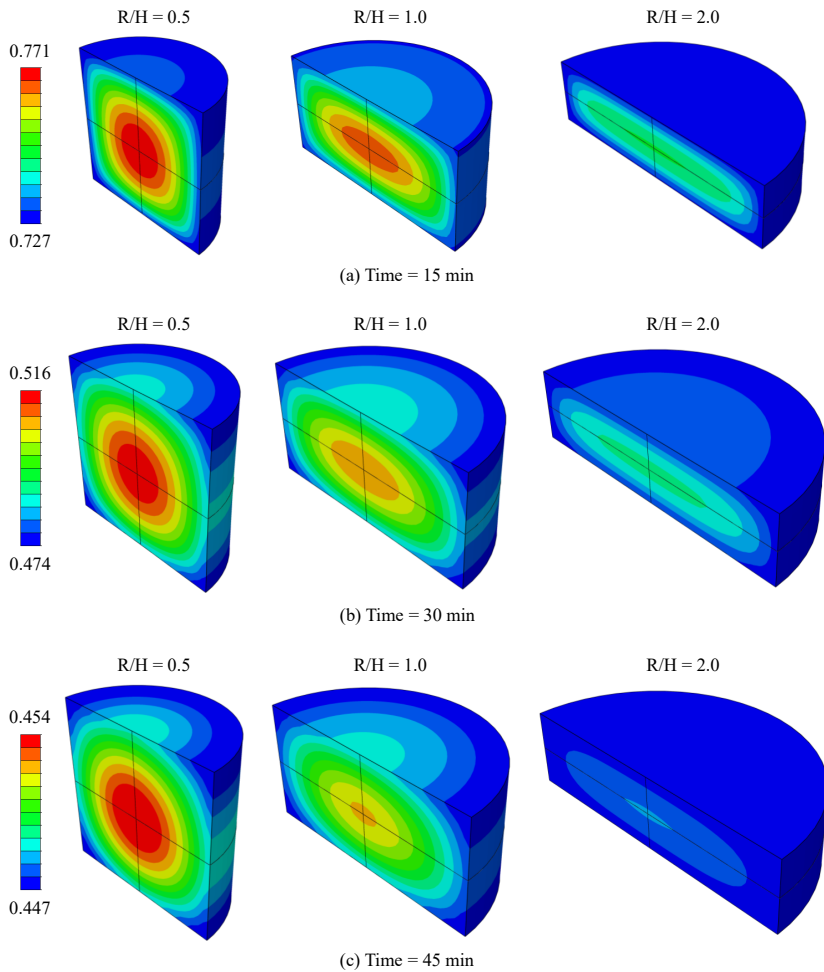
Figure 76: Comparison of the contour plots of the polymer volume fraction in Tetrahydrofuran after (a) 15 min, (b) 30 min, and (c) 45 min for the three different models with the ratio between radius and height equal to 0.5, 1.0, and 2.0.
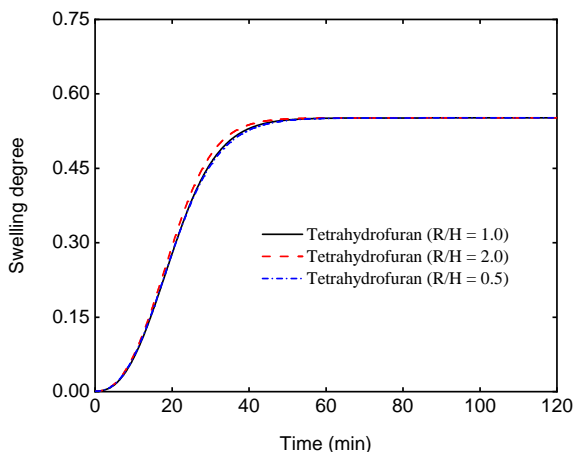
Figure 77: The time history plots of swelling degree in Tetrahydrofuran for the three different models with the ratio between radius and height equal to 1.0, 0.5, and 2.0.

phenomena can be ascribed to the higher interaction energy between the polymer molecules than that for their interaction with solvent molecules at this temperature condition of 298 K. Besides, it should be pointed out that the volume change process is not only the absorption and diffusion of solvent molecules but also the change in polymer structure of the EVA. As mentioned in [244], on the one hand, as solvent molecules penetrate into the interstructural space between polymer molecules, the supermolecular polymer structures are formed, which results into the interstructural swelling. On the other hand, the solvent molecules will also penetrate into the internal polymer molecule structures, leading to the so-called intrastructural swelling. From the sectional view of the cylindrical models in Fig. 76, it is also clearly observed that the polymer volume fraction ϕ increases from the boundary to the inside portion of EVA, which represents the solvent diffusion as well as the polymer swelling process. To better quantify the effects of ratio between radius and height, the time history responses of swelling degree for three different mod-
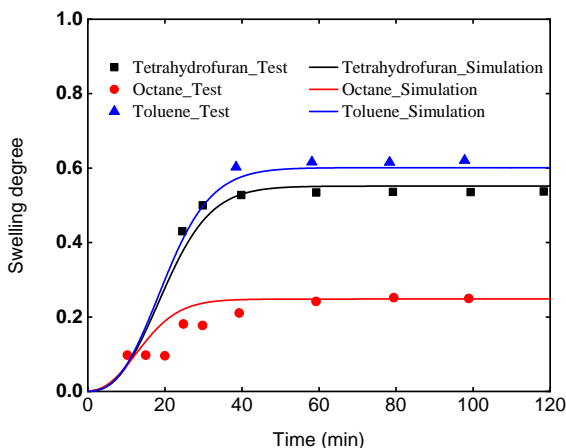
Figure 78: Comparison of the time history curves of swelling degree in the three different solvents between experiments and numerical simulation.

els in the solvent of Tetrahydrofuran are shown in Fig. 77. Generally, the time history curves of swelling degree for the three different models agree with each other very well, which indicates that the ratio between the radius and height has no significant influence on the swelling behavior of the EVA copolymer in solvents under the isothermal condition. In the remaining part of this section, only the cylindrical model with the ration between the radius and height equal to 1.0 will be considered.

The swelling phenomena in the EVA polymer-solvent system is mainly caused by the interactions due to the dispersive forces, but the solvent properties such as the molar volume and viscosity also greatly influence the kinetics. In the following, three solvents (Toluene, Tetrahydrofuran, and Octane) with different basic properties have been chosen in the numerical simulation of swelling tests of EVA samples with the cylindrical shape at the constant temperature of 298 K reported in [244]. The comparison of time history curves of swelling degree in the three different solvents between simulation and experiments are shown in Fig. 78. The
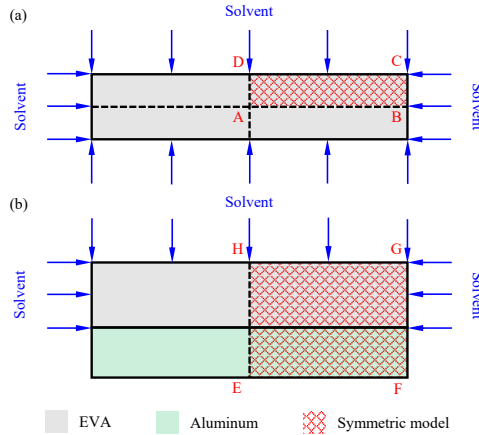
Figure 79: Schematic for the transient swelling of (a) pure EVA sample and (b) EVA/aluminum laminate.

swelling degree changed over time, and the volume change lasted until the equilibrium state when the swelling degree became constant. Also note that the same polymer reaches the different equilibrium swelling degrees in the three solvents due to the different molar volumes and viscosity parameters. Compared with the swelling behaviour of polymer samples in Tetrahydrofuran and Toluene, the corresponding equilibrium swelling degree in Octane is significantly lower because of its lower solubility parameter. As for the cases in Toluene and Tetrahydrofuran, not much difference of equilibrium swelling degree can be observed as a result of approximately equal Flory-Huggins parameter determined by the corresponding solvent properties. The swelling kinetics for EVA copolymer in the three solvents of different nature with respect to their interactions can be well predicted by the modeling method, and as shown in Fig. 78, the swelling time history curves obtained from simulation agree with the experimental data very well.

In the second numerical example, the influences of crosslinking treatment and mechanical constraints on the coupled responses of EVA polymer in PV recycling using the organic solvent method have been in-

vestigated in detail to further demonstrate the capability of the modeling framework. As mentioned in [247], the crosslinking process of EVA copolymer is indeed the formation of 3D polymer network that increases the stability of the elastomeric material. In this process, the hydrogen from terminal methyl groups of the EVA chains is abstracted by the cleaved radical species, and at the same time, the active radical site is transferred to the methyl group of EVA, which then creates the bond between the EVA chains through reaction. In PV lamination, the crosslinking reaction is basically the result of thermolysis at the temperature condition around 150 °C [248]. It has shown by chemical assessment in [249] that the crosslinking degree is strongly affected by both the temperature condition and lamination time during the manufacturing process. The initial crosslinking degree is considered here as a key parameter to the coupled chemo-mechanical response of the polymer-solvent system in PV recycling. In line with the tests reported in [72], both the pure EVA samples and samples bonded with aluminum plate have been taken into account in the simulation to study the mixing effects. As shown in Fig. 79, due to the symmetry, only a quarter of the pure EVA sample and a half of the EVA/laminate are modeled in the plane strain condition. The width and thickness of the EVA sample are 15 mm and 3 mm, respectively. For the elastic modeling of aluminum substrate using the Kirchhoff–Saint-Venant constitutive model, the Young's modulus and Poisson ratio are set to 69 GPa and 0.33, respectively, which are taken from [51]. In the first case of pure EVA sample, symmetric boundary conditions are imposed on the edges AB and AD, while in the second case of EVA/aluminum laminate, the symmetric boundary condition is applied to the edge EH. The solvent can penetrate into the two symmetric models from the edges BC, CD, GH, and part of edge FG that belongs to EVA, and the other edges are prescribed to zero-flux chemical boundary conditions.

The contour plots of polymer volume fraction ϕ of the pure EVA samples with the crosslinking degree $\alpha = 0.0$ and $\alpha = 1.0$ at 15 min, 30 min, and 45 min are shown in Fig. 80. It can be clearly seen the rectangular pure EVA samples in the plane strain condition gradually increase its
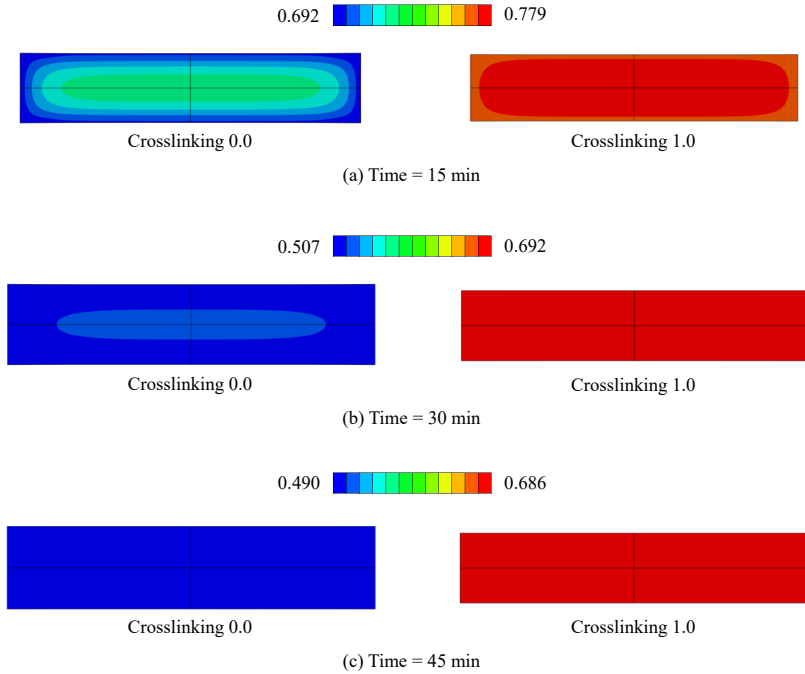
Figure 80: Comparison of the contour plots of the polymer volume fraction at (a) 15 min, (b) 30 min, and (c) 45 min between the pure EVA samples with crosslinking degree $\alpha = 0.0$ and $\alpha = 1.0$.
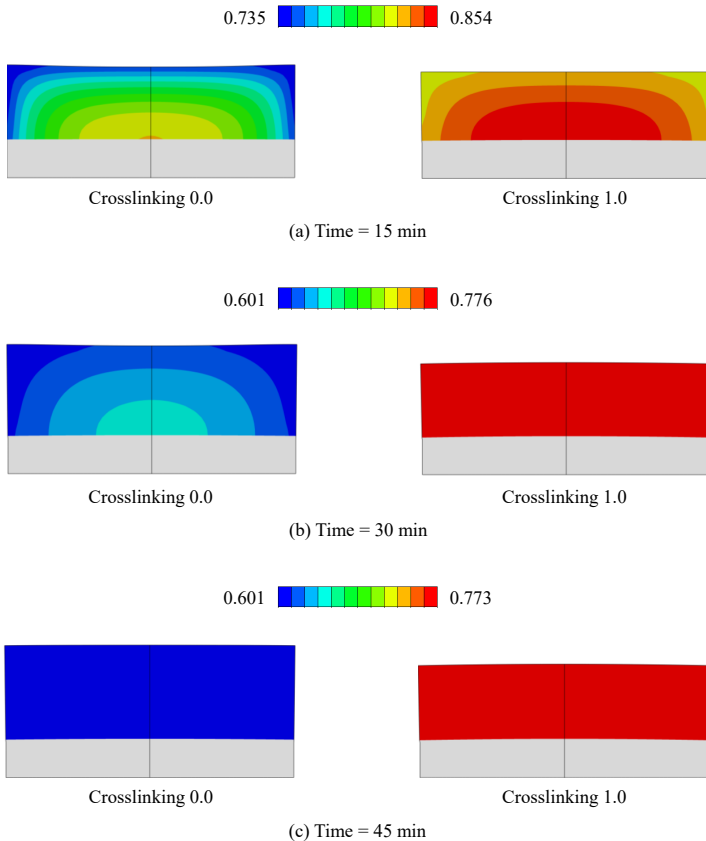
Figure 81: Comparison of the contour plots of the polymer volume fraction at (a) 15 min, (b) 30 min, and (c) 45 min between the EVA/aluminum laminate samples with crosslinking degree $\alpha = 0.0$ and $\alpha = 1.0$ (aluminum in grey color).

volume over time due to the penetration of solvent.The polymer volume fraction ϕ is higher in the area close to the edges than that in the middle areas as a result of the solvent diffusion. Also, the polymer volume fraction distribution in the EVA sample becomes lower with time for both the initial crosslinking degree $\alpha = 0.0$ and $\alpha = 1.0$. On the other hand, the contour plots of polymer volume fraction ϕ of the EVA/aluminum laminate samples with the crosslinking degree $\alpha = 0.0$ and $\alpha = 1.0$ at 15 min, 30 min, and 45 min are shown in Fig. 81. As in the previous case study of pure EVA samples, the volume of EVA in the laminate structure becomes bigger over time for both two crosslinking degrees. However, the EVA body can only change along the thickness direction in this case as the bottom edges are constrained by the aluminum substrate along the horizontal direction. Note that the difference between the predictions of EVA with two crosslinking degree is intensified compared with the previous case, which can be ascribed to the coupled diffusion-deformation in the presence of mechanical constraint from the aluminum substrate. Besides, it can also be seen from Fig. 81 that the EVA part of laminate sample with no initial crosslinking cannot maintain the rectangular shape with time because of the enhanced solvent flux from the two upper corners and faster diffusion process than that with the initial crosslinking $\alpha = 1.0$. The quantitative comparison of swelling degree between the pure EVA sample and EVA/aluminum laminate with two different initial crosslinking degree is shown in Fig. 82. The equilibrium swelling degree for both the pure EVA and EVA/aluminum laminate with no initial crosslinking is larger than that with initial crosslinking $\alpha = 1.0$ - this is because crosslinking can suppress the swelling behaviour of EVA due to part of its dissolution. It is also worth noting that the mechanical constraint directly influence the magnitude of equilibrium swelling degree, reducing from 0.5 to 0.385 with the initial crosslinking $\alpha = 0.0$ and from 0.31 to 0.225 with the initial crosslinking $\alpha = 1.0$.

The third numerical example addresses the numerical simulation of the recycling of complete PV laminate using the organic solvent method under gentle temperature condition. As pointed out in [72], the key problem in this recycling method is the cracking of PV silicon cells due to
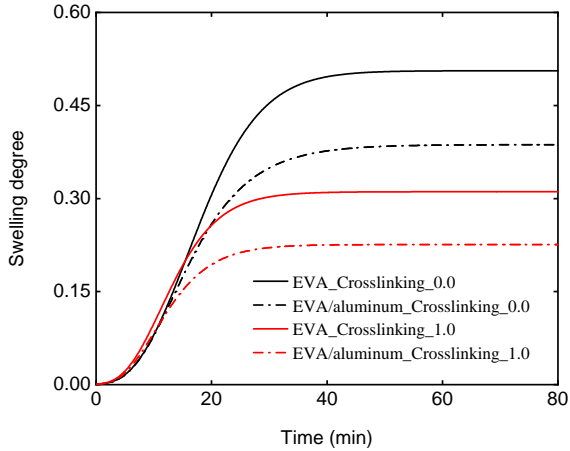
Figure 82: Comparison of the time history curves of swelling degree between the pure EVA samples and EVA/aluminum laminates with crosslinking degree $\alpha = 0.0$ and $\alpha = 1.0$.
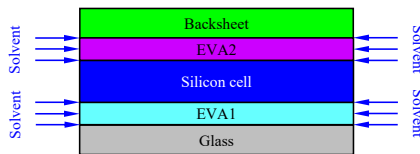
Figure 83: The sectional sketch of the PV module in the recycling process.
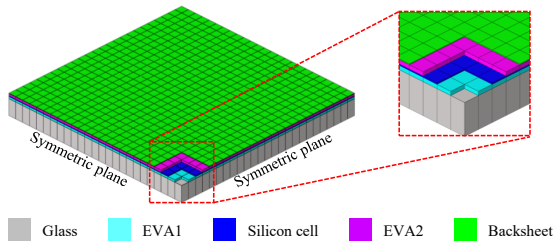
Figure 84: Finite element model of a quarter of the complete PV laminate.

Table 5: Mechanical properties for PV modules [86, 52].

	E (GPa)	Density (kg/m³)	ν
Backsheet	2.8	1200	0.3
Silicon	130	2329	0.2
Glass	73	2500	0.24

the swelling of EVA layers induced by solvent penetration. The characteristics of recycled intact silicon cells are of great importance to the high-value reuse and reduction of production cost. Hence, it is crucial to develop a reliable modeling framework to understand the coupled responses of EVA in different solvents during the PV recycling process. The sectional sketch of the PV laminate in the recycling process is shown in Fig. 83. A quarter of the complete PV laminate is modeled in the 3D setting to study the EVA swelling-induced deformation of silicon cells, as shown in Fig. 84. The thickness values of glass, EVA (no crosslinking), silicon cell, and backsheet are 4 mm, 0.5 mm, 0.166 mm, and 0.1 mm, respectively. Only elastic deformation is taken into account for the modeling of glass, silicon cell, and backsheet layers using the Kirchhoff–Saint-Venant constitutive model, and the basic mechanical properties are listed in Table 5. The zero chemical potential is prescribed on the outer surfaces of two EVA layers, and the initial potential for the dry EVA polymer is determined in the same way as in the previous two cases. Symmetric displacement boundary conditions are imposed on the symmetric planes, and the bottom surface of glass layer is constrained to remove rigid body motions.

The contour plots of polymer volume fraction ϕ of the first EVA layer (EVA1) in the three different solvents Toluene, Tetrahydrofuran, and Octane after 5 h, 10 h, and 15 h are shown in Fig. 85. At each of the three different time points, the polymer volume fraction of the first EVA layer (EVA1) in Toluene is lower than that in the other two solvents Tetrahydrofuran and Octane, which is mainly because of the high molar volume and viscosity of Toluene. The polymer volume fraction values of EVA1 at equilibrium in Toluene, Tetrahydrofuran, and Octane are approximately
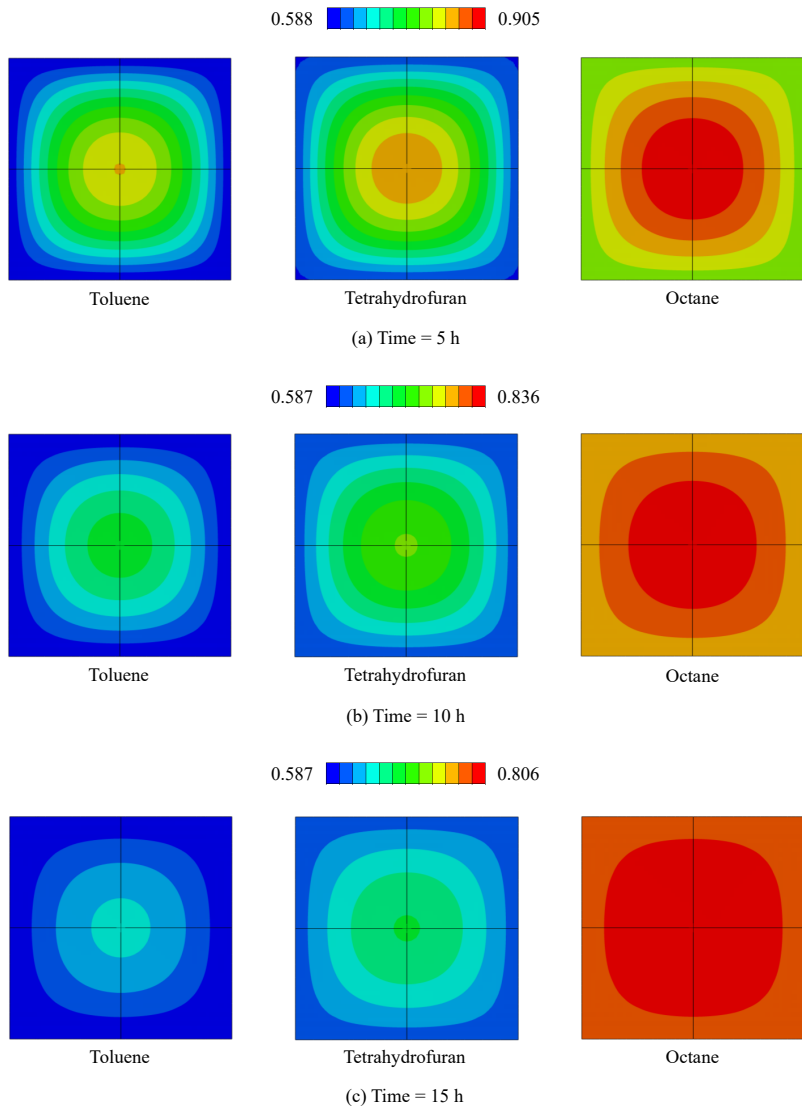
Figure 85: The contour plots of the polymer volume fraction ϕ of the first EVA layer (EVA1) in the three different solvents Toluene, Tetrahydrofuran, and Octane after (a) 5 h, (b) 10 h, and (c) 15 h.
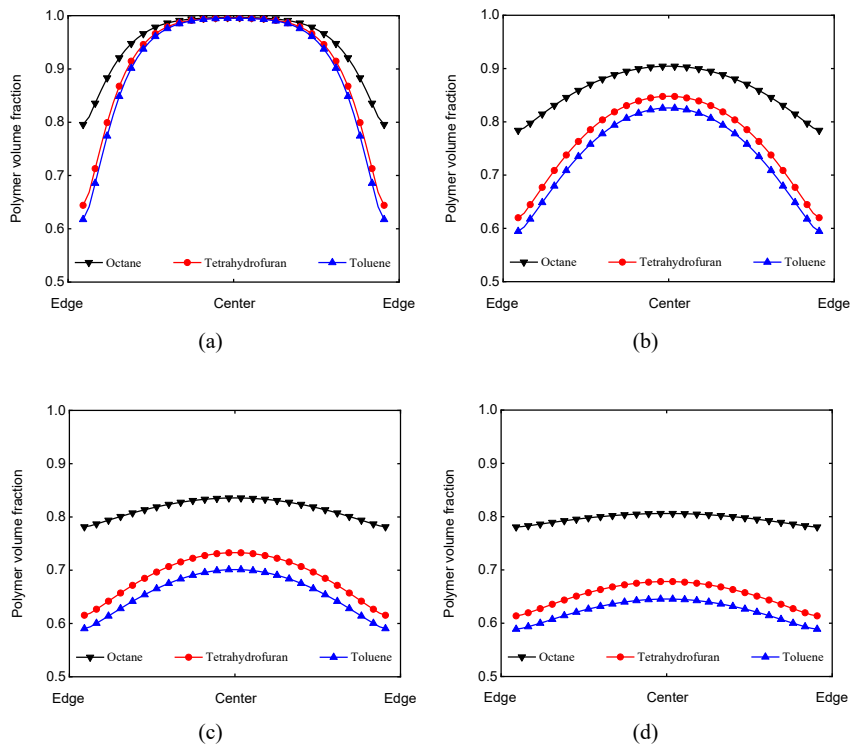
Figure 86: The spatial variation of the polymer volume fraction ϕ of the first EVA layer (EVA1) in the three different solvents Toluene, Tetrahydrofuran, and Octane after (a) 1 h, (b) 5 h, (c) 10 h, and (d) 15 h.

157

Figure 87: The contour plots of the polymer volume fraction ϕ of the second EVA layer (EVA2) in the three different solvents Toluene, Tetrahydrofuran, and Octane after (a) 5 h, (b) 10 h, and (c) 15 h.
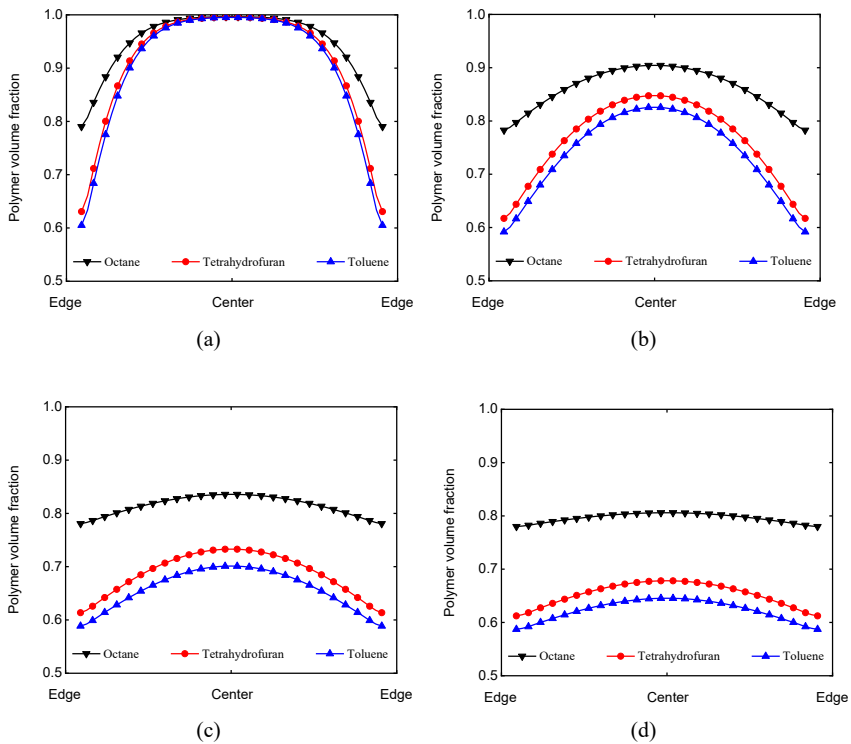
Figure 88: The spatial variation of the polymer volume fraction ϕ of the second EVA layer (EVA2) in the three different solvents Toluene, Tetrahydrofuran, and Octane after (a) 1 h, (b) 5 h, (c) 10 h, and (d) 15 h.

0.587, 0.612, and 0.780, respectively. After 15 h, the polymer volume fraction value in the middle area of EVA1 in Octane is the highest among the three cases, which can be ascribed to the lowest Flory-Huggins parameter. The spatial variation of the polymer volume fraction ϕ of the first EVA layer in the three different solvents after 1 h, 5 h, 10 h, and 15 h are shown in Fig. 86. At 1 h, the polymer volume fraction at the central area remains the value of 1.0 due to the lack of solvent penetration. No significant difference of the spatial distribution of polymer volume fraction in the solvents Tetrahydrofuran and Toluene can be observed at this time point because of their similar solubility parameters. After 15 h, it can be clearly seen from Fig. 86(d) that the polymer volume fraction distribution plot of EVA1 in Octane is much higher than the other two plots corresponding to Toluene and Tetrahydrofuran, which indicates least volume change of EVA in Octane. The contour plots and spatial variation of polymer volume fraction ϕ of the second EVA layer (EVA2) in the three different solvents Toluene, Tetrahydrofuran, and Octane after different time periods are shown in Fig. 87 and Fig. 88, respectively. It can be observed that the volume change and spatial variation of polymer volume fraction of EVA2 are similar to that of EVA1 in PV modules due to the fact that the thickness of silicon cell layer is very small. The time history evolution curves of EVA swelling degree of the two EVA layers in the three solvents Toluene, Tetrahydrofuran, and Octane are shown in Fig. 89. As expected, the volume of EVA layers in the PV modules increases with the penetration of solvents over time, but due to the different solubility parameters and molar volumes of three solvents, the corresponding time evolution curves of swelling degree show clear distinctions from each other.

The maximum principal stress plots of silicon solar cell layer of the PV modules in the three different solvents Toluene, Tetrahydrofuran, and Octane after 5 h, 10 h, and 15 h are shown in Fig. 90. Due to the enhanced solvent flux at the corners of EVA layers in the PV module, the stresses of silicon cell layer are higher at these marginal areas. After 5 h, the upper limit of maximum principal stress of silicon cell layer in Toluene is the highest among the three cases, with the value of 35.0 MPa, which
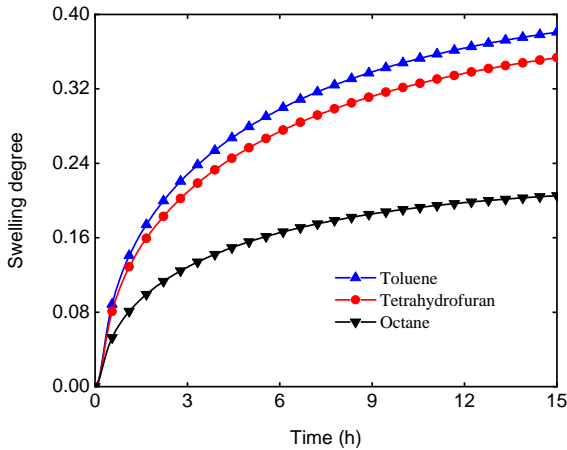
Figure 89: The time history evolution of the EVA swelling degree in the three different solvents Toluene, Tetrahydrofuran, and Octane.

can be ascribed to the highest swelling degree of EVA layers in this case. The maximum principal stress of silicon cell layer has the lowest value in Octane because of the lowest swelling degree of EVA layers in it. Note that the values of maximum principal stress of silicon solar cell layers in the three different solvents Toluene, Tetrahydrofuran, and Octane all increase over time as the solvents gradually penetrate into the middle area of EVA layers. After 15 h, the maximum principal stress at the outer areas of silicon cell layers with the three solvents reach the maximum values, indicating higher risks of silicon cracking at these areas. According to [193], the fracture stress of silicon mono-crystalline was approximately 30 MPa, which might be regarded as damage criterion here. Specifically, the silicon cells are considered to be damaged when the corresponding maximum principal stress values reach this criterion. The damage plots of silicon cell layer of the PV modulus in three different solvents after 5 h, 10 h, and 15 h are shown in Fig. 91. It is noteworthy that the onset of damage affects the stress distribution in the silicon (and hence the mechanical

Figure 90: The maximum principal stress plots of the silicon cell layer in the three different solvents Toluene, Tetrahydrofuran, and Octane after (a) 5 h, (b) 10 h, and (c) 15 h.

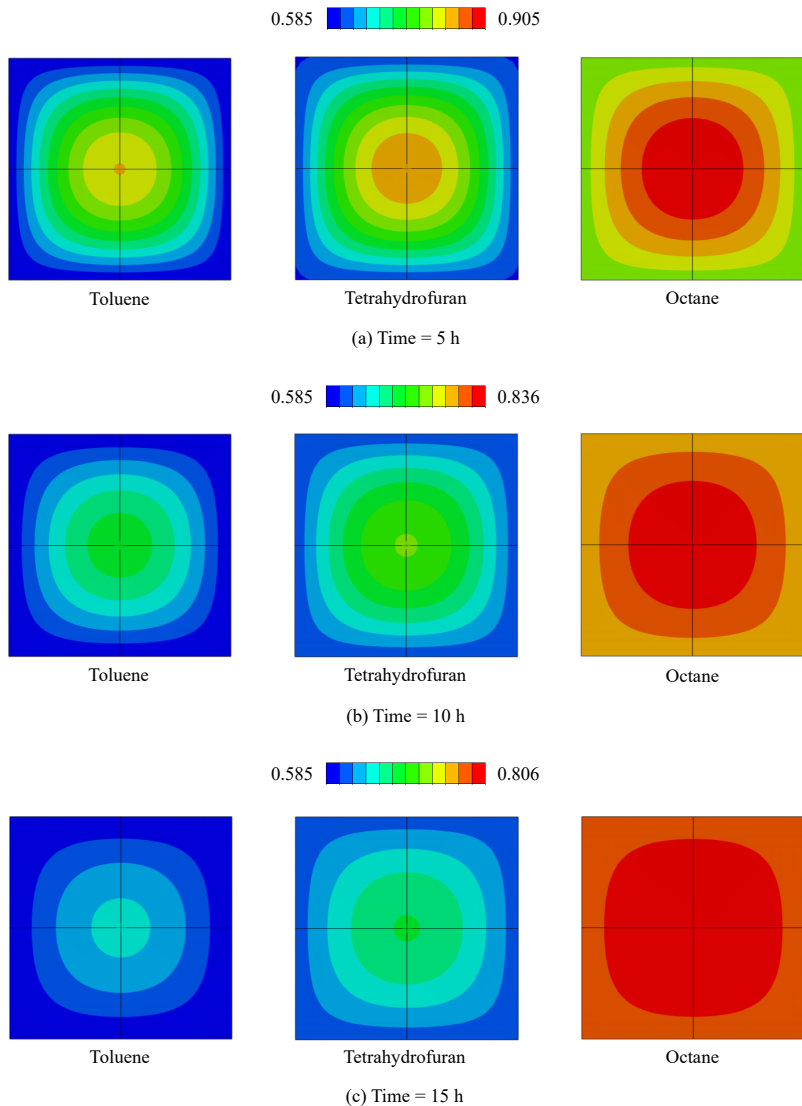equilibrium condition) but this is here not taken into account and is left for future investigations. Therefore, the obtained damage distributions should be considered just as a first step towards a more detailed fracture mechanics approach. However, in the limits of such approximation, they are certainly associated with different risks of damage in the different cases.

4.2 Peeling simulation of PV recycling

4.2.1 Humidity dose-based cohesive zone model

In this section, the humidity dose concept based polynomial CZM for the appropriate simulation of hygrothermal-mechanical behavior, subjected to large deformation like peeling, is presented. The formulations described subsequently are macroscopic models and developed for use within the framework of the finite element method.

Adhesion strength within the PV module under different environmental conditions degrades similarly in the form of exponential decay, which tends to decrease quickly in the beginning and then slow down after a certain period. Increased moisture causes the loss of interfacial strength, while temperature enhances the effect of humidity at a faster speed. In order to describe the environmental impact on the module over a time period, the relative humidity under ambient temperature must be transformed into the relative humidity at the interface of the module. The relative humidity inside the module is usually lower than the ambient relative humidity. Assuming the interface is in thermodynamic equilibrium with the environment and temperature inside the PV module is uniform [250], the ambient and module relative humidity are calculated as

$$RH_a = \frac{P_w}{P_s(T_a)} \tag{4.64a}$$

$$RH_m = \frac{P_w}{P_s(T_m)} = \frac{RH_a \times P_s(T_a)}{P_s(T_m)} \tag{4.64b}$$

where RH_a and RH_m are the ambient and module relative humidity, respectively, P_w is the water vapor pressure of the environment, and $P_s(T_a)$

(a) Time = 5 h

(b) Time = 10 h

(c) Time = 15 h

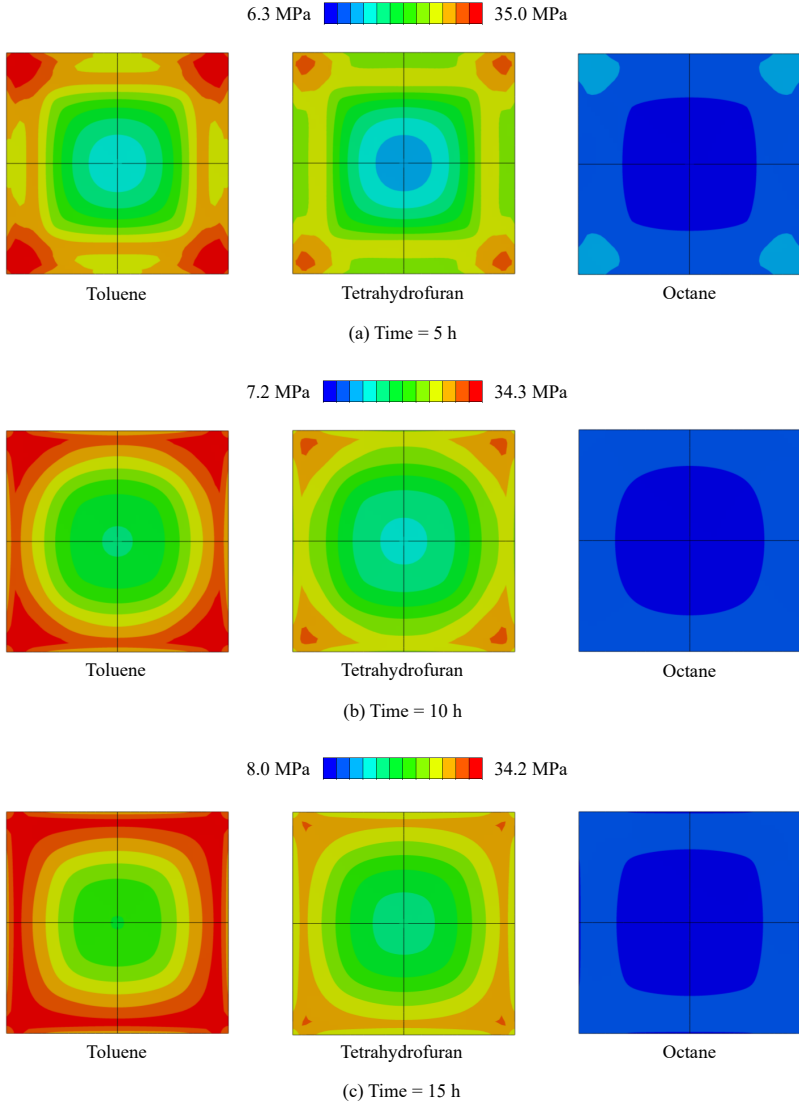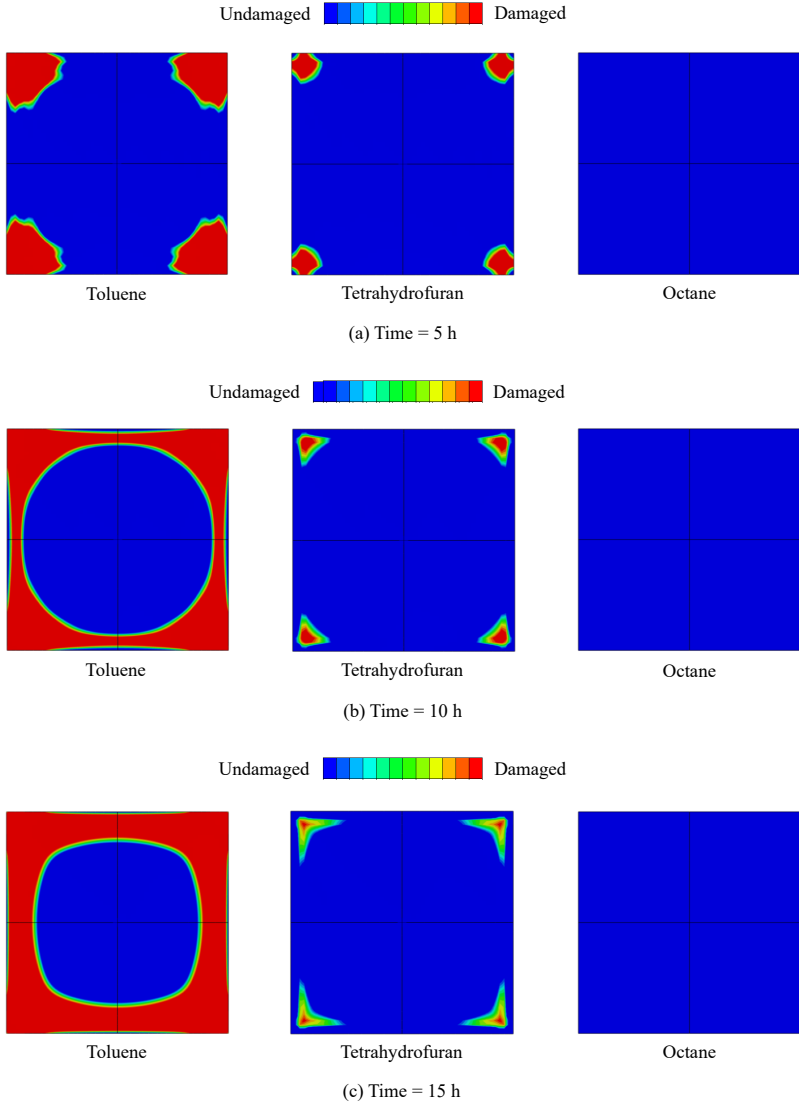**Figure 91:** The damage plots of the silicon cell layer in the three different solvents Toluene, Tetrahydrofuran, and Octane after (a) 5 h, (b) 10 h, and (c) 15 h.

and $P_s(T_m)$ are respective saturated water vapor pressures at ambient temperature and module temperature. The saturated and partial water vapor pressure of the environment are calculated as

$$P_s = f \times P_s' \tag{4.65a}$$

$$P_w = RH_a \times P_s = RH_a \times f \times P_s' \tag{4.65b}$$

where P_s and P_s' are the saturated water vapor pressure of environment and pure value, respectively, f is an enhancement coefficient. Substituting Eqs. (4.65a) and (4.65b) into Eq. (4.64b), the module relative humidity is formulated as

$$RH_m = \frac{P_w}{P_s(T_m)} = \frac{RH_a \times f(T_a) \times P_s'(T_a)}{f(T_m) \times P_s'(T_m)} \tag{4.66}$$

where $P_s'(T_a)$ and $P_s'(T_m)$ are pure saturation water vapor pressure at ambient temperature T_a and module temperature T_m, and $f(T_a)$ and $f(T_m)$ are enhancement coefficients at corresponding temperatures, respectively. Due to many different environmental factors such as irradiance, wind speed, heat exchange, and so on, module temperature is usually different from ambient temperature for outdoor exposure. However, for standard laboratory damp-heat test, the module temperature is identical to ambient temperature as experiments are performed in the environmental chambers. Thus, in this case, the relative humidity of the interface inside the PV module becomes approximately equal to the ambient relative humidity. The difference needs to be taken into account for the prediction of outdoor installation or for accelerated cyclic tests with fast non-equilibrium temperature variations.

The humidity dose model is established to quantify the environmental humidity and temperature effect on the interfacial degradation of PV modules within a certain time duration. In this model, relative humidity is regarded as the dominating factor, while the temperature is an accelerating factor, which can be described by an Arrhenius function. This Arrhenius form is an acceleration formulation to define relationships between degradation and contributing factors when a single mechanism dominates the influence [251], allowing to establish a consistent model

for different operating environments. The humidity dose is defined as a function of relative surface humidity with temperature as weighting factor within the time duration

$$dose = RH_\mathrm{m} \times \mathrm{e}^{-\frac{E_\mathrm{a}}{RT_\mathrm{m}}} \times \Delta t \qquad (4.67)$$

where R is Boltzmann's constant ($8.617 \times 10^{-5}\mathrm{eV/K}$), E_a is the activation energy and T_m is the module temperature in kelvin. Considering the relative module humidity defined in Eq. (4.66), the humidity dose can be formulated as follows,

$$dose = \frac{RH_\mathrm{a} \times f(T_\mathrm{a}) \times P'_\mathrm{s}(T_\mathrm{a})}{f(T_\mathrm{m}) \times P'_\mathrm{s}(T_\mathrm{m})} \times \mathrm{e}^{-\frac{E_\mathrm{a}}{RT_\mathrm{m}}} \times \Delta t \qquad (4.68)$$

This means the relative humidity of the PV module rather than the ambient relative humidity determines the moisture ingress. Besides, it also considers the temperature effect on moisture diffusion. The critical parameter in this dose model for the prediction of aging is the activation energy, which is determined as 0.65 eV by curve fitting [221].

Polynomial CZM proposed by Tvergaard [233] is a nonlinear constitutive relationship where the traction vector $\mathbf{T} = (\tau_\mathrm{s}, \tau_\mathrm{t}, \sigma)^\mathrm{T}$ is defined as a function of opening and sliding displacement of interface element with a softening part after reaching the maximum traction value. In this model, a non-dimensional parameter λ is firstly defined as

$$\lambda = \sqrt{\left(\frac{g_\mathrm{loc,s}}{\delta}\right)^2 + \left(\frac{g_\mathrm{loc,t}}{\delta}\right)^2 + \left(\frac{g_\mathrm{loc,n}}{\delta}\right)^2} \qquad (4.69)$$

where $g_\mathrm{loc,n}$, $g_\mathrm{loc,s}$ and $g_\mathrm{loc,t}$ are normal, in-plane shearing and out-of-plane shearing gap vector components, and δ is the corresponding ultimate displacement. In this research, both the shearing displacement values are set the same as the normal displacement one. Complete separation occurs when reaching the ultimate dimensionless displacement $\lambda = 1$. An exponential model can be used to describe the relation between ultimate displacement δ and humidity dose during degradation,

$$\delta = \delta_0 \mathrm{e}^{-\mathrm{k} \times dose} \qquad (4.70)$$

where k is the coefficient determined as 3.28×10^7 [221], and δ_0 is the initial ultimate displacement corresponding to no damp-heat effect, which is determined as approximate value 15 mm by the trial simulation to match experimental results.

To define the interface constitutive behavior, a function is defined as

$$P(\lambda) = \frac{27}{4}\sigma_{\max}(1 - 2\lambda + \lambda^2) \quad \text{for } 0 \leq \lambda \leq 1 \tag{4.71}$$

where $\sigma_{\max}$ is the maximum stress, which is defined by trial simulation and specified as a constant value of 0.3 MPa throughout this study for all the cases. Then the traction components are given by the following expressions

$$\sigma = \sigma_{\max}\frac{g_{\text{loc,n}}}{\delta}P(\lambda) \tag{4.72a}$$

$$\tau_{\text{s}} = \mu\sigma_{\max}\frac{g_{\text{loc,s}}}{\delta}P(\lambda) \tag{4.72b}$$

$$\tau_{\text{t}} = \mu\sigma_{\max}\frac{g_{\text{loc,t}}}{\delta}P(\lambda) \tag{4.72c}$$

where μ is the difference factor between tangential and normal separation, and set as 0.1 in this work. This cohesive zone formulation is viewed as a phenomenological model representing the average effect of the debonding mechanisms of PV interfaces. Its tangent constitutive matrix reads as

$$\mathbf{C} = \begin{bmatrix} \frac{\partial \tau_{\text{s}}}{\partial g_{\text{loc,s}}} & \frac{\partial \tau_{\text{s}}}{\partial g_{\text{loc,t}}} & \frac{\partial \tau_{\text{s}}}{\partial g_{\text{loc,n}}} \\ \frac{\partial \tau_{\text{t}}}{\partial g_{\text{loc,s}}} & \frac{\partial \tau_{\text{t}}}{\partial g_{\text{loc,t}}} & \frac{\partial \tau_{\text{t}}}{\partial g_{\text{loc,n}}} \\ \frac{\partial \sigma}{\partial g_{\text{loc,s}}} & \frac{\partial \sigma}{\partial g_{\text{loc,t}}} & \frac{\partial \sigma}{\partial g_{\text{loc,n}}} \end{bmatrix} \tag{4.73}$$

4.2.2 3D large deformation interface element and FE implementation

In the reference configuration for finite deformation setting, consider two deformable bodies $\mathcal{B}_0^{(1)} \subset \mathbb{R}^n$ and $\mathcal{B}_0^{(2)} \subset \mathbb{R}^n$ (identified as Body-1 and Body-2 in Fig. 92(a), where $n = 3$ stands for the space dimension. Both the boundary conditions: $\mathbf{t}^i = \hat{\mathbf{t}}_i$ on $\partial\mathcal{B}_{0,t}^{(i)}$ and $\mathbf{u}^i = \hat{\mathbf{u}}_i$ on $\partial\mathcal{B}_{0,u}^{(i)}$ and volume forces $\mathbf{F}_v^{(i)}$ with $i = 1, 2$ are imposed on the two separate bodies.
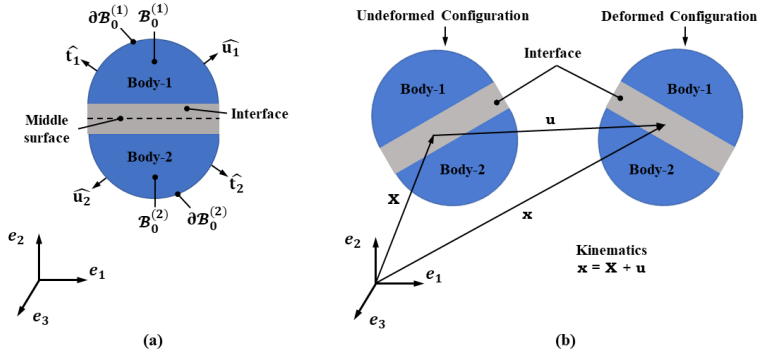
Figure 92: A sketch of schematic and kinematic definitions of the interface between two bodies along the deformation process

It is worth mentioning that two bodies can obey different constitutive material laws that characterize the mechanical performance within their domain. A deformation map $\varphi(\mathbf{X}) : \mathbf{X} \to \mathbf{x}$ is defined to relate material point in the reference configuration $\mathbf{X} \subset \mathcal{B}_0^{(i)}$ to the corresponding point in the deformed configuration $\mathbf{x} \subset \mathcal{B}_t^{(i)}$ at time t, see Fig. 92(b). To determine the linear map between the reference and deformed configuration, the deformation gradient of transformation is defined as: $\mathbf{F} := \partial_{\mathbf{X}}\varphi(\mathbf{x}, t)$ where $\partial_{\mathbf{X}}$ denotes the partial derivative with respect to the reference configuration. Jacobian can then be defined as the determinant of deformation gradient, which can be expressed as $J = \det[\mathbf{F}] > 0$. Noted that interface between two bodies $S_0 \subset \mathbb{R}^{n-1}$ is characterized by the polynomial cohesive zone formulation coupling with humidity dose model described in Sec. 4.2.1 for 3D applications.

Focusing on the analysis of the interface between the two bodies, its contribution to the Principle of Virtual Work of the whole mechanical system can be expressed as

$$\Pi_{\text{intf}}(\mathbf{g}_{\text{loc}}) = \int_{S_0} \mathbf{g}_{\text{loc}}^{\text{T}} \mathbf{T} \, dS \tag{4.74}$$

where $\mathbf{g}_{\text{loc}} = (g_{\text{loc},s}, g_{\text{loc},t}, g_{\text{loc},n})^{\text{T}}$ is the displacement gap vector including

both opening and sliding components between the two opposite sides of interface, and $\mathbf{T}$ is the traction vector conjugate to the gap vector. Note that the traction vector defined previously is the Piola-Kirchhoff stress defined in the reference configuration due to the geometrical nonlinearity. In a large deformation setting, the traction vector vanishes when the interface is undergoing rigid body motions owning to the frame indifference of this formulation. The variational form of interface contribution on the basis of the Principle of Virtual Work is expressed as

$$\delta\Pi_{\text{intf}}(\mathbf{g}_{\text{loc}}) = \int_{S_0} \left(\frac{\partial \mathbf{g}_{\text{loc}}}{\partial \mathbf{u}} \delta\mathbf{u} \right)^{\text{T}} \mathbf{T}\, dS = \delta\mathbf{u}^{\text{T}} \int_{S_0} \left(\frac{\partial \mathbf{g}_{\text{loc}}}{\partial \mathbf{u}} \right)^{\text{T}} \mathbf{T}\, dS \qquad (4.75)$$

In the case of large deformation, the position vector in the deformed configuration can be calculated as $\mathbf{x} = \mathbf{X} + \mathbf{u}$, see Fig. 92(b). To account for moderate rotations, it is convenient to define a middle plane of the interface by averaging the position and displacement vector of the upper and lower faces in the deformed configuration. Hence, the position vector for any material point vector on the middle surface $\bar{\mathbf{x}}$ can be determined by multiplying the position vector with an averaging operator $\mathbf{M}$,

$$\bar{\mathbf{x}} = \mathbf{M}\mathbf{x} \qquad (4.76)$$

Complying with the isoparametric concept, the discrete version of the position vector $\bar{\mathbf{x}}^{\text{e}}$ and $\bar{\mathbf{X}}^{\text{e}}$ can be obtained by the operator $\mathbf{N}$ that collects the shape functions,

$$\bar{\mathbf{x}}^{\text{e}} = \mathbf{N}\mathbf{M}\mathbf{x}^{\text{n}}, \quad \bar{\mathbf{X}}^{\text{e}} = \mathbf{N}\mathbf{M}\mathbf{X}^{\text{n}} \qquad (4.77)$$

where $\mathbf{x}^{\text{n}}$ and $\mathbf{X}^{\text{n}}$ represents the nodal position vector in the discrete domain of interface in the deformed and undeformed configuration, respectively, the superscript n denotes nodal quantities, and $\mathbf{N}$ is defined in the natural parametric space $\{\xi, \eta\} \in [-1, 1] \times [-1, 1]$, where ξ and η are natural coordinates defined in the middle surface of the element. The matrix form of $\mathbf{N}$ is expressed as

$$\mathbf{N} = \begin{bmatrix} N_1 \mathbf{1} & N_2 \mathbf{1} & N_3 \mathbf{1} & N_4 \mathbf{1} \end{bmatrix} \qquad (4.78)$$

where $\mathbf{1}$ is a 3×3 identity matrix, and N_1, N_2, N_3 and N_4 presents the following expression

$$N_1 = \frac{1}{4}(1 - \xi)(1 - \eta) \tag{4.79a}$$

$$N_2 = \frac{1}{4}(1 + \xi)(1 - \eta) \tag{4.79b}$$

$$N_3 = \frac{1}{4}(1 + \xi)(1 + \eta) \tag{4.79c}$$

$$N_4 = \frac{1}{4}(1 - \xi)(1 + \eta) \tag{4.79d}$$

The matrix form of $\mathbf{M}$ is given as

$$\mathbf{M} = \frac{1}{2}\begin{bmatrix} 1 & 0 & 0 & 0 & 1 & 0 & 0 & 0 \\ 0 & 1 & 0 & 0 & 0 & 1 & 0 & 0 \\ 0 & 0 & 1 & 0 & 0 & 0 & 1 & 0 \\ 0 & 0 & 0 & 1 & 0 & 0 & 0 & 1 \end{bmatrix} \tag{4.80}$$

where $\mathbf{0}$ denotes 3×3 null matrix. Similarly, the displacement vector of any material point belonging to the middle surface of the interface domain in the reference configuration $\bar{\mathbf{u}}^{e}$ can be calculated through the isoparametric scheme from the nodal vales

$$\bar{\mathbf{u}}^{e} = \mathbf{NMd} \tag{4.81}$$

where $\mathbf{d}$ denotes nodal displacement vector and is expressed as

$$\mathbf{d} = (u_1, v_1, u_2, v_2, u_3, v_3, u_4, v_4, u_5, v_5, u_6, v_6, u_7, v_7, u_8, v_8)^{\mathrm{T}} \tag{4.82}$$

In line with derivations proposed for 3D application [22], the convective shear vector $\mathbf{s}$, tangential vector $\mathbf{t}$ and normal vector $\mathbf{n}$ to the middle surface in the deformed configuration, see Fig. 93, are defined via the differentiation of average position vector with respect to the natural coordinates ξ and η, which is expressed as

$$\mathbf{s} = \frac{\partial \bar{\mathbf{x}}^{e}}{\partial \xi}, \quad \mathbf{t} = \frac{\partial \bar{\mathbf{x}}^{e}}{\partial \eta}, \quad \mathbf{n} = \mathbf{s} \times \mathbf{t} \tag{4.83}$$
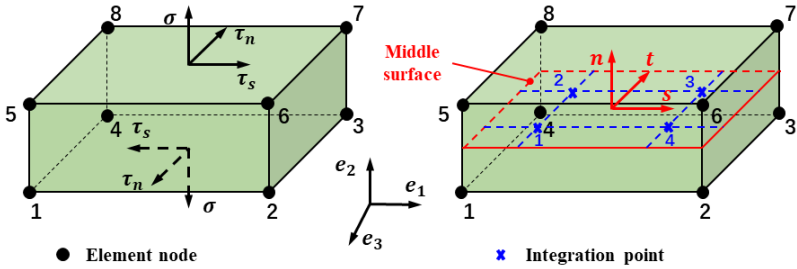
Figure 93: A sketch of three-dimensional interface element with element nodes and integration points

The gap vector **g** can be determined by multiplying the nodal displacement vector of the interface element with an appropriate operator **L**, which provides the difference between the bottom and upper surface displacements, and its expression is given by

$$\mathbf{g}^e = \mathbf{NLd} \tag{4.84}$$

where the difference matrix is defined as

$$\mathbf{L} = \begin{bmatrix} -1 & 0 & 0 & 0 & 1 & 0 & 0 & 0 \\ 0 & -1 & 0 & 0 & 0 & 1 & 0 & 0 \\ 0 & 0 & -1 & 0 & 0 & 0 & 1 & 0 \\ 0 & 0 & 0 & -1 & 0 & 0 & 0 & 1 \end{bmatrix} \tag{4.85}$$

To distinguish the different fracture modes such as Mode 1 and Mode 2, the constitutive relationship between the traction and gap vector of the interface is usually defined in the local frame given by Eq. (4.71). Therefore, the gap vector in this local frame needs to be computed by multiplying the gap vector in the global frame with a rotation matrix operator

$$\mathbf{g}^e_{loc} = \mathbf{Rg}^e = \mathbf{RNLd} \tag{4.86}$$

The rotation matrix reads

$$\mathbf{R} = \begin{bmatrix} s_x & s_y & s_z \\ t_x & t_y & t_z \\ n_x & n_y & n_z \end{bmatrix} \tag{4.87}$$

where its coefficients are all components of the convective normal and tangential vectors defined in Eq. (4.83). It is worth noting that this rotation operator is a function of the displacement vector in this large deformation setting. This dependency is subsequently considered in the consistent linearization of the discrete version of interface contribution to the Principle of Virtual Work solved by the Newton-Rapson scheme in this study. Note that this dependency on displacements will also lead to a geometrical contribution to the stiffness matrix. Regarding the virtual variation described in Eq. (4.75), the partial derivative of the local gap vector with respect to nodal displacements is given by

$$\frac{\partial \mathbf{g}^e_{loc}}{\partial \mathbf{d}} = \mathbf{R(d)NL} + \frac{\partial \mathbf{R(d)}}{\partial \mathbf{d}} \mathbf{NLd} \tag{4.88}$$

where the differentiation of rotation matrix $\mathbf{R}$ with respect to the components of displacement vector $\mathbf{d}$ is a third-order tensor. For convenience, the operator $\mathbf{B} = \mathbf{NL}$ is introduced to simplify the above equation as

$$\frac{\partial \mathbf{g}^e_{loc}}{\partial \mathbf{d}} = \mathbf{R(d)B} + \frac{\partial \mathbf{R(d)}}{\partial \mathbf{d}} \mathbf{Bd} \tag{4.89}$$

Inserting Eq. (4.89) into Eq. (4.75) for the virtual variation, where the displacement vector $\mathbf{u}$ is replaced by the nodal vector $\mathbf{d}$, the following general variational form of interface element considering both geometrical and material nonlinearity is derived as

$$\delta \Pi^e_{intf} = \delta \mathbf{d}^T \int_{S_0} \left(\mathbf{R(d)B} + \frac{\partial \mathbf{R(d)}}{\partial \mathbf{d}} \mathbf{Bd} \right)^T \mathbf{T} \, dS = \delta \mathbf{d}^T \mathbf{f}^e_{int} \tag{4.90}$$

where the vector $\delta \mathbf{d}$ represents the kinematically admissible virtual nodal displacement, and $\mathbf{f}^e_{int}$ is a nonlinear function of the nodal displacement vector, which stands for the internal force vector of interface at the element level in the Newton-Rapson iterative solution scheme. The linearization for the computation of the incremental correction of nodal displacement is derived by

$$\mathbf{K}^{e,k} \Delta \mathbf{d}^{k+1} = -\mathbf{f}^{e,k}_{int} \tag{4.91a}$$

$$\mathbf{d}^{k+1} = \mathbf{d}^k + \Delta \mathbf{d}^{k+1} \tag{4.91b}$$

For convenience, in case of no confusion, the superscript k is omitted in the following. The element stiffness $\mathbf{K}^e = \frac{\partial \mathbf{f}_{\text{int}}^e}{\partial \mathbf{d}}$ is evaluated by the displacement solution field at the iteration k, which is given by

$$\mathbf{K}^e = \int_{S_0} \left[2\mathbf{B}^T \frac{\partial \mathbf{R}^T}{\partial \mathbf{d}} \mathbf{T} + \left(\mathbf{B}^T \mathbf{R}^T + \mathbf{d}^T \mathbf{B}^T \frac{\partial \mathbf{R}^T}{\partial \mathbf{d}} \right) \frac{\partial \mathbf{T}}{\partial \mathbf{d}} \right] dS \qquad (4.92)$$

In this formulation, the second derivative of the rotation matrix with respect to the displacement vector that arises for the linearization is omitted for convenience. It was pointed out in [126] that this term has an almost negligible effect on the simulation results and thus it is reasonable to neglect it. The derivative of cohesive traction vector with respect to the nodal displacement vector can be obtained by chain rule as follows,

$$\frac{\partial \mathbf{T}}{\partial \mathbf{d}} = \frac{\partial \mathbf{T}}{\partial \mathbf{g}_{\text{loc}}} \frac{\partial \mathbf{g}_{\text{loc}}}{\partial \mathbf{d}} = \mathbf{C}\mathbf{R}(\mathbf{d})\mathbf{B} + \frac{\partial \mathbf{R}(\mathbf{d})}{\partial \mathbf{d}} \mathbf{B}\mathbf{d} \qquad (4.93)$$

where the tangent material stiffness matrix $\mathbf{C} = \frac{\partial \mathbf{T}}{\partial \mathbf{g}_{\text{loc}}}$ has been given in Sec. (4.2.1). Substituting Eq. (4.93) into Eq. (4.92), we can get the following element stiffness matrix

$$\mathbf{K}^e = \mathbf{K}_{\text{mat}}^e + \mathbf{K}_{\text{geom}}^e \qquad (4.94a)$$

$$\mathbf{K}_{\text{mat}}^e = \int_{S_0} \mathbf{B}^T \mathbf{R}^T \mathbf{C} \mathbf{R} \mathbf{B} \, dS \qquad (4.94b)$$

$$\mathbf{K}_{\text{geom}}^e = \int_{S_0} \left(2\mathbf{B}^T \frac{\partial \mathbf{R}^T}{\partial \mathbf{d}} \mathbf{T} + \mathbf{d}^T \mathbf{B}^T \frac{\partial \mathbf{R}^T}{\partial \mathbf{d}} \mathbf{C} \frac{\partial \mathbf{R}}{\partial \mathbf{d}} \mathbf{B}\mathbf{d} \right) dS$$
$$+ \int_{S_0} \left(\mathbf{B}^T \mathbf{R}^T \mathbf{C} \frac{\partial \mathbf{R}}{\partial \mathbf{d}} \mathbf{B}\mathbf{d} + \mathbf{d}^T \mathbf{B}^T \frac{\partial \mathbf{R}^T}{\partial \mathbf{d}} \mathbf{C}\mathbf{R}\mathbf{B} \right) dS \qquad (4.94c)$$

where $\mathbf{K}_{\text{geom}}^e$ and $\mathbf{K}_{\text{mat}}^e$ are the element geometrical stiffness matrix and material stiffness matrix, respectively. In small displacement, the element stiffness reduces to only material stiffness contribution, while in large displacement, the geometrical stiffness term also needs to be considered for the sake of accuracy. The present formulation has been implemented as a user element UEL in the finite element software ABAQUS.

173

4.2.3 Numerical examples

In this section, the coupled CZM in the three-dimensional interface element framework is firstly validated by comparing the numerical results with the experimental results in [221], and then difference between the specific energy required for peeling and crushing of a PV module is discussed to underline the potential application of the proposed modeling approach to design novel methods for PV recycling.

To better illustrate the constitutive behaviour of polynomial CZM and the performance of this 3D interface element, a benchmark simulation with one single element under uniaxial tension is performed, see the sketch in Fig. 94. The upper and lower bodies are both modeled using solid shell elements with rigid material properties, while the middle ply is modeled with the present large deformation interface finite element. The bottom surface of the lower body is constrained in the loading direction, and its reaction force is computed as the peeling force. Traction stress is calculated from reaction force divided by the interface area. In the simulation, the maximum stress of polynomial CZM is kept with the constant value of 0.3 MPa. The predictive traction vs. separation curves with different ultimate displacements ranging from 1 mm to 15 mm are shown in Fig. 95. The simulation results clearly demonstrate the generalized characteristics of the polynomial CZM incorporated into the 3D large deformation interface element. It can be seen that the stiffness of traction-separation curves before the peak traction decreases with increased ultimate displacement value. For each case, the resultant curve presents a softening stage when traction reaches the maximum value 0.3 MPa, and complete separation occurs at the corresponding ultimate displacement.

In the following, the large deformation interface element and polynomial CZM coupled with humidity dose model are applied for numerical study on the basis of the experimental work reported in [221] to prove the validity of the proposed modeling framework. In the experimental study, the degradation of adhesion strength between the backsheet and encapsulant layers at different humidity and temperature levels after a

174
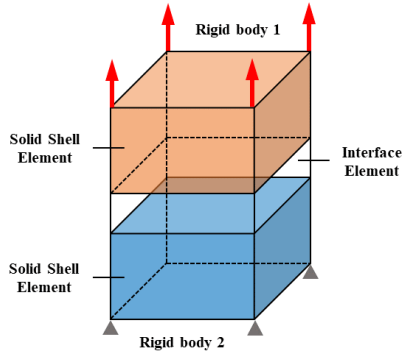
Figure 94: A sketch of one single element simulation

Table 6: Testing conditions for Photovoltaic modules.

T(°C)	RH		
	85%	65%	45%
95	√		
85	√	√	√
65	√		

certain time interval was investigated in detail. The encapsulant material is EVA with a thickness of 0.4 mm, and the backsheet is composed of two layers of PolyEthylene Terephthalate (PET) with a total thickness of 0.25 mm. Laminates were cut by CO_2 laser into the peel strips with a width of 10 mm and length of 100 mm for each one, see Fig. 96(a). The first 15 mm for each specimen was peeled off before the test to form a tap that can be held by the grip of the testing machine. Well-controlled 90-degree peeling tests were performed in the environmental chambers to obtain the adhesion strength during exposure to the damp-heat conditions. The loading speed is 50 mm/min for each test. The indoor accelerated tests were performed at five different temperature and humidity conditions, as listed in Table 6.

For the numerical simulation as shown in Fig. 96(b), the upper back-
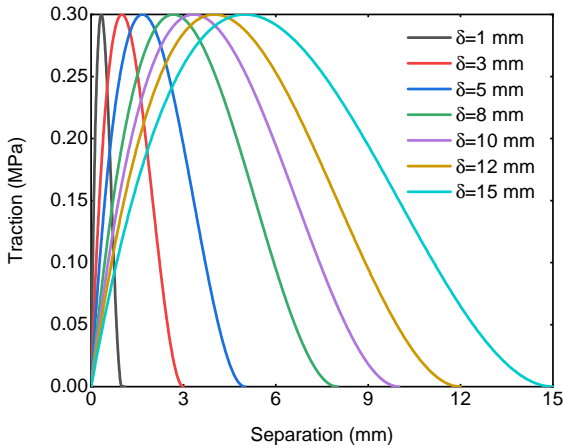
Figure 95: Traction separation curves of one single element simulation with different ultimate displacement values

sheet ply and lower ply are modeled using the 8-node solid shell elements in which both enhanced assumed strain method [252, 253] and assumed natural strain method [254, 255] are adopted to alleviate different locking phenomena. As elastic material properties of the backsheet are not given in [221], the values corresponding to the standard materials in the PV system [256, 52] are adopted in this study, see Table 5. Young's modulus of the backsheet is 2.8 GPa, and Poisson's ratio is set to 0.2. For the lower layer, its elastic properties are selected as the same values of glass properties with almost vanishing Poisson's ratio and Young's modulus equal to 73 GPa. Another uncertainty comes from how peeling extension was measured since it was not clearly pointed out in the experimental study. In the simulation, vertical displacement at the upper crack edge position (see Fig. 96(b)) is adopted. The size of solid shell elements for modeling the substrate layers is 1 mm, and the total number of solid shell elements is 2000. The middle ply with a thickness of 0.2 mm is modeled as the interface using the large deformation interface elements.
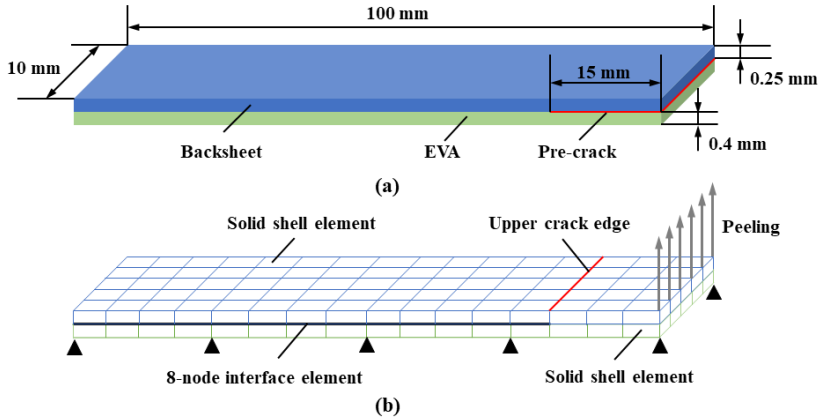
Figure 96: (a) 90-degree peeling test, and (b) discretization

There are a total number of 850 interface finite elements in this model. All the nodal degrees of freedom at the bottom surface are constrained, and vertical displacement boundary conditions are applied at the crack tip end of the laminate to peel off the upper backsheet. Reaction forces at all the constrained nodes add up to define the peeling force.

The displacement contour plot for the finite element model under large deformation used for peeling simulation is shown in Fig. 97. Simulation results regarding peeling force vs. vertical displacement of fictitious extension tip for different exposure duration at the same condition 85 °C/85% RH are plotted in Fig. 98. In this case, the only changeable parameter is the exposure duration, while all the other conditions are kept constant to investigate the effect of exposure on the adhesion degradation. All four curves for different exposure duration show a similar pattern. The peeling force increases gradually from the beginning of the peeling process as the loading displacement boundary condition is applied to the crack end of the specimen, and when the gaps of crack tip reach the ultimate displacement value set in the cohesive zone model, debonding occurs in these elements and the curves present an even platform during the subsequent crack propagation process.
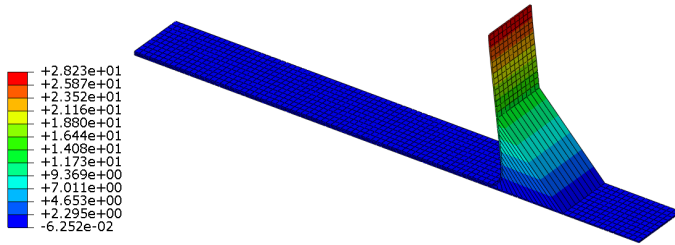
Figure 97: Displacement contour in the peeling direction along the simulation process
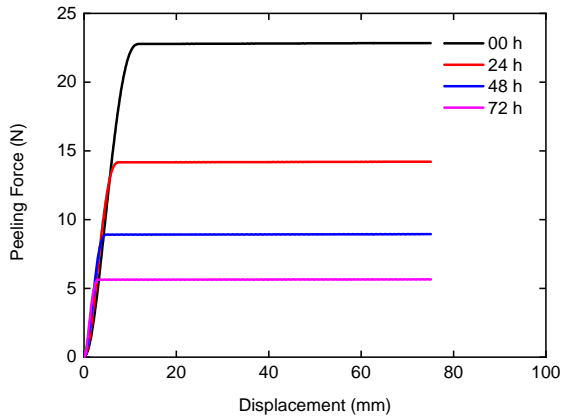
Figure 98: Peeling force vs. displacement curves obtained from simulation at the condition 85 °C/85% RH.
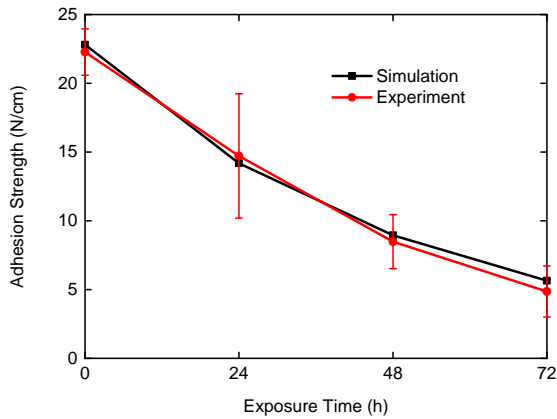
Figure 99: Comparison of adhesion strength between experiment and simulation with different exposure duration at the same condition 85 °C/85% RH.

In the experimental study [221], it is pointed out that testing curves for peeling presents inescapable differences even for the same batch of specimen due to the imperfect lamination quality and variation of the manufacturing process of materials. Therefore, the obtained experimental data of adhesion strength were the approximate average value for each test at a certain exposure and environmental condition. For calculation of numerical values, the resultant simulation curve is firstly integrated from the starting of debonding to the end. Then the adhesion strength can be obtained via the division of the integration value by the corresponding range. Comparison between experimental and numerical adhesion strength values for different exposure at a certain hygrothermal condition corresponding to 85 °C/85% RH is shown in Fig. 99. It is clearly demonstrated that exposure time significantly impacts PV interfacial adhesion as the strength of 22.81 N/cm degrades to 5.64 N/cm after exposure to the damp-heat condition for 72 hours. For the exposure duration of 0 h, 24 h, 48 h, and 72 h, numerical results correlate with individual experimental results very well, as shown in Fig. 99.

179
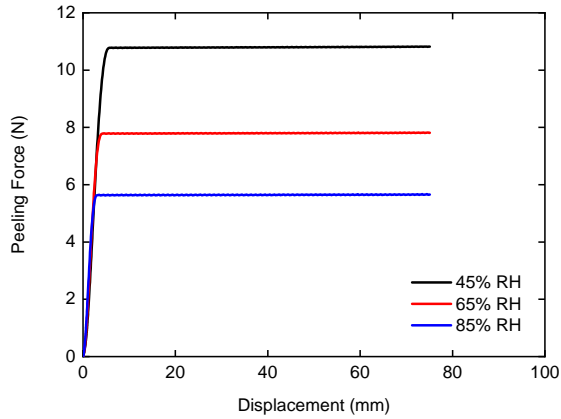
Figure 100: Peeling force vs. displacement curves obtained from simulation at the condition 85 °C.
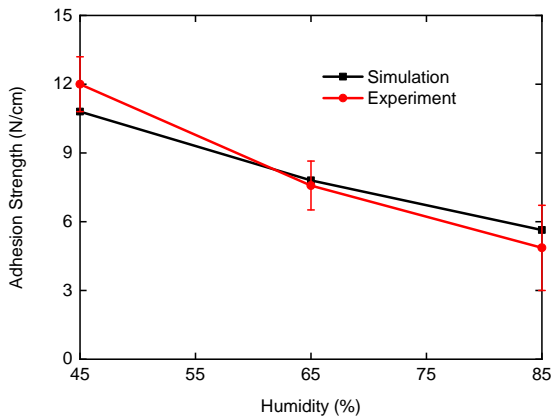
Figure 101: Comparison of adhesion strength between experiment and simulation for different relative humidity values at the same condition 85 °C and exposure duration of 72 h.
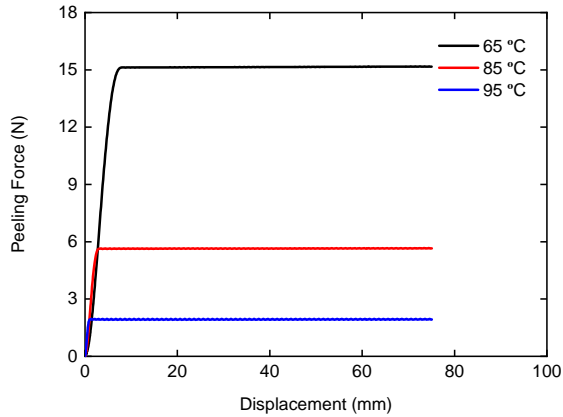
Figure 102: Peeling force vs. displacement curves obtained from simulation at the condition 85% RH.

Peeling force vs. vertical extension displacement curves for different relative humidity conditions obtained from finite element simulation are shown in Fig. 100. The temperature and exposure time are kept constant in this case, and set as 85 °C and 72 h, respectively. The curves show the different plateau values of the peeling force for the three different conditions. Higher relative humidity at the same temperature and exposure condition leads to increased degradation of adhesion strength. A comparison of adhesion strength at different humidity levels between experiment and simulation is shown in Fig. 101. Overall, the agreement between numerical predictions and experimental results is fairly good for any RH level.

Resultant curves for different temperature values at the condition of 85% RH with exposure time of 72 h are shown in Fig. 102. As mentioned before, temperature is regarded as the accelerating factor of humidity that indirectly affects the adhesion strength. The high-temperature condition would result in significant adhesion degradation in the PV system. As shown in Fig. 103, adhesion strength decreases from 15.17 N/cm to
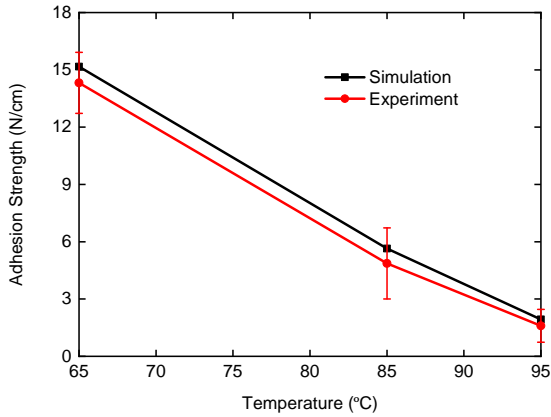
Figure 103: Comparison of adhesion strength between experiment and simulation for different temperature values at the same condition 85% RH and exposure duration of 72 h.

1.93 N/cm when the temperature increases from 65 °C to 95 °C. The numerical prediction matches the experimental results very well with slight difference for all the three cases. It should be pointed out that adhesion strength between different plies in PV laminate is affected by many additional complex failure mechanisms in the outdoor environment, and the comprehensive degradation model would require further work. This study mainly focuses on a reliable modeling method of the effect of steady humidity and temperature conditions following the experimental work [221]. In addition to the variation of same batch specimens, there are some other inevitable experimental error sources due to other failure mechanisms triggered during testing. Taking these into account, the difference between simulation and experiment can be acceptable.

To further assess the modeling strategy proposed in this study, all the numerical results obtained for different humidity, temperature, and exposure time conditions are compared with experimental results in terms of adhesion strength versus humidity dose values, as shown in Fig. 104. The experimental curve is obtained by curve fitting with all the exper-
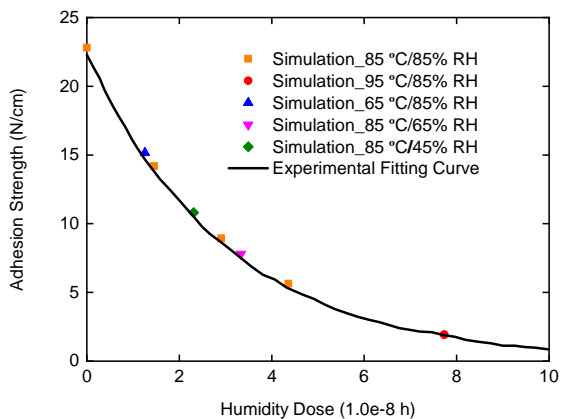
Figure 104: Comparison of adhesion strength versus humidity dose for different conditions between experimental fitting and numerical results

imental results reported in [221]. As mentioned in Sec. 4.2.1, humidity dose is introduced to provide a groundwork insight into the hygrothermal effect on adhesion, and it is defined in Eq. (4.67). This definition allows assessing the unified environmental influence under different relative humidity and temperature conditions. It can be seen that the predictions of adhesion strength show an exponential decay with respect to humidity dose values and also perfectly agree with the experimental fitting curve.

Although a PV system can produce green power for 25-30 years during its service phase, the total environmental impact should be assessed throughout its entire lifetime. Much attention has been focused on the environmentally friendly manufacturing of PV modules nowadays, but efforts toward the treatment of end-of-life products are still limited. Recycling can not only effectively prevents the toxic and hazardous substances in PV products from entering the groundwater and soil, and thus causing negative biochemical effects on the environment [195, 257], but also conserves precious metal materials such as Silver, Germanium,

Cadmium, etc. and energy-intensive pure material such as Silicon wafer [258]. In general, recycling of end-of-life PV products can significantly reduce carbon emission and global energy consumption, and alleviate lifecycle depletion of Silicon as well [55], which helps meet the growing demand of this raw material in PV industry. Despite these benefits, it is very difficult for recycling to be widely recognized without taking the economic factor into account. Studies [259, 257] have shown that recycling Silicon PV modules lacks economic sustainability due to high energy consumption of the adopted recycling process. Following the removal of external Aluminum frame and junction box of end-of-life PV products for recycling, the remainder of PV panel is usually subjected to the industrial crushing process including blade rotor crushing without any controlling sieve and hammer crushing with controlling sieve [260], which would inevitably consume a lot of energy and thus increase the recycling cost. An innovative idea is to explore the present modeling approach to virtually assess the efficacy of a different way to disassemble PV modules by peeling of the set of bonded laminae from the glass cover, to circumvent the crushing step.

The histogram of peeling energy per unit mass of testing specimen for different temperature and relative humidity conditions is shown in Fig. 105. At the same relative humidity, the specific energy required for peeling in high temperature condition is much lower than that in low temperature condition. At 85% RH, the maximum peeling energy in the 65 °C condition is equal to 1.572 J/g, which is approximately eight times the energy value of 0.2 J/g required for the 95 °C condition. Conclusion can be drawn that end-of-life PV modules installed in high temperature areas are much easier to be recycled by the peeling method compared to those installed in cold areas, since adhesion degradation is accelerated by temperature as mentioned before. Besides, it is also noted that moisture has the same negative effect as temperature on the required specific energy. Less energy would be required under increased relative humidity or moisture to peel off the different plies of PV laminate for recycling. At the temperature conditions of 85 °C, the peeling energy in 45% RH is 1.12 J/g, while in 85% RH condition, only specific energy value of 0.584 J/g is
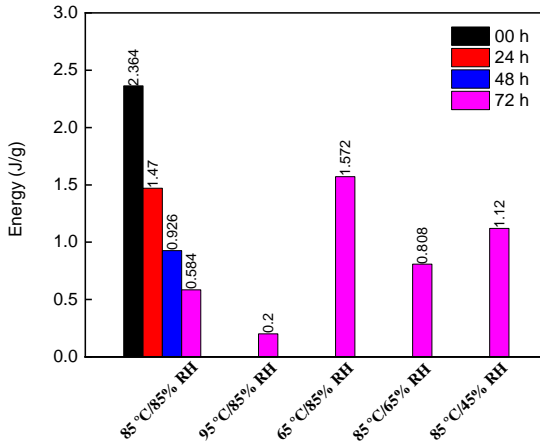
Figure 105: Comparison of the required specific energy for different relative humidity and temperature conditions

required as high relative humidity causes more severe adhesion degradation in PV, which means end-of-life PV installed in hot-humid areas should be more easily recycled through peeling. It should be pointed out that standard qualification tests to assess the constant temperature and moisture effect on the adhesion of PV is carried out in the 85 °C and 85% RH condition. Different specific peeling energy values for different exposure times 0 h, 24 h, 48 h and 72 h at this condition are listed in Fig. 105. It is clear that PV modules subjected to the hygrothermal degradation are prone to be recycled by peeling as compared with brand new products, since longer exposure times leads to less required specific peeling energy, as can be seen from the standard damp-heat condition of 85 °C and 85% RH.

To highlight the tremendous advantage of exploring peeling method for recycling over conventional crushing strategy, the tentative analysis and comparison between these two methods are discussed here. Relationship of average particle size with required crushing energy per unit mass of PV modules reported in [261] is shown in Fig. 106. The ba-
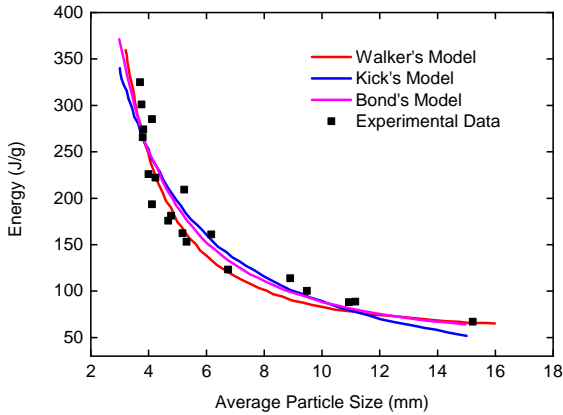
Figure 106: Relationship of average particle size with the required specific energy for crushing in recycling of PV [261]

sic trend is that particles during the crushing process of end-of-life PV modules concentrate on smaller size fraction with the increased energy. In [261], various models were adopted to fit the experimental results, and it was concluded that Walker's model is the best one to describe the relationship between particle size and specific energy required for recycling by crushing and fragmentation of PV modules. From this fitting curve and experimental results shown in Fig. 106, it can be evaluated that the input energy to dismantle the PV panel into 5 mm particles for subsequent recycling is approximately 180 J/g, which is more than hundred time the estimated specific energy required by peeling. Therefore, it can be concluded that recycling by peeling should be a much more economically promising method as compared to crushing, due to the extremely low energy consumption. The modeling framework proposed in this work can be very advantageous to explore new peeling setups to optimize disassembling operations and replace crushing for recycling end-of-life PV panels in the foreseeable future.

Chapter 5

Conclusion and future developments

5.1 Summary and further developments for the multiphysics modeling of photovoltaic modules

In this work, a comprehensive 3D finite element computational framework has been established for the modeling of multi-field problems in the thin-walled photovoltaic laminate with polymeric interface [16]. To simulate the thermo-mechanical response of the very thin laminae in the PV module, the consistent derivation of solid shell element formulation incorporating the EAS and ANS methods to alleviate the different locking pathologies is proposed. Besides, a 3D thermo-mechanical interface element formulation is developed to model the polymeric encapsulant layers between different laminae with a traction-separation constitutive law using the fractional calculus method for the description of rheologically complex thermo-visco-elastic behaviour. Moreover, given the difference of time scales between the moisture diffusion and thermo-mechanical problems, a staggered scheme is proposed to solve the partial differential equations governing the thermo-elasticity and heat transfer

problems in different laminae and polymeric interfaces, and then update the diffusion coefficient in the moisture diffusion analysis as well as its subsequent solution.

The computational methodology is successfully applied to the simulation of three standard qualification tests requested by the International Electrotechnical Commission, namely the damp heat test, humidity freeze test, and thermal cycling test. In the damp heat case, the numerical prediction is compared with the analytical solution together with experimental data, and good consistency proves the validity of the modeling method. To see the difference of moisture diffusion with and without thermo-mechanical coupling, the simulation of temperature dependent moisture diffusion in the humidity freeze case with cyclic temperature boundary condition is performed and compared with the previous damp heat simulation, which shows the capabilities of the proposed methodology for the modeling of spatial and temporal variation of moisture concentration inside the EVA layer. Finally, the thermal cycling test of a PV minimodule with a central crack in the middle solar cell is also simulated with a different cyclic temperature boundary condition from that of the humidity freeze test, and the predicted trend of crack enhanced moisture diffusion is experimentally validated with the electric degradation EL images taken at different stages. With this proposed computational tool at hand, it is possible to numerically perform the durability analysis of PV modules under different complex environmental conditions and thus open new possibilities for the design of more reliable products in the PV industry.

Future improvement on this modeling framework can be focused on the incorporation of swelling deformation into the mechanical energy part, more accurate material modeling of the EVA polymer layers, establishment of the quantitative connection between the diffusion and oxidation, more comprehensive description regarding the influence of different environmental factors on the reaction kinetics, and so on.

5.2 Concluding remarks and further developments for the global-local crack modeling of solar cells in the photovoltaic modules

In this work, a global-local phase field approach using the enhanced assumed strain solid shell formulation at finite deformation with the efficient quasi-Newton monolithic solution is proposed for the numerical prediction of solar cell crack events in the PV modules. The EAS method for the treatment of volumetric and Poisson thickness locking was employed through the postulation of multi-field variational framework, and the ANS method to alleviate the transverse shear and trapezoidal locking effects was also taken into account in the shell formulation [131].

Aiming at improving the computational efficiency without the sacrifice of robustness, an efficient quasi-Newton solution scheme is implemented within the phase field solid shell formulation in a monolithic manner, and its performance is demonstrated by comparison with the popular staggered Newton scheme through different paradigmatic boundary value problems, including single edge notched tension and shear, fracture of cylindrical structure under mixed bending and tension, and computationally demanding fatigue induced crack growth. Significant computational gains of the quasi-Newton monolithic scheme can be observed in all the numerical examples. It is also found that this scheme is very robust, capable of solving different benchmark problems of varying complexity without convergence issues frequently occurring in the conventional monolithic Newton solution.

Besides, in case that crack growth in the local region of interest has minor effect on the global stiffness, a specific global-local approach in the 3D setting tailored for the phase filed modeling with solid shells is proposed to save computational cost. Coarse mesh can be adopted for the global model while the mesh of local model can be more refined to deal with the appropriate displacement-phase field problem. The capability of this approach was demonstrated by simulating the crack growth of cylindrical thin-walled structure under both static and fatigue cyclic loadings, which could open up new possibilities in tackling realistic in-

dustrial problems concerning fracture events in large-scale thin-walled structures.

The proposed computational framework is subsequently extended to the fracture modeling of silicon solar cells in the photovoltaic modules by the incorporation of fracture anisotropy. Its capability to predict the preferential crack growth is demonstrated by the tension of a square plate consisting of two grains. Although the fracture anisotropy has negligible influence on the mechanical response in the simulation of this simple example, the different electrically inactive area in the silicon cells resulting from the crack patterns will lead to the different power loss, which is of great significance to the evaluation of PV performance. Besides, according to the experimental evidence, the silicon solar cell cracking barely has influence on the global stiffness of the photovoltaic module, and to save computational cost, the global local approach is adopted for the simulation of crack events of silicon solar cells when the photovoltaic modules are subjected to the two different loadings including tension and three point bending. The present modeling strategy constitutes a major progress with respect to the state of the art, since it provides the first proof of concept of a computational methodology integrating structural mechanics considerations for real PV installations and advanced fracture mechanics models for the assessment of damage distributions in solar cells.

Future developments regarding this modeling framework include the extension to the multifield problems as different environmental factors (such as moisture and temperature) influence the crack propagation, improvement on the global local approach by incorporation of adaptive mesh refinement and two-way coupling of global and local fields, extension to the high-cyle fatigue and dynamical cracking, and so on.

5.3 Final conclusions and futher developments for the recycling of photovoltaic modules

In the first part of this section, a thermodynamically consistent large-deformation theory for the modeling of the coupled EVA polymer-solvent

system has been presented in order to address the technical problems regarding the recycling of end-of-life PV modules [38]. The computational framework accounts for the solvent diffusion in the EVA layers, swelling and elastic deformation of EVA in solvents with different solubility parameters and molar volumes, as well as effects of crosslinking and mechanical constraints. The solvent diffusion and resulting swelling of EVA layers lead to the high risks of destroying the intactness of silicon cell layers, which is the key problem in PV recycling as pointed out in [72]. The computational modeling in this work is a first attempt to address this technical issue that is of great importance to the PV industry.

The numerical method was firstly applied to simulate the swelling experiments of EVA in three solvents of different nature according to [244], and very good agreement with the testing data has been achieved, which demonstrates the reliability of this method. Given the crosslinking of EVA in PV lamination, the second example has addressed its effects on the complex behaviour of polymer-solvent system, and also taken into account the coupled shrinking effects in the presence of mechanical constraints. The reduced volume change of EVA layer with higher initial crosslinking and mechanical constraints from substrate can be predicted for the different polymer-solvent systems. The last example concerns the modeling of complete PV laminates in the 3D setting to study the deformation of silicon cell layer induced by the solvent penetration and subsequent swelling of EVA layers. Solvents with different basic properties such as viscosity and molar volumes have direct impact on the coupled responses of PV modules, which further influences the recovery of nondestructive silicon wafers.

The proposed study allows to design virtual experimental procedures for the evaluation of effective impact of the coupled mechanisms on the recovery of structure-intact silicon wafers in PV recycling using the organic solvent method. Specifically, with the known basic properties of solvents and EVA copolymer used in PV modules, it is possible to identify suitable mechanical boundary conditions to guarantee the high integrity of reclaimed silicon wafers during the recycling process of end-of-life products. In the future work, the modeling framework can be com-

bined with phase field fracture approach proposed in chapter 3 to provide a more comprehensive methodology for the investigation of non-destructive recovery of silicon solar cells in the PV recycling using the solvent method.

In the second part of this work, to investigate the adhesion degradation of PV laminates due to humidity ingress and temperature effects, a modeling framework coupling the cohesive zone model with a humidity dose model was proposed in this study [1]. A 3D interface finite element considering large deformation including both geometrical and material nonlinearity is also established to accurately simulate the interfacial failure in the 90-degree peeling test. The corresponding FE implementation is based on the variational form of interface contribution to the Principle of Virtual Work of the whole mechanical system, and its subsequent consistent linearization considering large deformation is also detailed. To validate the modeling strategy, peeling between the backsheet and the encapsulant layer (EVA) has been simulated to assess the adhesion strength at different hygrothermal environments after certain exposure duration. Numerical results have been compared with experimental results [221] under different conditions of exposure time, humidity and temperature, and they correlate with damp-heat test results very well. All the predicted adhesion strength values show exactly the same exponential decay trend as the experimental one. With the aid of this modeling framework, considering large deformation and coupling of both temperature and humidity, a realistic numerical simulation of peeling for recycling of end-of-life PV panels is possible. Compared with the traditional crushing in PV recycling process, it has been assessed that the specific required energy for peeling is much lower, which indicates that the modeling framework proposed in this work can be very valuable for PV industry to virtually explore new economical solutions for recycling.

It has to be concluded that though adhesion strength, which is greatly affected by environmental moisture and temperature, is of utmost significance to the durability and performance of PV modules, no suitable modeling method within the large deformation framework addresses these factors. However, this modeling method can be beneficial to the

PV industry. For instance, to virtually peel off the different plies of end-of-life PV laminates for recycling so as to estimate how much energy it would require, such a reliable tool would help a lot since both large deformation and degradation due to hygrothermal effect in outdoor environment needs to be considered in this case. Regarding the possible future development on this work, the spatial variation of moisture and temperature along the interface can be taken into account for a more accurate prediction of the adhesion strength by the incorporation of the diffusion process in the modeling framework. Besides, future attempts with regard to the establishment of a more comprehensive mathematical formulation on the relationship between the environmental factors and degraded adhesion strength can be made as well.

Bibliography

[1] Z Liu, J Reinoso, and M Paggi. "A humidity dose-CZM formulation to simulate new end-of-life recycling methods for photovoltaic laminates". In: *Engineering Fracture Mechanics* 259 (2022), p. 108125.

[2] Davide Polverini et al. "Polycrystalline silicon PV modules performance and degradation over 20 years". In: *Progress in photovoltaics: research and applications* 21.5 (2013), pp. 1004–1015.

[3] Keith R McIntosh et al. "The effect of damp-heat and UV aging tests on the optical properties of silicone and EVA encapsulants". In: *Progress in Photovoltaics: Research and Applications* 19.3 (2011), pp. 294–300.

[4] Eric Schneller, Narendra S Shiradkar, and Neelkanth G Dhere. "Performance variation of commercially available modules after six months of outdoor system voltage stress testing". In: *2014 IEEE 40th Photovoltaic Specialist Conference (PVSC)*. IEEE. 2014, pp. 3216–3219.

[5] Michele Cândida Carvalho de Oliveira et al. "Comparison and analysis of performance and degradation differences of crystalline-Si photovoltaic modules after 15-years of field operation". In: *Solar Energy* 191 (2019), pp. 235–250.

[6] A Omazic et al. "Relation between degradation of polymeric components in crystalline silicon PV module and climatic conditions: A literature review". In: *Solar energy materials and solar cells* 192 (2019), pp. 123–133.

[7]   Michele Cândida Carvalho de Oliveira et al. "The causes and effects of degradation of encapsulant ethylene vinyl acetate copolymer (EVA) in crystalline silicon photovoltaic modules: A review". In: *Renewable and Sustainable Energy Reviews* 81 (2018), pp. 2299–2317.

[8]   Zhi-Sheng Li et al. "Application and development of solar energy in building industry and its prospects in China". In: *Energy Policy* 35.8 (2007), pp. 4121–4127.

[9]   Hans Schnitzer, Christoph Brunner, and Gernot Gwehenberger. "Minimizing greenhouse gas emissions through the application of solar thermal energy in industrial processes". In: *Journal of Cleaner Production* 15.13-14 (2007), pp. 1271–1286.

[10]   Saidur Mekhilef, Rahman Saidur, and Azadeh Safari. "A review on solar energy use in industries". In: *Renewable and sustainable energy reviews* 15.4 (2011), pp. 1777–1790.

[11]   Jinlin Xue. "Photovoltaic agriculture-New opportunity for photovoltaic applications in China". In: *Renewable and Sustainable Energy Reviews* 73 (2017), pp. 1–9.

[12]   Akira Yano, Mahiro Onoe, and Josuke Nakata. "Prototype semi-transparent photovoltaic modules for greenhouse roof applications". In: *Biosystems Engineering* 122 (2014), pp. 62–73.

[13]   PJ Sonneveld et al. "Performance of a concentrated photovoltaic energy system with static linear Fresnel lenses". In: *Solar Energy* 85.3 (2011), pp. 432–442.

[14]   Reda Hassanien Emam Hassanien, Ming Li, and Wei Dong Lin. "Advanced applications of solar energy in agricultural greenhouses". In: *Renewable and Sustainable Energy Reviews* 54 (2016), pp. 989–1001.

[15]   Changfu Han et al. "An innovative integrated system utilizing solar energy as power for the treatment of decentralized wastewater". In: *Journal of environmental sciences* 25.2 (2013), pp. 274–279.

[16]   Z Liu, J Reinoso, and M Paggi. "Hygro-thermo-mechanical modeling of thin-walled photovoltaic laminates with polymeric interfaces". In: *Journal of the Mechanics and Physics of Solids* 169 (2022), p. 105056.

[17] Jose-Maria Delgado-Sanchez et al. "Failure mode and effect analysis of a large scale thin-film CIGS photovoltaic module". In: *Engineering Failure Analysis* 76 (2017), pp. 55–60.

[18] Maurizio Verri et al. "Solution map analysis of a multiscale Drift–Diffusion model for organic solar cells". In: *Computer Methods in Applied Mechanics and Engineering* 331 (2018), pp. 281–308.

[19] Carlo De Falco et al. "Multiscale modeling and simulation of organic solar cells". In: *Computer Methods in Applied Mechanics and Engineering* 245 (2012), pp. 102–116.

[20] Oscar Kwame Segbefia, Anne Gerd Imenes, and Tor Oskar Saetre. "Moisture ingress in photovoltaic modules: A review". In: *Solar Energy* 224 (2021), pp. 889–906.

[21] Mirjam Theelen and Felix Daume. "Stability of Cu (In, Ga) Se2 solar cells: A literature review". In: *Solar Energy* 133 (2016), pp. 586–627.

[22] Taesoo D Lee and Abasifreke U Ebong. "A review of thin film solar cell technologies and challenges". In: *Renewable and Sustainable Energy Reviews* 70 (2017), pp. 1286–1297.

[23] Mariacristina Gagliardi, Pietro Lenarda, and Marco Paggi. "A reaction-diffusion formulation to simulate EVA polymer degradation in environmental and accelerated ageing conditions". In: *Solar Energy Materials and Solar Cells* 164 (2017), pp. 93–106.

[24] Patrick O'Connor and Andre Kleyner. *Practical reliability engineering*. John Wiley & Sons, 2012.

[25] MV Iseghem et al. "Failure modes after damp heat tests on PV modules". In: *Proceedings of the 27th European photovoltaic solar energy conference and exhibition*. 2012, pp. 3546–3548.

[26] Marc Köntges et al. "Review of failures of photovoltaic modules". In: (2014).

[27] Marc Köntges et al. *Assessment of Photovoltaic Module Failures in the Field: International Energy Agency Photovoltaic Power Systems Programme: IEA PVPS Task 13, Subtask 3: Report IEA-PVPS T13-09: 2017*. International Energy Agency, 2017.

[28] Marco Paggi, Mauro Corrado, and Irene Berardone. "A global/local approach for the prediction of the electric response of cracked solar cells in photovoltaic modules under the action of mechanical loads". In: *Engineering Fracture Mechanics* 168 (2016), pp. 40–57.

[29]   Michael D Kempe. "Modeling of rates of moisture ingress into photovoltaic modules". In: *Solar Energy Materials and Solar Cells* 90.16 (2006), pp. 2720–2738.

[30]   Ewan D Dunlop. "Lifetime performance of crystalline silicon PV modules". In: *3rd World Conference onPhotovoltaic Energy Conversion, 2003. Proceedings of*. Vol. 3. IEEE. 2003, pp. 2927–2930.

[31]   Fernando D Novoa, David C Miller, and Reinhold H Dauskardt. "Environmental mechanisms of debonding in photovoltaic backsheets". In: *Solar Energy Materials and Solar Cells* 120 (2014), pp. 87–93.

[32]   Fernando D Novoa, David C Miller, and Reinhold H Dauskardt. "Adhesion and debonding kinetics of photovoltaic encapsulation in moist environments". In: *Progress in Photovoltaics: Research and Applications* 24.2 (2016), pp. 183–194.

[33]   FJ Pern. "Factors that affect the EVA encapsulant discoloration rate upon accelerated exposure". In: *Solar Energy Materials and Solar Cells* 41 (1996), pp. 587–615.

[34]   Bart Rimez et al. "The thermal degradation of poly (vinyl acetate) and poly (ethylene-co-vinyl acetate), Part I: Experimental study of the degradation mechanism". In: *Polymer Degradation and Stability* 93.4 (2008), pp. 800–810.

[35]   Philip Hülsmann and Karl-Anders Weiss. "Simulation of water ingress into PV-modules: IEC-testing versus outdoor exposure". In: *Solar Energy* 115 (2015), pp. 347–353.

[36]   Przemyslaw Rupnowski and Bhushan Sopori. "Strength of silicon wafers: fracture mechanics approach". In: *International journal of fracture* 155 (2009), pp. 67–74.

[37]   S Pingel et al. "Mechanical stability of solar cells within solar panels". In: *Proc. of 24th EUPVSEC* (2009), pp. 3459–3464.

[38]   Z Liu et al. "A continuum large-deformation theory for the coupled modeling of polymer–solvent system with application to PV recycling". In: *International Journal of Engineering Science* 187 (2023), p. 103842.

[39]   Marc Köntges et al. "Impact of transportation on silicon wafer-based photovoltaic modules". In: *Progress in Photovoltaics: research and applications* 24.8 (2016), pp. 1085–1095.

[40] Marcus Assmus et al. "Measurement and simulation of vibrations of PV-modules induced by dynamic mechanical loads". In: *Progress in Photovoltaics: Research and Applications* 19.6 (2011), pp. 688–694.

[41] MA Munoz et al. "Early degradation of silicon PV modules and guaranty conditions". In: *Solar energy* 85.9 (2011), pp. 2264–2274.

[42] Brahmanandam Javvaji et al. "Fracture Properties of Graphene-Coated Silicon for Photovoltaics". In: *Advanced Theory and Simulations* 1.12 (2018), p. 1800097.

[43] Claudia Buerhop et al. "Evolution of cell cracks in PV-modules under field and laboratory conditions". In: *Progress in Photovoltaics: Research and Applications* 26.4 (2018), pp. 261–272.

[44] Jörg Käsewieter et al. "Cracks in solar cell metallization leading to module power loss under mechanical loads". In: *Energy Procedia* 55 (2014), pp. 469–477.

[45] Pooja Chaturvedi, Bram Hoex, and Timothy M Walsh. "Broken metal fingers in silicon wafer solar cells and PV modules". In: *Solar Energy Materials and Solar Cells* 108 (2013), pp. 78–81.

[46] Sarah Kajari-Schröder et al. "Spatial and orientational distribution of cracks in crystalline photovoltaic modules generated by mechanical load tests". In: *Solar Energy Materials and Solar Cells* 95.11 (2011), pp. 3054–3059.

[47] Lamprini Papargyri et al. "Modelling and experimental investigations of microcracks in crystalline silicon photovoltaics: A review". In: *Renewable Energy* 145 (2020), pp. 2387–2408.

[48] Hao Wu. "Wire sawing technology: A state-of-the-art review". In: *Precision engineering* 43 (2016), pp. 1–9.

[49] Frank Reil et al. "The effect of transportation impacts and dynamic load tests on the mechanical and electrical behaviour of crystalline PV modules". In: *Proc. 25h European PV Solar Energy Conference*. 2010, pp. 3989–3992.

[50] Karl-Anders Weiss et al. "Measurement and simulation of dynamic mechanical loads on PV-modules". In: *Reliability of photovoltaic cells, modules, components, and systems II*. Vol. 7412. SPIE. 2009, pp. 18–26.

[51] Yixian Lee and Andrew AO Tay. "Stress analysis of silicon wafer-based photovoltaic modules under IEC 61215 mechanical load test". In: *Energy Procedia* 33 (2013), pp. 265–271.

[52] Mauro Corrado, Andrea Infuso, and Marco Paggi. "Simulated hail impacts on flexible photovoltaic laminates: testing and modelling". In: *Meccanica* 52.6 (2017), pp. 1425–1439.

[53] Andreas Wade et al. "Beyond waste–the fate of end-of-life photovoltaic panels from large scale PV installations in the EU. The socio-economic benefits of high value recycling compared to reuse". In: *Proceedings of the 33rd European Photovoltaic Solar Energy Conference and Exhibition*. 2017, pp. 1507–1514.

[54] Garvin A Heath et al. "Research and development priorities for silicon photovoltaic module recycling to support a circular economy". In: *Nature Energy* 5.7 (2020), pp. 502–510.

[55] Beijia Huang et al. "Environmental influence assessment of China's multi-crystalline silicon (multi-Si) photovoltaic modules considering recycling process". In: *Solar Energy* 143 (2017), pp. 132–141.

[56] Marina M Lunardi et al. "Comparative life cycle assessment of end-of-life silicon solar photovoltaic modules". In: *Applied Sciences* 8.8 (2018), p. 1396.

[57] Marco Tammaro et al. "Experimental investigation to evaluate the potential environmental hazards of photovoltaic panels". In: *Journal of Hazardous Materials* 306 (2016), pp. 395–405.

[58] Michele L Bustamante and Gabrielle Gaustad. "Challenges in assessment of clean energy supply-chains based on byproduct minerals: A case study of tellurium use in thin film photovoltaics". In: *Applied Energy* 123 (2014), pp. 397–414.

[59] Flavia CSM Padoan, Pietro Altimari, and Francesca Pagnanelli. "Recycling of end of life photovoltaic panels: A chemical prospective on process development". In: *Solar Energy* 177 (2019), pp. 746–761.

[60] Pablo Dias et al. "Comprehensive recycling of silicon photovoltaic modules incorporating organic solvent delamination–technical, environmental and economic analyses". In: *Resources, Conservation and Recycling* 165 (2021), p. 105241.

[61] Sanna-Mari Nevala et al. "Electro-hydraulic fragmentation vs conventional crushing of photovoltaic panels–Impact on recycling". In: *Waste Management* 87 (2019), pp. 43–50.

[62] Maurianne Flore Azeumo et al. "Photovoltaic module recycling, a physical and a chemical recovery process". In: *Solar Energy Materials and Solar Cells* 193 (2019), pp. 314–319.

[63] Sheng Pang et al. "Enhanced separation of different layers in photovoltaic panel by microwave field". In: *Solar Energy Materials and Solar Cells* 230 (2021), p. 111213.

[64] Émilie Scheunemann Lovato et al. "Application of supercritical CO2 for delaminating photovoltaic panels to recover valuable materials". In: *Journal of CO2 Utilization* 46 (2021), p. 101477.

[65] TM Bruton. "Re-cycling of high value, high energy content components of silicon PV modules". In: *Proc. of 12th EC-PVSEC*. 1994, pp. 303–304.

[66] Marco Tammaro et al. "Thermal treatment of waste photovoltaic module for recovery and recycling: Experimental assessment of the presence of metals in the gas emissions and in the ashes". In: *Renewable Energy* 81 (2015), pp. 103–112.

[67] Valeria Fiandra et al. "Silicon photovoltaic modules at end-of-life: Removal of polymeric layers and separation of materials". In: *Waste Management* 87 (2019), pp. 97–107.

[68] Jeongeun Shin, Jongsung Park, and Nochang Park. "A method to recycle silicon wafer from end-of-life photovoltaic module and solar panels by using recycled silicon wafers". In: *Solar Energy Materials and Solar Cells* 162 (2017), pp. 1–6.

[69] Venkat Aryan, Mercè Font-Brucart, and Daniel Maga. "A comparative life cycle assessment of end-of-life treatment pathways for photovoltaic backsheets". In: *Progress in Photovoltaics: Research and Applications* 26.7 (2018), pp. 443–459.

[70] Valeria Fiandra et al. "End-of-life of silicon PV panels: A sustainable materials recovery process". In: *Waste Management* 84 (2019), pp. 91–101.

[71] Lingen Zhang and Zhenming Xu. "Separating and recycling plastic, glass, and gallium from waste solar cell modules by nitrogen pyrolysis and vacuum decomposition". In: *Environmental Science & Technology* 50.17 (2016), pp. 9242–9250.

[72]   Takuya Doi et al. "Experimental study on PV module recycling with organic solvent method". In: *Solar Energy Materials and Solar Cells* 67.1-4 (2001), pp. 397–403.

[73]   Sukmin Kang et al. "Experimental investigations for recycling of silicon and glass from waste photovoltaic modules". In: *Renewable Energy* 47 (2012), pp. 152–159.

[74]   DS Prasad et al. "Process optimization studies of essential parameters in the organic solvent method for the recycling of waste crystalline silicon photovoltaic modules". In: *Solar Energy Materials and Solar Cells* 245 (2022), p. 111850.

[75]   Ke Li et al. "A green method to separate different layers in photovoltaic modules by using DMPU as a separation agent". In: *Solar Energy Materials and Solar Cells* 245 (2022), p. 111870.

[76]   Youngjin Kim and Jaeryeong Lee. "Dissolution of ethylene vinyl acetate in crystalline silicon PV modules using ultrasonic irradiation and organic solvent". In: *Solar energy materials and solar cells* 98 (2012), pp. 317–322.

[77]   Wen-Hsi Huang et al. "Strategy and technology to recycle wafer-silicon solar modules". In: *Solar Energy* 144 (2017), pp. 22–31.

[78]   Yang Liu et al. "Recycling high purity silicon from solar grade silicon cutting slurry waste by carbothermic reduction in the electric arc furnace". In: *Journal of Cleaner Production* 224 (2019), pp. 709–718.

[79]   Jongsung Park et al. "An eco-friendly method for reclaimed silicon wafers from a photovoltaic module: from separation to cell fabrication". In: *Green Chemistry* 18.6 (2016), pp. 1706–1714.

[80]   Jun-Kyu Lee et al. "Simple pretreatment processes for successful reclamation and remanufacturing of crystalline silicon solar cells". In: *Progress in Photovoltaics: Research and Applications* 26.3 (2018), pp. 179–187.

[81]   M Gagliardi and M Paggi. "Multiphysics analysis of backsheet blistering in photovoltaic modules". In: *Solar Energy* 183 (2019), pp. 512–520.

[82]   Pietro Lenarda and Marco Paggi. "A geometrical multi-scale numerical method for coupled hygro-thermo-mechanical problems in photovoltaic laminates". In: *Computational Mechanics* 57 (2016), pp. 947–963.

[83] Zeng Liu et al. "A multifield coupled thermo-chemo-mechanical theory for the reaction-diffusion modeling in photovoltaics". In: *International Journal for Numerical Methods in Engineering* (2023).

[84] Marco Paggi, Mauro Corrado, and Maria Alejandra Rodriguez. "A multi-physics and multi-scale numerical approach to microcracking and power-loss in photovoltaic modules". In: *Composite Structures* 95 (2013), pp. 630–638.

[85] Ulrich Eitner et al. "Thermal stress and strain of solar cells in photovoltaic modules". In: *Shell-like Structures*. Springer, 2011, pp. 453–468.

[86] Marco Paggi, Sarah Kajari-Schröder, and Ulrich Eitner. "Thermomechanical deformations in photovoltaic laminates". In: *The Journal of Strain Analysis for Engineering Design* 46.8 (2011), pp. 772–782.

[87] Francesco Mainardi. "An introduction to mathematical models". In: *Fractional calculus and waves in linear viscoelasticity. Imperial College Press, London* (2010).

[88] Mario Di Paola, Francesco Paolo Pinnola, and Massimiliano Zingales. "A discrete mechanical model of fractional hereditary materials". In: *Meccanica* 48.7 (2013), pp. 1573–1586.

[89] Mi Di Paola, A Pirrotta, and A Valenza. "Visco-elastic behavior through fractional calculus: an easier method for best fitting experimental results". In: *Mechanics of materials* 43.12 (2011), pp. 799–806.

[90] Marco Paggi and Alberto Sapora. "An accurate thermoviscoelastic rheological model for ethylene vinyl acetate based on fractional calculus". In: *International Journal of Photoenergy* 2015 (2015).

[91] K Rah et al. "Optimal low-order fully integrated solid-shell elements". In: *Computational Mechanics* 51.3 (2013), pp. 309–326.

[92] L Vu-Quoc and XG Tan. "Optimal solid shells for non-linear analyses of multilayer composites. I. Statics". In: *Computer Methods in Applied Mechanics and Engineering* 192.9-10 (2003), pp. 975–1016.

[93] Y Başar and Y Ding. "Shear deformation models for large-strain shell analysis". In: *International Journal of Solids and Structures* 34.14 (1997), pp. 1687–1708.

[94] P Betsch, F Gruttmann, and E Stein. "A 4-node finite shell element for the implementation of general hyperelastic 3D-elasticity at finite strains". In: *Computer Methods in Applied Mechanics and Engineering* 130.1-2 (1996), pp. 57–79.

[95] Boštjan Brank. "Nonlinear shell models with seven kinematic parameters". In: *Computer methods in applied mechanics and engineering* 194.21-24 (2005), pp. 2336–2362.

[96] Norbert Büchter, Ekkehard Ramm, and Deane Roehl. "Three dimensional extension of non-linear shell formulation based on the enhanced assumed strain concept". In: *International Journal for Numerical Methods in Engineering* 37.15 (1994), pp. 2551–2568.

[97] H Parisch. "A continuum-based shell theory for non-linear applications". In: *International Journal for Numerical Methods in Engineering* 38.11 (1995), pp. 1855–1883.

[98] JC Simo, MS Rifai, and DD Fox. "On a stress resultant geometrically exact shell model. Part IV: Variable thickness shells with through-the-thickness stretching". In: *Computer Methods in Applied Mechanics and Engineering* 81.1 (1990), pp. 91–126.

[99] C Miehe. "A theoretical and computational model for isotropic elastoplastic stress analysis in shells at large strains". In: *Computer Methods in Applied Mechanics and Engineering* 155.3-4 (1998), pp. 193–233.

[100] J Reinoso and A Blázquez. "Application and finite element implementation of 7-parameter shell element for geometrically nonlinear analysis of layered CFRP composites". In: *Composite structures* 139 (2016), pp. 263–276.

[101] M Harnau and K Schweizerhof. "About linear and quadratic "solid-shell" elements at large deformations". In: *Computers & structures* 80.9-10 (2002), pp. 805–817.

[102] S Klinkel and W Wagner. "A geometrical non-linear brick element based on the EAS-method". In: *International Journal for Numerical Methods in Engineering* 40.24 (1997), pp. 4529–4545.

[103] M Schwarze and S Reese. "A reduced integration solid-shell finite element based on the EAS and the ANS concept—geometrically linear problems". In: *International Journal for Numerical Methods in Engineering* 80.10 (2009), pp. 1322–1355.

[104] M Braun, M Bischoff, and E Ramm. "Nonlinear shell formulations for complete three-dimensional constitutive laws including composites and laminates". In: *Computational Mechanics* 15.1 (1994), pp. 1–18.

[105] Klaus-Jürgen Bathe and Eduardo N Dvorkin. "A four-node plate bending element based on Mindlin/Reissner plate theory and a mixed interpolation". In: *International Journal for Numerical Methods in Engineering* 21.2 (1985), pp. 367–383.

[106] M Bischoff and E Ramm. "Shear deformable shell elements for large strains and rotations". In: *International Journal for Numerical Methods in Engineering* 40.23 (1997), pp. 4427–4449.

[107] Ralf Hauptmann, Karl Schweizerhof, and Stefan Doll. "Extension of the 'solid-shell'concept for application to large elastic and large elastoplastic deformations". In: *International Journal for Numerical Methods in Engineering* 49.9 (2000), pp. 1121–1141.

[108] Joze Korelc and Peter Wriggers. "Consistent gradient formulation for a stable enhanced strain method for large deformations". In: *Engineering Computations* (1996).

[109] JC Simo, F Armero, and RL Taylor. "Improved versions of assumed enhanced strain tri-linear elements for 3D finite deformation problems". In: *Computer methods in applied mechanics and engineering* 110.3-4 (1993), pp. 359–386.

[110] Juan C Simo and MS Rifai. "A class of mixed assumed strain methods and the method of incompatible modes". In: *International journal for numerical methods in engineering* 29.8 (1990), pp. 1595–1638.

[111] RA Valente et al. "On the use of an enhanced transverse shear strain shell element for problems involving large rotations". In: *Computational Mechanics* 30.4 (2003), pp. 286–296.

[112] P Betsch and E Stein. "An assumed strain approach avoiding artificial thickness straining for a non-linear 4-node shell element". In: *Communications in Numerical Methods in Engineering* 11.11 (1995), pp. 899–909.

[113] Eduardo N Dvorkin and Klaus-Jürgen Bathe. "A continuum mechanics based four-node shell element for general non-linear analysis". In: *Engineering computations* (1984).

[114] Rui PR Cardoso et al. "Enhanced assumed strain (EAS) and assumed natural strain (ANS) methods for one-point quadrature solid-shell elements". In: *International Journal for Numerical Methods in Engineering* 75.2 (2008), pp. 156–187.

[115] F Gruttmann and W Wagner. "Structural analysis of composite laminates using a mixed hybrid shell element". In: *Computational Mechanics* 37.6 (2006), pp. 479–497.

[116] Eric P Kasper and Robert L Taylor. "A mixed-enhanced strain method: Part II: Geometrically nonlinear problems". In: *Computers & Structures* 75.3 (2000), pp. 251–260.

[117] Gustavo Weber and Lallit Anand. "Finite deformation constitutive equations and a time integration procedure for isotropic, hyperelastic viscoplastic solids". In: *Computer Methods in Applied Mechanics and Engineering* 79.2 (1990), pp. 173–202.

[118] S Bargmann and Paul Steinmann. "Theoretical and computational aspects of non-classical thermoelasticity". In: *Computer methods in applied mechanics and engineering* 196.1-3 (2006), pp. 516–527.

[119] Ellen Kuhl et al. "Application of the material force method to thermo-hyperelasticity". In: *Computer Methods in Applied Mechanics and Engineering* 193.30-32 (2004), pp. 3303–3325.

[120] Mauro Corrado and Marco Paggi. "Nonlinear fracture dynamics of laminates with finite thickness adhesives". In: *Mechanics of Materials* 80 (2015), pp. 183–192.

[121] Pietro Lenarda and Marco Paggi. "A computational framework for rheologically complex thermo-visco-elastic materials". In: *International Journal of Solids and Structures* 236 (2022), p. 111297.

[122] Alberto Sapora and Marco Paggi. "A coupled cohesive zone model for transient analysis of thermoelastic interface debonding". In: *Computational Mechanics* 53.4 (2014), pp. 845–857.

[123] Sven Klinkel, Friedrich Gruttmann, and Werner Wagner. "A robust non-linear solid shell element based on a mixed variational formulation". In: *Computer Methods in Applied Mechanics and Engineering* 195.1-3 (2006), pp. 179–201.

[124] Juan-Carlos Simo and Francisco Armero. "Geometrically non-linear enhanced strain mixed methods and the method of incompatible modes". In: *International Journal for Numerical Methods in Engineering* 33.7 (1992), pp. 1413–1449.

[125] J Reinoso et al. "Experimental and three-dimensional global-local finite element analysis of a composite component including degradation process at the interfaces". In: *Composites Part B: Engineering* 43.4 (2012), pp. 1929–1942.

[126] Jose Reinoso and Marco Paggi. "A consistent interface element formulation for geometrical and material nonlinearities". In: *Computational Mechanics* 54.6 (2014), pp. 1569–1581.

[127] John Crank. *The mathematics of diffusion*. Oxford University Press, 1979.

[128] Changwoon Han. "Analysis of moisture-induced degradation of thin-film photovoltaic module". In: *Solar Energy Materials and Solar Cells* 210 (2020), p. 110488.

[129] Irene Berardone and Marco Paggi. "Nondestructive monitoring of damage caused by accelerated ageing in photovoltaic modules". In: *Proceedings of the Institution of Mechanical Engineers, Part C: Journal of Mechanical Engineering Science* 233.23-24 (2019), pp. 7565–7572.

[130] DR Wolters. "On the oxidation kinetics of silicon: the role of water". In: *Journal of the Electrochemical Society* 127.9 (1980), p. 2072.

[131] Z Liu, J Reinoso, and M Paggi. "Phase field modeling of brittle fracture in large-deformation solid shells with the efficient quasi-Newton solution and global–local approach". In: *Computer Methods in Applied Mechanics and Engineering* 399 (2022), p. 115410.

[132] Xinhai Xu et al. "Nondestructive silicon wafer recovery by a novel method of solvothermal swelling coupled with thermal decomposition". In: *Chemical Engineering Journal* 418 (2021), p. 129457.

[133] Marco Paggi and Peter Wriggers. "A nonlocal cohesive zone model for finite thickness interfaces–Part I: mathematical formulation and validation with molecular dynamics". In: *Computational Materials Science* 50.5 (2011), pp. 1625–1633.

[134] Marco Paggi and Peter Wriggers. "A nonlocal cohesive zone model for finite thickness interfaces–Part II: FE implementation and application to polycrystalline materials". In: *Computational Materials Science* 50.5 (2011), pp. 1634–1643.

[135] Marco Paggi et al. "A numerical investigation of the interplay between cohesive cracking and plasticity in polycrystalline materials". In: *Computational materials science* 77 (2013), pp. 81–92.

[136] Marco Paggi and Peter Wriggers. "Stiffness and strength of hierarchical polycrystalline materials with imperfect interfaces". In: *Journal of the Mechanics and Physics of Solids* 60.4 (2012), pp. 557–572.

[137] Andrea Infuso, Mauro Corrado, and Marco Paggi. "Image analysis of polycrystalline solar cells and modelling of intergranular and transgranular cracking". In: *Journal of the European Ceramic Society* 34.11 (2014), pp. 2713–2722.

[138] Michael Ortiz and Anna Pandolfi. "Finite-deformation irreversible cohesive elements for three-dimensional crack-propagation analysis". In: *International journal for numerical methods in engineering* 44.9 (1999), pp. 1267–1282.

[139] Julia Mergheim, Ellen Kuhl, and Paul Steinmann. "A finite element method for the computational modelling of cohesive cracks". In: *International Journal for Numerical Methods in Engineering* 63.2 (2005), pp. 276–289.

[140] Julia Mergheim and Paul Steinmann. "A geometrically nonlinear FE approach for the simulation of strong and weak discontinuities". In: *Computer Methods in Applied Mechanics and Engineering* 195.37-40 (2006), pp. 5037–5052.

[141] Lucie Spannraft, Paul Steinmann, and Julia Mergheim. "A generalized anisotropic damage interface model for finite strains". In: *Journal of the Mechanics and Physics of Solids* 174 (2023), p. 105255.

[142] Nicolas Moës, John Dolbow, and Ted Belytschko. "A finite element method for crack growth without remeshing". In: *International journal for numerical methods in engineering* 46.1 (1999), pp. 131–150.

[143] JC Simo, J Oliver, and F Armero. "An analysis of strong discontinuities induced by strain-softening in rate-independent inelastic solids". In: *Computational mechanics* 12.5 (1993), pp. 277–296.

[144] Javier Oliver et al. "Stability and robustness issues in numerical modeling of material failure with the strong discontinuity approach". In: *Computer Methods in Applied Mechanics and Engineering* 195.52 (2006), pp. 7093–7114.

[145]   A Simone, Carlos Armando Duarte, and E Van der Giessen. "A generalized finite element method for polycrystals with discontinuous grain boundaries". In: *International Journal for Numerical Methods in Engineering* 67.8 (2006), pp. 1122–1145.

[146]   Christian Miehe, Martina Hofacker, and Fabian Welschinger. "A phase field model for rate-independent crack propagation: Robust algorithmic implementation based on operator splits". In: *Computer Methods in Applied Mechanics and Engineering* 199.45-48 (2010), pp. 2765–2778.

[147]   Michael J Borden et al. "A phase-field description of dynamic brittle fracture". In: *Computer Methods in Applied Mechanics and Engineering* 217 (2012), pp. 77–95.

[148]   Marco Paggi, Mauro Corrado, and José Reinoso. "Fracture of solar-grade anisotropic polycrystalline Silicon: A combined phase field–cohesive zone model approach". In: *Computer Methods in Applied Mechanics and Engineering* 330 (2018), pp. 123–148.

[149]   Valerio Carollo, José Reinoso, and Marco Paggi. "A 3D finite strain model for intralayer and interlayer crack simulation coupling the phase field approach and cohesive zone model". In: *Composite Structures* 182 (2017), pp. 636–651.

[150]   Gilles A Francfort and J-J Marigo. "Revisiting brittle fracture as an energy minimization problem". In: *Journal of the Mechanics and Physics of Solids* 46.8 (1998), pp. 1319–1342.

[151]   Michel Frémond and Boumediene Nedjar. "Damage, gradient of damage and principle of virtual power". In: *International journal of solids and structures* 33.8 (1996), pp. 1083–1103.

[152]   RHJ Peerlings et al. "A critical comparison of nonlocal and gradient-enhanced softening continua". In: *International Journal of solids and Structures* 38.44-45 (2001), pp. 7723–7746.

[153]   Claudia Comi and Umberto Perego. "Fracture energy based bi-dissipative damage model for concrete". In: *International journal of solids and structures* 38.36-37 (2001), pp. 6427–6454.

[154]   M Hofacker and C Miehe. "A phase field model of dynamic fracture: Robust field updates for the analysis of complex crack patterns". In: *International Journal for Numerical Methods in Engineering* 93.3 (2013), pp. 276–301.

[155] Marreddy Ambati, Tymofiy Gerasimov, and Laura De Lorenzis. "Phase-field modeling of ductile fracture". In: *Computational Mechanics* 55 (2015), pp. 1017–1040.

[156] Osman Gültekin, Hüsnü Dal, and Gerhard A Holzapfel. "A phase-field approach to model fracture of arterial walls: theory and finite element analysis". In: *Computer methods in applied mechanics and engineering* 312 (2016), pp. 542–566.

[157] Christian Miehe, Lisa-Marie Schaenzel, and Heike Ulmer. "Phase field modeling of fracture in multi-physics problems. Part I. Balance of crack surface and failure criteria for brittle crack propagation in thermo-elastic solids". In: *Computer Methods in Applied Mechanics and Engineering* 294 (2015), pp. 449–485.

[158] JD Clayton and J Knap. "Phase field modeling of directional fracture in anisotropic polycrystals". In: *Computational Materials Science* 98 (2015), pp. 158–169.

[159] JD Clayton and J Knap. "Phase field modeling and simulation of coupled fracture and twinning in single crystals and polycrystals". In: *Computer Methods in Applied Mechanics and Engineering* 312 (2016), pp. 447–467.

[160] John H Wohlgemuth et al. "The effect of cell thickness on module reliability". In: *2008 33rd IEEE Photovoltaic Specialists Conference*. IEEE. 2008, pp. 1–4.

[161] Barbara Terheiden et al. "Manufacturing 100-μm-thick silicon solar cells with efficiencies greater than 20% in a pilot production line". In: *physica status solidi (a)* 212.1 (2015), pp. 13–24.

[162] Per Arne Wang. "Industrial challenges for thin wafer manufacturing". In: *2006 IEEE 4th World Conference on Photovoltaic Energy Conference*. Vol. 1. IEEE. 2006, pp. 1179–1182.

[163] Pavan Kumar Asur Vijaya Kumar et al. "Nonlinear thermo-elastic phase-field fracture of thin-walled structures relying on solid shell concepts". In: *Computer Methods in Applied Mechanics and Engineering* 396 (2022), p. 115096.

[164] Pavan Kumar Asur Vijaya Kumar et al. "Thermo-elastic solid shell formulation with phase field fracture for thin-walled FGMs". In: *Thin-Walled Structures* 179 (2022), p. 109535.

[165] Heike Ulmer, Martina Hofacker, and Christian Miehe. "Phase field modeling of fracture in plates and shells". In: *PAMM* 12.1 (2012), pp. 171–172.

[166] Fatemeh Amiri et al. "Phase-field modeling of fracture in linear thin shells". In: *Theoretical and Applied Fracture Mechanics* 69 (2014), pp. 102–109.

[167] Karsten Paul et al. "An adaptive space-time phase field formulation for dynamic fracture of brittle shells based on LR NURBS". In: *Computational Mechanics* 65.4 (2020), pp. 1039–1062.

[168] Josef Kiendl et al. "Phase-field description of brittle fracture in plates and shells". In: *Computer Methods in Applied Mechanics and Engineering* 312 (2016), pp. 374–394.

[169] Davide Proserpio et al. "A framework for efficient isogeometric computations of phase-field brittle fracture in multipatch shell structures". In: *Computer Methods in Applied Mechanics and Engineering* 372 (2020), p. 113363.

[170] Karsten Paul et al. "Isogeometric continuity constraints for multi-patch shells governed by fourth-order deformation and phase field models". In: *Computer Methods in Applied Mechanics and Engineering* 370 (2020), p. 113219.

[171] G Kikis et al. "Phase-field model of brittle fracture in Reissner–Mindlin plates and shells". In: *Computer Methods in Applied Mechanics and Engineering* 373 (2021), p. 113490.

[172] Udit Pillai et al. "Phase-field modelling of brittle fracture in thin shell elements based on the MITC4+ approach". In: *Computational Mechanics* 65.6 (2020), pp. 1413–1432.

[173] José Reinoso, Marco Paggi, and Christian Linder. "Phase field modeling of brittle fracture for enhanced assumed strain shells at large deformations: formulation and finite element implementation". In: *Computational Mechanics* 59.6 (2017), pp. 981–1001.

[174] Marreddy Ambati and Laura De Lorenzis. "Phase-field modeling of brittle and ductile fracture in shells with isogeometric NURBS-based solid-shell elements". In: *Computer Methods in Applied Mechanics and Engineering* 312 (2016), pp. 351–373.

[175]   P Areias, T Rabczuk, and MA Msekh. "Phase-field analysis of finite-strain plates and shells including element subdivision". In: *Computer Methods in Applied Mechanics and Engineering* 312 (2016), pp. 322–350.

[176]   Davide Proserpio et al. "Phase-field simulation of ductile fracture in shell structures". In: *Computer Methods in Applied Mechanics and Engineering* 385 (2021), p. 114019.

[177]   Christian Miehe, Fabian Welschinger, and Martina Hofacker. "Thermodynamically consistent phase-field models of fracture: Variational principles and multi-field FE implementations". In: *International journal for numerical methods in engineering* 83.10 (2010), pp. 1273–1311.

[178]   Blaise Bourdin, Gilles A Francfort, and Jean-Jacques Marigo. "Numerical experiments in revisited brittle fracture". In: *Journal of the Mechanics and Physics of Solids* 48.4 (2000), pp. 797–826.

[179]   Samuel Forest. "Micromorphic approach for gradient elasticity, viscoplasticity, and damage". In: *Journal of Engineering Mechanics* 135.3 (2009), pp. 117–131.

[180]   Osman Gültekin, Hüsnü Dal, and Gerhard A Holzapfel. "Numerical aspects of anisotropic failure in soft biological tissues favor energy-based criteria: A rate-dependent anisotropic crack phase-field model". In: *Computer methods in applied mechanics and engineering* 331 (2018), pp. 23–52.

[181]   TT Nguyen et al. "Multi-phase-field modeling of anisotropic crack propagation for polycrystalline materials". In: *Computational Mechanics* 60 (2017), pp. 289–314.

[182]   John D Clayton and J Knap. "A geometrically nonlinear phase field theory of brittle fracture". In: *International Journal of Fracture* 189.2 (2014), pp. 139–148.

[183]   R Cavuoto et al. "Failure through crack propagation in components with holes and notches: An experimental assessment of the phase field model". In: *International Journal of Solids and Structures* 257 (2022), p. 111798.

[184]   Mohammed A Msekh et al. "Abaqus implementation of phase-field model for brittle fracture". In: *Computational Materials Science* 96 (2015), pp. 472–484.

[185] Jian-Ying Wu, Yuli Huang, and Vinh Phu Nguyen. "On the BFGS monolithic algorithm for the unified phase field damage theory". In: *Computer Methods in Applied Mechanics and Engineering* 360 (2020), p. 112704.

[186] Hermann Matthies and Gilbert Strang. "The solution of nonlinear finite element equations". In: *International journal for numerical methods in engineering* 14.11 (1979), pp. 1613–1626.

[187] Eduard Marenić, Ivica Skozrit, and Zdenko Tonković. "On the calculation of stress intensity factors and J-integrals using the submodeling technique". In: *Journal of pressure vessel technology* 132.4 (2010).

[188] AE Bogdanovich and I Kizhakkethara. "Three-dimensional finite element analysis of double-lap composite adhesive bonded joint using submodeling approach". In: *Composites Part B: Engineering* 30.6 (1999), pp. 537–551.

[189] DS Mikhaluk et al. "Experimental observations and finite element modelling of damage initiation and evolution in carbon/epoxy non-crimp fabric composites". In: *Engineering Fracture Mechanics* 75.9 (2008), pp. 2751–2766.

[190] Fadi Aldakheel et al. "Multilevel global–local techniques for adaptive ductile phase-field fracture". In: *Computer Methods in Applied Mechanics and Engineering* 387 (2021), p. 114175.

[191] Fadi Aldakheel et al. "A global–local approach for hydraulic phase-field fracture in poroelastic media". In: *Computers & Mathematics with Applications* 91 (2021), pp. 99–121.

[192] Nima Noii et al. "An adaptive global–local approach for phase-field modeling of anisotropic brittle fracture". In: *Computer Methods in Applied Mechanics and Engineering* 361 (2020), p. 112744.

[193] Martin Sander et al. "Systematic investigation of cracks in encapsulated solar cells after mechanical loading". In: *Solar Energy Materials and Solar Cells* 111 (2013), pp. 82–89.

[194] Pietro Carrara et al. "A framework to model the fatigue behavior of brittle materials based on a variational phase-field approach". In: *Computer Methods in Applied Mechanics and Engineering* 361 (2020), p. 112731.

[195]   Jing Tao and Suiran Yu. "Review on feasible recycling pathways and technologies of solar photovoltaic modules". In: *Solar Energy Materials and Solar Cells* 141 (2015), pp. 108–124.

[196]   Stephanie Weckend, Andreas Wade, and Garvin A Heath. *End of life management: solar photovoltaic panels*. Tech. rep. National Renewable Energy Lab.(NREL), Golden, CO (United States), 2016.

[197]   Marco Paggi et al. "Fatigue degradation and electric recovery in Silicon solar cells embedded in photovoltaic modules". In: *Scientific Reports* 4.1 (2014), pp. 1–7.

[198]   F Corcelli, M Ripa, and S Ulgiati. "End-of-life treatment of crystalline silicon photovoltaic panels. An emergy-based case study". In: *Journal of Cleaner Production* 161 (2017), pp. 1129–1142.

[199]   Rong Deng et al. "A techno-economic review of silicon photovoltaic module recycling". In: *Renewable and Sustainable Energy Reviews* 109 (2019), pp. 532–550.

[200]   Haoyang He et al. "The role of data source selection in chemical hazard assessment: A case study on organic photovoltaics". In: *Journal of Hazardous Materials* 365 (2019), pp. 227–236.

[201]   Preeti Nain and Arun Kumar. "Ecological and human health risk assessment of metals leached from end-of-life solar photovoltaics". In: *Environmental Pollution* 267 (2020), p. 115393.

[202]   CC Farrell et al. "Technical challenges and opportunities in realising a circular economy for waste photovoltaic modules". In: *Renewable and Sustainable Energy Reviews* 128 (2020), p. 109911.

[203]   Caijie Liu, Qin Zhang, and Hai Wang. "Cost-benefit analysis of waste photovoltaic module recycling in China". In: *Waste Management* 118 (2020), pp. 491–500.

[204]   Rong Deng, Yuting Zhuo, and Yansong Shen. "Recent progress in silicon photovoltaic module recycling processes". In: *Resources, Conservation and Recycling* 187 (2022), p. 106612.

[205]   Dheeraj Sah, Sushil Kumar, et al. "Recovery and analysis of valuable materials from a discarded crystalline silicon solar module". In: *Solar Energy Materials and Solar Cells* 246 (2022), p. 111908.

[206]   Xiaopu Wang et al. "A review of end-of-life crystalline silicon solar photovoltaic panel recycling technology". In: *Solar Energy Materials and Solar Cells* 248 (2022), p. 111976.

[207]   Hao Cui et al. "Technoeconomic analysis of high-value, crystalline silicon photovoltaic module recycling processes". In: *Solar Energy Materials and Solar Cells* 238 (2022), p. 111592.

[208]   AD Drozdov. "Mechanical behavior of temperature-sensitive gels under equilibrium and transient swelling". In: *International Journal of Engineering Science* 128 (2018), pp. 79–100.

[209]   Eanna Fennell et al. "A strain induced softening and hardening constitutive model for superabsorbent polymers undergoing finite deformation". In: *International Journal of Engineering Science* 154 (2020), p. 103346.

[210]   Seungik Baek and Thomas J Pence. "On swelling induced degradation of fiber reinforced polymers". In: *International Journal of Engineering Science* 47.11-12 (2009), pp. 1100–1109.

[211]   Stefano A Mezzasalma et al. "Rubber elasticity of polymer networks in explicitly non-Gaussian states. Statistical mechanics and LF-NMR inquiry in hydrogel systems". In: *International Journal of Engineering Science* 176 (2022), p. 103676.

[212]   Toyoichi Tanaka and David J Fillmore. "Kinetics of swelling of gels". In: *The Journal of Chemical Physics* 70.3 (1979), pp. 1214–1218.

[213]   Fernando P Duda, Angela C Souza, and Eliot Fried. "A theory for species migration in a finitely strained solid with application to polymer network swelling". In: *Journal of the Mechanics and Physics of Solids* 58.4 (2010), pp. 515–529.

[214]   Mohammad Reza Bayat, Kui Wang, and Mostafa Baghani. "Visco-hyperelastic swelling and mechanical behavior of tough pH-sensitive hydrogels: theory development and numerical implementation". In: *International Journal of Engineering Science* 152 (2020), p. 103294.

[215]   Malte Sauerwein and Holger Steeb. "Modeling of dynamic hydrogel swelling within the pore space of a porous medium". In: *International Journal of Engineering Science* 155 (2020), p. 103353.

[216]   Akhilesh Dadaniya and Naresh Varma Datla. "Degradation prediction of encapsulant-glass adhesion in the photovoltaic module under outdoor and accelerated exposures". In: *Solar Energy* 208 (2020), pp. 419–429.
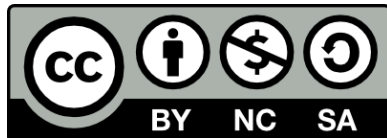
[217] Neelkanth G Dhere et al. "Outdoor performance testing of thin-film PV modules in the hot and humid climate". In: *2013 IEEE 39th Photovoltaic Specialists Conference (PVSC)*. IEEE. 2013, pp. 2994–2997.

[218] Michael Kempe. "Overview of scientific issues involved in selection of polymers for PV applications". In: *2011 37th IEEE Photovoltaic Specialists Conference*. IEEE. 2011, pp. 000085–000090.

[219] V Svorčiék et al. "Permittivity of polyethylene and polyethyleneterephtalate". In: *Journal of materials science letters* 19.20 (2000), pp. 1843–1845.

[220] Timothy P Ferguson and Jianmin Qu. "An engineering model for moisture degradation of polymer/metal interfacial fracture toughness". In: *Proceedings. International Symposium on Advanced Packaging Materials: Processes, Properties and Interfaces, 2005.* IEEE. 2005, pp. 298–301.

[221] Dan Wu et al. "Degradation of interfacial adhesion strength within photovoltaic mini-modules during damp-heat exposure". In: *Progress in Photovoltaics: Research and Applications* 22.7 (2014), pp. 796–809.

[222] NV Datla et al. "Effects of hygrothermal aging on the fatigue behavior of two toughened epoxy adhesives". In: *Engineering Fracture Mechanics* 79 (2012), pp. 61–77.

[223] Ronald Krueger. "Virtual crack closure technique: History, approach, and applications". In: *Appl. Mech. Rev.* 57.2 (2004), pp. 109–143.

[224] Arne Hillerborg. "Fracture mechanics concepts applied to moment capacity and rotational capacity of reinforced concrete beams". In: *Engineering Fracture Mechanics* 35.1-3 (1990), pp. 233–240.

[225] A Carpinteri. "Finite deformation effects in homogeneous and interfacial fracture". In: *Eng Fract Mech* 32 (1989), pp. 265–278.

[226] Alberto Carpinteri. "Cusp catastrophe interpretation of fracture instability". In: *Journal of the Mechanics and Physics of Solids* 37.5 (1989), pp. 567–582.

[227] Alberto Carpinteri. "Softening and snap-back instability in cohesive solids". In: *International Journal for Numerical Methods in Engineering* 28.7 (1989), pp. 1521–1537.

[228] Roberta Massabò and Hossein Darban. "Mode II dominant fracture of layered composite beams and wide-plates: a homogenized structural approach". In: *Engineering Fracture Mechanics* 213 (2019), pp. 280–301.

[229] Marco Paggi and Peter Wriggers. "A nonlocal cohesive zone model for finite thickness interfaces–Part I: mathematical formulation and validation with molecular dynamics". In: *Computational Materials Science* 50.5 (2011), pp. 1625–1633.

[230] Marco Paggi and José Reinoso. "An anisotropic large displacement cohesive zone model for fibrillar and crazing interfaces". In: *International Journal of Solids and Structures* 69 (2015), pp. 106–120.

[231] Sushovan Roychowdhury, Yamuna Das Arun Roy, and Robert H Dodds Jr. "Ductile tearing in thin aluminum panels: experiments and analyses using large-displacement, 3-D surface cohesive elements". In: *Engineering Fracture Mechanics* 69.8 (2002), pp. 983–1002.

[232] M.J. van den Bosch, P.J.G. Schreurs, and M.G.D. Geers. "A cohesive zone model with a large displacement formulation accounting for interfacial fibrilation". In: *European Journal of Mechanics - A/Solids* 26.1 (2007), pp. 1–19.

[233] Viggo Tvergaard. "Effect of fibre debonding in a whisker-reinforced metal". In: *Materials science and engineering: A* 125.2 (1990), pp. 203–213.

[234] Morton E Gurtin, Eliot Fried, and Lallit Anand. *The mechanics and thermodynamics of continua*. Cambridge University Press, 2010.

[235] Peter Wriggers. *Nonlinear finite element methods*. Springer Science & Business Media, 2008.

[236] Aidin Hajikhani, Peter Wriggers, and Michele Marino. "Chemo-mechanical modelling of swelling and crosslinking reaction kinetics in alginate hydrogels: A novel theory and its numerical implementation". In: *Journal of the Mechanics and Physics of Solids* 153 (2021), p. 104476.

[237] Berkin Dortdivanlioglu and Christian Linder. "Diffusion-driven swelling-induced instabilities of hydrogels". In: *Journal of the Mechanics and Physics of Solids* 125 (2019), pp. 38–52.

[238] Dominic Zäh and Christian Miehe. "Multiplicative electro-elasticity of electroactive polymers accounting for micromechanically-based network models". In: *Computer Methods in Applied Mechanics and Engineering* 286 (2015), pp. 394–421.

[239] Eduardo Dıéez et al. "Turbidimetric and intrinsic viscosity study of EVA copolymer–solvent systems". In: *Polymer Bulletin* 71.1 (2014), pp. 193–206.

[240] Shawn A Chester and Lallit Anand. "A thermo-mechanically coupled theory for fluid permeation in elastomeric materials: application to thermally responsive gels". In: *Journal of the Mechanics and Physics of Solids* 59.10 (2011), pp. 1978–2006.

[241] I Espinasse et al. "Characterization of crosslinking of random polymer network by rheological and equilibrium swelling data". In: *Journal of Applied Polymer Science* 54.13 (1994), pp. 2083–2089.

[242] Stefan-H Schulze et al. "Cure state assessment of EVA-copolymers for PV-applications comparing dynamic-mechanical, dielectric and calorimetric properties". In: *Solar Energy Materials and Solar Cells* 143 (2015), pp. 411–417.

[243] Gernot M Wallner et al. "Comparison of crosslinking Kinetics of UV-Transparent ethylene-vinyl acetate copolymer and polyolefin elastomer encapsulants". In: *Polymers* 14.7 (2022), p. 1441.

[244] HJ Mencer and Z Gomzi. "Swelling kinetics of polymer-solvent systems". In: *European Polymer Journal* 30.1 (1994), pp. 33–36.

[245] A Badiee, IA Ashcroft, and Ricky D Wildman. "The thermo-mechanical degradation of ethylene vinyl acetate used as a solar panel adhesive and encapsulant". In: *International Journal of Adhesion and Adhesives* 68 (2016), pp. 212–218.

[246] Suvendu Padhi, P GANGA RAJU ACHARY, and Nimai C Nayak. "Molecular transport behaviour of organic solvents through halloysite nanotubes filled ethylene–vinyl acetate copolymer". In: *Bulletin of Materials Science* 38.4 (2015), pp. 925–933.

[247] AW Czanderna and FJ Pern. "Encapsulation of PV modules using ethylene vinyl acetate copolymer as a pottant: A critical review". In: *Solar Energy Materials and Solar Cells* 43.2 (1996), pp. 101–181.

[248] Ch Hirschl et al. "Determining the degree of crosslinking of ethylene vinyl acetate photovoltaic module encapsulants—A comparative study". In: *Solar Energy Materials and Solar Cells* 116 (2013), pp. 203–218.

[249] Ronald FM Lange et al. "The lamination of (multi) crystalline and thin film based photovoltaic modules". In: *Progress in Photovoltaics: Research and Applications* 19.2 (2011), pp. 127–133.

[250] Michael Koehl, Markus Heck, and Stefan Wiesmeier. "Modelling of conditions for accelerated lifetime testing of Humidity impact on PV-modules based on monitoring of climatic data". In: *Solar Energy Materials and Solar Cells* 99 (2012), pp. 282–291.

[251] David Chuen Chun Lam, Fan Yang, and Pin Tong. "Chemical kinetic model of interfacial degradation of adhesive joints". In: *IEEE Transactions on Components and Packaging Technologies* 22.2 (1999), pp. 215–220.

[252] M. Bischoff and E. Ramm. "Shear deformable shell elements for large strains and rotations". In: *International Journal for Numerical Methods in Engineering* 40.23 (1997), pp. 4427–4449.

[253] S. Klinkel and W. Wagner. "A geometrical non-linear brick element based on the EAS-method". In: *International Journal for Numerical Methods in Engineering* 40.24 (1997), pp. 4529–4545.

[254] E.N. Dvorkin and K. Bathe. "A continuum mechanics based four-node shell element for general non-linear analysis". In: *Engineering Computations* 1.1 (1984), pp. 77–88.

[255] P. Betsch and E. Stein. "An assumed strain approach avoiding artificial thickness straining for a non-linear 4-node shell element". In: *Communications in Numerical Methods in Engineering* 11.11 (1995), pp. 899–909.

[256] M Paggi, S Kajari-Schröder, and U Eitner. "Thermomechanical deformations in photovoltaic laminates". In: *The Journal of Strain Analysis for Engineering Design* 46.8 (2011), pp. 772–782.

[257] Idiano D'Adamo, Michela Miliacca, and Paolo Rosa. "Economic feasibility for recycling of waste crystalline silicon photovoltaic modules". In: *International Journal of Photoenergy* 2017 (2017).

[258] Michele Goe and Gabrielle Gaustad. "Strengthening the case for recycling photovoltaics: An energy payback analysis". In: *Applied Energy* 120 (2014), pp. 41–48.

[259] Federica Cucchiella, Paolo Rosa, et al. "End-of-Life of used photo-voltaic modules: A financial analysis". In: *Renewable and Sustainable Energy Reviews* 47 (2015), pp. 552–561.

[260] G Granata et al. "Recycling of photovoltaic panels by physical operations". In: *Solar energy materials and solar cells* 123 (2014), pp. 239–248.

[261] Bai-Peng Song et al. "Recycling experimental investigation on end of life photovoltaic panels by application of high voltage fragmentation". In: *Waste Management* 101 (2020), pp. 180–187.